



**University of  
Leicester**

**Using multiwavelength observations of  
short GRBs to constrain their progenitors**

**Beatrix Antonia Rowlinson**

**Supervisors:**  
Paul O'Brien  
Nial Tanvir

Thesis submitted for the degree of  
Doctor of Philosophy  
at the University of Leicester

X-ray & Observational Astronomy Group  
Department of Physics and Astronomy  
University of Leicester

August 2011

# Declaration

I hereby declare that no part of this thesis has been previously submitted to this or any other University as part of the requirement for a higher degree. The work described herein was conducted by the undersigned, except for contributions from colleagues as acknowledged in the text.

Beatrix Antonia Rowlinson

August 2011

# Using multiwavelength observations of short GRBs to constrain their progenitors

Beatrix Antonia Rowlinson

## Abstract

Short gamma-ray bursts (SGRBs) are extremely bright flashes of gamma-rays, lasting less than 2 s, originating from beyond the Milky Way but their progenitors remain unknown. The most popular progenitor theory involves the merger of two compact objects, either two neutron stars (NSs) or a NS and a black hole (BH), which then collapse to form a BH. A small proportion of SGRBs may instead be giant flares from extragalactic soft gamma-ray repeaters (SGRs) in nearby galaxies. The aim of this Thesis is to place constraints on the progenitors of SGRBs using multiwavelength observational data.

The extragalactic SGR giant flare theory is tested by considering the properties of three candidate SGRBs which may have occurred in nearby host galaxies. It is likely that only one of the three was an extragalactic SGR giant flare and, although they are all shown to be consistent with this progenitor, GRB 070201 is most convincing candidate. Afterglow predictions are made for future candidates.

Following on from the giant flare candidates, more typical SGRBs are considered. GRB 080905A is the nearest confirmed SGRB, occurring offset from a spiral galaxy at  $z \sim 0.12$  which is studied using spatially resolved spectroscopy. The properties of GRB 080905A are shown to be consistent with a compact binary merger. GRB 090515 was a SGRB with an extremely unusual bright X-ray plateau and extremely steep decay phase. However, the prompt and late time properties are consistent with typical SGRBs. The plateau is explained by an unstable magnetar, formed during the SGRB, which collapses to form a BH within a few hundred seconds. The magnetar is suggested to be formed via the merger of two NSs. Many *Swift* SGRBs are shown to have evidence of energy injection within their X-ray lightcurves and 44–76% are consistent with forming a magnetar.

*In loving memory of my Dad*

*(1945-2010)*

# Acknowledgements

Without the support of many people, this Thesis would not have come into existence. I would like to thank the following:

My Supervisors, Paul and Nial, have been the best supervisors I could ask for. During the last three years, they have been highly supportive and have directed me towards interesting projects whilst encouraging me to develop my own ideas. They have provided extremely useful advice and feedback with regards to both my work and career. Through this they have taught me about the many different roles of a researcher, providing me with invaluable skills which I hope to apply within my research for many years to come.

Also thank you to the whole *Swift* team at Leicester as they made me feel a welcome part of the team from the very beginning. It was fantastic being involved in the BA and XBS duties (even at 3am when that GRB has just woken you up...) and I greatly appreciate the responsibility and experience this provided. I'm especially grateful to Kim and Phil who taught me how to analyse *Swift* data and have given much valued support when needed.

Klaas and Rhaana have provided me with much valuable knowledge, ranging from how to analyse specific data to collaborating on papers to careers advice. I'd also like to thank Owen for our discussions sharing new ideas and skills. Some have already been mentioned, but I thank all the occupants of G17 who have shared this time with me; it has truly been an interesting, educational and entertaining experience making it a pleasure to come into work every day. Additionally, thank you to all the people who I have collaborated with.

I'd also like to thank all my friends, near and far, who encouraged me to pursue a PhD and have provided much valued support during my studies. Especially, I'd like to mention Helen Pollard (my A-level teacher who showed me how great Physics is and encouraged me to study it at university) and Paula Chadwick (who provided invaluable advice for applying for PhDs).

My family have always been incredibly supportive and I will always be grateful for that. I thank my brother Nic and his family (Mei-Mei, Katherine and Rachel) for their encouragement throughout this time.

Above all, I want to thank my Mum and Dad, I could not have achieved any of this without them. Their unending support when going through all of my studies and then their whole hearted support of my career change. Their "always do your best" and "pursue your goals" attitudes have got me where I am today. I wish my Dad was here to see the completion of this Thesis so he could see what I have achieved thanks to him but, sadly, this was not to be. Lastly a special thank you to Mum, for her continuing support despite the challenges she has faced in the last few years.

# Publication List

## Published Papers

- *The unusual X-ray emission of the short Swift GRB 090515: Evidence for the formation of a magnetar?*  
Rowlinson et al., 2010, MNRAS, 409, 531
- *Discovery of the afterglow and host galaxy of the low redshift short GRB 080905A*  
Rowlinson et al., 2010, MNRAS, 408, 383
- *A new analysis of the short-duration, hard-spectrum GRB 051103, a possible extragalactic soft gamma repeater giant flare*  
Hurley, Rowlinson et al., 2010, MNRAS, 403, 342
- *Discovery of the nearby long, soft GRB 100316D with an associated supernova*  
Starling et al., 2011, MNRAS, 411, 2792
- *GRB 090429B as an Extreme-Redshift Gamma-Ray Burst*  
Cucchiara et al., 2011, ApJ, 736, 7

## Papers in Prep

- *Evidence of energy injection in short GRB lightcurves and the role of magnetars as central engines*  
Rowlinson et al.
- *On the nature of the “hostless” short GRBs*  
Tunnicliffe et al.
- *Subthreshold GRBs detected by the INTEGRAL satellite*  
Rowlinson et al.

## GCNs and GCN Reports

- *As First Author :*

12283, 12282, 12079, 12071, 11909, 11760, 11335, 11039, 10639, 10444, 10435, 10430, 10135, 9857, 9642, 9378, 9374, 9298, 9073, 9052, 8840, 8828

- *Other GCNs :*

12279, 12173, 12158, 12065, 11941, 11931, 12082, 11941, 11931, 11658, 11572, 11848, 11448, 11331, 11318, 11288, 11277, 11214, 11203, 11181, 11159, 11031, 11009, 11004, 10894, 10884, 10834, 10826, 10824, 10741, 10737, 10708, 10703, 10628, 10612, 10581, 10489, 10442, 10436, 10434, 10432, 10256, 10191, 10148, 10130, 10048, 9978, 9913, 9854, 9718, 9706, 9659, 9633, 9625, 9621, 9545, 9400, 9386, 9384, 9377, 9356, 9281, 9280, 9254, 9223, 9149, 9135, 9133, 9101, 9066, 9062, 8964, 8939, 8861, 8804, 8687

- *GCN Reports :*

334, 305, 296, 256, 239, 235, 228, 215, 208, 207, 206, 195

# CONTENTS

<b>1</b>	<b>Introduction</b>	<b>1</b>
1.1	History . . . . .	1
1.1.1	The <i>Pioneer Venus Orbiter</i> . . . . .	2
1.1.2	The Inter Planetary Network . . . . .	2
1.1.3	The <i>CGRO</i> and BATSE Era . . . . .	4
1.1.4	<i>Beppo-SAX</i> . . . . .	4
1.1.5	Other missions . . . . .	6
1.1.6	<i>Swift</i> . . . . .	6
1.1.7	<i>Fermi</i> . . . . .	8
1.2	Fireball Model . . . . .	9
1.2.1	Central Engine . . . . .	9
1.2.2	Jets . . . . .	11

1.2.3	Observational properties of prompt emission . . . . .	13
1.2.4	Redshift distribution of GRBs and possible correlations . . . . .	14
1.2.5	Internal shock theory . . . . .	16
1.2.6	Poynting flow theory . . . . .	16
1.2.7	Curvature Effect . . . . .	17
1.2.8	Reverse and External shocks . . . . .	18
1.2.9	Observed Afterglows . . . . .	18
1.3	Host galaxies . . . . .	22
1.3.1	Host galaxies of LRGBs . . . . .	22
1.3.2	Host galaxies of SGRBs . . . . .	24
1.4	Classification methods . . . . .	26
1.4.1	Evidence for two populations . . . . .	26
1.4.2	Extended Emission bursts . . . . .	28
1.4.3	Intermediate GRBs . . . . .	29
1.5	Progenitor Theories . . . . .	29
1.5.1	Collapsar . . . . .	29
1.5.2	Compact binary mergers . . . . .	31
1.6	Soft Gamma-ray Repeaters . . . . .	34
1.6.1	SGR giant flares . . . . .	35

1.6.2	SGR giant flares and SGRBs . . . . .	36
1.7	Neutron Stars . . . . .	37
1.8	This Thesis . . . . .	39
<b>2</b>	<b>Extragalactic SGR giant flares</b>	<b>41</b>
2.1	Introduction . . . . .	41
2.2	GRB 051103 . . . . .	42
2.2.1	Prompt properties . . . . .	42
2.2.2	Optical Observations and Analysis . . . . .	46
2.2.3	Progenitor option 1: a SGRB . . . . .	49
2.2.4	Progenitor option 2: an SGR giant flare in M81 . . . . .	51
2.2.5	Conclusions regarding GRB 051103 . . . . .	57
2.3	GRB 070201 . . . . .	58
2.3.1	Methods . . . . .	58
2.3.2	Conclusions regarding GRB 070201 . . . . .	66
2.4	GRB 110406A . . . . .	66
2.5	Implications for future studies . . . . .	67
2.6	Extragalactic SGR giant flare rate in the local Universe . . . . .	72
2.7	Overall Conclusions . . . . .	74

<b>3</b>	<b>GRB 080905A</b>	<b>76</b>
3.1	Introduction . . . . .	76
3.2	Observations and Analysis . . . . .	77
3.2.1	Prompt emission properties . . . . .	77
3.2.2	X-ray Afterglow Observations . . . . .	78
3.2.3	Optical Observations . . . . .	79
3.2.4	Host Galaxy Spectroscopy . . . . .	84
3.3	Host galaxy properties . . . . .	87
3.3.1	Host morphology . . . . .	87
3.3.2	Rotation curve . . . . .	88
3.3.3	Spatially resolved properties . . . . .	89
3.4	Discussion . . . . .	95
3.5	Conclusions . . . . .	96
<b>4</b>	<b>GRB 090515</b>	<b>98</b>
4.1	Introduction . . . . .	98
4.2	Observations . . . . .	99
4.2.1	Swift Observations . . . . .	99
4.2.2	Early Optical Observations . . . . .	101

4.2.3	Gemini Observations . . . . .	103
4.3	Comparison to other GRBs . . . . .	106
4.3.1	GRBs with similar fluence to GRB 090515 . . . . .	111
4.3.2	GRBs with steep decays . . . . .	112
4.4	Discussion . . . . .	112
4.4.1	An under-luminous naked LGRB . . . . .	112
4.4.2	An unstable millisecond pulsar (magnetar) central engine . . . . .	114
4.5	Conclusions . . . . .	119
<b>5</b>	<b>Energy Injection in SGRBs</b>	<b>121</b>
5.1	Introduction . . . . .	121
5.2	“Canonical” SGRB lightcurves . . . . .	123
5.3	Magnetar model . . . . .	138
5.3.1	Theory . . . . .	138
5.3.2	SGRBs fitted with the magnetar model . . . . .	140
5.3.3	Analysis . . . . .	149
5.3.4	Discussion . . . . .	165
5.3.5	Gravitational Wave Signals . . . . .	173
5.4	Conclusions . . . . .	177

<b>6</b>	<b>Conclusions</b>	<b>183</b>
6.1	Progress towards the progenitors and central engines of SGRBs . . . . .	183
6.1.1	Extragalactic SGR giant flares . . . . .	183
6.1.2	Compact Binary Mergers . . . . .	185
6.1.3	Magnetars as the central engine of some SGRBs . . . . .	186
6.2	The future . . . . .	188
6.2.1	Detection of SGRBs . . . . .	188
6.2.2	LOFAR . . . . .	189
6.2.3	ALMA . . . . .	190
6.2.4	Neutrino Detectors . . . . .	190
6.2.5	Advanced LIGO and ET . . . . .	191
6.3	Final concluding remarks . . . . .	191

# LIST OF FIGURES

1.1	BATSE $T_{90}$ distribution . . . . .	5
1.2	The fireball model . . . . .	9
1.3	The curvature effect . . . . .	13
1.4	Cumulative redshift distribution of GRBs . . . . .	15
1.5	The “canonical” lightcurve . . . . .	19
1.6	GRB locations in their host galaxies . . . . .	23
1.7	SGR 1806-20 giant flare lightcurve . . . . .	35
1.8	NS equations of state . . . . .	38
2.1	The field of GRB 051103 . . . . .	44
2.2	The light curve of GRB 051103 . . . . .	45
2.3	<i>GALEX</i> image showing the UV sources within the error ellipse . . . . .	55
2.4	GRB 070201: Location with respect to M31 . . . . .	61

2.5	GRB 070201: UV image . . . . .	62
2.6	2XMM and optical properties in comparison to AGN . . . . .	65
2.7	GRB 110406A SPI-ACS Lightcurve . . . . .	68
2.8	GRB 110406A <i>Konus-Wind</i> Lightcurve . . . . .	69
2.9	GRB 110406 and NGC 404 . . . . .	70
3.1	The combined BAT and XRT luminosity and rest frame light curve for GRB 080905A	80
3.2	The optical afterglow of GRB 080905A . . . . .	81
3.3	The host galaxy of GRB 080905A . . . . .	82
3.4	The observed spectra in the northern spiral arm, the central bulge and the southern spiral arm of the host galaxy of GRB 080905A . . . . .	90
3.5	Properties of the host galaxy of GRB 080905A . . . . .	92
4.1	The combined light curve for GRB 090515 . . . . .	100
4.2	The optical afterglow of GRB 090515 . . . . .	105
4.3	The fluence in the energy band 0.3 – 10 keV versus the 15 – 150 keV flux for all Swift SGRBs . . . . .	108
4.4	The BAT-XRT light curve and hardness ratios for GRB 090515 in comparison to other GRBs . . . . .	109
4.5	Optical flux light curves for all observed SGRB afterglows in the R band . . . . .	110
4.6	Graphs showing the magnetic field and period for a millisecond pulsar formed during GRB 090515 . . . . .	116

4.7	The effect of beaming the emission of GRB 090515 on the magnetic field and spin period	120
5.1	BAT-XRT lightcurves for SGRB sample . . . . .	127
5.2	Break times of “canonical” like SGRB lightcurves . . . . .	129
5.3	Temporal indices of “canonical” like SGRB lightcurves . . . . .	130
5.4	Prompt properties versus XRT flux at 100 s for SGRBs . . . . .	132
5.5	Photon index comparisons for different phases of SGRB lightcurves . . . . .	133
5.6	Comparison of prompt and plateau fluence . . . . .	134
5.7	Spectral versus temporal indices for SGRBs . . . . .	136
5.8	Plateau flux or luminosity versus the plateau duration . . . . .	137
5.9	SGRB lightcurves fit with the magnetar model . . . . .	146
5.10	Magnetic field and spin period of magnetar candidates . . . . .	150
5.11	Prompt emission properties of magnetar sample . . . . .	151
5.12	XRT fluxes of the magnetar sample at different times . . . . .	154
5.13	Prompt emission photon index versus the plateau photon index . . . . .	156
5.14	Intrinsic restframe absorption of the magnetar sample . . . . .	157
5.15	Flux lightcurves comparing optical and X-ray data for the SGRB magnetar sample . . . . .	159
5.16	Flux lightcurves comparing optical and X-ray data for the other SGRB sample . . . . .	163
5.17	Optical flux versus the X-ray flux during the plateau regime . . . . .	164

5.18	Accretion effects on the spin period and rotational energy available for a magnetar . . .	168
5.19	Mass accreted by different magnetar candidates . . . . .	170
5.20	Energy emitted during plateau phase in comparison to that emitted during the prompt phase . . . . .	172
5.21	The spin parameter for magnetar candidates . . . . .	175

# LIST OF TABLES

1.1	Satellites used to study GRBs . . . . .	3
1.2	GRBs with associated SN . . . . .	30
1.3	Extra-galactic SGR giant flare candidates . . . . .	37
2.1	The observed fluence of SGRBs with observed R band magnitudes at approximately 3 days . . . . .	50
2.2	Candidate X-ray source and SNR matches . . . . .	60
2.3	Candidate X-rays and optical data . . . . .	64
2.4	X-ray afterglow flux predictions at a distance of M81. . . . .	71
3.1	Log of observations of the afterglow and host of GRB 080905A . . . . .	85
4.1	The optical observations of the field of GRB 090515 . . . . .	102
4.2	Log of Gemini observations for GRB 090515 . . . . .	104
4.3	Photometry of the nearby galaxies in the field of GRB 090515 . . . . .	106

4.4	GRBs compared to GRB 090515 . . . . .	107
5.1	Fits for SGRB lightcurves and spectra . . . . .	124
5.2	Properties of the SGRB magnetar sample . . . . .	141
5.3	Magnetar model fits to the SGRB sample . . . . .	144
5.4	Plateau spectral fits for the SGRB magnetar sample . . . . .	155
5.5	Gravitational wave predictions for magnetars formed by NS mergers . . . . .	176
5.6	Magnetar sample summary table . . . . .	178

# Chapter

# 1

## Introduction

In 1963 the first Vela satellites were launched to monitor the nuclear test ban treaty and on 2nd July 1967 they detected an extraterrestrial flash of gamma-rays. This Gamma-Ray Burst (GRB) known as GRB 670702 (Year, Month, Day) was the first of a series of GRB detections, with durations ranging from 0.3 to 30 s, by the Vela satellites (Klebesadel et al., 1973). In 1974, at the Texas Symposium, Ruderman (1975) reviewed the various theories to describe GRBs. There were 140 different models described ranging from comet collisions in the Oort cloud to star quakes. GRBs are now known to be the most powerful explosions in the Universe and in just a few seconds they radiate as much energy as the Sun will radiate during its entire lifetime.

### 1.1 History

By 1981, it had become clear that GRBs have erratic variability and a non-thermal spectrum, no two GRBs were the same and they were never seen to repeat. There were also the first signs that there may be more than one type of GRB: those with single long pulses, those with multiple pulses and a distinct group with very short durations (Mazets & Golenetskii, 1981). Paczynski (1986) predicted that these events were cosmological however, as the amount of energy required was staggering, a Galactic origin was favoured.

The millisecond variability of GRBs can be used to calculate the maximum size of the emitting region,  $D$ , using Equation 1.1 where  $c$  is the speed of light and  $\Delta t$  is the minimum variability observed. A variation of 1 ms gives an emitting region of 300 km, so GRBs originate from a compact source (Schmidt, 1978).

$$D < c\Delta t \quad (1.1)$$

Since the discovery of GRBs, a several satellite missions have been used to study their properties. They are summarised in Table 1.1 and the following Sections.

### 1.1.1 The Pioneer Venus Orbiter

The *Pioneer Venus Orbiter* was launched on 20th May 1978. It arrived at Venus and began observations on 4th December 1978. On board was the Orbiter Gamma Burst Detector (OGBD; Klebesadel et al., 1980). OGBD detected 225 GRBs during its operation and this enabled the all sky rate to be determined for the first time. The rate was consistent with a uniform spatial distribution of progenitors (Chuang et al., 1992).

### 1.1.2 The Inter Planetary Network

The Inter Planetary Network (IPN, recent results published by Hurley et al., 2010a) was the first experiment explicitly designed to study GRBs and comprises of a number of gamma-ray detectors onboard satellites throughout the Solar System. The IPN initially started with the launch of *Ulysses* (Wenzel et al., 1992) which carried a GRB experiment and missions with gamma-ray detectors, such as the *Pioneer Venus Orbiter*, were included while they were operational. The IPN has evolved with the launch of new missions and as older missions have retired. Currently contributing satellites include: *Swift*,

Satellite	Instrument	Energy Band	Operational
<i>Vela</i>		3 – 12 keV	1963 – 1972
<i>Pioneer Venus Orbiter</i>	OGBD	100 keV – 2 MeV	1978 – 1992
<i>IPN</i>	Various	Various	1990 – present
<i>CGRO</i>	BATSE	20 – 1000 keV	1991 – 2000
	EGRET	30 MeV – 10 GeV	
<i>GGG-Wind</i>	Konus	10 keV – 10 MeV	1994 – present
<i>RXTE</i>		2 – 250 keV	1995 – present
<i>Beppo-SAX</i>		0.1 – 700 keV	1996 – 2002
<i>HETE II</i>		0.2 – 600 keV	2000 – 2006
<i>Suzaku</i>		0.2 – 600 keV	2003 – present
<i>INTEGRAL</i>	ISGRI	15 keV – 10 MeV	2004 – present
<i>Swift</i>	BAT	15 – 350 keV	2004 – present
	XRT	0.3 – 10 keV	
	UVOT	2.07 – 7.29 eV	
<i>Agile</i>		300 keV – 100 MeV	2007 – present
<i>Fermi</i>	GBM	8 keV – 40 MeV	2009 – present
	LAT	20 MeV – 300 GeV	
<i>ISS</i>	MAXI	0.3 – 30 keV	2009 – present

Table 1.1: This Table gives a summary of the main satellites used to study GRBs and a selection of the instruments on board.

*Konus-Wind*, *HETE-II* and *Mars Odyssey*<sup>1</sup>. In a similar way to the *Vela* satellites, but on larger scale, the IPN uses timing analysis between pairs of satellites to triangulate the position of a GRB. This gives rise to characteristically long (several degrees) and narrow error trapezia. Unfortunately, the positions are not communicated to the ground rapidly and it can take several days before the GRB and its position is known. GRB 991208 was the first GRB localised by only the IPN with a detected afterglow (Hurley et al., 2000a).

### 1.1.3 The *CGRO* and *BATSE* Era

The Burst and Transient Source Experiment (*BATSE*) was launched on board the *Compton Gamma-Ray Observatory (CGRO)* on the 5th April 1991 (Fishman et al., 1985). The *BATSE* results showed an isotropic distribution, ruling out a Galactic plane origin but still allowing the GRBs to originate from the extended Galactic halo or from an extragalactic source population (Meegan et al., 1992).

Kouveliotou et al. (1993) calculated the duration during which 90% of the fluence of a GRB is emitted leading to the definition of the  $T_{90}$  duration now used for all GRBs. They identified a bimodal distribution in the  $T_{90}$  durations of the *BATSE* sample, shown in Figure 1.1. Using the hardness ratio,  $\frac{100-300 \text{ keV}}{50-100 \text{ keV}}$ , *BATSE* showed that SGRBs are on average spectrally harder than LGRBs (Kouveliotou et al., 1993).

Also onboard *CGRO* was the Energetic Gamma-Ray Experiment Telescope (*EGRET*) which detected high energy ( $>30 \text{ MeV}$ ) emission for five of the GRBs detected by *BATSE* (e.g. Schneid et al., 1992).

### 1.1.4 *Beppo-SAX*

*Beppo-SAX* was an Italian–Dutch satellite (Boella et al., 1997) which detected GRBs and slewed to point an X-ray telescope at the GRB location within 5–12 hours after the trigger time. This enabled the first detections of X-ray afterglows with positions accurate to within a few arcmins. The X-ray afterglow detected for GRB 970228 (Costa et al., 1997) enabled the first detection of an optical afterglow

---

<sup>1</sup>Further information about the IPN and contributing satellites can be found here: <http://www.ssl.berkeley.edu/ipn3/>

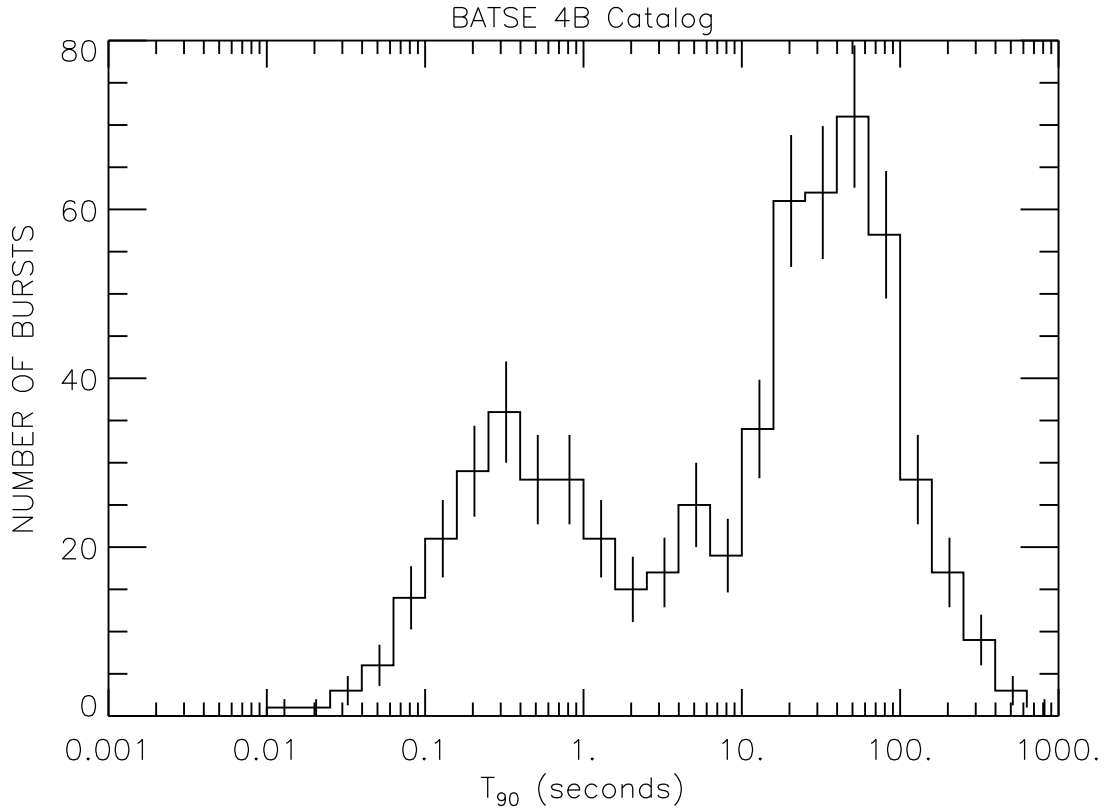


Figure 1.1: This figure shows the  $T_{90}$  distribution published in the final BATSE catalogue (Paciesas et al., 1999). This clearly shows two peaks in the distribution with a dividing line at  $\sim 2$  s. This led to the definition of short GRBs (SGRBs) with  $T_{90} \leq 2$  s and long GRBs (LGRBs) with  $T_{90} \geq 2$  s (Kouveliotou et al., 1993). Obviously there is an overlap between the two distributions.

and a host galaxy association (van Paradijs et al., 1997). A few months later, GRB 970508 had the first detection of an afterglow redshift,  $z \sim 0.835$ , proving these events were cosmological (Metzger et al., 1997).

The *Beppo-SAX* observations showed that GRBs fade with approximately a powerlaw decay,  $t^{-\alpha}$  where  $\alpha \sim 1.4$ , and the X-ray afterglows had a spectrum of  $\nu^{-\beta}$  where  $\beta \sim 0.9$  (Piro, 2001). The results from *Beppo-SAX* also allowed the discovery of X-ray Flashes (XRFs, e.g. Heise et al., 2001), and identification of potential correlations between observed properties and possible jet breaks. 90% of the GRBs observed by *Beppo-SAX* had detected X-ray afterglows and 50% had optical counterparts (de Pasquale et al., 2003).

### 1.1.5 Other missions

Konus-Wind – Konus-Wind was launched in November 1994 on board the *Global Geospace Science satellite* (GGs-Wind; Aptekar et al., 1995) and detects in excess of 100 GRBs per year providing lightcurves and spectra.

*RXTE* – The *Rossi X-ray Timing Explorer (RXTE)*<sup>2</sup> was launched in 30th December 1995. *RXTE* has detected the X-ray afterglows of several GRBs and detected variability in the X-ray afterglow of GRB 970828 (Yoshida et al., 2000).

*HETE 2* – The *High Energy Transient Explorer (HETE 2)*<sup>3</sup> was launched on 9th October 2000 after the failure to deploy *HETE 1* in 1996. It was particularly sensitive to XRFs, provided precise locations within 100 s and led to the detection of the first SGRB with an optical counterpart (Hjorth et al., 2005a; Villasenor et al., 2005; Covino et al., 2006)

*INTEGRAL* – The *International Gamma-Ray Astrophysics Laboratory (INTEGRAL; Winkler, Pace, & Volonté, 1993)* was launched in October 2002 with 4 instruments on board. *INTEGRAL* is highly sensitive and is useful for identifying the faintest GRB populations (Mereghetti, Götz, & Borkowski, 2004; Foley et al., 2009; Vianello, Götz, & Mereghetti, 2009; Ubertini et al., 2011, Rowlinson et al. private communication).

MAXI – The Monitor of All-sky X-ray Image (MAXI; Matsuoka et al., 2009) is an X-ray imager which has detected 14 GRBs and XRFs to date. It is installed in the Japanese Experiment Module on board the International Space Station (ISS) and was operational from August 2009.

### 1.1.6 *Swift*

The *Swift* satellite is dedicated to the multi-wavelength study of GRBs (Gehrels et al., 2004) and much of this Thesis uses *Swift* observations. On board are three instruments; the Burst Alert Telescope (BAT), the X-ray Telescope (XRT) and the Ultra-Violet and Optical Telescope (UVOT).

---

<sup>2</sup><http://heasarc.gsfc.nasa.gov/docs/xte>

<sup>3</sup><http://heasarc.gsfc.nasa.gov/docs/hete2>

BAT is a coded mask telescope which detects the GRBs, with accurate imaging, giving positions to 1–4 arcmins, and spectroscopy over 15 – 150 keV (Barthelmy et al., 2005a). BAT triggers using a variety of criteria including a threshold of  $6.5\sigma$  above the background level.

XRT operates in the energy band 0.3 – 10 keV and is a grazing incidence X-ray telescope that has four different modes for taking observations: Image Mode (IM), Photon Diode (PD), Window Timing (WT) and Photon Counting (PC) (Burrows et al., 2005a). IM is used when the satellite first slews to a GRB target, the CCD is used to give an image of the source giving the first accurate position but the image is often highly piled up. After IM, the PD mode was to be used for high accuracy timing and gave no positional information as the chip was read as if it were 1 pixel. Due to a micrometeorite hit within the first 6 months, PD mode is no longer usable as it was not possible to calibrate. WT mode reads off each column of pixels within the CCD, so the observation is summarised in a 1D image. This mode is used for the slew data and the brightest sources which would otherwise saturate the CCD.

PC mode reads each individual pixel of the CCD; however this is slow and hence bright sources can cause the CCD to become piled up. Pile up occurs when more than 1 photon arrives at a pixel during the time it takes to read the pixel out. Therefore, it cannot be determined if the signal in a pixel is due to 1 photon of high energy or several photons of low energy. In PC mode, the source in an image can be fitted with a gaussian with a full-width-half-maximum given by the resolution of XRT (14 arcsec). The position of the source is defined to be the peak of the gaussian. However, the peak cannot be determined precisely due to noise, giving a position error of typically  $\sim 4$  arcsec. This position can be improved further using UVOT images as the exact relative position between XRT and UVOT is known. The positions of known stars in the UVOT field can be used to more accurately determine the pointing of *Swift* reducing the error in the XRT positions. The positions are typically improved to  $\sim 1 - 2$  arcsec using UVOT images (UVOT enhanced positions; Goad et al., 2007).

The XRT data are now automatically analysed by the UK *Swift* Science Data Centre and the analysis is described in Evans et al. (2007, 2009). After a GRB is detected by BAT, *Swift* slews to point XRT at the burst location and observations typically start  $\sim 100$  s after the trigger time. However, a rapid slew was not always possible due to observing constraints related to the Sun, Earth and Moon.

A few hundred seconds after a trigger and shortly after XRT, UVOT starts taking observations (Roming et al., 2005). It then takes a finding chart using the v band filter to determine if there is a detected optical afterglow and then cycles through the different filters.

On 9th May 2005, *Swift* detected the first X-ray afterglow of a SGRB, GRB 050509B, leading to the association of this SGRB to an old elliptical host galaxy (Gehrels et al., 2005; Barthelmy et al., 2005b; Hjorth et al., 2005a). Another highlight of the *Swift* mission was GRB 080319B, the “naked eye” burst (Racusin et al., 2008) which a human eye, if looking in the right direction and at the right time, would have been able to detect the optical flash.

*Swift* has made great leaps in the quest to see the furthest objects in the Universe. April 2009 led to the discovery of two extremely high redshift GRBs within just 1 week: GRB 090423 at a spectroscopic redshift of 8.2 (Tanvir et al., 2009; Salvaterra et al., 2009) and GRB 090429B at a photometric redshift of 9.4 (Cucchiara et al., 2011).

The effective areas of BATSE and BAT are comparable at  $\sim 150$  keV. However at energies  $\leq 100$  keV the effective area of BATSE drops significantly whereas BAT peaks at 30 – 100 keV. At  $\geq 150$  keV BATSE remains sensitive up to 1 MeV. The sensitivity of BAT drops rapidly at  $> 150$  keV and does not operate above 350 keV. Therefore BATSE is able to detect much harder GRBs than BAT (Sakamoto et al., 2011). Additionally, BATSE used rate triggers to identify new GRBs but BAT requires an image to confirm the trigger. This means that faint hard bursts are less likely to trigger BAT (Sakamoto et al., 2011). Also BAT and BATSE could classify GRBs differently, for example a short hard burst with extended emission may be identified as a LGRB by BAT and a SGRB by BATSE (which is insensitive to the much softer extended emission; Norris & Bonnell, 2006). These factors can explain the different rates of SGRBs found by BAT and BATSE: 25% of GRBs detected by BATSE were SGRBs compared to just 10% for BAT.

### 1.1.7 *Fermi*

The *Fermi* satellite was launched on 11th June 2008 with two instruments on board, the Large Area Telescope (LAT, 20 MeV – 300 GeV; Atwood et al., 2009) and the Gamma-ray Burst Monitor (GBM,

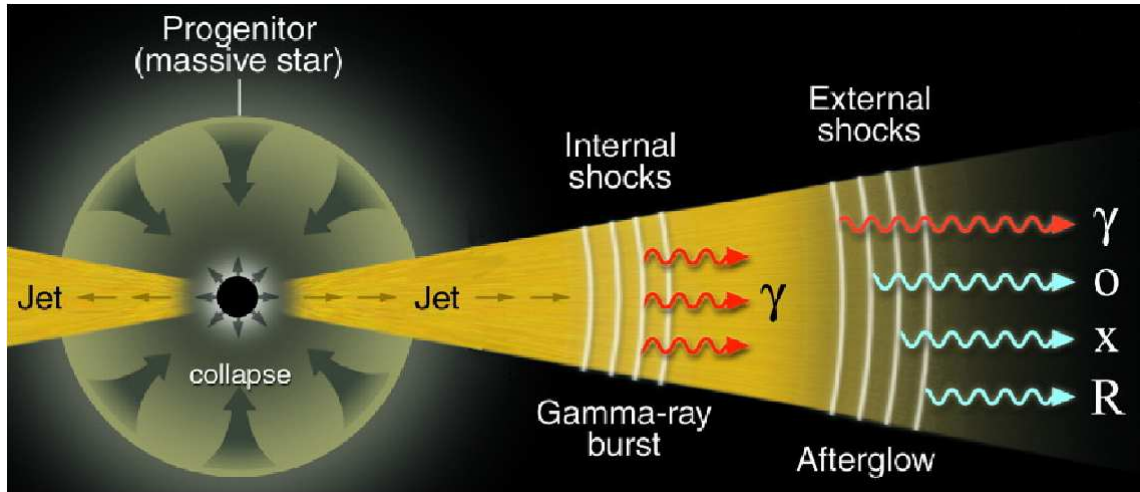


Figure 1.2: This figure, adapted from Mészáros (2001), shows the main components of the fireball model assuming a massive star progenitor (a binary merger would also produce these jets and have the same emission properties).

8 keV – 40 MeV; Meegan et al., 2009). GBM provides poor position errors,  $\sim 5$  degrees with ground analysis, and typically detects 1 GRB every 2 days. LAT has detected 12 GRBs to date with very high energy emission although most GRBs in the LAT field of view are not detected (Akerlof et al., 2011).

## 1.2 Fireball Model

This section will describe the main features of the popular Fireball model used to describe the emission from GRBs and illustrated in Figure 1.2. This model is the favoured explanation for the majority of both LGRBs and SGRBs.

### 1.2.1 Central Engine

The rapid variability of GRBs shows the central engine needs to be a compact source and two objects have the required compactness: black holes (BHs) and neutron stars (NSs).

### Black Hole Central Engine

The typical model of a GRB involves the rapid formation of a BH and the surrounding material collapsing into an accretion disk. The energy supply is the matter in the accretion disk and the BH has an extremely high accretion rate ( $0.01-1.0 M_{\odot} \text{ s}^{-1}$ ). The extremely hot ( $T \sim 10^{10} \text{ K}$ ) and dense ( $\rho \sim 10^{16} \text{ g cm}^{-3}$ ) accretion disk produces neutrinos and anti-neutrinos which preferentially annihilate above and below the accretion disk. When the neutrinos and anti-neutrinos annihilate they produce a plasma of  $e^{\pm}$  and photons, known as a fireball, which is formed along the rotation axis of the star. This fireball is then further accelerated and collimated producing a jet along the axis of rotation (although the exact process is still unclear, e.g. Popham, Woosley, & Fryer, 1999). This central engine is capable of emitting vast amounts of energy ( $E_{iso} \sim 10^{54} \text{ erg}$ , rest mass of  $0.6 M_{\odot}$ ) within a few thousand seconds. However, as discussed further in Section 1.2.2, the central engine is thought to beam this emission. If the emission is beamed the actual energy released is given by equation 1.2 (Frail et al., 2001). For  $E_{iso} \sim 10^{54} \text{ erg}$  and assuming a beaming angle of 3 degrees, the energy emitted would instead be  $E_{\gamma} \sim 1.4 \times 10^{51} \text{ erg}$ . This corresponds to the rest mass of  $8 \times 10^{-4} M_{\odot}$  being released as energy.

$$E_{\gamma} = (1 - \cos \theta) E_{iso}(\gamma) \quad (1.2)$$

### Magnetar Central Engine

Alternative theories suggest that the compact object does not necessarily collapse to form a BH and can instead leave behind a highly magnetic NS known as a magnetar (Usov, 1992; Duncan & Thompson, 1992; Wheeler et al., 2000; Thompson, Chang, & Quataert, 2004). Magnetars have extremely high magnetic fields ( $\geq 10^{15} \text{ G}$ ) and are born rapidly rotating ( $P \sim 1-10 \text{ ms}$ ). The extreme magnetic fields originate from the amplification of magnetic fields which could be due to a convective dynamo (Duncan & Thompson, 1992). The energy available is extracted via the emission of numerous neutrinos and from

the immense amount of rotational energy that this newly formed magnetar has and is given by:

$$E_{total} \sim 10^{52} \left( \frac{P}{1 \text{ ms}} \right)^{-2} \text{ erg} \quad (1.3)$$

This equation is simply the rotational kinetic energy of an object which is proportional to its moment of inertia and the square of its angular velocity. It has assumed typical values for the mass and radius of a neutron star to quantify the moment of inertia. Bucciantini et al. (2009) have used simulations to show that relativistic jets can be launched by magnetars but with relatively low Lorentz factors. Therefore, the magnetar model may not explain very energetic GRBs such as GRB 080721 (Starling et al., 2009; Cenko et al., 2010).

This model is different to the proposed magnetar giant flares which may also produce events similar to GRBs (discussed in more detail in Section 1.6).

### 1.2.2 Jets

The size of the emitting region causes a problem known as the “compactness problem”. The photons produced by the fireball have much more energy than is required for pair production of electrons and positrons. Also they are in extremely close proximity making it highly likely that pair production will occur (Ruderman, 1975; Schmidt, 1978; Goodman, 1986; Rhoads, 1997; Piran, 1999). Therefore the region should have a huge optical depth, as it is opaque to its own radiation, and the original photons would not be able to escape. So the only observable emission should be a thermal spectrum. This is solved if there is a highly relativistic outflow because the source region can be much larger than initially thought. This is because the observed variability in equation 1.1 should be replaced with the rest frame variability which is much longer in duration (a factor of  $2\gamma^2$ ). Additionally, the original distribution photons could be of much lower energy (and blue shifted in the relativistic outflow to the observed energies) so fewer photons are available with sufficient energy for pair production. Therefore, the central engine is thought to launch two relativistic jets although the exact mechanism remains unknown. The jets may be launched in a similar way to the Blandford & Znajek (1977) mechanism, in which accretion onto a rotating BH surrounded by a magnetic accretion disk leads to the formation of

jets (e.g. Barkov & Komissarov, 2008).

The composition of the jets is another mystery with the main contenders being a baryonic plasma (e.g. GRB 080319B; Kumar & Panaitescu, 2008) or a magnetised plasma (e.g. GRB 080916C; Zhang & Pe'er, 2009b). The jet starts optically thick (as the photons have more energy than is required for pair production) and flows out relativistically in two narrow beams.

Radio observations have provided strong evidence for relativistic jets (Frail et al., 1997, 1999). Jet opening angles for LGRBs are thought to be typically a few degrees (Harrison et al., 1999; Halpern et al., 2000; Panaitescu & Kumar, 2001; Racusin et al., 2009).

SGRBs are also thought to have jets although less beamed than LGRBs with observed values ranging from 4–25 degrees (Berger et al., 2005; Grupe et al., 2006; Panaitescu, 2006; Soderberg et al., 2006; Burrows et al., 2006; Nakar, 2007). The models by Janka et al. (2006) suggest that SGRBs have beaming angles  $\sim 20$  degrees, depending on how rapidly energy is deposited into the jet, and that the emission drops off very rapidly when viewing SGRBs off axis. Rezzolla et al. (2011) have completed simulations of NS-NS mergers in which the magnetic field orientates itself into two jet like funnels into which jets could be launched with half opening angles of 8–30 degrees. Although they are not relativistic and do not actually launch jets, it is the first step towards understanding them.

When the jets decelerate to non-relativistic velocities they rapidly spread sideways making a much larger emitting region, however this is only a small effect (van Eerten & MacFadyen, 2011) A more important factor is the Doppler beaming effect, as the jet slows down (i.e.  $\Gamma$  reduces) the opening angle of the jet increases ( $\theta \propto \frac{1}{\Gamma}$ , as shown in Figure 1.3). The Doppler beaming effect originates from the Lorentz transformations applied to the velocity of photons. If photons were only emitted parallel to the relativistic motion, then there would be no obvious effect (they remain travelling at the speed of light). However photons which are emitted at some angle,  $\theta$ , have a parallel velocity component which increases, tending towards the speed of light, but the perpendicular velocity component reduces as  $\frac{1}{\Gamma}$ . The observing angle is given by  $\tan \theta = \frac{\text{perpendicular velocity component}}{\text{parallel velocity component}} \propto \frac{1}{\Gamma}$  and in the small angle approximation  $\tan \theta \sim \theta$ . Even though the actual beaming angle can be much larger, the observer only sees the region of the jet given by the opening angle due to this Doppler beaming effect.

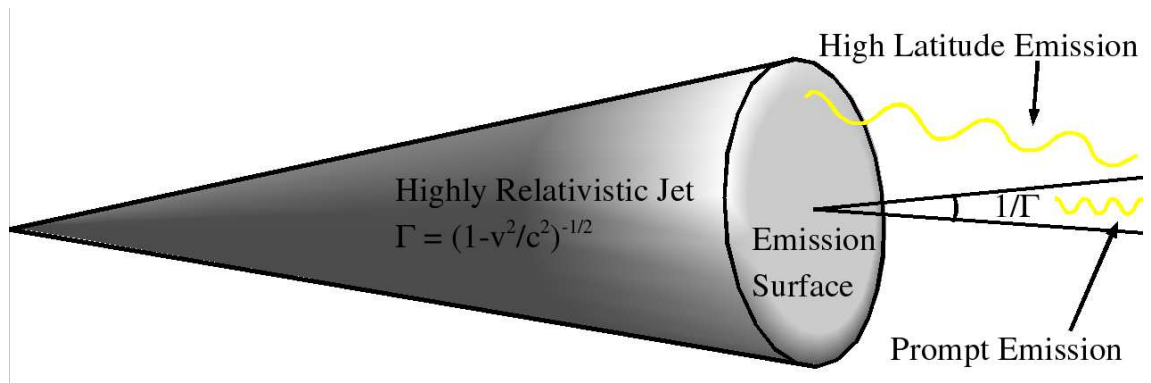


Figure 1.3: This shows the region of the jet observed during the prompt emission phase and the high latitude emission responsible for the curvature effect.

As the opening angle of the jet increases, the emission is spread over a larger viewing surface leading to a sudden drop in luminosity giving a jet break in the observed lightcurve (a lightcurve is a plot showing how flux or luminosity evolves with time; Rhoads, 1999; Sari, Piran, & Halpern, 1999).

The jet break would be achromatic (the same in all energy bands). Jet breaks are thought to have been observed and can be used to derive the total energy within the jet (e.g. GRB 990510 and recently GRB 080319B; Harrison et al., 1999; Tanvir et al., 2010a).

However, after the launch of the *Swift* satellite it became clear there were major problems with this theory as  $< 10\%$  of the *Swift* sample of GRBs have observed jet breaks (Mészáros, 2006; Willingale et al., 2007; Sato et al., 2007a). New theories suggest that jet breaks may not be the clear achromatic break expected as other components can dominate (Nardini et al., 2011) and this may resolve the missing jet break problems. Jet breaks are very rare for SGRBs (a likely jet break was detected for GRB 090426 by Nicuesa Guelbenzu et al., 2011).

### 1.2.3 Observational properties of prompt emission

The prompt emission often consists of combinations of FRED pulses (Fast Rise Exponential Decay; Norris et al., 1996). These pulses do not appear to evolve with time (Ramirez-Ruiz & Fenimore, 2000) and there can be quiescent times during the prompt emission (Ramirez-Ruiz & Merloni, 2001;

Quilligan et al., 2002). There is often a different arrival time for low frequency photons in comparison to the high frequency photons, this is known as the spectral lag and is calculated using cross-correlation of different energy bands, and there is a broadening of peaks at lower energies. For LGRBs the lag time typically varies from 20–1000 ms (Ukwatta et al., 2010) while SGRBs have negligible lag times (Norris & Bonnell, 2006; Yi et al., 2006).

The observed spectra of the prompt emission is typically fitted using the Band Spectrum (Band et al., 1993). There is often evolution from hard spectra to softer spectra during the prompt emission (Norris et al., 1986). Recent observations by *Fermi* LAT suggest there may be an additional high energy component observed in some GRBs which does not fit the typical fireball model (e.g. Zou, Fan, & Piran, 2009; Ghisellini et al., 2010; Zhang et al., 2011). Using the prompt emission spectra it is possible to subdivide the GRB population into Classical GRBs (CGRBs), X-ray Rich GRBs (XRRs) and X-ray Flashes (XRFs) (Sakamoto et al., 2008a). These may be different populations of GRBs or part of the same distribution. As the BATSE results showed, SGRBs tend to have harder prompt spectra and higher peak energies (Band et al., 1993; Malozzi et al., 1995; Ghirlanda, Ghisellini, & Celotti, 2004; Kaneko et al., 2006). Ghirlanda et al. (2009) showed that SGRB prompt pulses are harder with a higher peak energy ( $E_{peak}$ ) but are otherwise the same as LGRBs.

#### 1.2.4 Redshift distribution of GRBs and possible correlations

The average redshift of GRBs detected by the *Swift* satellite is  $z = 2.19$  and Figure 1.4 shows the redshift distribution of those GRBs (Jakobsson et al. Submitted)<sup>4</sup>. The GRB redshift distribution gives a unique method to study the star formation rate of the Universe (Fruchter et al., 1999; Christensen et al., 2004; Tanvir et al., 2004; Jakobsson et al., 2006) and may show evidence of an evolving star formation rate with redshift (Daigne et al., 2006, Jakobsson et al. Submitted).

As GRBs are observable across the Universe, it is highly desirable to find correlations to make them standard candles. A standard candle is a source with a known luminosity or total energy which can be used to measure the actual physical distance to the source, an invaluable quantity for cosmology.

<sup>4</sup><http://www.raunvis.hi.is/~pja/GRBsample.html>

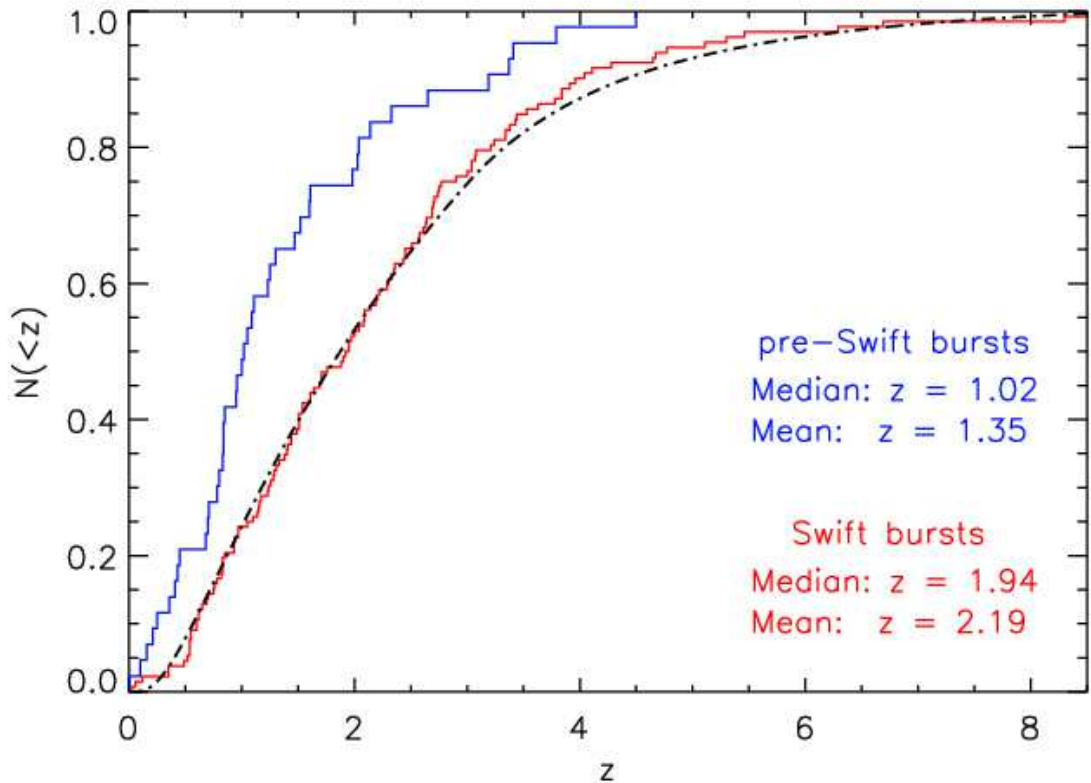


Figure 1.4: The normalised cumulative redshift distribution for all GRBs detected up to 30<sup>th</sup> May 2011, the dashed line represents the expected GRB rate for a given star formation history (Jakobsson et al. Submitted). Image taken from <http://www.raunvis.hi.is/~pja/GRBsample.html>

Several have been proposed including:

1. The Amati Relation suggests there is a correlation between the peak energy in the spectrum and the isotropic energy of the GRB. The original samples showed a correlation (Amati et al., 2002; Amati, 2006) however the inclusion of *Swift* and *Fermi* data have led to significantly more scatter (Amati, 2010). Additionally, SGRBs and some LGRBs do not fit on this relation (Butler et al., 2007).
2. The Ghirlanda Relation is a correlation between the peak energy and the beaming corrected energy emitted as gamma-rays (Ghirlanda, Ghisellini, & Firmani, 2005; Ghirlanda et al., 2008). However, *Swift* and *Fermi* results have shown there is significantly more scatter than thought (McBreen et al., 2010). Additionally, SGRBs do not fit this relation but do fit a similar relation

between the peak luminosity and isotropic energy (Ghirlanda et al., 2009).

3. The Asymmetry-Lag paradigm is an anti-correlation between the observed lag time and the peak luminosity of pulses which appears to work for both the prompt emission and X-ray flares (Norris, Marani, & Bonnell, 2000; Margutti et al., 2010; Ukwatta et al., 2010). However SGRBs with extended emission (see Section 1.4.2) do not fit the relation and neither do SGRBs as they have no observed lag times (Yi et al., 2006; Norris & Bonnell, 2006; Gehrels et al., 2006).

### 1.2.5 Internal shock theory

At a large distance from the central engine, some of the energy within the jet is emitted giving the observed prompt emission. The prompt emission is only observable for angles within the relativistic beaming angle,  $\theta \propto \frac{1}{\Gamma}$ , which corresponds to an emission area which is  $\propto \Gamma^2$ , where  $\Gamma$  is the bulk Lorentz factor of the jet (Piran, 2004).

GRBs show rapid variability during the main prompt emission which may be caused by internal collisionless shocks within the jets. The central engine emits shells, with different relativistic velocities, which collide within the jet giving internal shocks (Rees & Meszaros, 1994; Paczynski & Xu, 1994; Kobayashi, Piran, & Sari, 1997; Daigne & Mochkovitch, 1998, 2000). These shocks are known as collisionless because the thickness of the shells being shocked is much less than the collisional mean free path within that region (Piran, 2004). Electrons are accelerated across the shocks and emit synchrotron emission, these photons can then be up-scattered to higher energies via the inverse Compton effect (Shaviv & Dar, 1995; Lazzati et al., 2004). As the electrons used for the inverse Compton effect were the original source of the synchrotron emission, this is a special case of the inverse Compton effect known as synchrotron self Compton (Waxman, 1997; Ghisellini & Celotti, 1999).

### 1.2.6 Poynting flow theory

An alternative theory for the prompt emission, for a Poynting flow dominated jet with highly ordered magnetic field, is that the prompt emission originates from magnetic energy dissipation within the jets

(Thompson, 1994; Mészáros & Rees, 1997; Vlahakis & Königl, 2003). Extra components observed within the prompt emission of GRB 080916C (Zhang et al., 2009) and GRB 100724B (Guiriec et al., 2011) have been explained using this model.

One method to distinguish between these theories may be the observation of polarisation within the prompt emission (e.g. Fan, Zhang, & Proga, 2005) and this has been attempted for several GRBs with wide ranging and often controversial results (Coburn & Boggs, 2003; Rutledge & Fox, 2004; Wigger et al., 2004; Mundell et al., 2007; Götz et al., 2009; Steele et al., 2009).

### 1.2.7 Curvature Effect

During the prompt phase, the emission observed is only from a region of angular size  $\theta = \frac{1}{\Gamma}$  however the emission is likely to be spread out over a larger angle. The emission from angles  $\theta > \frac{1}{\Gamma}$  is not beamed directly towards the Earth but provides a significant contribution to the observed emission. As the emitting surface is thought to be curved, photons from larger angles have to travel a further distance which gives a time delay. Also, as the photons are not beamed directly towards us, they are at a lower frequency. Therefore, the high latitude emission arrives at a later time and lower frequency than the prompt emission. This process of observing the high latitude emission is known as the curvature effect (Kumar & Panaitescu, 2000) and is illustrated in Figure 1.3.

In the fireball model, the external shocks between the jets and the Interstellar Medium (ISM) give the multi-wavelength afterglow. However, if a GRB occurs in a very low density environment this component would be too faint to be detected. In this case, the only emission observable would be the prompt and high latitude emission. Therefore, the emission would fade extremely rapidly as described by the curvature effect and there would be no typical afterglow. GRBs with this kind of behaviour are described as “naked” GRBs, for example GRB 050421 (Godet et al., 2006). Additionally, as the popular progenitor theories for SGRBs occur in low density environments, SGRBs might be expected to also be “naked” GRBs.

### 1.2.8 Reverse and External shocks

When the jets collide with the ISM or the circum-stellar medium (CSM), two shocks are expected to form: one directed forwards into the ISM (the external shock, shown in Figure 1.2) and a reverse shock which propagates back through the jet. This reverse shock has been modelled by Sari, Piran, & Halpern (1999) and Akerlof et al. (1999). Reverse shocks are predicted to have an associated optical flash and there are several candidates which may have this feature (e.g. Sari & Piran, 1999a,b; McMahan, Kumar, & Piran, 2006).

The afterglow emission of GRBs is predicted to be associated with the relativistic jets shocking with the ISM, giving the external shocks (Rees & Meszaros, 1992; Mészáros & Rees, 1993). These shocks are expected to give synchrotron and inverse Compton spectra and are much less variable with time. The afterglow is then expected to fade as a powerlaw which is dependent on the frequency (as the afterglow is fading, the peak frequency of the synchrotron spectrum is also decreasing as the shock loses energy):

$$F_\nu(t) \propto t^{-\alpha} \nu^{-\beta} \quad (1.4)$$

$$\beta = \Gamma - 1 \quad (1.5)$$

where  $F_\nu(t)$  is the flux as a function of frequency ( $\nu$ ) and time ( $t$ ),  $\alpha$  is the temporal index and  $\beta$  is the spectral index. Equation 1.5 gives the relationship between  $\beta$  and the observed photon index  $\Gamma$ . The spectral index is obtained from the flux at a given energy (i.e.  $F \propto E^{-\beta}$ ). Whereas, the observed photon index is obtained from the flux of photons of a given energy plotted against the energy of the photon, i.e.  $\frac{F}{E} \propto E^{-\Gamma} \rightarrow F \propto E^{-\Gamma} E \propto E^{-(\Gamma-1)}$ .

### 1.2.9 Observed Afterglows

#### X-ray Afterglows

The *Swift* satellite has revolutionised the study of X-ray afterglows by identifying significant structure in the X-ray lightcurves including multiple breaks and flares. Evans et al. (2009) completed an in

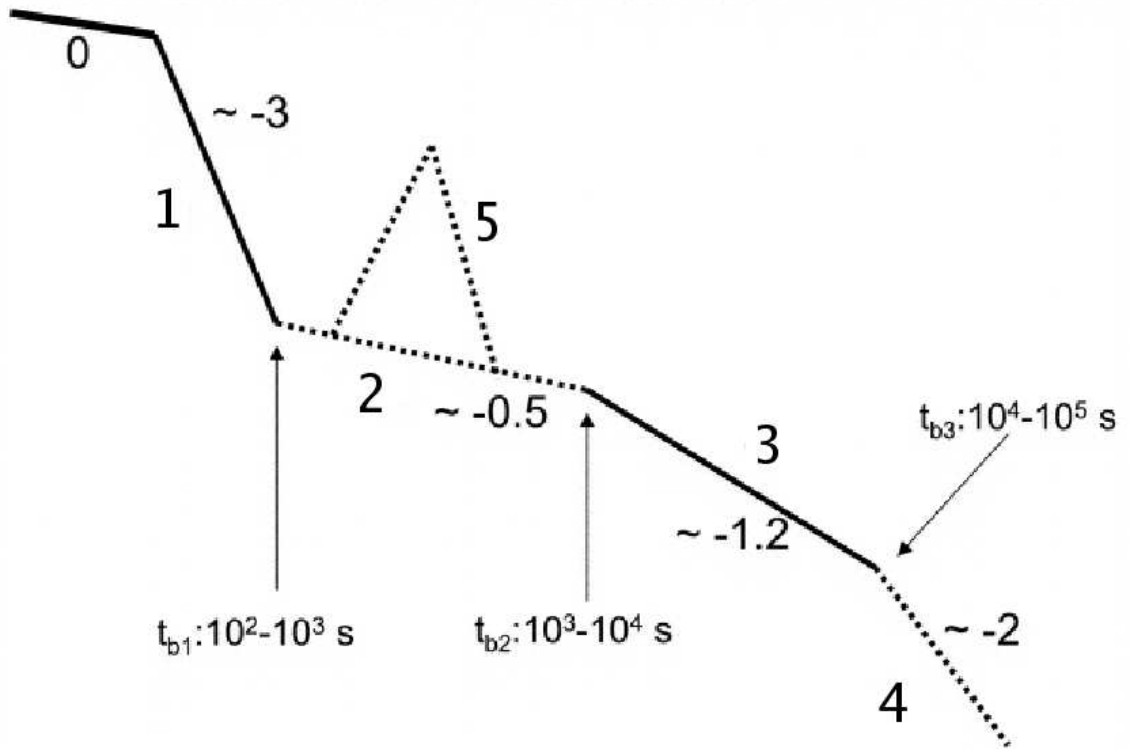


Figure 1.5: This figure illustrates the 5 main components and timescales of the “canonical” lightcurve observed in many X-ray afterglows of *Swift* GRBs. This figure is taken from Zhang et al. (2006) and shows how the flux varies with time with typical timescales and temporal indices.

depth study of the X-ray afterglows detected by *Swift* and found afterglows had four basic forms. They showed supporting evidence that 42% *Swift* GRBs have a “canonical” lightcurve as proposed by Nousek et al. (2006), O’Brien et al. (2006) and Zhang et al. (2006). The “canonical” lightcurve is shown in Figure 1.5 and comprises of the following stages:

1. Steep decay phase – the decay from the prompt emission, caused by high latitude emission and the curvature effect. The decay slope predicted by the curvature effect is given in equation 1.6. There is a smooth transition from the prompt emission to afterglow phase (O’Brien et al., 2006; Zhang et al., 2006).

$$\alpha = \beta + 2 \quad (1.6)$$

2. Shallow decay phase – thought to show ongoing energy injection from the central engine and cannot be explained in the typical fireball model (Nousek et al., 2006; Zhang et al., 2006).
3. Standard afterglow phase – the power law decline observed pre-*Swift*.
4. Jet break, as described in Section 1.2.2.
5. Flares – these can be comparable in energy to the prompt emission and  $\sim 50\%$  of the *Swift* sample have flares. They are interpreted as late time central engine activity and are thought to have the same emission mechanism as the prompt emission pulses (Burrows et al., 2005b; Falcone et al., 2006; Burrows et al., 2007; Curran et al., 2008; Chincarini et al., 2010). Theories include late time accretion (King et al., 2005), refreshed shocks (Panaitescu, 2006) and magnetic explosions on a newly formed magnetar (Dai et al., 2006).

The first X-ray afterglow for a SGRB was detected by the *Swift* satellite for GRB 050509B (Gehrels et al., 2005) and to date *Swift* has detected 31 SGRB afterglows. They fade more rapidly than LGRB afterglows and are generally fainter, but otherwise appear to share many features with LGRBs (Berger, 2007, Rowlinson et al. private communication). The significant structure in SGRB afterglows is problematic in the favoured theories for SGRBs and is discussed in more detail in Chapter 5 of this Thesis.

### Optical afterglows

The first optical afterglow was detected for the long GRB 990123 (Akerlof et al., 1999), the first for a SGRB was GRB 050724 (Fox et al., 2005; Hjorth et al., 2005a) and now many optical afterglows have been studied for both LGRBs and SGRBs.

The *Swift* sample of GRBs have dimmer optical afterglows than expected (Roming et al., 2006). BAT detects a fainter distribution of GRBs, which are either intrinsically fainter GRBs or more distant, therefore the optical afterglow is also fainter.

There are a category of optically dark bursts, in which the optical afterglow is subluminal with respect to the X-ray afterglow. One definition of a dark burst is given by  $\beta_{OX} < 0.5$ , where  $\beta_{OX}$  is the optical

to X-ray spectral index (Jakobsson et al., 2004). This definition arises from a change of 0.5 in the powerlaw of the afterglow spectrum due to a cooling break. If the cooling break occurs at  $\nu_c$  then, for a given energy distribution of the electrons ( $p$ ), the spectral index is governed by equations 1.7 and 1.8 (e.g. Sari, Piran, & Narayan, 1998). These GRBs could be either low luminosity GRBs, GRBs with high optical absorption or GRBs at very high redshift (Fynbo et al., 2001; Kann et al., 2010). Alternatively, this could be related to a spectral break between the X-ray and Optical spectra, for example the electron self-absorption frequency (Shen & Zhang, 2009).

$$\beta = p/2 - 1/2(\nu < \nu_c) \quad (1.7)$$

$$\beta = p/2(\nu > \nu_c) \quad (1.8)$$

Melandri et al. (2008) compared the optical and X-ray lightcurves of 24 LGRBs and found they often demonstrated different behaviour (chromatic and achromatic breaks). 10 of their sample were not consistent with the standard forward shock model. Nysewander, Fruchter, & Pe'er (2009) completed a systematic study of GRB afterglows and found a correlation between the prompt fluence and the afterglow at 11 hours after the trigger time. The optical afterglows of SGRBs and LGRBs have been compared by Nysewander, Fruchter, & Pe'er (2009) who concluded that the SGRB afterglows are not necessarily less bright due to their surrounding medium but is most likely due to having much lower fluences.

### **Radio afterglows**

The first radio afterglow of a GRB was detected for GRB 970508 (Frail et al., 1997). Within the radio observations there was evidence of significant radio “twinkling” or scintillation, more than is normally expected for radio sources. The “twinkling” originates from diffractive scintillation at the source and can be used to calculate the size of the emitting region (the diffractive angle is proportional to the size of the emitting region). Radio observations of variability caused by this effect showed the emitting

region of GRB 970508 started extremely small and then relativistically expanded (Frail et al., 1997). This provided important observational evidence of relativistic jets.

An advantage of using radio observations is that they are significantly delayed with respect to the rest of the GRB emission as there is a strong dependence on the frequency of the emission and the arrival time due to scattering processes within the intergalactic medium (e.g. Inoue, 2004). Therefore, observed afterglow emission in radio energy bands does not peak for many days (Sari, Piran, & Halpern, 1999). Radio observations can be used to identify when jets become sub-relativistic and this can be used to calculate the total energy emitted during the GRB (Waxman, Kulkarni, & Frail, 1998). The first SGRB radio afterglow was detected for GRB 050724 which allowed the measurement of the isotropic energy  $(3-15)\times 10^{50}$  erg (Berger et al., 2005).

## 1.3 Host galaxies

The host galaxies of GRBs have provided vital observational clues about the progenitors of these highly energetic events, from their cosmological origin to association with different stellar populations.

### 1.3.1 Host galaxies of LGRBs

Although many LGRBs are too distant for the identification of host galaxies, there are a number of identified host galaxies which have been studied using telescopes including the *Hubble Space Telescope* (*HST*). These host galaxies tend to be small, with mean effective radii of 1.7 kpc, moderately low metallicity and are actively star forming (Bloom et al., 1998; Djorgovski et al., 1998; Fruchter et al., 1999; Bloom, Kulkarni, & Djorgovski, 2002; Fruchter et al., 2006; Wainwright et al., 2007). However, there are some LGRBs found in high metallicity environments (Levesque et al., 2010b,c). Fruchter et al. (2006) and Svensson et al. (2010) found that LGRBs occur preferentially on the brightest pixels of their host galaxies, showing they tend to occur on regions of active star formation. The locations of LGRBs were compared to the locations of SNe and GRBs were found to be more tightly distributed than the SNe as shown in Figure 1.6.

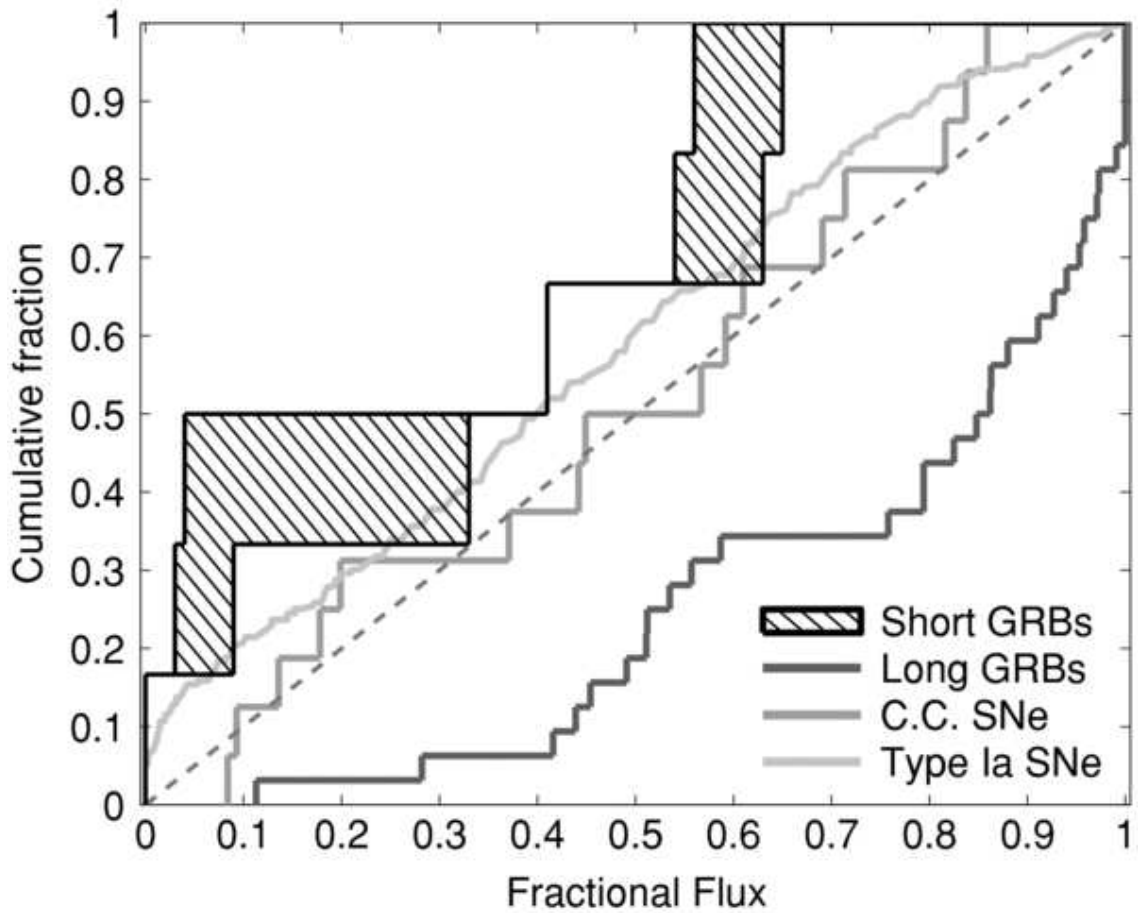


Figure 1.6: This figure, taken from Fong, Berger, & Fox (2010), shows the cumulative distribution of the fractional flux at each GRB location. The fractional flux quantifies the proportion of the host galaxy’s light in pixels fainter than the GRB location. The dashed line represents the expected distribution if the distribution of sources tracks the light distribution. The shaded region represents the results obtained for SGRBs using two different filters (the exact filters and instruments vary depending on the GRB and are described in Fong, Berger, & Fox, 2010). The two light grey lines show the distribution of core collapse SNe and Type Ia SNe for reference. The dark grey line shows the distribution for LGRBs and clearly shows that LGRBs are concentrated on the brightest regions of their host galaxies. This means they are associated with more extreme star formation than typical SNe. Conversely, this figure also shows that SGRBs tend to either trace the SNe or are on the faintest regions of their hosts (note that hostless SGRBs are not included, further emphasising the differences between LGRBs and SGRBs).

### 1.3.2 Host galaxies of SGRBs

Until the launch of the *Swift* satellite, it was not possible to pinpoint the position of SGRBs accurately as their afterglows faded too rapidly to allow their detection so little was known about their origins. *Swift* enabled the detection of the X-ray afterglows giving positions accurate enough for some host galaxy and optical afterglow identifications. However, as the optical afterglows are faint and fade rapidly it is extremely difficult to get redshifts from the afterglows. Typically SGRB redshifts come from host galaxy associations and it is possible that the original progenitor is just in chance alignment with this host galaxy and they are not related (chance alignments can be calculated using the methods described in Hogg et al., 1997). Additionally, SGRBs often appear to occur offset from their host galaxies further adding to the possibility of chance alignments. Multiple host candidates can further complicate this task, for example GRB 050813 which has candidate hosts at  $z=0.7$  and  $z=1.8$  (Berger, 2005; Ferrero et al., 2007), GRB 050509B (Bloom et al., 2006) and GRB 060912A (Levan et al., 2007). Therefore, it is important to be cautious when considering individual SGRB redshifts and host galaxies. However, it is equally important to note that many of these host associations will be correct so the sample as a whole can provide important clues about the progenitors of SGRBs. Tunnicliffe et al. (private communication) have used a set of random positions and field galaxies in comparison to the SGRB sample to show that, when the probability of chance alignment is low, the host galaxy identification is likely to be correct. However, when the host galaxy candidate is significantly offset it is more likely to be a typical field galaxy and unassociated with the SGRB. They showed that all host galaxies identified using an optical afterglow are  $>95\%$  confident (81% of these are  $>99\%$  confident) and when only using an X-ray position the identification is much less certain.

Studies of SGRB hosts have shown that SGRBs occur in both early and late type galaxies, while some may be associated with galaxy clusters, in direct contrast to LGRBs. Early type galaxies are old elliptical galaxies whereas late type galaxies include young spiral galaxies, irregular galaxies and galaxy mergers. Although it appears that the proportion of SGRBs occurring in star forming galaxies dominate this sample (Berger, 2009), it has been found that there may be an observational bias against detecting  $z\sim 1$  early type galaxies as those SGRBs may have fainter afterglows (for example GRB 100117A; Fong, Berger, & Fox, 2010).

Wainwright et al. (2007) compared SGRB and LGRB host galaxies and showed that SGRB host galaxies tend to have larger effective radii than LGRBs but fewer interacting or irregular host galaxies. There is some evidence that SGRBs may trace star formation, but in a different way to LGRBs ruling out a common progenitor (Virgili et al., 2011). Berger et al. (2009) compared SGRB host galaxies to LGRB host galaxies and field galaxies, finding a 0.3% chance that SGRBs are drawn from the same population of galaxies as LGRBs but a 60% chance that they are from the same distribution as typical field galaxies. SGRB hosts also tend to be higher in luminosity and from a wider range of host types than LGRBs (Berger et al., 2009). The position of SGRBs within their host galaxies and the fractional flux of that position (in comparison to the flux of the host galaxy) were studied by Fong, Berger, & Fox (2010) in comparison to the LGRB sample. They found that SGRBs are distributed more diffusely throughout their host galaxies than the LGRB population as shown in Figure 1.6.

From the first associations with elliptical galaxies it was clear that SGRBs can be associated with an older stellar population and lower star formation rates (SFRs) than LGRBs (Nakar et al., 2006; Zhang et al., 2007; Gal-Yam et al., 2008; Berger et al., 2009). The metallicity of SGRB host galaxies is typically much higher than that of LGRB host galaxies and resembles that of the field galaxies (Berger et al., 2009).

Studies of SGRB host galaxies by Leibler & Berger (2010) showed that SGRBs are consistent with an older stellar population tracking the stellar mass distribution and may partially track star formation with a delay time. Within early type galaxies the delay time between star formation and the SGRB is about 3 Gyr but for late type galaxies it is 0.3 Gyr (Leibler & Berger, 2010). If SGRBs track stellar mass alone then equal numbers would be expected in early and late type galaxies, which has not been observed but this may be related to an observational bias (Berger, 2009; Fong, Berger, & Fox, 2010).

Some of the SGRBs are significantly offset from their host galaxies (e.g. Berger et al., 2005; Fox et al., 2005; Bloom et al., 2006; Troja et al., 2008; Fong, Berger, & Fox, 2010; Church et al., 2011). Fong, Berger, & Fox (2010) showed that SGRB offsets cover the range 1–64 kpc with a median of 5 kpc and 50% occurring at offsets less than 30 kpc. Therefore, SGRB progenitors are likely to have been kicked away from their birthplaces and there has been a significant delay between this and the SGRB.

There is a population of SGRBs without an associated host galaxy, it is unclear whether these have been significantly kicked out of nearby host galaxies or are associated with high redshift or faint host galaxies which are undetected in the optical images. An example of a hostless SGRB is GRB 090515 (considered in Chapter 4). Berger (2010) considered a sample of hostless SGRB galaxies and determined that they typically have fainter afterglows, a lower prompt fluence and are shorter in duration. Tunnicliffe et al. (private communication) have suggested that the hostless GRBs are likely to be at low redshift and ejected from their host galaxies rather than at high redshift.

## 1.4 Classification methods

### 1.4.1 Evidence for two populations

Since the identification of two categories of GRB using their durations (Kouveliotou et al., 1993) it has become clearer that there are two distinct populations. Their differences have been highlighted in the previous Sections. SGRBs tend to be at lower redshifts ( $\langle z_{SGRB} \rangle = 0.4$  and  $\langle z_{LGRB} \rangle = 2.3$ ; Berger et al., 2009) and have lower isotropic energies than LGRBs. However, there may be a low redshift bias for SGRBs for example due to: the bias against elliptical host galaxies at  $z \sim 1$  (Fong, Berger, & Fox, 2010), lack of a strong host galaxy candidate or not being able to measure the redshift of the candidate. Therefore, the difference between the average redshifts and isotropic energies of SGRBs and LGRBs may not be as large (indeed there are SGRBs known at higher redshifts, e.g. GRB 090426; Levesque et al., 2009). They do not fit in with the majority of potential correlations found in the prompt emission for LGRBs and they have negligible lags. Their afterglows are fainter ( $\langle F_x \rangle = 7 \times 10^{-10} \text{ erg cm}^{-2} \text{ s}^{-1}$  for SGRBs and  $\langle F_x \rangle = 3 \times 10^{-9} \text{ erg cm}^{-2} \text{ s}^{-1}$  for LGRBs; Nysewander, Fruchter, & Pe'er, 2009) and fade more rapidly than for LGRBs. Their locations within host galaxies and the types of host galaxies are also in stark contrast to the LGRBs.

However, there is clearly overlap between the distributions of LGRBs and SGRBs shown in Figure 1.1. Additionally, this distribution is dependent on the sensitivity and energy band of the instrument being used to detect them. This is also an observed frame distribution, there are many effects which come

into play when attempting to redshift these into their restframes further confusing the distribution.

When considering individual GRBs, this overlap can still cause confusion as there are cases where the properties of the GRBs makes it difficult to assign them into a particular category. Examples of these GRBs are:

- **GRB 050724**,  $T_{90} = 3$  s, occurred in a nearby elliptical galaxy which, among other properties, associated it with the SGRB population despite the long duration (Barthelmy et al., 2005b; Berger et al., 2005).
- **GRB 060121**,  $T_{90} = 1.97$  s, occurred at a higher redshift and in a more dusty environment than is expected for a typical SGRB (Donaghy et al., 2006; Levan et al., 2006a; de Ugarte Postigo et al., 2006).
- **GRB 060505**,  $T_{90} = 5$  s, had no associated supernova but had a spectral lag which is consistent with the LGRB population, was located within a star formation region in a host galaxy at  $z = 0.09$  and its classification is still not firmly established (Fynbo et al., 2006; Ofek et al., 2007; Jakobsson & Fynbo, 2007; Thöne et al., 2008; McBreen et al., 2008; Bloom, Butler, & Perley, 2008; Xu et al., 2009).
- **GRB 060614**,  $T_{90} = 102$  s, had no associated supernova to highly constraining limits, a negligible spectral lag and a host galaxy more consistent with the population of SGRBs (Fynbo et al., 2006; Gal-Yam et al., 2006; Gehrels et al., 2006; Della Valle et al., 2006; Zhang et al., 2007).
- **GRB 060912A**,  $T_{90} \sim 5$  s, occurred near a large elliptical galaxy so it may be a SGRB associated with this galaxy but there was also an underlying  $z=0.9$  galaxy so it is more likely to be a LGRB (Levan et al., 2007).
- **GRB 090426**,  $T_{90} = 1.28$  s, the most distant SGRB at a redshift of  $z = 2.609$  which may be problematic for the energy constraints of the SGRB progenitor theory. (Levesque et al., 2009) It is concluded that the simplest explanation is that the progenitor was a collapsar (Levesque et al., 2009; Antonelli et al., 2009; Thöne et al., 2011a).
- **GRB 090510**,  $T_{90} = 0.30$  s, at  $z=0.9$  had a long lived high energy component detected by *Fermi*

LAT and was extensively studied (de Pasquale et al., 2010; Giuliani et al., 2010; Ghirlanda, Ghisellini, & Nava, 2010; Ackermann et al., 2010). The progenitor is proposed to be a binary merger by Corsi, Guetta, & Piro (2010) although Panaitescu (2011) suggest it originated from the collapse of a massive star.

### 1.4.2 Extended Emission bursts

There is a sample of GRBs which have a typically long  $T_{90}$  duration but which do not appear to fit the LGRB sample, these GRBs share common properties in their prompt emission as they all have a short hard peak followed by long soft extended emission. Typical examples include GRBs 060505 (Fynbo et al., 2006; McBreen et al., 2008), 060614 (Fynbo et al., 2006; Gal-Yam et al., 2006; Gehrels et al., 2006; Della Valle et al., 2006; Zhang et al., 2007) and 080503 (Perley et al., 2009a). These GRBs had no associated SNe and a negligible spectral lag. If these bursts had been detected by BATSE, the long soft extended emission may be undetectable and they could appear as SGRBs. Norris & Bonnell (2006) reanalysed the BATSE data and discovered 8 GRBs with an initial short hard spike followed by soft extended emission. These GRBs are often referred to as SGRBs with extended emission (EE SGRBs).

This poses the question: do SGRBs and EE SGRBs share a common progenitor? The *Swift* sample of SGRBs have been studied by Norris, Gehrels, & Scargle (2010) for evidence of extended emission,  $\sim 25\%$  do show evidence of this component however there are many SGRBs which do not have extended emission. Norris, Gehrels, & Scargle (2011) have suggested that these EE SGRBs have longer lived afterglows and are likely to have a different progenitor to typical SGRBs.

These EE SGRBs are also the only LGRBs which are definitely missing SNe counterparts. EE SGRBs tend to occur nearer to their host galaxies than typical SGRBs while SGRBs with a large offset do not have EE and are less likely to have an optical afterglow (Troja et al., 2008).

The extended emission observed in GRB 080503 is potentially explained as an off-axis jet or a re-freshed shock (Perley et al., 2009a, and references therein). An alternative model for extended emission involves 2 jets, one short in duration and the other narrower and long lived, was proposed by Barkov & Pozanenko (2011). Alternatively, ongoing emission from a magnetar central engine has also been

suggested by Metzger et al. (2011). Despite these theories, it is still unclear what these EE SGRBs are and no theory satisfactorily explains all their properties.

### 1.4.3 Intermediate GRBs

Using the BATSE sample, it has been claimed that there is a third statistically significant population of GRBs with an intermediate duration (Mukherjee et al., 1998; Horváth, 1998). It is not clear what the progenitor of these would be and if they are a distinct population. The next stages are searching for examples of GRBs which do not fit into either the LGRB or the SGRB progenitor categories. However, as it is not unambiguously clear what a SGRB or a LGRB is, this will prove difficult.

## 1.5 Progenitor Theories

### 1.5.1 Collapsar

Prior to the publication of the first GRBs by Klebesadel et al. (1973), it was predicted by Colgate (1968) that SN could be accompanied by a flash of gamma-rays. LGRBs are now thought to originate from the death of a rapidly rotating Wolf-Rayet star that has lost its hydrogen and helium envelopes giving a type I b/c supernova (b means no silicon observed in the SN spectrum and c means no silicon or helium; Paczynski, 1986; Woosley, 1993; Paczynski, 1998).

If the massive star originates in a low metallicity environment then it will lose less mass via stellar winds and thus retain the majority of its angular momentum (MacFadyen & Woosley, 1999; Hirschi, Meynet, & Maeder, 2005; Woosley & Bloom, 2006; Langer & Norman, 2006; Yoon, Langer, & Norman, 2006). It is thought this will lead to fast rotation speeds which are important for launching the jet.

There are now six cases where a GRB or an XRF and SN have been associated with each other and they are summarised in Table 1.2. In all cases these were type Ic hypernovae, unusually powerful SN. However, only GRB 030329 was a typical GRB as GRB 980425 was underluminous and the others are

GRB	SN	Satellite detecting GRB	Classification of GRB
980425	1998bw	<i>Beppo-SAX</i>	Underluminous <sup>(1,2,3)</sup>
030329	2003dh	<i>HETE 2</i>	Typical GRB <sup>(4,5)</sup>
031203	2003lw	<i>INTEGRAL</i>	XRF <sup>(6,7)</sup>
060218	2006aj	<i>Swift</i>	XRF and underluminous <sup>(8,9,10,11)</sup>
080109	2008D	<i>Swift(XRT)</i>	Weak XRF <sup>(12)</sup>
100316D	2010bh	<i>Swift</i>	XRF and underluminous <sup>(13)</sup>

Table 1.2: These GRBs/XRFs have been associated with type Ic hypernovae, providing supporting evidence for the massive star progenitor model.

<sup>(1)</sup>Paczynski (1998), <sup>(2)</sup>Galama et al. (1998), <sup>(3)</sup>Kulkarni et al. (1998), <sup>(4)</sup>Stanek et al. (2003),  
<sup>(5)</sup>Hjorth et al. (2003), <sup>(6)</sup>Malesani et al. (2004), <sup>(7)</sup>Thomsen et al. (2004), <sup>(8)</sup>Campana et al. (2006),  
<sup>(9)</sup>Pian et al. (2006), <sup>(10)</sup>Soderberg et al. (2006), <sup>(11)</sup>Mazzali et al. (2007), <sup>(12)</sup>Mazzali et al. (2008),  
<sup>(13)</sup>Starling et al. (2011).

classified as very long XRFs.

In addition to the GRB-SN detections, there are now several cases where a SN “bump” has been detected in the lightcurves of known GRBs (e.g. Castro-Tirado & Gorosabel, 1999; Bloom et al., 1999; Cano et al., 2011). It has been shown that all observations of typical LGRBs are consistent with being associated with Ib/c SN although not all of these SN can produce LGRBs (Woosley & Bloom, 2006).

Although this association is widely accepted, there are still significant issues. There are examples of XRFs where it is expected that the SN counterpart would be detected, but there was no association (Soderberg et al., 2005; Levan et al., 2005). The class of LGRBs which are also known as SGRBs with extended emission do not have SN counterparts to deep and constraining limits (Fynbo et al., 2006). An XRF without an associated SN could be explained as belonging to the SGRB with extended emission group where the initial short hard spike was missed (Soderberg et al., 2005). Even when the SN “bump” is observed, there are cases where they simply do not fit the current models (e.g. GRB 020305 and XRF 030723; Gorosabel et al., 2005; Fynbo et al., 2004; Tominaga et al., 2004; Butler et al., 2005).

### 1.5.2 Compact binary mergers

The progenitor of SGRBs needs to explain the observed differences between them and LGRBs; especially the lower isotropic energies (Berger, Morrell, & Roth, 2007; Nakar, 2007), lack of observed SN to deep limits and association with older stellar populations. The most popular theory is the merger of two compact objects, typically two NSs or a NS and a BH, to form a black hole although an alternative progenitor is the accretion induced collapse (AIC) of a white dwarf (WD) (Lattimer & Schramm, 1976; Paczynski, 1986; Goodman, 1986; Eichler et al., 1989; Narayan, Paczynski, & Piran, 1992; Meszaros & Rees, 1992; Rosswog & Ramirez-Ruiz, 2003; Dermer & Atoyan, 2006; King, Olsson, & Davies, 2007; Lee & Ramirez-Ruiz, 2007; Metzger, Quataert, & Thompson, 2008). During the merger, a torus of material is produced that then accretes onto a central black hole powering the GRB in a similar manner to that produced during a collapsar. The energy available for the GRB is proportional to the mass of the accretion disk: for NS-NS (NS-BH) mergers this is  $0.01 M_{\odot}$  ( $0.1 M_{\odot}$ ) whereas a collapsar has a torus of a few  $M_{\odot}$  (e.g. Lee & Ramirez-Ruiz, 2007). This explains why SGRBs tend to have lower isotropic energies than LGRBs. As these systems are the old remnants from massive stars this progenitor would also explain the lack of SN and association with older stellar populations. The accretion rate is very high so the torus is accreted onto the central BH within  $\sim 0.3$  s (e.g. Rezzolla et al., 2011) which is consistent with the short durations. As some material is ejected from the merger, there have been predictions of a “mini” SN or “macronova” (Li & Paczyński, 1998; Rosswog et al., 1999; Rosswog, 2005; Kulkarni, 2005; Metzger et al., 2010).

Simulations of these mergers are vital to aid in the understanding of how the system merges, the remnant formed, how the jet is launched and its duration. However, these simulations are highly complex. NSs and BHs have extreme relativistic gravitational fields so full general relativity, in a regime it has not been tested in, is needed to model these systems. In addition to their extreme gravitational fields the nuclear equation of state of NSs also needs to be taken into account, as this will describe the remnant and torus formed, but again we do not know how matter behaves in the incredibly high densities that NSs experience. The extreme magnetic fields that occur during these mergers are likely to be important and are also difficult to model. Additionally, these simulations are very computationally expensive and hence are often run for very short durations, i.e. the first 1-2 s after the merger. This makes it very dif-

difficult to use these simulations to constrain late time properties. Many theorists have modelled different aspects of these compact binary mergers and a recent review of these simulations is given by Rosswog (2010).

Although a BH is generally considered to be the remnant of the merger, there is increasing evidence that a stable or unstable massive NS (likely a magnetar) may be formed instead (Dai & Lu, 1998a; Dai et al., 2006; Yu & Huang, 2007) and this option is discussed in more detail in Chapters 4 and 5 of this Thesis.

This theory relies upon the formation of compact binary star systems. Several stellar population studies have been completed and it is possible, although difficult, to produce compact binary systems (a recent example population study was completed by Eldridge, Langer, & Tout, 2011). The typical formation route (as described in, for example, Tauris & van den Heuvel, 2006) starts with two massive stars (of masses  $\geq 12 M_{\odot}$ ). The most massive star evolves first, becoming a red supergiant, leading to mass transfer to the smaller star via Roche Lobe overflow. After  $\sim 15$  Myr, the most massive star undergoes a SN explosion leaving behind a NS (or a BH for very massive primary stars). The secondary star then evolves, also becoming a red supergiant with Roche Lobe overflow so the secondary star accretes matter onto the NS (giving a high mass X-ray binary). As the secondary star continues to expand there is a common envelope phase causing the NS and the core to spiral in. After  $\sim 25$  Myr the secondary star has lost its envelope and undergoes a SN explosion. This leaves behind a NS-NS binary system which will slowly spiral inwards towards each other. The system will form in a region of active star formation however, as it can take  $> 10^7$  yr for the system to spiral inwards (see equation 1.9), the galaxy may have significantly evolved before the merger occurs. This means that NS mergers will be associated with older stellar populations and consequently can be found in all types of host galaxy.

During their formation within SN, the NS may receive a “kick” (e.g. Fryer, 2004) which may disrupt the binary system. If the binary is not disrupted, then the whole system will travel away from its original birth place. When the second NS is formed, there is again a chance that the “kick” will disrupt the binary (although the second NS may not receive such a “kick”; van den Heuvel, 2010). There are many uncertainties surrounding the formation of these systems making it very difficult to estimate the rate of mergers expected and uncertainties in beaming angles leads to further issues in estimating the

number of SGRBs expected. Many studies have been completed to estimate the rates with uncertainties covering several orders of magnitude (e.g. at  $z=0$  NS-NS merger rate  $1 - 800 \text{ per yr}^{-1} \text{ Gpc}^{-3}$ , NS-BH merger rate  $0.1 - 1000 \text{ per yr}^{-1} \text{ Gpc}^{-3}$ ; Lee & Ramirez-Ruiz, 2007).

If the binary survives both SNe, and the NSs are close enough, then the orbits of the NSs will decay via gravitational radiation. This was proved for the Galactic binary NS system observed by Hulse & Taylor (1974), Taylor et al. (1992) and Weisberg & Taylor (2005) and this system will merge in  $\sim 3 \times 10^8$  years. The time till the two NSs merge can be described by:

$$\tau_{\text{inspiral}} = 10^7 \text{ yr} P_{\text{orb},h}^{\frac{8}{3}} \left( \frac{M}{M_{\odot}} \right)^{\frac{2}{3}} \left( \frac{\mu}{M_{\odot}} \right)^{-1} (1 - e^2)^{\frac{7}{2}} \quad (1.9)$$

where  $\tau_{\text{inspiral}}$  is the number of years before the NSs will merge,  $e$  is the eccentricity of the system,  $P_{\text{orb},h}$  is the orbital period in hours,  $M$  is the mass of the system,  $\mu$  is the reduced mass of the system ( $\mu = \frac{m_1 m_2}{m_1 + m_2}$ ; Lorimer, 2005).

During the final stages of the merger vast amounts of gravitational waves are expected to be emitted. These signals were searched for by the Laser Interferometric Graviational Wave Observatory (LIGO, the most recent results are published in Abadie et al., 2010a) and would provide the “smoking gun” observation required to confirm compact binary mergers as a SGRB progenitor. To date no binary mergers have been detected by LIGO although this is not surprising as they are typically too distant to be observed. GRB 070201 may be associated with M31, however LIGO has discounted a binary merger in M31 (Abbott et al., 2008). However in 2014 Advanced-LIGO comes online which is expected to detect binary mergers within 445 Mpc (Abadie et al., 2010b). If no gravitational waves are still detected, it will start to place interesting constraints on the SGRB progenitor theory.

Combining the “kicks” and long merger timescales, the binary system could travel a long way before merging. If the “kick” velocity is  $\geq 100 \text{ km s}^{-1}$  then it could be unbound from its host galaxy (depending on the mass of the host galaxy) and this may explain some hostless SGRBs (Berger, 2010). For smaller “kicks” they would remain bound to the galaxy and would trace the distribution of old stellar populations. In both cases an offset from the host galaxy is expected. The predicted offset of SGRBs from their host galaxies are found to be consistent with the observed distributions (Belczynski et al.,

2006; Church et al., 2011).

## 1.6 Soft Gamma-ray Repeaters

After a giant flare of gamma-rays on 5th March 1979, resembling a GRB, there were multiple bursts from the same location (Mazets et al., 1982). Typical GRBs have never been observed to repeat from the same location which suggested this source had a different progenitor. Now several sources are known to emit repeating bursts of soft gamma-rays. These Soft Gamma Repeaters (SGRs) have been identified as Galactic sources. Some have been associated with quiescent X-ray sources (Hurley et al., 1996, 2000b; Kulkarni et al., 2003; Molkov et al., 2005; Tiengo et al., 2007), supernova remnants (SNRs, e.g. Kulkarni & Frail, 1993; Vasisht et al., 1994) and clusters of massive stars (e.g. Mirabel & Fuchs, 1999; Vrba et al., 2000; Figer et al., 2005). However, there are examples which are clearly not associated with SNRs or massive star clusters. SGRs are now known to belong to the special class of NSs known as magnetars, with magnetic fields ranging from  $10^{14}$ – $10^{15}$  G (these fields are a billion times stronger than can be made on Earth). They are known to have spin periods of 2–9 s and are spinning down rapidly, implying that they formed with millisecond spin periods and have spun down within a few hundred years. Due to the large magnetic fields, it is thought that SGRs are more likely to experience anisotropy during their formation which leads to large than average kick velocities, even as high as  $\sim 1000 \text{ km s}^{-1}$  (Gaensler et al., 2001). They are also believed to be young NSs, approximately  $10^4$  years, which were formed from bright SN in star forming regions (Duncan & Thompson, 1992; Thompson & Duncan, 1995; Mereghetti, 2008). As some have been observationally associated with clusters of massive stars we can place lower limits on the mass of the progenitor stars. SGR 1806-20 has  $M_{\text{progenitor}} > 40 M_{\odot}$  (Mirabel & Fuchs, 1999) and SGR 1900+14 has  $M_{\text{progenitor}} > 25 M_{\odot}$  (Vrba et al., 2000). This supports the massive star progenitor theory.

This is not the only potential progenitor of these magnetars, Levan et al. (2006b) have proposed that magnetars can be formed via the accretion induced collapse of a white dwarf (WD) or WD–WD mergers. In this case, there would be no accompanying SN and the magnetar would be associated with an older stellar population or even kicked out of the host galaxy. Alternatively, as previously discussed,

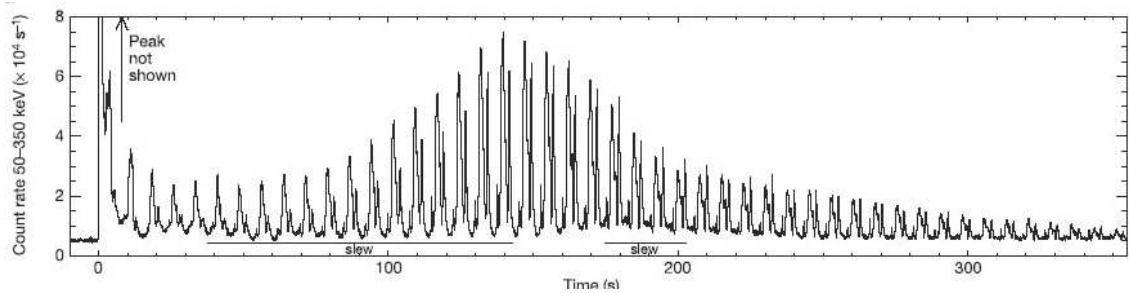


Figure 1.7: This figure shows the BAT count rate lightcurve (50 – 350 keV) of the giant flare observed from SGR 1806-20. The initial peak is not shown as it has an exceptionally high count rate. The tail shows periodic emission which gives the spin period of the magnetar (Palmer et al., 2005).

magnetars could be formed within and power some GRBs.

These young, highly magnetic NSs are thought to be unstable. During the gamma-ray flares, the crust is thought to rearrange itself giving a “magnetar quake”. This drives a strong current which energises particles trapped within the magnetic field lines. As the field rearranges itself into a more stable configuration a fireball of the energetic particles is released giving the gamma-ray flare (Thompson & Duncan, 1995). However, some of the fireball may become trapped within the magnetic field lines giving a ringing down signature in the lightcurves.

In 1981, the first anomalous X-ray pulsar was discovered (AXP; Fahlman & Gregory, 1981) and there are now several candidates. It was postulated that these were also a type of magnetar (Thompson, Lyutikov, & Kulkarni, 2002) and AXPs have now been observed to behave like SGRs (e.g. Israel et al., 2010; Kumar & Safi-Harb, 2010).

### 1.6.1 SGR giant flares

On 5th May 1979, SGR 0526-66 was observed to emit a giant flare of gamma-rays. The energy emitted in this explosion was  $\sim 2 \times 10^{45}$  ergs (Fenimore, Klebesadel, & Laros, 1996). Giant flares are thought to originate from massive large scale restructuring in the crust of the magnetar (Thompson & Duncan, 1995). It is still unclear how many giant flares a magnetar can emit during its lifetime and a giant flare has never been seen to repeat to date.

Since this date two other SGRs have been observed to emit giant flares: SGR 1900+14 (Hurley et al., 1999) and SGR 1806-20 with the enormous luminosity of  $2 \times 10^{47}$  erg s<sup>-1</sup> on 27th December 2004 (Hurley et al., 2005; Palmer et al., 2005). The giant flare from SGR 1806-20 was the brightest extra-solar transient ever observed, causing ionisation in the Earth's upper atmosphere (Inan et al., 2007) and had a measurable reflection from the surface of the Moon (Frederiks et al., 2007a). The lightcurve from this event is shown in Figure 1.7 and the periodic tail emission provides the spin period of the magnetar. Hurley et al. (2005) showed that this event would have been visible out to several tens of Mpc and would resemble a SGRB.

### 1.6.2 SGR giant flares and SGRBs

After determining that SGR giant flares could be the origin of some SGRBs at redshifts  $\ll 0.1$ , the next step would be identify candidate events. The main requirement would be an association with a nearby galaxy. Although these extra-galactic giant flares should be easily detectable, the accompanying optical afterglow would be very faint (Eichler, 2002; Levan et al., 2008). Tanvir et al. (2005) completed a cross-correlation of BATSE positions with nearby galaxies and found that a small proportion of SGRBs appear to originate in very nearby galaxies. Lazzati, Ghirlanda, & Ghisellini (2005) considered the spectra of BATSE SGRBs in comparison to that of SGR giant flares and found 3 candidate events, implying SGR 1806-20 is either closer to Earth than 15 kpc or that there are fewer SGRs in the local Universe than expected. Recent work by Bibby et al. (2008) and Crowther et al. (2011) show that the recent revision in the distance to SGR 1806-20 means the results by Lazzati, Ghirlanda, & Ghisellini (2005) are consistent.

Several potential extra-galactic SGR giant flares have been proposed and are listed in Table 1.3. When considering the expected rate of these events given those detected in our own Galaxy, it is unlikely that these are all SGR giant flares (Chapman, Priddey, & Tanvir, 2009). Three of these candidate events (GRBs 051103, 070201 and 110406A) will be discussed in more detail in Chapter 2 of this Thesis.

GRB	Galaxy Association	Duration (s)	$E_{iso}$ (erg)
000420B	M74	0.3	- <sup>(1)</sup>
050906	IC328	0.128 s	$1.5 \times 10^{46}$ <sup>(2)</sup>
051103	M81	0.3	$4.7 \times 10^{48}$ <sup>(3,4,5)</sup>
070201	M31	0.2	$1.2 \times 10^{47}$ <sup>(6,7)</sup>
110406A	NGC 404	3	$3.7 \times 10^{46}$ <sup>(8)</sup>

Table 1.3: This table summarises the SGRBs which are candidate extra-galactic SGR giant flares, all were detected using the *IPN* except GRB 050906 which was found using *Swift*. Data are not publically available to calculate the isotropic energy for GRB 000420B.

<sup>(1)</sup> Ofek (2007), <sup>(2)</sup> Levan et al. (2008), <sup>(3)</sup> Ofek et al. (2006), <sup>(4)</sup> Frederiks et al. (2007a), <sup>(5)</sup> Hurley et al. (2010b), <sup>(6)</sup> Mazets et al. (2008), <sup>(7)</sup> Ofek et al. (2008), <sup>(8)</sup> Rowlinson et al. (2011).

## 1.7 Neutron Stars

The structure of NSs is still unknown as it is unclear how matter behaves at such high densities, and many theoretical models have been proposed to describe how the mass and radius of NSs vary. These models are all attempting to describe the equation of state of a NS and a selection are shown in Figure 1.8. The equation of state of a NS is very important for the merger of two NSs, if it is a “soft” equation of state then the material is highly compressible resulting in rapid collapse to form a BH whereas “hard” equations of state lead to stable massive NSs (e.g. Oechslin, Janka, & Marek, 2007).

The mass range and maximum mass of NSs is vital when studying the merger of two NSs, so it is important to measure the masses of known NSs. The maximum measured mass is for the Black Widow Pulsar with a mass of  $2.4 M_{\odot}$  but this value is subject to large uncertainties as it was measured using the radial velocity of its binary companion (van Kerkwijk, Breton, & Kulkarni, 2011). The most massive reliable mass is  $1.97 M_{\odot}$  measured using Shapiro time delay (Demorest et al., 2010) and may have formed with this mass (Tauris, Langer, & Kramer, 2011). The NS mass distribution can be modelled using stellar evolution codes, which predict that NSs have masses typically peaking at 1.3 and 1.8  $M_{\odot}$ .

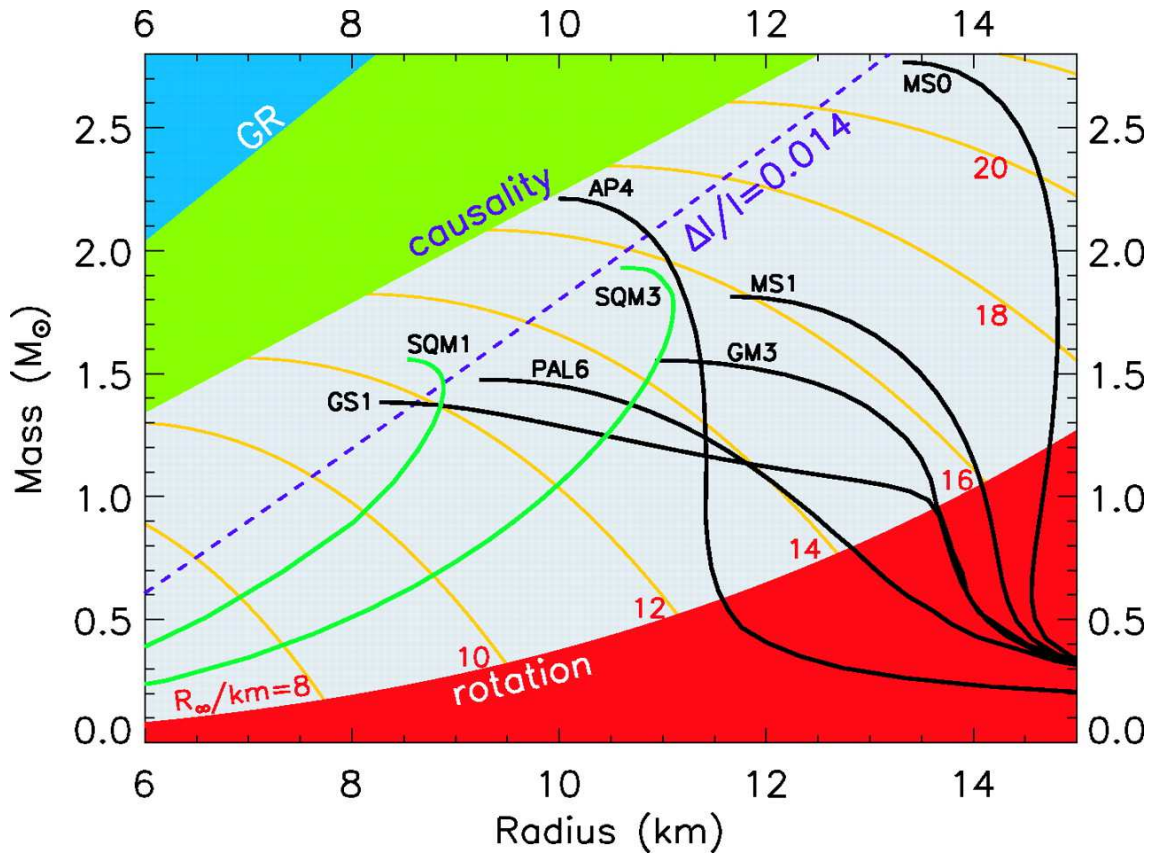


Figure 1.8: This figure shows some example NS equations of state giving the relationship between the mass and radius of NSs (Lattimer & Prakash, 2004). The red region shows where the NS is rotating so fast that the NS breaks up and the green region is forbidden via causality (speed of sound on NS surface  $>$  speed of light).

Accretion onto a NS can allow higher masses to be attained. Using Bayesian block analysis of known NS masses, there is a narrow distribution with  $M \sim 1.37 M_{\odot}$  and a broad distribution at  $M \sim 1.73 M_{\odot}$  (Valentim, Rangel, & Horvath, 2011).

If NSs with masses  $\sim 2 M_{\odot}$  are allowed, it is possible to make massive NSs (magnetars) during the merger of two NSs. If rotating rapidly, it is even more likely a massive NS can temporarily support itself from gravitational collapse via rotation up to  $1.4 M_{max}$ , where  $M_{max}$  is the maximum allowed mass of a NS (dependent on the equation of state), and for a stable NS up to  $1.2 M_{max}$ . Therefore if the Black Widow Pulsar mass is correct ( $2.4 M_{\odot}$ ; van Kerkwijk, Breton, & Kulkarni, 2011) then an unstable magnetar would be formed if  $M < 3.4 M_{\odot}$  and a stable magnetar would be formed if

$M < 2.9 M_{\odot}$ . Assuming the average mass of a NS is  $1.4 M_{\odot}$  then typical mergers could result in a stable magnetars. The most reliable maximum mass,  $\sim 2 M_{\odot}$ , would imply that an unstable magnetar would be formed via the merger of 2 average NSs. The stability of the final magnetar is dependent on the maximum possible mass of a NS. Its lifetime depends on the amount of mass accreted after formation and the loss of angular momentum by gravitational waves or magnetic torques (e.g. Shibata & Taniguchi, 2006; Oechslin, Janka, & Marek, 2007). Morrison, Baumgarte, & Shapiro (2004) studied the effect that the equation of state of a NS and rotation would have on the remnant of a compact merger, i.e. whether a NS or a BH is formed. Using 6 known Galactic NS binaries and a range of equations of state, Morrison, Baumgarte, & Shapiro (2004) predict that the majority of mergers of the known binaries will form a massive NS.

## 1.8 This Thesis

This Thesis will focus on the ongoing question of what are the progenitors of SGRBs using a variety of observational data to place constraints on the current theories. In Chapter 2 the progenitor of GRB 051103, a candidate extragalactic SGR giant flare, will be debated in light of an in depth analysis of observational data. The work on GRB 051103 is based on Hurley et al. (2010b). This Chapter will also consider new results for GRBs 070201 and 110406A, two other candidate extragalactic SGR giant flares observed by the IPN.

GRB 080905A, was a typical SGRB detected by the *Swift* satellite with an accompanying optical afterglow which allowed the identification of the host galaxy. Chapter 3, based on Rowlinson et al. (2010a), uses spatially resolved spectroscopy of the host galaxy to determine the nature of the local environment and hence place constraints on the progenitor, which is most likely a compact binary merger.

Chapter 4 addresses the nature of the unusual X-ray afterglow of GRB 090515 which shows evidence of significant ongoing energy injection followed by an extremely rapid decay phase. The origin of this energy injection is suggested to be from an unstable magnetar formed via the merger of two NSs. This Chapter comprises work published in Rowlinson et al. (2010b).

Following on from GRB 090515, Chapter 5 examines the X-ray afterglows of all *Swift* SGRB and finds evidence of energy injection in a significant fraction of SGRBs. Additionally, the magnetar model is fit to these afterglows and is postulated to explain this energy injection phase. This work is based on Rowlinson et al. (in prep).

The final Chapter will summarise the key findings from the science Chapters whilst using them to draw conclusions about the nature of the progenitor of SGRBs. Additionally, it will make suggestions for future work using upcoming observational facilities.

Throughout this Thesis, a cosmology with  $H_0 = 71 \text{ km s}^{-1} \text{ Mpc}^{-1}$ ,  $\Omega_m = 0.27$ ,  $\Omega_\Lambda = 0.73$  is adopted. Errors are quoted at 90% confidence for X-ray data and at  $1\sigma$  for optical data and results from theoretical models.

# Chapter 2

## Extragalactic SGR giant flares as progenitors of some SGRBs

### 2.1 Introduction

The main focus of this Chapter is GRB 051103 as a possible extragalactic soft gamma repeater (SGR) giant flare and is based on work completed for the paper Hurley et al. (2010b) (specifically Sections 2.2.2, 2.2.3, 2.2.4 and 2.2.5 are from that paper and were written by the author of this Thesis). Following on from this two other candidates are studied: GRB 070201 and GRB 110406A.

GRB 051103 was an unusually bright burst detected by the Inter-Planetary Network (IPN) at 09:25:42 UT. It had a fluence of  $2.34 \times 10^{-5}$  erg cm<sup>-2</sup> (20keV – 10MeV) with a T<sub>90</sub> burst duration of 0.17s (Golenetskii et al., 2005). Ofek et al. (2006) presented optical (with limiting magnitude 20.5) and radio observations (with a  $3\sigma$  limiting flux of 1.5 mJy) of the entire provisional error quadrilateral provided in the GCN circular (Golenetskii et al., 2005). No new sources were identified, however it was determined that the error quadrilateral did cross over star forming regions of M81. The studies conducted by Frederiks et al. (2007a) focused on the gamma-ray light curve and energy characteristics of GRB 051103. They showed the error quadrilateral overlapped the extended HI disk of M81 and argued for

the presence of a stellar population, linked to tidal interactions between M81 and M82 approximately 200 million years ago, throughout much of this region (Frederiks et al., 2007a). Section 2.2 presents new, much deeper optical data than previously reported for the Section of the refined error ellipse closest to M81, taken 3 days after GRB 051103 (and approximately 16 hours after the Golenetskii et al., 2005, GCN notice). These data were used to search for possible optical counterparts of this SGRB, and discuss the implications of its non-detection for its progenitor and putative association with M81. This Chapter utilizes the distance modulus of M81, 27.8 mag, determined by HST observations of Cepheids (3.6 Mpc, Freedman et al., 1994).

In Section 2.3, GRB 070201 is considered in more detail with new results obtained within the position error box that have interesting consequences for the progenitor of this GRB. As stated in the introduction, GRB 070201 appears to be associated with M31 and has been suggested to be an SGR giant flare (Mazets et al., 2008; Ofek et al., 2008). Abbott et al. (2008) have used LIGO observations to rule out a compact binary merger in M31 at >99.9% confidence.

GRB 110406A was also detected by the IPN and *INTEGRAL*, with a duration of 3 s (Savchenko et al., 2011) and a fluence of  $4.8 \times 10^{-5}$  erg cm<sup>-2</sup> (20 keV – 10 MeV; Golenetskii et al., 2011) and may be associated with NGC 404 (Rowlinson et al., 2011). This association is discussed in more detail in Section 2.4.

Implications of these results on the study of future extragalactic SGR giant flare candidates are discussed in the final part of this Chapter.

## 2.2 GRB 051103

### 2.2.1 Prompt properties

The first part of Hurley et al. (2010b), completed by K. Hurley and collaborators, focused on the prompt emission observations obtained by the IPN using a number of satellites and are summarised in this Section. Hurley et al. (2010b) produced a new refined error ellipse, shown in Figure 2.1. The refined

error ellipse was created using annuli between pairs of detectors on board the following satellites: *Konus-Wind* (Aptekar et al., 1995), *HETE 2* (Atteia et al., 2003), *RHESSI* (Smith et al., 2002), *INTEGRAL* (Winkler, Pace, & Volonté, 1993), *Swift* (Gehrels et al., 2004) and *Mars Odyssey* (Hurley et al., 2006).

The prompt emission lightcurve, observed by BAT on board *Swift*, was investigated for evidence of a periodic component in the tail of the emission by creating periodograms and using a Monte Carlo analysis to quantify the significance of any peaks. A periodic component has been observed in all of the giant flares observed to date, but would not be expected in the light curve of a typical SGRB with a binary merger progenitor. The lightcurve of GRB 051103 from *RHESSI* is shown in Figure 2.2. No periodic component was identified in the light curve of GRB 051103 but it was shown that a non-detection would not be surprising for an SGR on M81. Hurley et al. (2010b) scaled the periodic component observed in the giant flare from SGR 1806-20 to the distance of M81 and determined the signal, using a significance cut, would be  $0.01\sigma$ .

The energy spectrum of SGR giant flares is typically very hard during the initial spike with a soft spectrum for the decaying tail, indeed sometimes the initial spike is consistent with a high temperature blackbody spectrum (Mazets et al., 1979; Fenimore et al., 1981; Hurley et al., 1999; Mazets et al., 1999; Hurley et al., 2005; Frederiks et al., 2007b). Spectral fits were conducted by Hurley et al. (2010b) using data from *RHESSI*, *Suzaku* (Yamaoka et al., 2009) and *Konus-Wind*. These spectra show the spectral evolution expected for an SGR was observed for GRB 051103 as they were consistent with the observed values for the giant flare from SGR 1806-20 (Hurley et al., 2005; Palmer et al., 2005; Boggs et al., 2007; Frederiks et al., 2007b). It is possible to fit a blackbody to the high energy spectrum of GRB 051103 although an additional high energy power-law component is favoured in these fits, which was not observed for SGR 1806-20. However, the results are also consistent with observations of SGRBs.

Hence, Hurley et al. (2010b) showed the prompt emission properties are consistent with the SGR giant flares but cannot rule out a typical SGRB.

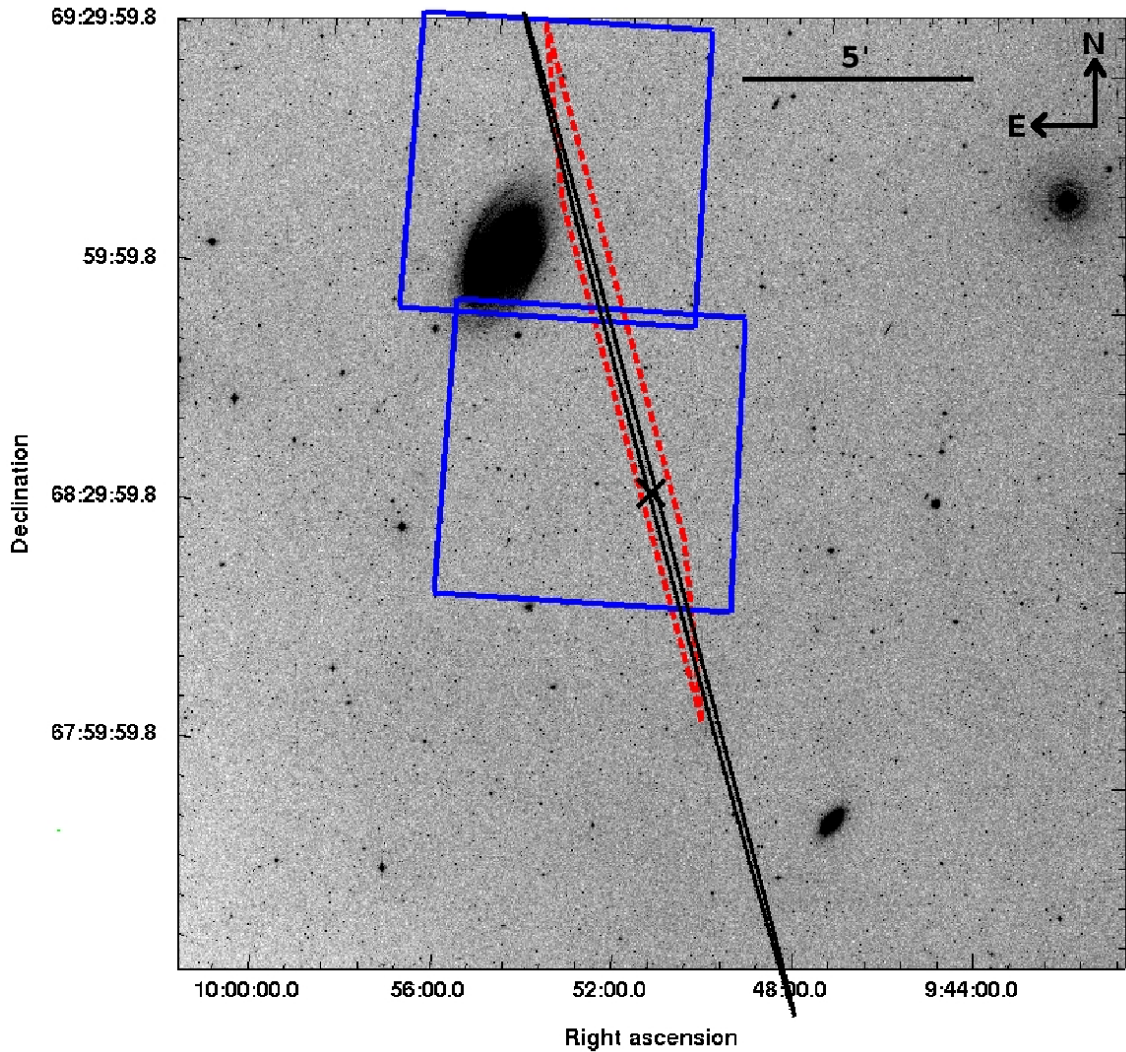


Figure 2.1: The original IPN error trapezium (dashed line), the  $3\sigma$  refined error ellipse for the position of GRB 051103 (solid line), and the fields of the region studied using KPNO (large squares). The cross indicates the center of the ellipse and the most likely arrival direction of the burst. Approximately 65 square arcminutes of the ellipse are contained within the old error box. These are overlaid upon an image of the area surrounding M81 from the Digital Sky Survey. The possibility that this burst came from the inner disk of M81 is firmly ruled out. However, the brightest GALEX UV knots noted by Ofek et al. (2006) are within the ellipse and indicate possible ongoing star formation in the outer spiral arm. (Lipunov et al., 2005) noted the presence of two galaxies within the initial error box, PGC 2719634 and PGC 028505. The former galaxy lies at the 18% confidence contour of the ellipse, and remains a plausible host candidate, while the latter lies at the 0.03% contour, and is unlikely to be the host.

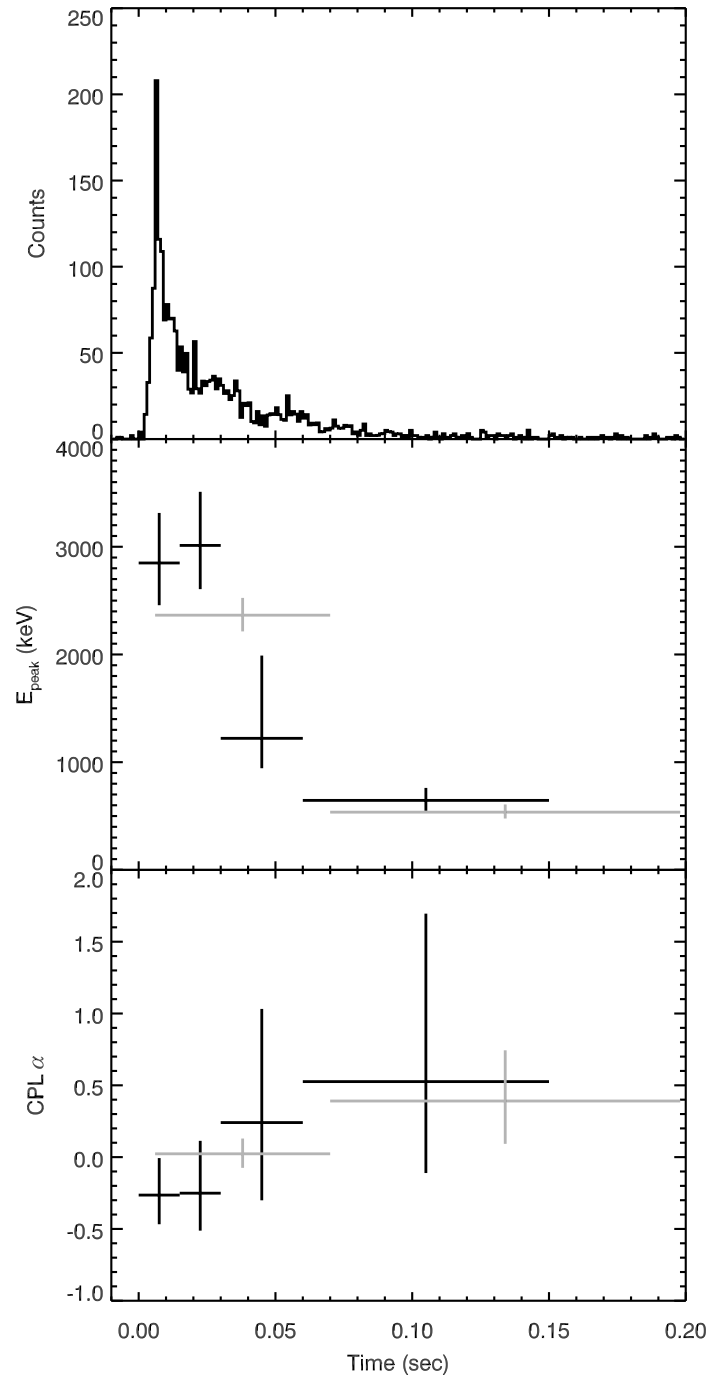


Figure 2.2: This figure, taken from Hurley et al. (2010b), shows the lightcurve of GRB 051103 in the top panel obtained from *RHESSI* (60 keV – 3 MeV, 1 ms time resolution). The middle and bottom panels show the evolution of the peak spectral energy and the power-law index of the spectrum fitted using *RHESSI* data (black) and joint fits with *Konus-Wind* (grey).

### 2.2.2 Optical Observations and Analysis

Observations were obtained on 6<sup>th</sup> November 2005 using the Mosaic wide field optical imaging camera at the Kitt Peak National Observatory (KPNO) 4m telescope. These data reach a limiting magnitude of  $\sim 24.5$  mag in the R band (measured by identifying the faintest known point sources within the images), which is considerably deeper than the study completed by Ofek et al. (2006) which had a limiting magnitude of 20.5 mag. The observations covered the majority of the original error region, and in particular that part nearest to the galaxy M81. The images were flat-fielded and sky subtracted using standard tasks within IRAF<sup>1</sup>.

For comparison, pipeline-reduced images of the region from Canada France Hawaii Telescope Legacy Survey (CFHTLS) were obtained via the Virtual Observatory (Walton et al., 2006)<sup>2</sup>. The data were found and downloaded by using the VODesktop and VOExplorer (Tedds, 2009). These formed part of the wide synoptic survey in the R band, also to a limiting magnitude of  $\sim 25$  (Ilbert et al., 2006). Coincidentally, the region was imaged on 1<sup>st</sup> November 2005, 2 days prior to the burst, and re-imaged within 1 month after the burst. This provided an ideal data set for comparison to the KPNO images as the timescale between the first images by CFHT and the images from KPNO is only 6 days, minimising any modulation in long-period variable stars in the disk/halo of M81.

Figure 2.1 shows the previous error quadrilateral, the refined  $3\sigma$  error ellipse and the fields covered by the KPNO observations, in relation to M81. The observations were positioned to cover the original error quadrilateral but still cover 62% of the refined  $3\sigma$  ellipse and contain 76% of the total likelihood. It is important to note that the observations cover the region closest to M81, and therefore this search addresses the possible association of GRB 051103 with M81.

Initially, the images were searched for variability of afterglow counterparts, either at the distance of M81 or in the background, by visual inspection (i.e. the images prior and after the GRB were blinked between and new sources were looked for) and no obvious afterglow candidate was found. The mag-

---

<sup>1</sup>IRAF is distributed by the National Optical Astronomy Observatories, which are operated by the Association of Universities for Research in Astronomy, Inc., under cooperative agreement with the National Science Foundation.

<sup>2</sup>This work makes use of EURO-VO software, tools or services. The EURO-VO has been funded by the European Commission through contracts RI031675 (DCA) and 011892 (VO-TECH) under the 6th Framework programme and contracts 212104 (AIDA) and 261541 (VO-ICE) under the 7th Framework Programme.

nitudes of sources within these images were then studied using SExtractor (Bertin & Arnouts, 1996) within the Graphical Astronomy and Image Analysis Tool (GAIA)<sup>3</sup>. They were all calibrated to the r band magnitudes of stars in the surrounding region as published in the Sloan Digital Sky Survey (SDSS Adelman-McCarthy et al., 2008). This calibration was completed using the magnitudes given by SExtractor and comparing them to the known magnitudes of stars within the field. The zeropoint magnitude used within SExtractor was adjusted until the magnitudes of the stars were consistent with the known values for that filter. The r band filter used by CFHT matched the filter used in SDSS however the filter used by KPNO was a Cousins R band filter. Although this is partially taken into account in the calibration to r band magnitudes, there are some sources which have large colour differences, for example very red sources. If a source appeared to differ in magnitude between the CFHT and KPNO images, the colour correction was calculated using equation 2.1 developed by Lupton (2005) and it was then determined if the magnitude difference was due to colour effects. The required g band data were from the SDSS catalogue when available or via photometry of g band images from the CFHTLS calibrated using SDSS sources in the field (Adelman-McCarthy et al., 2008; Ilbert et al., 2006). If it was not due to colour effects, the source was investigated further. It is important to note that there may be a source within the field which was varying but has not been identified due to this colour correction method. However, this method would only miss objects with a variability of  $\leq 0.3$  magnitude (the average colour correction factor used).

$$R = r - 0.1837 \times (g - r) - 0.0971 \quad (2.1)$$

In nearly all cases, stars whose magnitudes varied significantly between the images were found to have been caused by other factors, for example, being near chip edges or large diffuse galaxies unidentified by SExtractor. Chip edges often had noisy pixels which interfered with real sources or were misidentified as sources by SExtractor. The large galaxies were often split into multiple sources by SExtractor, this could be corrected using the SExtractor parameters but then other sources were missed. One of the stars in the region studied has a varying magnitude on the images studied

<sup>3</sup>GAIA is a derivative of the Skycat catalogue and image display tool, developed as part of the VLT project at ESO. Skycat and GAIA are free software under the terms of the GNU copyright.

and further investigation confirmed it is likely a variable star. This star was a point like object whose magnitude varied between the three different epochs of the r band images (6 days after the first CFHT observations it was  $\sim 1$  magnitude brighter in the KPNO images but was a comparable magnitude in the CFHT images  $\sim 1$  month later). Additionally, this source was present in images from different bands and epochs in the CFHTLS observations. This star is consistent with being a type II Cepheid within our own galaxy (e.g. Sandage & Tammann, 2006).

The extended sources were checked to look for a conventional SGRB afterglow within a moderately distant host galaxy, with a limiting magnitude of  $\sim 23.3$  mag. If an extended source appeared to be varying due to a possible point source being superimposed on it, the colour correction was calculated and the object was studied in more depth by eye. This involved using the software to match seeing conditions and measure the size of the object, and then to check if there was an indication of a change in shape which might indicate a superimposed afterglow component. No candidates were found using this analysis.

In addition to the photometry described above, PSF-matched image subtraction was also used to search for afterglow candidates, using a modified version of the ISIS code (Alard & Lupton, 1998; Alard, 2000). ISIS first uses the location of sources on a reference image to check and correct for any rotation or shift between the images being subtracted. The images are then subtracted from the reference image using a small stamp around each identified source. This method gives a better chance of finding sources that are blended with other, brighter objects (i.e. bright host galaxies). Cosmic ray cleaning was completed to remove elliptical artifacts and bright pixels caused by cosmic rays hitting the detector. The images were resampled onto a common pixel grid; the KPNO and CFHT images had different numbers of pixels and had different pixel scales so it was necessary to put them onto the same grid to allow subtraction. The KPNO data were subtracted from the CFHT data taken before and with the data taken after the burst. No credible afterglow candidates were found.

The analysis of the images found no optical afterglow candidate in the region studied 3 days after GRB 051103. This can place constraints on the progenitor of GRB 051103 by considering the expected results for the potential progenitors.

### 2.2.3 Progenitor option 1: a SGRB

The optical afterglows of various SGRBs have been studied and these data can be used to predict the range of afterglow properties of an SGRB of a particular gamma-ray fluence. There is evidence for a reasonable correlation, to first order, between gamma-ray fluence and afterglow flux (Nysewander, Fruchter, & Pe'er, 2009; Gehrels et al., 2008). Using XSPEC (Dorman & Arnaud, 2001), a model spectrum of GRB 051103 was created by creating a dummy spectrum in the *RHESSI* and Konus-Wind energy band, fit with the *RHESSI* and Konus-Wind joint fits in (Table 1; Hurley et al., 2010b) and the normalisation was then calibrated to give the published fluence values. The fit was then extrapolated to the *Swift* energy band to give the 15–150 keV fluence. The estimated 15–150 keV fluence of GRB 051103 is approximately  $9.6_{-3.7}^{+14.5} \times 10^{-7} \text{erg cm}^{-2}$ .

It is possible to compare GRB 051103 to other SGRBs in the BAT catalogue (Sakamoto et al., 2008b) using the approximate fluence, calculated for the energy band 15-150 keV, and the photon indices (given in Table 1; Hurley et al., 2010b). GRB 051103 is isolated at the extreme bright, hard end of the SGRBs in the *Swift* distribution (c.f. Figure 14 from Sakamoto et al., 2008b). Similarly, in the study of short bursts by Mazets et al. (2004) over the much wider Konus-Wind energy range (10 keV – 10 MeV), of the 109 spectra which could be characterized by an  $E_{peak}$ , none exceeded 2.53 MeV. The peak energy of GRB 051103 is approximately 3 MeV (Hurley et al., 2010b). Thus if GRB 051103 is an SGRB rather than an SGR giant flare, it is a fairly extreme case.

The fluence of this burst was compared to other SGRBs observed by the *Swift* Satellite. Table 2.1 provides the data of SGRB with fluences in the band 15-150keV and late optical observations, obtained from the relevant GCNs, and measured optical afterglows in the R band, approximately 3 days after each burst<sup>1</sup>. For two of the bursts it was necessary to estimate the fluence in the correct energy band using the same method as with GRB 051103. This is not a complete sample of SGRBs, as there are a number with a relatively low gamma-ray fluence that were either not observed optically, were not observed for longer than a few hours, or did not have a detected optical afterglow. This sample was chosen so it does not rely on the assumption that the light curve can be extrapolated to later epochs and because they are of a similar gamma-ray fluence to GRB 051103. Comparing the SGRBs in Table 2.1

<sup>1</sup>It is important to note the classification of some of these SGRBs are currently being debated (Zhang et al., 2009)

Table 2.1: The observed fluence, in the energy band 15-150keV, of SGRBs with observed R band magnitudes at approximately 3 days.

SGRB	Fluence $10^{-7} \text{ erg cm}^{-2}$	R band Magnitude at 3 days mag
051221A	$11.6 \pm 0.4$ <sup>(1)</sup>	$24.12 \pm 0.28$ <sup>(2)</sup>
051227	$2.3 \pm 0.3$ <sup>(3)</sup>	$25.49 \pm 0.09$ <sup>(4)</sup>
060121	$26.7^{+5.3}_{-20.2}$ <sup>(5)</sup>	$25 \pm 0.25$ <sup>(6)</sup>
060614	$217 \pm 4$ <sup>(7)</sup>	$22.74 \pm 0.31$ <sup>(8)</sup>
061006	$14.3 \pm 1.4$ <sup>(9)</sup>	$>23.96 \pm 0.12$ <sup>(10)</sup>
070707	$0.334^{+0.753}_{-0.316}$ <sup>(11)</sup>	$26.62 \pm 0.18$ <sup>(12)</sup>
070714B	$7.2 \pm 0.9$ <sup>(13)</sup>	$<25.5$ <sup>(14)</sup>
071227	$2.2 \pm 0.3$ <sup>(15)</sup>	$>24.9$ <sup>(16)</sup>
080503	$20.0 \pm 1$ <sup>(17)</sup>	$25.90 \pm 0.23$ <sup>(18)</sup>

<sup>(1)</sup> Cummings et al. (2005) <sup>(2)</sup> Soderberg et al. (2006) <sup>(3)</sup> Hullinger et al. (2005) <sup>(4)</sup> D'Avanzo et al. (2009) <sup>(5)</sup> an approximate fluence calculated using spectral parameters published by Golenetskii et al. (2006) <sup>(6)</sup> based on observations by Levan et al. (2006a) <sup>(7)</sup> Barthelmy et al. (2006) <sup>(8)</sup> Mangano et al. (2007) <sup>(9)</sup> Krimm et al. (2006) <sup>(10)</sup> an upper limit based on observations 2 days after the burst completed by D'Avanzo et al. (2009) <sup>(11)</sup> an approximate fluence calculated using spectral parameters published by Golenetskii et al. (2007) <sup>(12)</sup> Piranomonte et al. (2008) <sup>(13)</sup> Barbier et al. (2007) <sup>(14)</sup> a lower limit based on observations 4 days after the burst completed by Perley et al. (2009a) <sup>(15)</sup> Sato et al. (2007b) <sup>(16)</sup> a  $3\sigma$  upper limit published by D'Avanzo et al. (2009) <sup>(17)</sup> Ukwatta et al. (2008) <sup>(18)</sup> Perley et al. (2009a)

to GRB 051103 the optical afterglow is predicted to have an R band magnitude of  $\sim 24$  mag as it is at the higher end of the fluence distribution. This is within the limiting magnitude of the KPNO and CFHTLS images used, but would have been unobservable in the images obtained by Ofek et al. (2006). As no afterglow was observed, this rules out most typical SGRBs in the region of the error ellipse covered by these images. However, there are cases of SGRBs with extremely faint optical afterglows, for example GRB 080503, which had a similar fluence to GRB 051103 and an r band magnitude of  $25.90 \pm 0.23$  mag at 3 days (Perley et al., 2009a). So the observations cannot rule out an unusually faint SGRB in this region similar to GRB 080503. Additionally, GRB 051103 could be a classical SGRB in the part of the error ellipse not studied in this Chapter.

#### 2.2.4 Progenitor option 2: an SGR giant flare in M81

Conversely, GRB 051103 could be an SGR giant flare in M81 with similar energy to the giant flare from SGR 1806-20 (Golenetskii et al., 2005) and a very faint optical afterglow (Eichler, 2002; Levan et al., 2008). Using observations of the giant flare from SGR 1806-20, the apparent optical magnitude of an SGR in M81 can be predicted. The distance to SGR 1806-20 has proven difficult to determine; the distance modulus adopted by many authors is 15.8 mag (Corbel et al., 1997), although Bibby et al. (2008) recently obtained a revised distance modulus estimate of  $14.7 \pm 0.35$  mag. This Chapter continues to use the larger distance modulus as this will provide an approximate upper limit on the absolute magnitude. The giant flare from SGR 1806-20 had an observed radio afterglow and this has been used by Wang et al. (2005) to make predictions of the apparent R band magnitude of the afterglow. Their analysis suggests that the giant flare would have had an apparent magnitude of  $\sim 22$  at 3 days, and hence an absolute magnitude of  $M \approx 6$  mag. Taking this as the absolute magnitude of any afterglow of GRB 051103 if it is an SGR giant flare, and using the distance modulus to M81 of 27.8 (Freedman et al., 1994) and equation 2.2, the afterglow would be expected to have an apparent magnitude of  $> 34$  mag. Despite the many uncertainties involved in this calculation, there is some confidence that such an afterglow would not be detectable with the data available.

$$m - M = 5 \log d - 5 \quad (2.2)$$

SGRs have been observed during periods of activity using ROTSE-I (Akerlof et al., 2000) and *Swift* (for example Cummings et al., 2009), and IR observations have been obtained for SGR 1900+14 4.1 days after outburst detecting no variability (Oppenheimer et al., 1998). These have provided upper limits on the optical afterglows from the softer spectrum, shorter, and weaker bursts seen during active phases of SGRs but it is important to note that there have been no reported rapid optical follow up observations of galactic SGR giant flares, which have a significantly higher fluence and are spectrally harder than these bursts. Therefore, this Section is completely reliant on theoretical predictions and future observations may show discrepancies with these predictions. Indeed, these observations with a limiting magnitude of 24.5 mag, giving an absolute magnitude -3.3 mag assuming it is at a distance of 3.6 Mpc, constitute one of the deepest absolute magnitude searches for an afterglow from a possible SGR giant flare. This absolute magnitude is only exceeded by the search for an afterglow from GRB 070201, which is a candidate SGR giant flare in M31, corresponding to an absolute magnitude of -7.4 mag obtained 10.6 hours after the burst (Ofek et al., 2008). However, as discussed later, it is unlikely that both of these events were SGR giant flares (Chapman, Priddey, & Tanvir, 2009).

From the *GALEX* UV imaging (Martin et al., 2005), there is evidence that the error ellipse does contain star forming regions in the outer disk of M81. The two brightest UV sources are marked on Figure 2.3 (Ofek et al., 2006). These young stellar regions in M81 could host an SGR which could emit a giant flare. Similarly, these UV regions could be the locations of massive star clusters, and SGRs 1900+14 and 1806-20 have been associated with massive star clusters (Mirabel & Fuchs, 1999; Vrba et al., 2000). However, if GRB 051103 is an SGR giant flare in M81, a young (up to  $\sim 10^4$  years old; Duncan & Thompson, 1992) SNR might also be expected in the nearby region, although this association is still being debated (Gaensler et al., 2001, 2005). When an SGR is formed, it is theoretically possible that it is given a kick of up to  $1000 \text{ km s}^{-1}$  or more (Duncan & Thompson, 1992) and therefore could have traveled a distance of  $>10 \text{ pc}$  from the SNR. However, this is only equivalent to an angular separation of  $\sim 0.6 \text{ arcsec}$  at a distance of 3.6 Mpc (Freedman et al., 1994). Hence, an accompanying SNR would

still be expected to fall within the error ellipse. Of the known SNR in M81 (Matonick & Fesen, 1997), there are none within the error ellipse.

M81 has been studied by the *Chandra X-Ray Observatory* (Swartz et al., 2003) and three X-ray sources are within the error ellipse. However, they have not been identified in visible or radio observations. Additionally, they have not been identified with known SNR, nearby stars, are not co-incident with HII starforming regions (the expected location of SGRs; Duncan & Thompson, 1992) and are more likely to be X-ray binary systems than unidentified SNR (Swartz et al., 2003). This X-ray survey had a limiting luminosity of  $3 \times 10^{36} \text{ erg s}^{-1}$ , which means it would detect very young supernovae, as the oldest supernovae with detected X-ray afterglows had a luminosity of  $\sim 10^{37} \text{ erg s}^{-1}$  and an age of  $\sim 60$  years (Soria & Perna, 2008). Additionally, this survey would detect the X-ray luminous SNR as these have a luminosity of up to  $\sim 10^{37} \text{ erg s}^{-1}$  but would not detect the X-ray faint SNRs which have a luminosity of  $\sim 10^{34} \text{ erg s}^{-1}$  (Immler & Kuntz, 2005). SGRs are well known to be quiescent soft X-ray emitters and Mereghetti et al. (2000) have measured the soft X-ray flux of SGR 1806-20 to be approximately  $10^{-11} \text{ erg cm}^{-2} \text{ s}^{-1}$ . Frederiks et al. (2007a) determined that the *Chandra Observatory* would be unable to observe directly the persistent X-ray flux from an SGR like SGR 1806-20 in M81.

An alternative method of searching for SNR is to use  $\text{H}\alpha$  and [OIII] narrow band observations. The Isaac Newton Telescope (INT) has been used to search for planetary nebulae in M81 by Magrini et al. (2001) and they have found 171 potential candidates, some of which are in the nearby region of the refined error ellipse. Their criteria for differentiating between an SNR and a planetary nebula is that planetary nebulae cannot be spatially resolved and SNR are. A young SNR, as required for an SGR, could be misidentified as a planetary nebula by this criterion, since a one arcsec region corresponds to a physical size of  $\sim 20 \text{ pc}$ . Young SNRs may well be significantly smaller than this, since an expansion velocity of a few thousand  $\text{km s}^{-1}$  over a magnetar lifetime of  $\sim 10^4$  years leads to sizes of  $10 - 50 \text{ pc}$ . Indeed, many SNRs in M82 appear (based on radio maps) to be fairly compact (Fenech et al., 2008). However, the nearest is still  $\sim 23$  arcsec from the error ellipse, and earlier in this Chapter it was shown that an SGR in M81 would only be able to travel  $\sim 0.6$  arcsec from its birthplace. The  $\text{H}\alpha$  luminosity of SNRs in nearby disk galaxies tends to be greater than  $\sim 10^{36} \text{ erg s}^{-1}$  (de Grijs et al., 2000) and the work by Magrini et al. (2001) had a limiting  $\text{H}\alpha$  flux of less than  $6 \times 10^{-17} \text{ erg cm}^{-2} \text{ s}^{-1}$  which corresponds to a limiting luminosity of  $\sim 10^{35} \text{ erg s}^{-1}$ . Therefore, their survey would be expected to

find a candidate SNR. The recently published  $H\alpha$  and [OIII] images from the INT Wide Field Camera Imaging Survey (McMahon et al., 2001) were used, with a limiting luminosity of  $\sim 10^{35}$  erg  $s^{-1}$  at the distance of M81 as these are the same images as used by Magrini et al. (2001), and compared with 21cm radio images from THINGS (Walter et al., 2008) and Chandra X-ray source positions (Swartz et al., 2003) to search for previously unidentified SNRs within the error ellipse. There is a possible circular 21cm radio source coincident with a Chandra X-ray source of approximately the right flux for an SNR in M81 (source 15 in Swartz et al., 2003). However, the 21cm radio source is too large for an SNR of the required age and there is no convincing supporting evidence of a source within the other images studied. Using the published known X-ray sources it might have been expected to find an SNR if it was very young or bright and it would have been expected to find an associated SNR using the  $H\alpha$  images. No convincing associated SNR candidates within the error ellipse were identified, however not all Galactic SGRs have been associated with SNRs so this non-detection is inconclusive.

Although it has been determined that the error ellipse does cross potential star formation regions as required by the majority of SGR models, it should also be noted that this is not essential for all. An alternative route has been proposed for producing a magnetar by white dwarf (WD) mergers or the accretion induced collapse (AIC) of a WD (King, Pringle, & Wickramasinghe, 2001; Levan et al., 2006b). As WD have long lifetimes, WD-WD mergers would be associated with older populations of stars. It is possible that AIC will drive off a fraction of the envelope, leaving something akin to an SNR behind (e.g. Baron et al., 1987). The mechanisms underlying AIC are poorly understood, and the physical characteristics and detectability of such remnants are not clear. Therefore a SGR produced through these channels could be formed in an old stellar population within the outer disk or halo, and the non-detection of an SNR within the region does not place constraints on this model.

If the progenitor was an SGR giant flare, then there might be significant similarities in the light curve and spectrum of GRB 051103 to the giant flare from SGR 1806-20, e.g. the hardness of their spectra or a periodic component in the emission following the main peak. Ofek et al. (2006) noted that the light curve of these two events were consistent, i.e. the light curve of GRB 051103 is similar to what would be expected from an extragalactic version of the giant flare from SGR 1806-20. From Table 1 in Hurley et al. (2010b), for the joint RHESSI + KW fits, initially  $\alpha = 0.13^{+0.14}_{-0.11}$  and it softens to  $\alpha = 0.39^{+0.35}_{-0.30}$ . Although this is unusually hard for a GRB, it is consistent with the photon index of

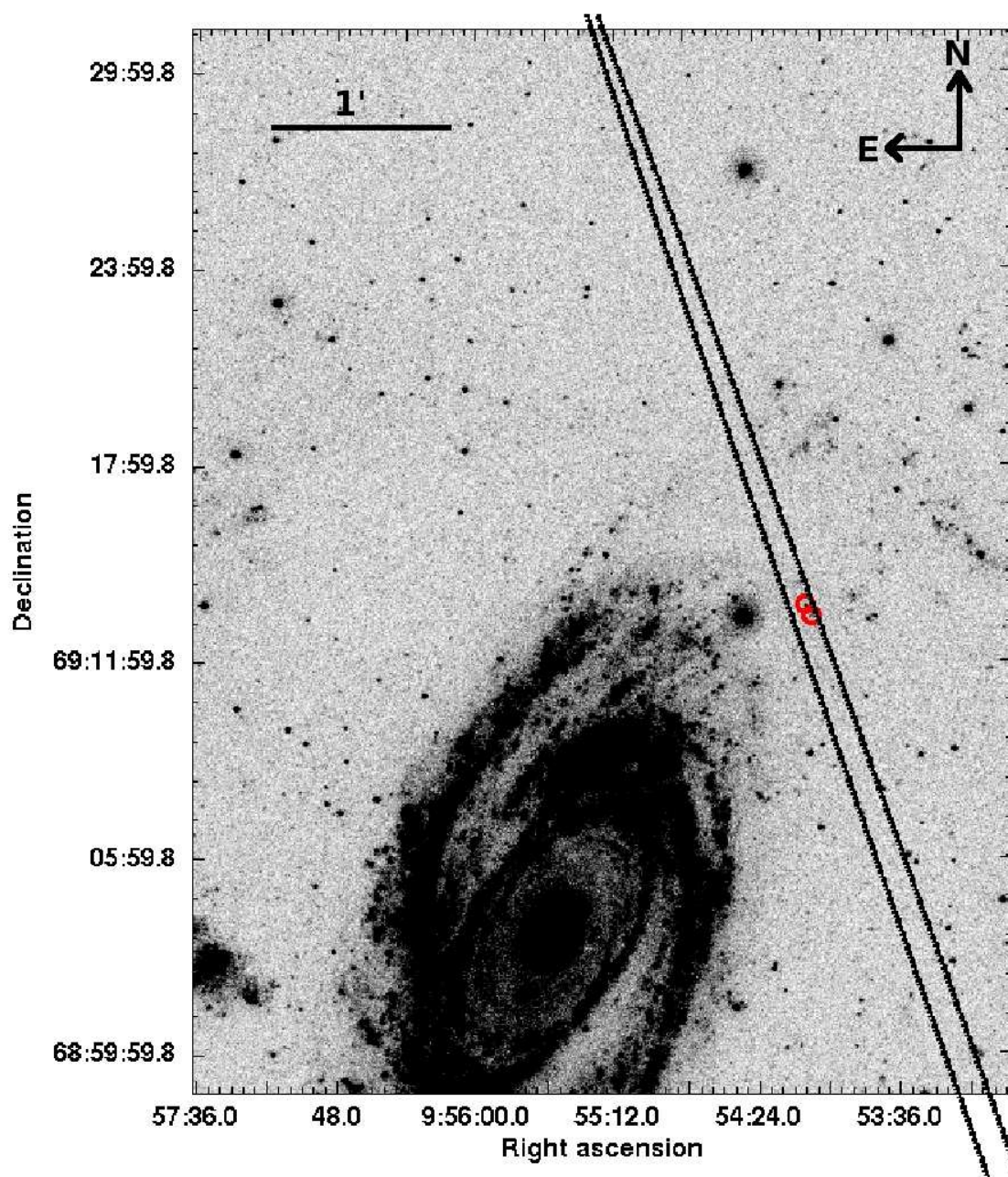


Figure 2.3: *GALEX* image showing the UV sources within the error ellipse. Two of the brightest sources discussed by Ofek et al. (2006) are highlighted by the circles within the ellipse.

the giant flare from SGR 1806-20,  $\alpha = 0.2 \pm 0.3$  (Palmer et al., 2005). The peak luminosity of GRB 051103, assuming it was from an SGR in M81, is approximately  $4.7 \times 10^{48} \text{ erg s}^{-1}$ . This is a factor of 10 brighter than the peak luminosity of the giant flare from SGR 1806-20, which is  $2 - 5 \times 10^{47} \text{ erg s}^{-1}$  assuming it is at a distance of 15 kpc (Hurley et al., 2005). With the revised distance estimate from Bibby et al. (2008), the peak luminosity of the giant flare from SGR 1806-20 would be  $7 \times 10^{46} \text{ erg s}^{-1}$ , suggesting that a much smaller percentage of SGRBs are SGR giant flares. This value is 30 times fainter than the peak luminosity of GRB 051103 if it was from an SGR giant flare in M81 and in this case GRB 051103 would be the most luminous SGR giant flare observed. In comparison, the peak luminosity of GRB 070201 is  $1.14 \times 10^{47} \text{ erg s}^{-1}$  assuming it was in M31 (Ofek et al., 2008), which is an order of magnitude fainter than GRB 051103 and comparable to the giant flare from SGR 1806-20. It is important to note however, that there is currently no theoretical upper limit for the energy of a giant flare. Duncan & Thompson (1992) showed that the total energy available is given by equation 2.3 where  $B_{15} = B/10^{15} \text{ G}$ . Therefore, the magnetic field (B) of SGR 1806-20 would only need to increase by a factor of  $\sim 5$  to produce a giant flare with an energy that is 30 times greater than the one from SGR 1806-20.

$$E \propto 3 \times 10^{47} B_{15}^2 \text{ erg} \quad (2.3)$$

Although the gamma-ray data suggest that GRB 051103 may be an extragalactic SGR giant flare, it is important to note that SGR giant flares are rare events. Considering plausible luminosity functions, Chapman, Priddey, & Tanvir (2009) calculated the probability that the IPN would observe a giant flare, with energy greater than the energy emitted by the giant flare from SGR 1806-20, in the region surveyed during the 17 years it has operated. For one giant flare, they calculated the probability to be 10%. However, as discussed in the introduction, there are five potential candidates for extragalactic SGR giant flares, including GRB 070201 near M31 which has been proposed to be an SGR giant flare by Mazets et al. (2008) and new results will be shared in Section 2.3. The probability that the IPN has detected two SGR giant flares, with energy greater than the giant flare from SGR 1806-20, is 0.6% (Chapman, Priddey, & Tanvir, 2009). Recently, several new SGR candidates have been identified

including 0501+4516, 1550-5418 and possibly 0623-0006 (Barthelmy et al., 2008a; Krimm et al., 2008; Barthelmy et al., 2008b), which may imply that the number of SGRs in the Milky Way is higher than previously thought. In this case, the luminosity of the giant flare from SGR 1806-20 would have to be at the peak of the luminosity function of SGR giant flares and therefore giant flares of this luminosity must be extremely rare events. This argues that GRB 051103 is unlikely to be a second SGR giant flare in the nearby Universe.

### 2.2.5 Conclusions regarding GRB 051103

This Section has presented new optical observations of GRB 051103 and have determined that there is no R band optical afterglow with a limiting magnitude of  $\sim 24.5$  mag (for an afterglow overlapping a host galaxy, the limiting magnitude is  $\sim 23.3$  mag) in the region of the error ellipse covered by these observations. Comparison of the prompt emission of GRB 051103 with a sample of other SGRBs leads to the conclusion that if it was a classical SGRB an optical afterglow would have been expected in these observations.

In contrast, if GRB 051103 were an SGR giant flare in M81, non-detection of an afterglow would not be surprising as the expectations for optical afterglow emission lie significantly below the limits obtained here, or the limits likely to be attained via current technology. The case for an SGR origin would be strengthened if there were an accompanying SNR within the error ellipse, but there is no evidence of this. An SGR produced via AIC of a WD or WD mergers (Levan et al., 2006b) would, however, remove the requirement for an SNR. Additionally, the luminosity of GRB 051103, assuming it is from an SGR giant flare in M81, is significantly higher than known SGR giant flares but still attainable with current theoretical models. Giant flares with luminosity similar to the giant flare from SGR 1806-20 are extremely rare and it is unlikely that GRB 051103 and GRB 070201 are both extragalactic SGR giant flares.

These findings, and the conclusions drawn from the prompt emission (Hurley et al., 2010b), show that GRB 051103 could be a giant flare from an extragalactic SGR in M81. However, it is very difficult to confirm this progenitor for GRB 051103 and shows the challenges of identifying any SGRB as an

extragalactic SGR giant flare.

Although this option has not been considered in detail, it is possible that the progenitor of GRB 051103 was a compact binary merger in M81. In this case, it would just be within the reach of current gravitational wave searches. This scenario was ruled out at  $>99.9\%$  confidence for GRB 070201 in M31 using the Laser Interferometer Gravitational-wave Observatory (LIGO) observations, and distances out to 3.5 Mpc were ruled out to 90% confidence (Abbott et al., 2008). The LIGO Scientific Collaboration is currently considering a search for gravitational-wave signals in the data surrounding GRB 051103 (G. Jones and P. Sutton, private communication).

## 2.3 GRB 070201

Ofek et al. (2008) and Mazets et al. (2008) conducted an in depth analysis of the properties of GRB 070201, a candidate extragalactic SGR giant flare from the Andromeda Galaxy (M31) at a distance of 770 kpc. This GRB was detected by the IPN and would have an isotropic energy of  $\sim 1.4 \times 10^{45}$  erg if it was in M31. No optical afterglow was found to a limiting magnitude of  $R < 17.1$  mag at 10.6 hours after the trigger time. Using archival data, Ofek et al. (2008) showed several X-ray sources and SNRs within the error trapezium which may be associated with this GRB. They found no X-ray source showing periodic behaviour as might be expected for an SGR and showed that the counterpart would have an 0.2–10 keV X-ray flux of  $10^{-17}$ – $10^{-14}$  erg cm $^{-2}$  s $^{-1}$  (based on known SGR luminosities which range between  $10^{33}$ – $10^{36}$  erg s $^{-1}$ ).

### 2.3.1 Methods

This Section revisits GRB 070201 using up-to-date archival data within the Virtual Observatory (Walton et al., 2006). As described for GRB 051103, if the SGR was formed within a SN explosion, then it may be possible to find a candidate quiescent X-ray counterpart associated with a SNR. It was previously noted in Section 2.2.4 that an SGR could travel  $>10$  pc from the counterpart SNR during its  $10^4$  year lifetime, this corresponds to an angular separation of  $\sim 3$  arcsec at 770 kpc. Using 3 arcsec as the

maximum separation within errors, the 2XMMi catalogue (Watson et al., 2009) was crossmatched with all known SNR positions in M31 (Magnier et al., 1995) using Topcat<sup>4</sup>. 8 candidate matches were found using this method, however only 1 resides within the error trapezium (source 1 in the tables). These candidates and the error trapezium are shown in Figure 2.4 and data are provided in Table 2.2. Using the area of M31 (44610 square arcmin, calculated using the HyperLeda data; Paturel et al., 2003) and the area of the error trapezium crossing M31 ( $\sim 400$  square arcmins), the number of expected crossmatches by chance found within the error trapezium is 0.07.

The probability of randomly picking a position within the boundary of M31 which is 3 arcsec away from a SNR is given by the ratio of the area covered by SNRs and the total area of M31. Using the published diameters of SNRs within M31 (or assuming a point source where no diameter is given; Magnier et al., 1995), plus 3 arcsec, the total area covered by SNRs in M31 is 38.211 square arcmin. Therefore, the chance of randomly picking a position within M31 which is within 3 arcsec of a SNR is 0.086%. Completing the same calculation for all the 2XMM sources within M31 and a typical position error of 2 arcsec, the chance of randomly picking a position within M31 that is 3 arcsec away from a 2XMM source is 0.141%. The chance of choosing a position that is 3 arcsec away from both a 2XMM source and a SNR is 0.012%, assuming they are unrelated, and the probability that there is 1 random match out of the 8 candidates is 0.096%. Therefore, the matches are unlikely to be due to random chance.

X-ray source 1 (the source in the trapezium) is faint ( $\sim 7 \times 10^{-14}$  erg cm<sup>-2</sup> s<sup>-1</sup>) and is located  $3.2 \pm 2.4$  arcsec from a candidate SNR. This luminosity is consistent with the predictions for SGR quiescent counterparts by Ofek et al. (2008). The SNR identification is uncertain (a knot in a nebula with a diameter of 1.8 mm on the photographic plate; Baade & Arp, 1964) but if it is a young SNR, as expected for an SGR, it may be more difficult to identify. Additionally the source is located on the edge of a ring of star formation around M31 (Devereux et al., 1994). Figure 2.5 shows the location of the candidate match on a UV composite image (using GALEX observations; Martin et al., 2005), the source is on the edge of a bright UV emission region marking the presence of ongoing star formation or massive stars as might be expected for an SGR candidate (e.g. Duncan & Thompson, 1992; Thompson & Duncan, 1995; Mirabel & Fuchs, 1999; Vrba et al., 2000; Figer et al., 2005; Mereghetti, 2008).

---

<sup>4</sup><http://www.starlink.ac.uk/topcat/>

Table 2.2: The 8 candidate X-ray sources and their separation from the associated SNR. Diameters of the SNRs are provided where available. The separations are from the X-ray source and the centre of the SNR, the errors are given by the sum of the 2XMM position errors and the position error for the SNR.

Number	SNR ID	Diameter (arcsec)	Separation from X-ray source (arcsec)	Comments
1	BA212	-	$3.22 \pm 2.9$	
2	1-008	16.6	$2.81 \pm 5.5$	Source within SNR
3	3-041	1.2	$2.55 \pm 3.9$	
4	3-072	11.9	$2.74 \pm 5.3$	Source within SNR
5	3-079	22.6	$3.97 \pm 3.8$	Source within SNR
6	BA521	-	$1.88 \pm 0.7$	
7	K594	-	$1.39 \pm 4.7$	
8	BA650	-	$3.17 \pm 2.2$	

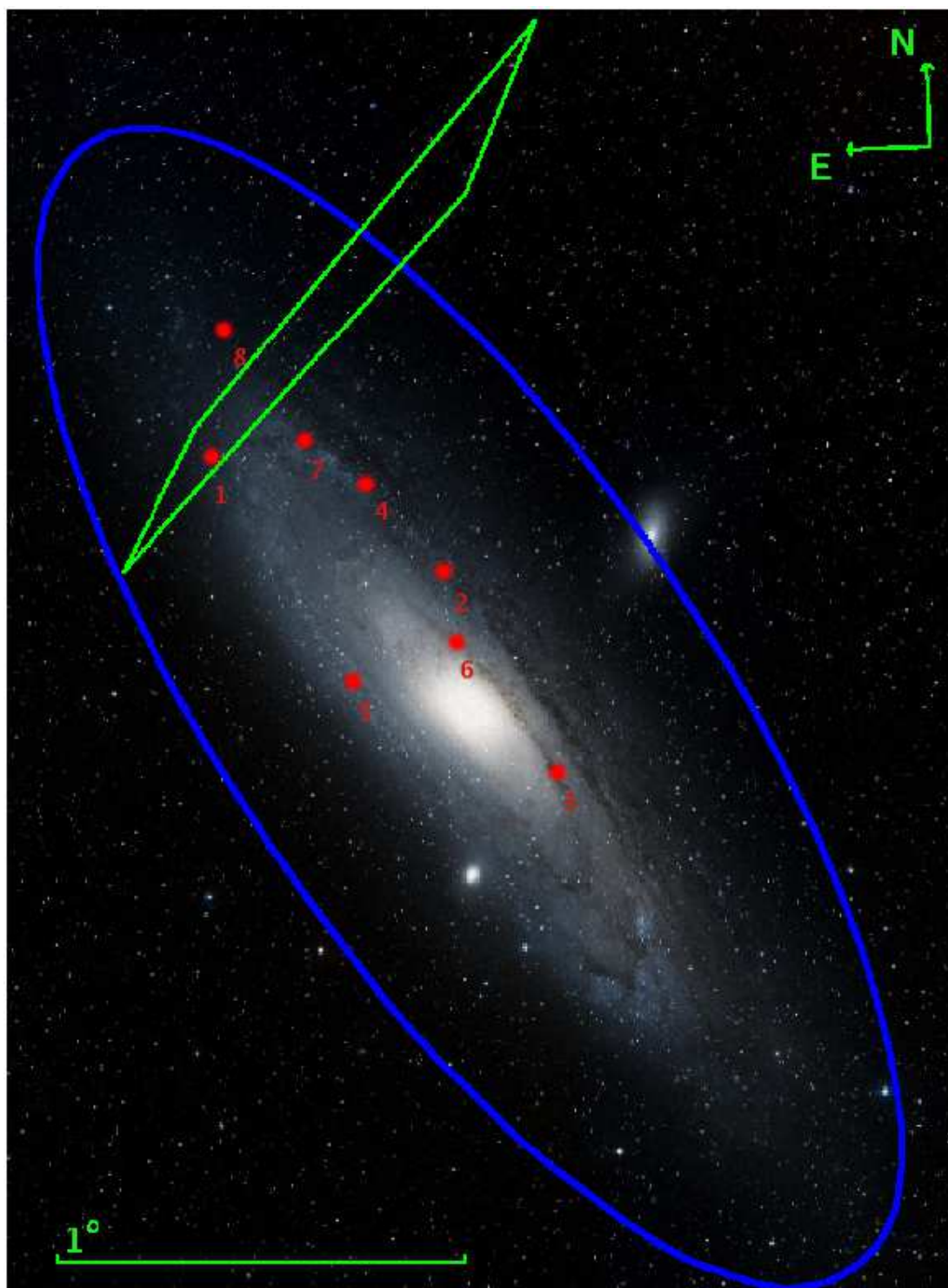


Figure 2.4: The error trapezium of GRB 070201 is overlaid, in green, upon the Digitised Sky Survey optical image of M31. The extent of M31 is shown in blue using the HyperLeda data (Paturel et al., 2003) and the 8 SNR-2XMM crossmatched sources are shown using the red stars. This image was created using Aladin (Bonnarel et al., 2000).

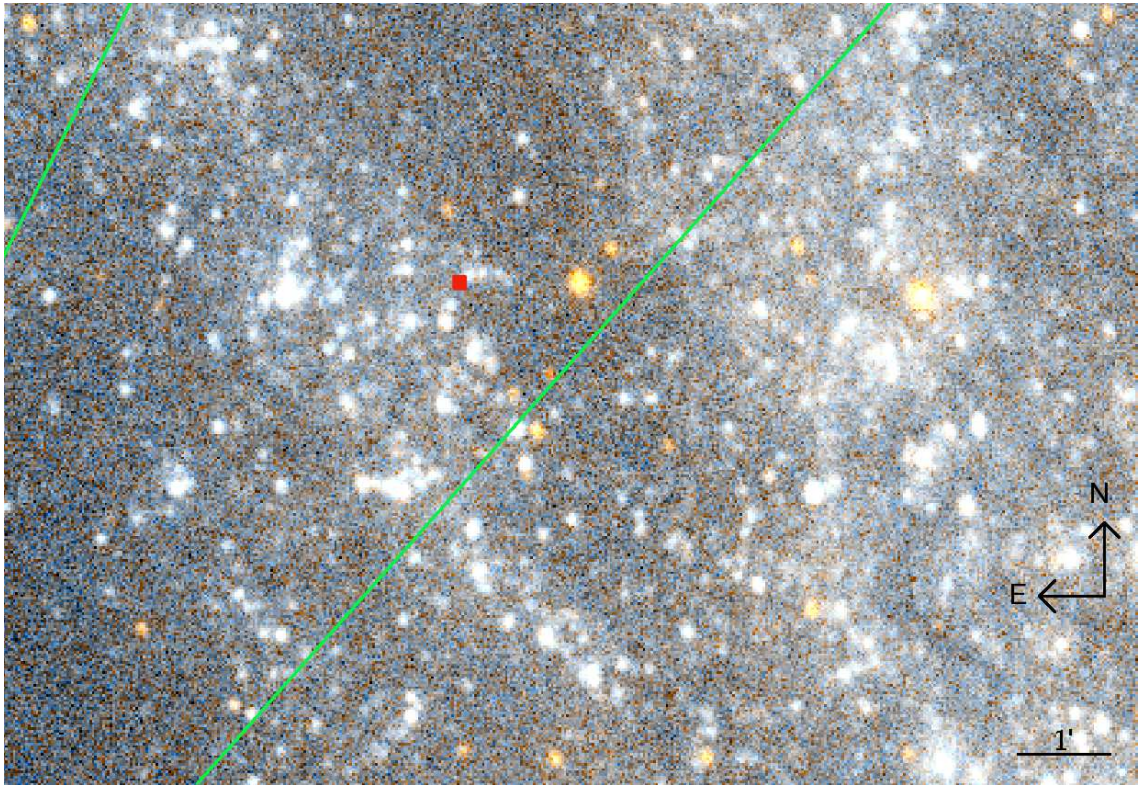


Figure 2.5: A composite NUV (red) and FUV (blue) image using *GALEX* data of M31 created using Aladin (Bonnarel et al., 2000). The green lines represent the boundaries of the error trapezium. The red box is the SNR and X-ray source match, located on a UV emission region indicating ongoing SF or massive stars.

Background active galactic nuclei (AGNs) make a large contribution to the X-ray sources in the 2XMM catalogue so each of the 8 SNR-2XMM source crossmatches were checked to ensure the source was not a background AGN. Pineau et al. (2011) completed a cross correlation of 2XMM sources and the Sloan Digital Sky Survey to identify AGN candidates and characterise their properties. In order to compare the 8 candidate matches to the AGN sample, CFHTLS images (Ilbert et al., 2006) were obtained using the Virtual Observatory (Walton et al., 2006). The R band magnitudes were calibrated using US Navy Observatory (USNO) objects<sup>5</sup>. The magnitudes provided are for any sources lying within the 2XMM position error for each source or the limiting magnitude of the CFHTLS survey ( $\sim 25$  mag; Ilbert et al., 2006). The 2XMM properties of the 8 candidate matches and the deepest optical limit or detection are

<sup>5</sup>This research has made use of the USNO Image and Catalogue Archive operated by the United States Naval Observatory, Flagstaff Station (<http://www.nofs.navy.mil/data/fchpix/>)

listed in Table 2.3. The ratio  $\frac{F_X}{F_R}$  was calculated using equation 2.4 from Chiappetti et al. (2005). It is important to note that the large errors associated with the X-ray fluxes have a large impact on the values for sources 1, 2 and 4 making them upper limits. These values were then compared to the AGN population identified by Pineau et al. (2011) and shown in Figure 2.6. The candidates without a detected optical source are generally inconsistent with the AGN population, whereas the others are candidate AGN. However, sources 2 and 4 lie within the SNRs and they are likely to be associated. Source 1, the candidate SGR counterpart, is unfortunately the only source which cannot be conclusively ruled out as an AGN, although the nearby optical source may be related to the active star formation region and not a background galaxy. Further X-ray observations are required to reduce the position error and the X-ray flux errors which will assist in ruling out an AGN. Although it cannot be ruled out as an AGN, these observations also do not rule out source 1 being an SGR counterpart.

$$\log\left(\frac{F_X}{F_R}\right) = \log F_X + 5.51 + \frac{R}{2.5} \quad (2.4)$$

This source may be detectable by current X-ray observatories, for example *Swift*, and a count rate can be predicted using WebPIMMS<sup>6</sup>. It is assumed that this source is an SGR with a spectrum comparable to SGR 1806-20 (photon index  $\sim 2.9$ , obtained using the *Swift* automated data products produced by Evans et al., 2009) and a Galactic absorption of  $N_H = 1.5 \times 10^{21} \text{ cm}^{-2}$  for this position (Kalberla et al., 2005). Source 1, with a 0.2 – 12 keV flux of  $(7.6 \pm 7.7) \times 10^{-14} \text{ erg cm}^{-2} \text{ s}^{-1}$ , would have a *Swift* XRT (0.3 – 10 keV) count rate of  $2.8_{-2.8}^{+2.7} \times 10^{-3} \text{ count s}^{-1}$ . Hence, it is predicted that a 10 ks observation would detect  $\sim 30$  counts from this source. This would enable a significantly improved position and spectrum which may be able to exclude an AGN.

<sup>6</sup>WebPIMMS is a Web version of the PIMMS (v4.3) tool. PIMMS was developed by Koji Mukai at the HEASARC. <http://heasarc.gsfc.nasa.gov/Tools/w3pimms.html>

Table 2.3: The 2XMM catalogue properties of the 8 candidate X-ray sources and the deepest optical observation of that position. HR2 is the hardness ratio between XMM bands 2 and 3. The optical magnitudes were converted into fluxes and compared to the X-ray fluxes using the method described in Pineau et al. (2011). These sources are then compared to the AGN population identified in Pineau et al. (2011).

Number	Source ID	RA	Dec	Position Error (arcsec)	Flux ( $F_x$ ) ( $\text{erg cm}^{-2} \text{s}^{-1}$ )	HR2	Optical limit (magnitude)	$\log\left(\frac{F_x}{F_R}\right)$
1	2XMMi J004604.1+415236	11.5171	41.8768	2.6	$(7.6 \pm 7.7) \times 10^{-14}$	$0.20 \pm 0.87$	20.7	$< 1.23$
2	2XMMi J004304.4+413609	10.7683	41.6026	2.5	$(5.8 \pm 8.2) \times 10^{-15}$	$-1.00 \pm 0.58$	21.1	$< 0.35$
3	2XMM J004135.6+410655	10.3986	41.1156	0.9	$(1.4 \pm 0.7) \times 10^{-14}$	$-0.57 \pm 0.09$	$> 25$	$> 1.33$
4	2XMM J004404.8+414844	11.0202	41.8123	2.3	$(1.1 \pm 7.0) \times 10^{-14}$	$-0.49 \pm 0.24$	20.1	$< 0.72$
5	2XMMi J004413.4+411954	11.0561	41.3319	0.8	$(1.2 \pm 0.5) \times 10^{-14}$	$-0.44 \pm 0.08$	$> 25$	$> 1.34$
6	2XMM J004253.3+412550	10.7225	41.4307	0.4	$(3.4 \pm 0.3) \times 10^{-14}$	$-0.71 \pm 0.03$	$> 25$	$> 1.98$
7	2XMM J004452.7+415458	11.2196	41.9162	1.7	$(1.2 \pm 0.5) \times 10^{-14}$	$-0.29 \pm 0.19$	$> 25$	$> 1.34$
8	2XMMi J004556.6+421107	11.4862	42.1852	1.9	$(1.3 \pm 1.1) \times 10^{-14}$	$0.97 \pm 0.14$	$> 25$	$> 0.79$

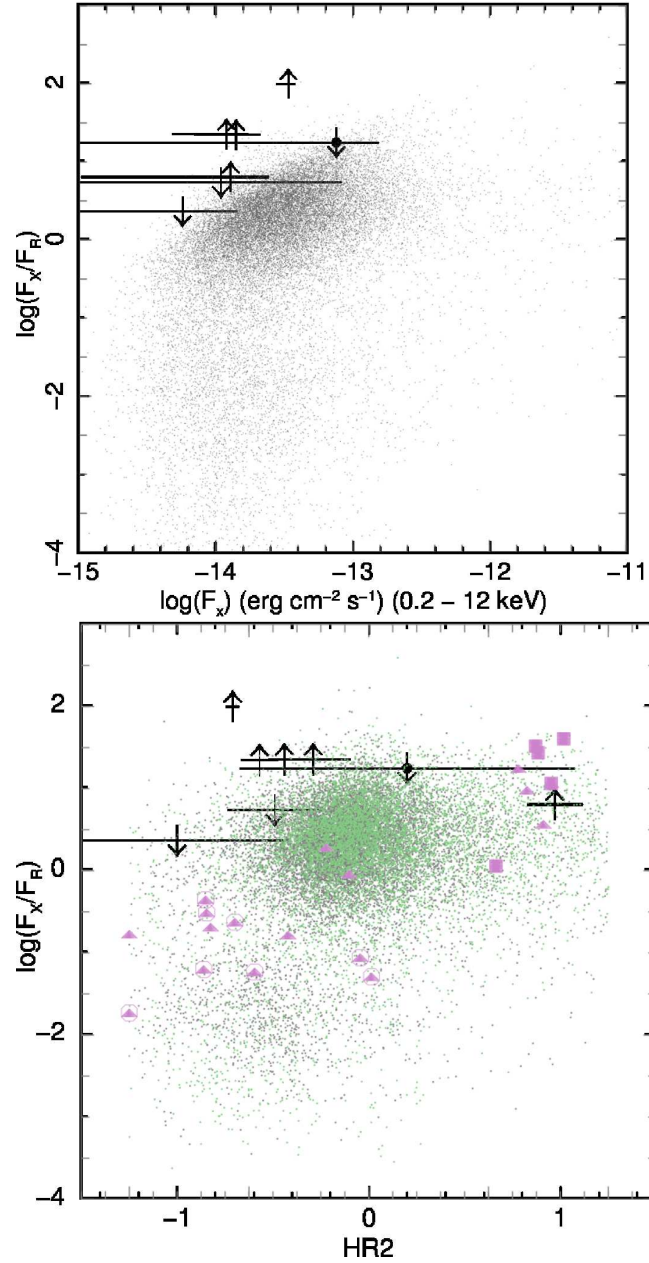


Figure 2.6: (a)  $\log\left(\frac{F_X}{F_R}\right)$  and the 0.2 – 12 keV flux of each of the X-ray sources which are associated with SNRs overlaid upon the results for the AGN population (Figure 4c from Pineau et al., 2011). Source 1 is marked with a filled black circle. (b)  $\log\left(\frac{F_X}{F_R}\right)$  and HR2, the hardness ratio between XMM bands 2 and 3, for the X-ray sources studied (Source 1 is marked with a filled black circle) overlaid upon the AGN population. The grey data points were unresolved in the SDSS, the green data points were resolved in the SDSS and the pink symbols represent AGN which are type 2 QSOs (square) or X-ray selected AGN (triangle) (Figure 8d from Pineau et al., 2011)

### 2.3.2 Conclusions regarding GRB 070201

It has been shown that an SGR kicked from its formation place would be a distance of  $\sim 3$  arcsec from an associated SNR at a distance of M31. This Section has identified an X-ray source located  $3.2 \pm 2.4$  arcsec from a SNR within the error trapezium of GRB 070201. There were only 7 other such matches within M31 so the chances of finding 1 within the error trapezium is very low. The likelihood of a chance alignment of a SNR and a 2XMMi source, within the boundary of M31, has also been shown to be unlikely giving increased confidence that all 8 matches are associated with each other. This source has the flux expected for a quiescent SGR counterpart in M31, lies at approximately the right distance from a SNR and is located in a region of active star formation as expected for a massive star progenitor. It is an ideal candidate quiescent counterpart for an SGR giant flare.

However, it is not possible to discount this source as a background AGN due to large uncertainties in the X-ray observations, it has been shown that the other 7 matches are unlikely to be background AGN as expected. There are also large positional uncertainties for GRB 070201 and uncertainties in both the SNR candidacy. With future deep observations of the X-ray source, it may be possible to clearly identify it with the SNR but, as no SGR has been observed to emit multiple giant flares, it is unlikely to be unambiguously associated with GRB 070201.

This Section has shown the methods that could be used to identify quiescent counterparts in the future given improved GRB positions and deep X-ray observations.

## 2.4 GRB 110406A

GRB 110406A was among the brightest bursts detected by SPI-ACS (anti-coincidence system) on board *INTEGRAL* with a duration  $\sim 3$  s and peak flux of  $3.8 \times 10^5$  counts  $s^{-1}$  (Savchenko et al., 2011). The  $T_{90}$  duration is calculated using the published 80 keV – 100 MeV lightcurve<sup>7</sup> (shown in Figure 2.7) and a program developed by R. Willingale for Rowlinson et al. (private communication), giving

<sup>7</sup>Available here:  
[http://www.isdc.unige.ch/integral/ibas/cgi-bin/ibas\\_acs\\_web.cgi/?trigger=2011-06-10T15-21-32.000-00000-00000-0](http://www.isdc.unige.ch/integral/ibas/cgi-bin/ibas_acs_web.cgi/?trigger=2011-06-10T15-21-32.000-00000-00000-0)

$$T_{90} = 1.017 \pm 0.035 \text{ s.}$$

This GRB was also detected using *Konus-Wind* identifying a total duration of 8 s and a non-zero spectral lag ( $\sim 130$  ms for 300 – 1160 keV versus 18 – 70 keV lightcurves; Golenetskii et al., 2011) which is extremely unusual for typical SGRBs (Norris & Bonnell, 2006). The *Konus-Wind* lightcurve is shown in Figure 2.8. The total time-integrated spectrum of this burst was fitted by the Band et. al. (1993) model with  $\alpha = -1.24^{+0.08}_{-0.07}$ ,  $\beta = -2.30^{+0.15}_{-0.25}$  and a peak energy of  $E_p = 326^{+49}_{-42}$  keV (20 keV – 10 MeV; Golenetskii et al., 2011). This spectral fit gives a fluence of  $(4.8 \pm 0.5) \times 10^{-5}$  erg cm $^{-2}$  and peak flux of  $(1.5 \pm 0.1) \times 10^{-4}$  erg cm $^{-2}$  s $^{-1}$ .

The IPN triangulated the position of this GRB (Hurley et al., 2011), shown in Figure 2.9 using the red trapezium. This overlays much of the nearby (3 Mpc) galaxy NGC 404, which is clearly visible in UV despite a nearby bright star. At this distance the isotropic energy release of this GRB would be  $6 \times 10^{46}$  erg, consistent with the giant flare from SGR 1806-20 (Rowlinson et al., 2011). NGC 404 has a high star formation intensity of  $2.2 \times 10^{-5}$  M $_{\odot}$  yr $^{-1}$  kpc $^{-2}$ , much of which occurs in a bright HI ring ( $2.5 \times 10^{-3}$  M $_{\odot}$  yr $^{-1}$ , visible in the UV image) around the galaxy showing evidence of a recent galaxy merger event (Thilker et al., 2010). The presence of active star formation suggests that there are massive stars available as may be required for the progenitor of an SGR (as previously mentioned for GRBs 051103 and 070201).

Unfortunately, this location was in Sun constraint for many weeks after the GRB so no follow-up observations were possible. However, this remains an extremely interesting candidate extra-Galactic SGR giant flare.

## 2.5 Implications for future studies

For future reference, it is important to note that with more accurate positions and rapid follow up observations it may be possible to observe the optical afterglows of extragalactic giant flares. Theoretical models of SGR giant flares often assume they are similar to the blast wave model used to describe classical GRBs. Wang et al. (2005) use the blast wave model and radio observations of the giant flare from

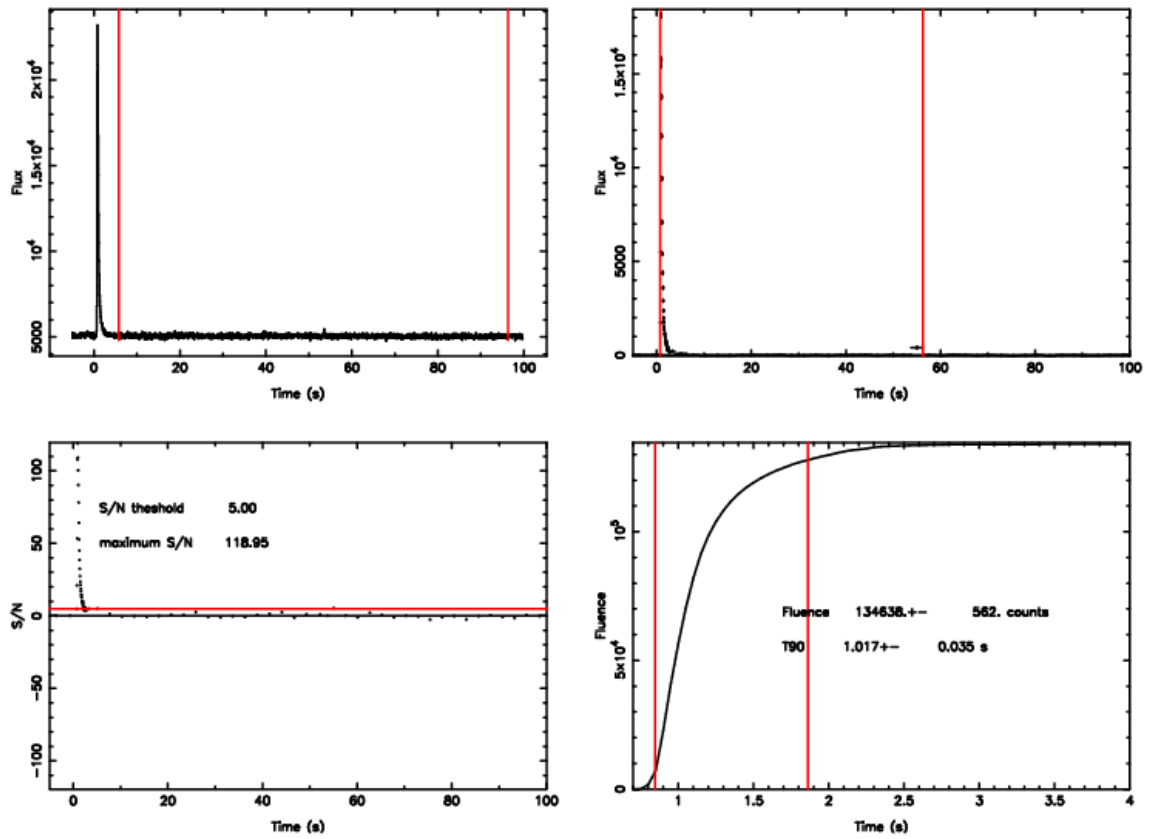


Figure 2.7: The 80 keV – 100 MeV SPI-ACS lightcurve for GRB 110406A. The top left corner shows the lightcurve with 50 ms binning, the red lines represent the background region chosen. Top right is the  $5\sigma$  signal-to-noise binning, the red lines represent the start and end of the significant bins. Bottom left is the significance of each bin relative to the background rate, the red lines represent the start and end of the significant bins. Bottom right is the cumulative fluence (in counts) for the duration of the transient, the red lines represent the  $T_{90}$  duration.

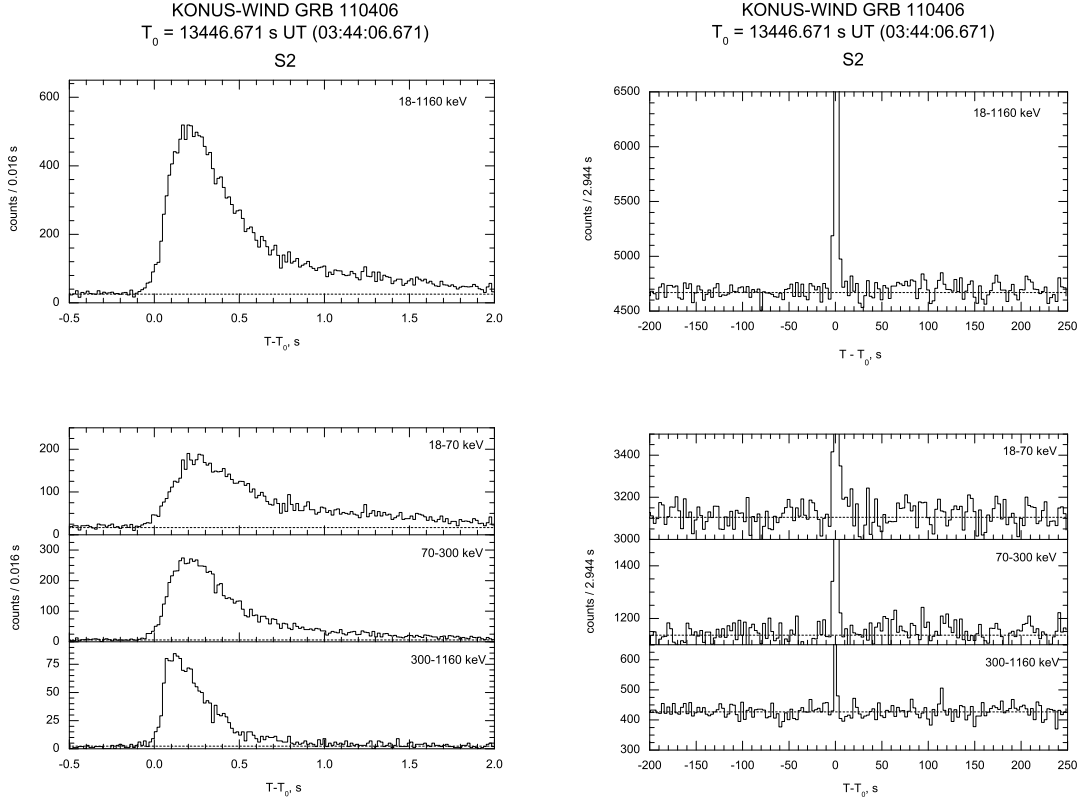


Figure 2.8: The *Konus-Wind* Lightcurve of GRB 110406A, with a 16 ms time resolution on the left and a 2.944 s time resolution on the right. (Golenetskii et al., 2011)

SGR 1806-20 to extrapolate the predicted optical afterglow. Shifting their prediction to the distance of M81 (as in Section 2.2.4 and using equation 2.2), if there were a second potential giant flare in M81 the optical afterglow is predicted to have a peak apparent K band magnitude of  $\sim 20$  mag at 86 s after the giant flare and would fall to  $\sim 26$  mag at 1 hour. This is observable with current and upcoming facilities, for example the European Extremely Large Telescope (E-ELT). However, these predictions are subject to many assumptions and future multi-wavelength observations are required to determine the luminosity and behaviour of SGR giant flare afterglows.

With the prompt slewing capabilities of *Swift* and upcoming missions like *SVOM*, it is more likely that an X-ray afterglow is detected for SGRBs providing a more accurate position and other properties. If GRB 051103 had been an SGR giant flare in M81, would an X-ray afterglow be observable? Although gamma-ray afterglows have been observed for SGR giant flares, at 400 – 900 s after the giant flare

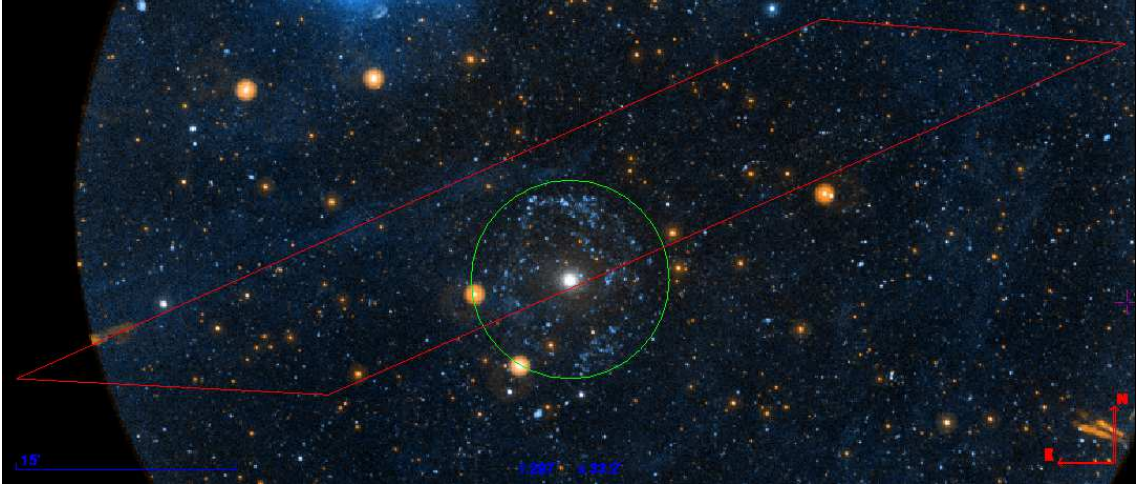


Figure 2.9: The red error trapezium of GRB 110406A overlaid upon a composite NUV (red) and FUV (blue) image using *GALEX* data of NGC 404 (the green circle illustrates the extent of this galaxy obtained using the HyperLeda catalogue). This image was created using data from the Virtual Observatory (Walton et al., 2006) and Aladin (Bonnarel et al., 2000).

(Boggs et al., 2007; Mereghetti et al., 2005), no X-ray afterglow has yet been observed as there have been no rapid X-ray follow up observations reported. Using the spectral fit for the afterglow (Boggs et al., 2007) and the observed light curve (Mereghetti et al., 2005), the 20 keV – 20 MeV peak afterglow flux was converted to the 0.3 – 10 keV flux:  $(2_{-2}^{+700}) \times 10^{-9} \text{ erg cm}^{-2} \text{ s}^{-1}$ . Scaled to the distance of M81, this would correspond to a flux of  $(3_{-3}^{+1000}) \times 10^{-14} \text{ erg cm}^{-2} \text{ s}^{-1}$ . Using WebPIMMS<sup>1</sup>, the Galactic  $N_H$  in the direction of M81 ( $5.6 \times 10^{20} \text{ cm}^{-2}$ ; Kalberla et al., 2005) and the spectrum published in Boggs et al. (2007), the *Swift* XRT flux would be  $\sim 3.6_{-3.6}^{+11974} \times 10^{-4} \text{ count s}^{-1}$ . Rapid observations with a duration of  $>10$  ks would be required to confidently detect such an afterglow component. Due to the significant errors on these values, from the uncertainty in the spectral fit, it is not possible to determine if an X-ray afterglow is expected.

An alternative method to estimate the X-ray afterglow assumes that the emission mechanism for SGR giant flares is the same as for the normal flares observed. X-ray afterglows have been observed from flares originating from SGR 1900+14 with a typical decay of  $\alpha \sim 0.4$  and luminosities of  $\sim 10^{36} \text{ erg s}^{-1}$  at 0.1 s after the flares (Nakagawa et al., 2008). The giant flare observed from SGR 1900+14

<sup>1</sup>WebPIMMS is a Web version of the PIMMS (v4.0) tool. PIMMS was developed by Koji Mukai at the HEASARC. <http://heasarc.gsfc.nasa.gov/Tools/w3pimms.html>

Table 2.4: X-ray afterglow flux predictions at a distance of M81. **include adopted distances column**

Template Event	Adopted Distance (kpc)	Predicted X-ray Afterglow Peak Luminosity (erg s <sup>-1</sup> )	Flux at 0.1 s (erg cm <sup>-2</sup> s <sup>-1</sup> )	Flux at 100 s (erg cm <sup>-2</sup> s <sup>-1</sup> )	Predicted Swift XRT Count Rates (count s <sup>-1</sup> )
SGR 1900+14	13.5	$9 \times 10^{37}$	$6 \times 10^{-14}$	$3 \times 10^{-15}$	$8 \times 10^{-5}$
SGR 1806-20	14.5	$9 \times 10^{38}$	$6 \times 10^{-13}$	$3 \times 10^{-14}$	$8 \times 10^{-4}$
GRB 051103	$3.6 \times 10^3$	$2 \times 10^{40}$	$1 \times 10^{-11}$	$8 \times 10^{-13}$	$2 \times 10^{-2}$

was detected by *BeppoSAX* with a peak count rate of  $1.5 \times 10^5$  counts  $s^{-1}$ , this is a lower limit as the detector was saturated (Feroci et al., 2001). Using WebPIMMS, this was converted into a BAT count rate and compared it to the peak flux of flares giving a scaling factor to predict the X-ray afterglow. Table 2.4 gives the X-ray afterglow predictions for events like SGR 1900+14, SGR 1806-20 and GRB 051103 scaled to a distance of M81. The flux predictions are then given at 100 s, assuming a decay of  $\alpha \sim 0.4$  and a prompt slew of an X-ray telescope to the afterglow location (this is typically achieved by *Swift*). The prediction for an SGR 1806-20 like event at M81 using this method is consistent with the previous prediction using the gamma-ray afterglow. The predicted count rates also show that, with a prompt slew and observation for 1 ks, *Swift* would be able to detect the afterglow of a giant flare in M81. This analysis used the typical flares observed from SGRs and scales them up to a giant flare, however it is becoming increasingly clear that there is an intermediate type of flare which are brighter than typical flares and exhibit a long lived (1 – 8 ks) X-ray tail with a thermal spectrum (Lenters et al., 2003; Gogus et al., 2011). These tails constitute  $\sim 1 - 2$  % of the total energy output in the flare and this percentage appears to be dependent on the SGR (Gogus et al., 2011). If giant flares exhibit a similar tail emission, then the X-ray fluxes predicted in this Section may be underestimates.

Given the predictions given in this Section, it seems the X-ray afterglow of an extragalactic SGR giant flare might be detectable at the distance of M81 given a rapid slew to the position. However, the predictions all have significant errors, due to extrapolating observations to different timescales and energy bands, and are based on assumptions about SGR giant flare afterglows. More multi-wavelength follow up on Galactic SGR flares, giant flares and candidate extragalactic SGR giant flares is required.

## 2.6 Extragalactic SGR giant flare rate in the local Universe

It has been shown statistically that both GRB 051103 and GRB 070201 are extremely unlikely to both be SGR giant flares by Chapman, Priddey, & Tanvir (2009). However, since that calculation has been completed several new SGRs have been identified and AXPs have exhibited SGR-like behaviour so it is worth revisiting. There are now 9 SGRs and 12 AXPs known in the Milky Way and the Magellanic

Clouds<sup>8</sup>. Since the discovery of the first giant flare 32 years ago, there have only been 3 detected giant flares from all the known SGRs giving the Galactic giant flare rate of  $0.094 \text{ yr}^{-1}$ . For each known SGR this gives a giant flare rate of  $0.0104 \text{ yr}^{-1}$ . As AXPs have now been observed to exhibit SGR-like behaviour, if they are also capable of producing giant flares this rate drops to  $0.0045 \text{ yr}^{-1}$  per known SGR or AXP. The 3 observed giant flares would be detectable out to  $\sim 4 \text{ Mpc}$ , which encompasses all three extragalactic candidates considered in this Chapter.

As the typical progenitors of magnetars are massive stars, the giant flare rate might be expected to trace the star formation rate ( $0.68 - 1.45 M_{\odot} \text{ yr}^{-1}$  for the Milky Way; Robitaille & Whitney, 2010). Recently there was an UV survey of galaxies within 11 Mpc using *GALEX* observations (Lee et al., 2011). Converting the FUV magnitudes of all galaxies within 4 Mpc to star formation rates using equation 2.5 (Kennicutt, 1998), the total star formation rate within 4 Mpc is calculated to be  $8.5 M_{\odot} \text{ yr}^{-1}$ .

$$SFR(M_{\odot} \text{ yr}^{-1}) = 1.4 \times 10^{-28} L_{\nu}(\text{erg s}^{-1} \text{ Hz}^{-1}) \quad (2.5)$$

Assuming the SGR giant flare rate is directly proportional to the star formation rate, this would give a SGR giant flare rate within 4 Mpc of  $0.55 - 1.2 \text{ yr}^{-1}$ . Within the 21 year lifetime of the IPN, 11 – 25 SGR giant flares are expected to be detected within 4 Mpc. This is much higher than expected given current observations, so it is likely that this result is over simplified (e.g. the assumptions that the giant flares are of similar magnitude and that they directly trace star formation are not good enough for this analysis). Given the work by Chapman, Priddey, & Tanvir (2009), one of the candidates presented within this Chapter is likely to be an SGR giant flare but it is extremely unlikely that 2 or more are real SGR giant flares. It is important to note that all these rates are uncertain as they are based on small number statistics within the Milky Way and the Magellanic Clouds and an assumption that the rate is proportional to the star formation rate. The rates also exclude magnetar formation routes not associated with older stellar populations such as NS-NS mergers (see Chapters 4 and 5), WD-WD mergers and

---

<sup>8</sup><http://www.physics.mcgill.ca/~pulsar/magnetar/main.html>

AIC of a WD. Hence, although it is unlikely that more than 1 of these candidates are SGR giant flares, this option cannot be fully discounted.

## 2.7 Overall Conclusions

Some SGRBs may be associated with nearby galaxies and are giant flares from extragalactic SGRs, however, given current observations, they are very difficult to conclusively prove. Three good candidates detected by the IPN have been presented in this Chapter.

- GRB 051103 was considered in depth in this Chapter, however the properties of this GRB are consistent with both progenitor theories showing how difficult it is to discriminate between them. Therefore, the progenitor of GRB 051103 remains elusive.
- The catalogued objects within the error trapezium of GRB 070201, one of the best cases for an extragalactic SGR giant flare, has been reanalysed and a candidate quiescent counterpart has been identified. Although this is not conclusively associated, it is unlikely that an X-ray source and nearby SNR would be found within the error trapezium. With more accurate positions from missions such as *Swift* and the future mission *SVOM*, associations like this will be essential for confirming the progenitor.
- GRB 110406A was unfortunately in Sun constraint preventing all follow-up observations so remains inconclusive. However, the prompt properties and host galaxy association are consistent with an SGR giant flare.
- Both of the error boxes for GRBs 070201 and 110406A cross over active star formation rings within their potential host galaxies, this suggests that the stellar populations present are consistent with SGR progenitors and timely for their formation.
- It has been shown statistically that it is extremely unlikely that more than 1 of GRB 051103, GRB 070201 and GRB 110406A are SGR giant flares. Given the published results and the findings of this Chapter, the most likely candidate is GRB 070201. However, this calculation is subject to

small number statistics and assumptions about the SGR population tracing average star formation rates in the local Universe.

- These candidates have illustrated the necessity for rapid, deep, multi-wavelength follow-up observations. With accurate positions, firm associations with host galaxies can be made and regions within those hosts can be studied in detail. This, along with analysis of the afterglow, can lead to the identification of which are likely SGR giant flares and which are “typical” SGRBs.

This Chapter has focused on a potential progenitor for a small number SGRBs within the local universe, however it is clear that SGR giant flares are not energetic enough to explain the cosmological distribution of SGRBs. The next Chapter uses an in depth study of a SGRB host galaxy to place constraints on the typical progenitor of SGRBs.

# Chapter 3

## Discovery of the afterglow and host galaxy of the low redshift short GRB 080905A

### 3.1 Introduction

This Chapter presents the discovery of the optical afterglow and host galaxy of the short GRB 080905A, as published in Rowlinson et al. (2010a), and uses these observations to place constraints on the progenitor. Its faint afterglow pinpointed its location to a spiral host galaxy at  $z = 0.1218$ , making it the most local short burst yet known. SGRB 050709 has the next lowest confirmed redshift for a SGRB at  $z = 0.16$  (Fox et al., 2005), followed by SGRB 050724 associated with a host galaxy at  $z = 0.257$  (Barthelmy et al., 2005b; Berger et al., 2005). SGRB 061201 may be associated with a galaxy at lower redshift of  $z = 0.111$  but it was not possible to confirm this as it was offset by 17 arc (Stratta et al., 2007). In Section 3.2, the observations obtained of the afterglow of GRB 080905A are described and the spectra obtained for the host galaxy. These data are analysed in Section 3.3, the implications of these findings are discussed in Section 3.4 and conclusions are drawn in Section 3.5.

A redshift of  $z = 0.1218$  gives a luminosity distance of 562.3 Mpc, and 1 arcsec corresponds to 2.17 kpc.

## 3.2 Observations and Analysis

### 3.2.1 Prompt emission properties

GRB 080905A was detected by Swift at 11:58:54 UT. It is a SGRB with  $T_{90}$  duration of  $1.0 \pm 0.1$  s. The Burst Alert Telescope (BAT) detected three flares peaking at  $T + 0.04067 \pm 0.0007$  s,  $T + 0.17^{+0.03}_{-0.10}$  s and  $T + 0.869 \pm 0.003$  s. The time averaged BAT spectrum was best fit by a power law with a photon index of  $\Gamma = 0.85 \pm 0.24$  and the fluence was  $(1.4 \pm 0.2) \times 10^{-7}$  erg  $\text{cm}^{-2}$  in the 15 - 150 keV energy band (Cummings et al., 2008a). GRB 080905A was also detected by *INTEGRAL* (Pagani & Racusin, 2008) and the *Fermi* Gamma-ray Burst Monitor (GBM; Bissaldi et al., 2008). Using the redshift of 0.1218, the isotropic energy released is  $4.7 \pm 0.7 \times 10^{49}$  erg in the 15 - 150 keV energy band.

Some short GRBs show evidence for a soft extended emission component in the prompt emission (e.g Barthelmy et al., 2005b; Norris & Bonnell, 2006). There is no evidence of soft extended emission in the BAT 15-25 keV light curve for GRB 080905A, with a limiting flux of  $< 5.2 \times 10^{-7}$  erg  $\text{cm}^{-2}$   $\text{s}^{-1}$ . Additionally, short GRBs have negligible spectral lag in their prompt emission unlike long GRBs (Norris & Bonnell, 2006; Yi et al., 2006). A spectral lag analysis of GRB 080905A was performed, based upon the cross correlation function methodology used in Ukwatta et al. (2010). The cross correlation function method looks for similarities within lightcurves of different energy bands and then determines if high energy emission arrives at a different time to lower energy emission. This method is more complex and accurate than simply comparing the arrival times of peaks which assumes the structure of a peak and may struggle with highly variable lightcurves. The analysis considered several timescales using 128, 64, 32, 16, 8 and 4 ms binned lightcurves and compared all six pairing combinations of the BAT's four energy channels. There is a lack of emission below 25 keV, which results in very low cross correlation amplitudes for paired lightcurves containing channel 1. Channels 2 and 4 also have relatively low emission, so in this analysis cross correlation between channels 2 and 3 were used and the lag was determined using a gaussian fit. The  $1\sigma$  error is calculated using 1000 lag Monte Carlo simulations. The lag time of GRB 080905A is  $4 \pm 17$  ms, which is consistent with zero as expected for a short GRB.

### 3.2.2 X-ray Afterglow Observations

The fading X-ray afterglow was located by *Swift* with an enhanced position of RA (J2000): 19 10 41.74 and Dec (J2000): -18 52 48.8 with an uncertainty of 1.6 arcsec (90% confidence; Evans, Osborne, & Goad, 2008).

The time averaged X-ray Telescope (XRT) spectrum using the photon counting (PC) data is best fit by an absorbed power law with photon index  $\Gamma = 1.45 \pm 0.25$  and with an intrinsic absorption  $N_{\text{H}} = 1.6 \pm 1.0 \times 10^{21} \text{ cm}^{-2}$  in excess of the Galactic absorption of  $N_{\text{H}} = 9 \times 10^{20} \text{ cm}^{-2}$  (Kalberla et al., 2005). The combined BAT-XRT lightcurve can be fit with a broken power law decay model with one break. The best fit model is  $\alpha_1 = 2.62_{-0.13}^{+0.25}$ , breaking at  $T_1 = 443_{-84}^{+408}$  s to a decay of  $\alpha_2 = 1.49_{-3.66}^{+0.60}$ .

#### Combined BAT-XRT lightcurves

The XRT lightcurve and raw BAT data were obtained from the UK *Swift* Data Centre (Evans et al., 2007, 2009). To make a combined BAT-XRT lightcurve, the BAT data were processed using standard HEASOFT routines<sup>1</sup> and the BAT lightcurve was rebinned using  $3\sigma$  significance bins using a code produced by A. Beardmore and P. Evans. The BAT spectrum was then fit using a powerlaw in XSPEC (Dorman & Arnaud, 2001), the total counts in the spectrum were recorded ( $CR_{total}$ ), and then the fit was extrapolated to provide a total 0.3 – 10 keV flux ( $F_x$ ). Each count rate data point ( $CR_{\gamma}$ ) in the BAT lightcurve was then converted from 15 – 150 keV to 0.3 – 10 keV flux using the conversion in equation 3.1. The BAT lightcurve data points are then included in the XRT lightcurve. The resulting lightcurve does not include spectral evolution during the burst, however as it is for a SGRB there are insufficient data for detailed conversion. A program was written to automate several of these steps and this method is used to make BAT-XRT lightcurves throughout this Thesis.

$$flux = CR_{\gamma} \times \frac{F_x}{CR_{total}} \quad (3.1)$$

<sup>1</sup><http://heasarc.gsfc.nasa.gov/lheasoft/>

### Restframe lightcurves

It is often useful to compare the restframe lightcurves of GRBs, by converting each flux,  $f$ , data point in the BAT-XRT lightcurve to a luminosity,  $L$ , with a restframe time (calculated using equation 3.2, where  $z$  is the redshift and  $t_{obs}$  is the observed time). The flux is converted to a luminosity using equation 3.3 where the luminosity distance,  $D_l$ , is found iteratively for a given redshift. There is a factor,  $k_{corr}$  (Bloom, Frail, & Sari, 2001), which takes into account the spectral shape and the required energy bands. This Thesis uses an adapted and automated program, initially developed by R. Willingale to convert fluences to energies, to convert observed lightcurves into restframe lightcurves.

$$t_{rest} = \frac{t_{obs}}{1+z} \quad (3.2)$$

$$L = 4\pi D_l^2 f k_{corr} \quad (3.3)$$

Using the redshift of 0.1218, the combined BAT-XRT lightcurve of GRB 080905A has been converted to the rest-frame time and 0.3 – 10 keV luminosity lightcurve, shown in Figure 3.1.

### 3.2.3 Optical Observations

Early optical imaging of GRB 080905A obtained only upper limits on the afterglow flux, which were found by UVOT at T+ 114 s ( $V > 21.3$  mag, where T is the trigger time; Brown & Pagani, 2008), the Mt. John Observatory at T+ 2580 s ( $R > 20.8$  mag; Tristram et al., 2008), and the MITSuME telescope at T+ 2520 s ( $R > 17.6$  mag; Nakajima et al., 2008).

The observations began at the Nordic Optical Telescope (NOT)<sup>2</sup> 8.5 hours after the burst, with further epochs obtained with the Very Large Telescope (VLT)<sup>3</sup> utilizing the FOcal Reducer and low dispersion Spectrograph 2 (FORS2; Appenzeller & Rupprecht, 1992) taking place 14.3 and 36 hours after

<sup>2</sup>Based on observations made with the Nordic Optical Telescope, operated on the island of La Palma jointly by Denmark, Finland, Iceland, Norway, and Sweden, in the Spanish Observatorio del Roque de los Muchachos of the Instituto de Astrofísica de Canarias.

<sup>3</sup>Based on observations at ESO telescopes at Paranal Observatory under programme ID 081.D-0588.

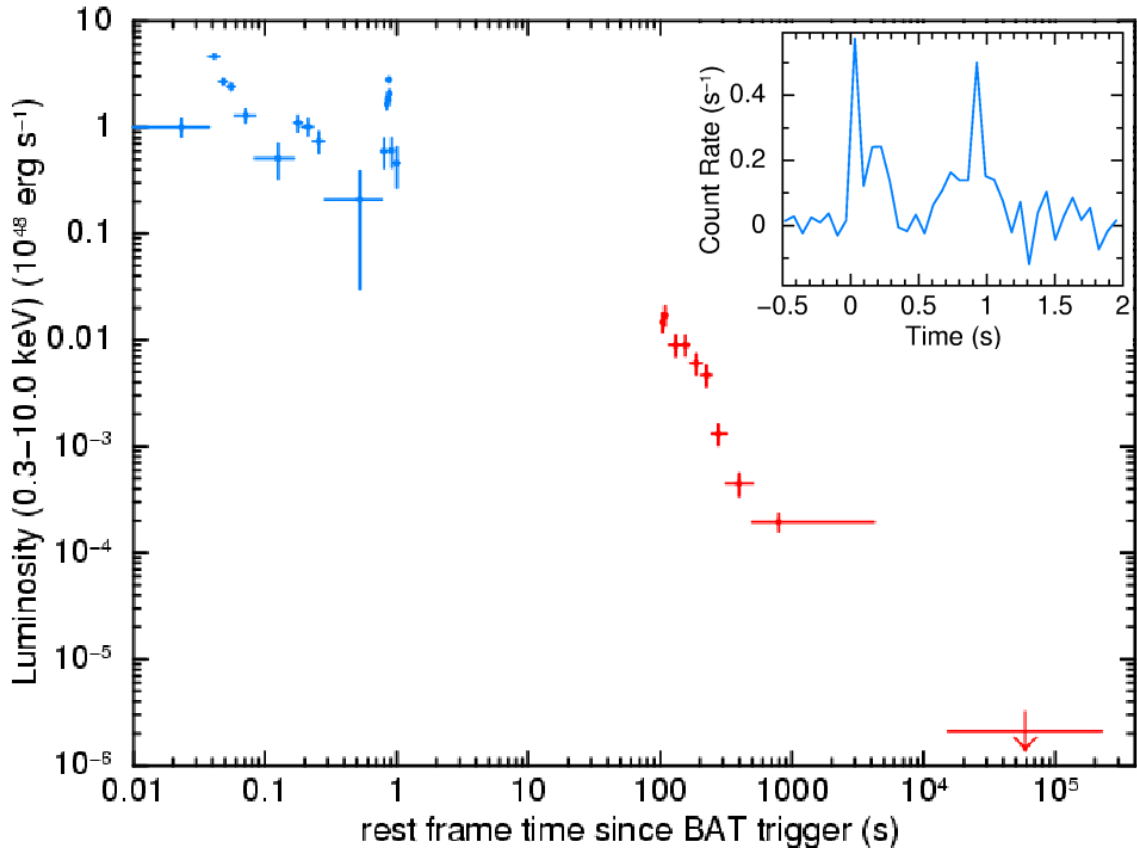


Figure 3.1: This shows the combined BAT and XRT luminosity and rest frame light curve for GRB 080905A. The BAT data are plotted until  $\sim 2$  s and the XRT data are plotted starting at  $\sim 100$  s. Inset is the BAT lightcurve with linear observed time on the horizontal axis and BAT count rate on the vertical axis.

the burst. A final R-band observation was made on 23 September, 17.5 days post burst. Using the Infrared Spectrometer And Array Camera (ISAAC; Moorwood, 1997) a further K-band observation was obtained on 1 October, 25.5 days post burst. Comparison of these observations allowed the discovery of both a faint optical afterglow, and an underlying spiral host galaxy (Malesani et al., 2008; de Ugarte Postigo et al., 2008).

The optical images were reduced in the standard fashion, and magnitudes for the afterglow derived in comparison to US Navy Observatory (USNO)<sup>4</sup> and Two Micron All Sky Survey (2MASS)<sup>5</sup> objects

<sup>4</sup>This research has made use of the USNO Image and Catalogue Archive operated by the United States Naval Observatory, Flagstaff Station (<http://www.nofs.navy.mil/data/fchpix/>).

<sup>5</sup>This publication makes use of data products from the Two Micron All Sky Survey, which is a joint project of the University of Massachusetts and the Infrared Processing and Analysis Center/California Institute of Technology, funded by

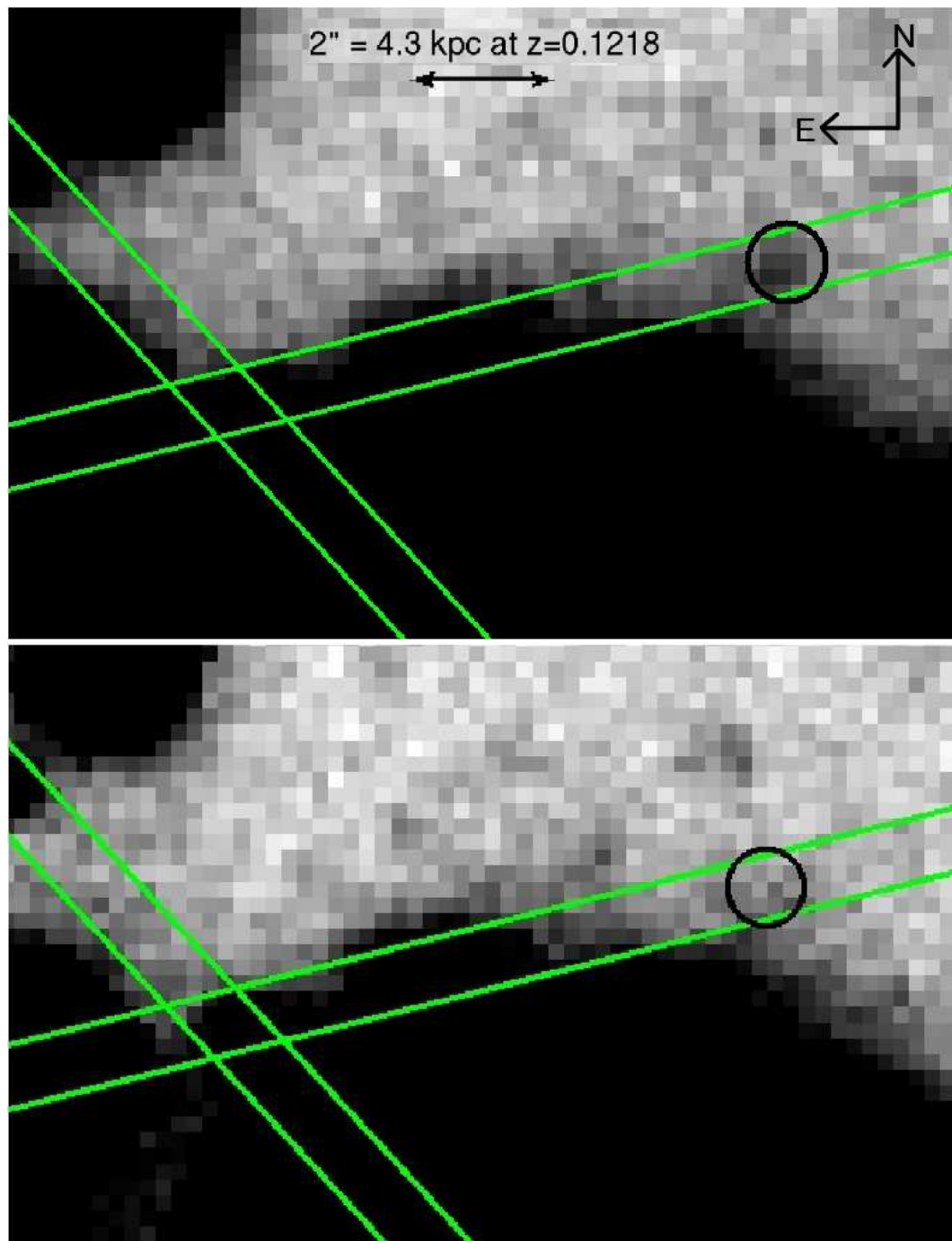


Figure 3.2: The circle marks the location of the afterglow of GRB 080905A on the R special filter images obtained using the VLT. the top image is from epoch 2 (5<sup>th</sup> September 2008), observed 14.3 hours after the trigger time, and the bottom image is from epoch 4 (23<sup>rd</sup> September 2008),  $\sim 18$  days after the trigger time (see Table 3.1). For reference, the two slit positions used for spectroscopy have also been included.

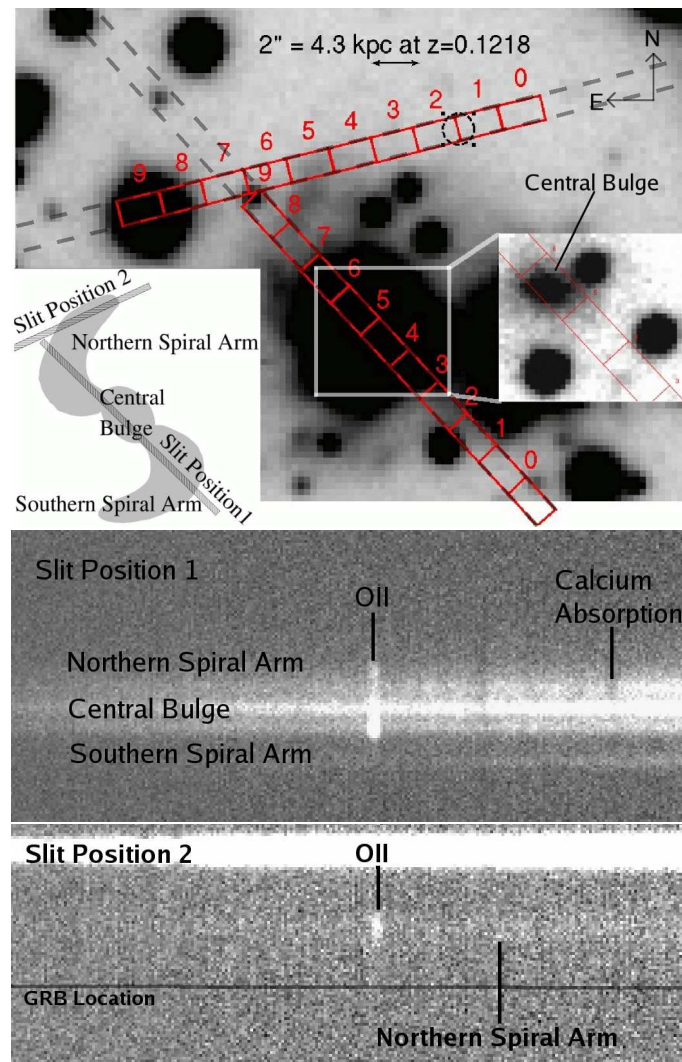


Figure 3.3: This shows the locations of the two slit positions used to obtain the spectra (dashed lines) and the subapertures into which the spectra was divided into subspectra. The dashed circle shows the location of the optical afterglow. The main image shows the spiral arms in the R special filter observation taken using the VLT. The inset on the right shows the central bulge of the galaxy in the K short filter on the VLT. In the bottom left corner, there is a sketch of the structure of the galaxy. The bottom two panels are 2D spectra obtained using the grism on VLT. In the middle panel is the 2D spectra for slit position 1 in which the emission lines get fainter when moving from the southern spiral arm to the northern spiral arm and the absorption features dominate more in the northern spiral arm than in the southern spiral arm. Additionally, the continuum in the northern spiral arm is fainter than the southern spiral arm bluewards of the D4000 break. In the bottom panel is the 2D spectra for slit position 2 in which faint emission lines can be observed and the continuum of the northern spiral arm. The horizontal line shows the location of the GRB<sub>82</sub>

within the field (since conditions were not photometric at the time of the observations). As the afterglow lies on the edge of its spiral host the host subtracted afterglow fluxes are obtained by subtraction of the light from this galaxy, assuming zero contribution of transient light in the final epoch of optical images. The resulting magnitudes are shown in Table 3.1. The afterglow is faint  $R \sim 24$  mag, even for a SGRB, and demonstrates the necessity of deep and rapid observations at the location of SGRBs. Converting the optical magnitude of GRB 080905A to a flux of  $\sim 7 \times 10^{-30}$  erg cm $^{-2}$  s $^{-1}$  Hz $^{-1}$  and comparing it to the sample at 11 hours considered by Nysewander, Fruchter, & Pe'er (2009), it is one of the faintest afterglows detected and, with a optical luminosity of  $\sim 6.7 \times 10^{25}$  erg s $^{-1}$  Hz $^{-1}$ , the lowest luminosity optical afterglow detected and lies below the trend observed between optical afterglow intensity and isotropic energy, suggesting that this GRB occurred in a low density environment. A reasonable extrapolation of the X-ray light curve, using the broken power law model (described in Section 3.2.2) fitted within QDP, to the time of the optical imaging was used to determine that the non-detection of the X-ray afterglow is consistent with the decay observed. The location of the optical afterglow is RA(J2000): 19 10 41.71 and Dec(J2000): -18 52 47.62, with an error of 0.76 arcsec, and is shown in Figure 3.2.

The afterglow is located  $\sim 9$  arcsec from the centre of an  $R \sim 18$  mag galaxy and it was concluded that this is the host galaxy. To calculate the likelihood of a chance alignment of a similar or brighter galaxy within 10 arcsec of the afterglow, the size of the host galaxy was compared to the area of the sky that field galaxies of this magnitude or brighter would cover, giving the likelihood of finding a field galaxy at this location (Hogg et al., 1997). The probability of a chance alignment is less than 1%. A more accurate method would be to use the half light radius of the galaxy as described in Fong, Berger, & Fox (2010), however it is difficult to calculate this due to contamination of foreground stars. The low chance probability and the fact that the afterglow location lies within the stellar field of the galaxy both support the conclusion that this is the host galaxy of GRB 080905A. As for many GRBs without afterglow redshifts, it is possible that GRB 080905A is associated with a higher redshift galaxy which is fainter than the deep limiting magnitude of the optical images ( $R > 25$  mag).

The location of the afterglow is offset from the centre of the host galaxy by a projected radial distance of 18.5 kpc. This is a relatively large offset, but is comparable to several other SGRB locations (Troja 

---

the National Aeronautics and Space Administration and the National Science Foundation (Skrutskie et al., 2006).

et al., 2008; Fong, Berger, & Fox, 2010) and it is important to note that the host galaxy is relatively large so the host-normalised offset would be much smaller. Host-normalised offsets are calculated by normalising the offset to the effective (half light) radius of the host galaxy.

At a redshift of  $z = 0.1218$  a supernova like SN 1998bw would reach a peak magnitude of roughly  $R \sim 19.5$  mag, a factor of  $>100$  brighter than any object present in the final epoch. The lack of any visible supernova component is in keeping with searches which have been done in other SGRBs, supporting the classification of GRB 080905A as a member of the SGRB population. For example, Hjorth et al. (2005a) conducted an early search for a SN component for SGRB 050509B finding any accompanying SN would be fainter than typical SNe and Fox et al. (2005) conducted place deep limits for a SN component for SGRB 050709. These observations can also be used to probe the possible production of radioactive Nickel during GRB 080905A. The ejection of radioactive material in the process of an NS-NS merger may create a visible electromagnetic signal described as a mini-SN (Li & Paczyński, 1998; Kulkarni, 2005; Metzger, Piro, & Quataert, 2008; Kocevski et al., 2010). The absence of any late time emission brighter than  $R \sim 24$  mag, coupled with the known low redshift makes these constraints strong in the case of GRB 080905A, although the cadence of the observations is sensitive to either relatively fast, or slow rise time (but not those of intermediate duration). This suggests that the radioactive yield associated with GRB 080905A is  $< 0.01M_{\odot}$ , based on the low redshift model developed by Perley et al. (2009a) for GRB 080503 and the general models in Kulkarni (2005).

### 3.2.4 Host Galaxy Spectroscopy

To characterize the host galaxy, deep spectroscopy was obtained on September 24th 2008, using FORS1 on UT2 of the VLT, Chile. These observations were obtained after the optical afterglow had faded. To maximize wavelength coverage the 300V grism was used with the GG375 filter to suppress contamination by the second spectral order. This results in a wavelength range  $\sim 3700$  to  $9200 \text{ \AA}$ .

The 1.0 arcsec wide slit was oriented along two different fixed position angles, illustrated in Figure 3, and  $4 \times 450$  second exposures were acquired for each slit position. The two slit positions (-104.1 and -42.7 degrees) were chosen to cut through the host galaxy covering the nucleus as well as spiral

Epoch	Date mid point (UT)	Time after trigger (hours)	Telescope	Exposure time (s)	Filter/grism	Seeing (arcsec)	Magnitude (mag)
1	Sep 05 20:30 UT	8.5	NOT	1800	R	0.9	$24.04 \pm 0.47$
2	Sep 06 02:39 UT	14.3	VLT	2400	R special	1.05	$24.26 \pm 0.31$
3	Sep 07 00:29 UT	36	VLT	2400	R special	0.85	$> 25.0$
4	Sep 23 00:44 UT	-	VLT	2400	R special	0.85	-
5	Oct 01 01:15 UT	-	VLT	7200	K short	0.65	-
(slit position 1)	Sep 24 01:39 UT	-	VLT	3600	grism	0.9	-
(slit position 2)	Sep 24 02:27 UT	-	VLT	3600	grism	0.9	-

Table 3.1: Log of observations of the afterglow and host of GRB 080905A. The magnitudes shown for the afterglow are host subtracted, assuming zero contamination from the afterglow in epoch 4. Magnitudes have been corrected for foreground extinction of  $E(B - V) = 0.14$  mag.

arms on either side of the galaxy (hereafter “slit position 1”), and to cover the afterglow position and cut through a nearby spiral arm (hereafter “slit position 2”). Seeing conditions during the observations were reasonable with an average seeing of 0.9 arcsec and mean airmass of 1.2 (slit position 1) and 1.3 (slit position 2). The data were reduced by Klaas Wiersema using standard procedures in Image Reduction and Analysis Facility (IRAF)<sup>6</sup>. The four exposures per slit position were combined before extraction, removing cosmic rays in the process.

The spectra of slit position 1 and 2 were extracted in the same way: the relatively bright continuum of the bulge (slit position 1) or a nearby bright star (slit position 2) were used to fit the shape of the trace function, and extract using 10 adjoining, equally sized subapertures following this trace. Subapertures are 7 pixels in size in both slit position 1 and 2 data, which corresponds to 1.76 arcsec per subaperture (pixel scale is 0.252 arcsec per pixel), i.e. a value matched to twice the seeing full-width-at-half-maximum (FWHM). At the redshift of the host galaxy, this corresponds to a physical scale of 3.8 kpc per subaperture. In the following, the spectra extracted with these small apertures are referred to as subspectra. Figure 4 shows examples of extracted subspectra. The GRB location is covered only by slit position 2, and falls in subapertures 1 and 2. The subspectra are wavelength calibrated using He, HgCd and Ar lamp spectra. From the FWHM of a Gaussian fit on the arc lines a nominal spectral resolution of 11 Å at the central wavelength is measured. This corresponds to a velocity resolution of 511 km s<sup>-1</sup>. However, this is the FWHM of a Gaussian fit to the emission line so the central position of the Gaussian can be determined more accurately. The central wavelengths are used to determine the redshift and the radial velocities of the host galaxy (in Section 3.3.2) allowing significantly more accurate measurements.

Flux calibration of the subspectra was done using observations of the spectrophotometric standard star LDS 749B, Atmospheric extinction correction was done by applying the average Cerro Tololo Inter-American Observatory (CTIO) atmospheric extinction curve (Hamuy et al., 1994). A Galactic dust extinction correction was performed by using the  $E(B - V)$  value of 0.14 mag (Schlegel et al., 1998), assuming a Galactic extinction law  $A_\lambda/A_V$  expressed as  $R_V = A_V/E(B - V)$  (Cardelli et al., 1989). The standard assumption  $R_V = 3.1$  mag is made (Rieke & Lebofsky, 1985). No Galactic Na I or K I

<sup>6</sup>IRAF is distributed by the National Optical Astronomy Observatories, which are operated by the Association of Universities for Research in Astronomy, Inc., under cooperative agreement with the National Science Foundation (Tody, 1993).

absorption is detected in the spectrum, consistent with the  $E(B - V)$  value from Schlegel et al. (1998). Note that this calibration provides a good *relative* flux calibration which is needed to evaluate changes between the different subspectra, e.g in the strength of emission line ratios or some continuum features, but does not provide a full absolute calibration.

From the detected emission lines the redshift of the GRB host galaxy is measured to be  $z = 0.1218 \pm 0.0003$ .

### 3.3 Host galaxy properties

#### 3.3.1 Host morphology

Visual inspection of the images in the R and K bands shows the host to be a nearly face-on galaxy, with clear bulge, disk and spiral arm components. At least two spiral arms can be distinguished, one on either side of the galaxy, which are hard to see due to a great number of foreground stars. Figure 3 shows the spiral arms as observed in the R band and inset is an image of the central bulge in the K band. The detection of spiral arms in combination with the detected emission and absorption lines allows us to loosely classify the host of GRB 080905A as an Sb/c galaxy.

By subtracting foreground stars from the images (conducted by Andrew Levan), the host of GRB 080905A has an R-band magnitude of  $R \sim 18.0 \pm 0.5$  mag. The large error arises not due to the faintness of the object, but due to the uncertainty in subtracting the significant number of foreground sources which overlap the spiral structure. Correcting for foreground extinction ( $E(B - V) = 0.14$  mag) this corresponds to an absolute magnitude of  $M_V \sim -21$  mag, and suggests that the host of GRB 080905A is broadly similar to the Milky Way.

Using the near-infrared mass-light ratio, equation 3.4 (Thronson & Greenhouse, 1988), and the K-band magnitude of the host galaxy<sup>7</sup>  $K = 16.2^{+0.4}_{-0.7}$  mag, the mass of the host galaxy is determined to be  $M_{*,old} = 2 \pm 1 \times 10^{10} M_{\odot}$ . The errors are estimated based on the uncertainties in subtraction of the

<sup>7</sup>Converted to Jy using the NICMOS units conversion form ([http://www.stsci.edu/hst/nicmos/tools/conversion\\_form.html](http://www.stsci.edu/hst/nicmos/tools/conversion_form.html))

foreground stars and identifying the extent of the host galaxy.

$$M_{*,old}(M_{\odot}) = 2.6 \times 10^8 D^2(\text{Mpc}) F_k(\text{Jy}) \quad (3.4)$$

### 3.3.2 Rotation curve

The nearly face-on orientation of the host galaxy gives an excellent view of the location of the GRB within the host, similar to GRB 060505 which also occurred in nearly face-on Sbc galaxy (Thöne et al., 2008). However, this favourable geometry complicates measurements of the host dynamical mass, required to test the consistency of this host, and GRB spiral hosts in general, with the mass – metallicity relation at this redshift.

Visual inspection of the 2D spectrum shows no clear slant in the [S II],  $H\alpha$ , [N II], [O III],  $H\beta$  and [O II] lines ([O II] are shown in 3.3). To determine the rotation curve of the galaxy (or upper limits), the *fxcor* routines in the IRAF *rv* package were used to Fourier cross-correlate the spectra of different subapertures of the slit position 1 spectra, finding their relative radial velocity as a function of distance to the galactic nucleus. Spectral sections around the brightest emission lines are correlated, as well as the full subaperture spectra (using also absorption features). A Gaussian function is fit to the cross correlation peak to determine its centre and width. Between the two subspectra with the highest signal to noise emission lines, subapertures 3 and 7, a formal radial velocity difference of  $19 \pm 38 \text{ km s}^{-1}$  is found. Using symmetrical subapertures about the galactic centre (4 and 8) the radial velocity is found to be  $30 \pm 160 \text{ km s}^{-1}$ . This value is using very weak emission lines in subaperture 8, so is a much less constraining limit.

Using the GALFIT software package (Peng et al., 2002) the host galaxy is decomposed to identify the inclination angle. The acquisition images for the spectra are used, which have the best seeing conditions. An empirical PSF is used as modelled through the IRAF DAOPHOT routines using several moderately bright stars close to the GRB position. An inclination angle of  $\sim 23^\circ$  is found, however there are large errors associated with this value due to poor signal to noise, contamination by bright

stars and the near face-on inclination. This angle appears to be smaller than that identified for LGRB 980425,  $\sim 50^\circ$  (Christensen et al., 2008).

### 3.3.3 Spatially resolved properties

The middle and bottom panels of Figure 3.3 show the subspectra from slit position 1 and 2, in which differences in continuum shape and line properties can be seen, reflecting subtle changes in stellar population properties dominating the differing subspectra. From Figure 3.3 it is clear that several field stars are located close to and on top of the host. Some of the subspectra appear affected by light from these stars, which can be seen by the presence of Balmer, Na and Ca lines at zero redshift, and from the shape of the continuum.

The 2D spectra show clearly several basic properties of the host. In Figure 3.4, subspectra from subapertures 4 (northern spiral arm), 6 (central bulge) and 8 (southern spiral arm) from slit position 1 are shown. Additionally shown is the subspectra from subaperture 2 for slit position 2, corresponding to the GRB location. The slit position 1 spectrum shows that the nebular emission lines, e.g. [O III] and [O II], are strongest in the southern part of the host, and get dramatically weaker northwards of the nucleus. This shows that the star formation rate is strongest in the spiral arm diametrically opposite the GRB position, in stark contrast to the spiral host galaxy of LGRBs 980425, that show strongest star formation at, or near, the location of the burst (Christensen et al., 2008). The GRB location appears to lie in the extension of a spiral arm. The 2D spectrum of slit position 2, which probes this arm, clearly shows strong nebular absorption lines of [O III] and [O II], and weaker  $H\alpha$  and  $H\beta$  at the location of the spiral arm, but no emission line flux is detected at the location of the burst. At and near the GRB location a weak, near featureless continuum can be seen.

The slit position 1 subspectra that are dominated by bulge light show clear absorption features common to old populations and ISM gas (Na I, Ca II, 4000 Å break, G band), and show stellar atmosphere Balmer absorption underneath the nebular Balmer emission. The other spectra have brighter nebular lines and weaker 4000 Å breaks. As several of the subspectra are contaminated by light from foreground stars, and the resolution of the spectra is low, the analysis is limited in this Chapter to the

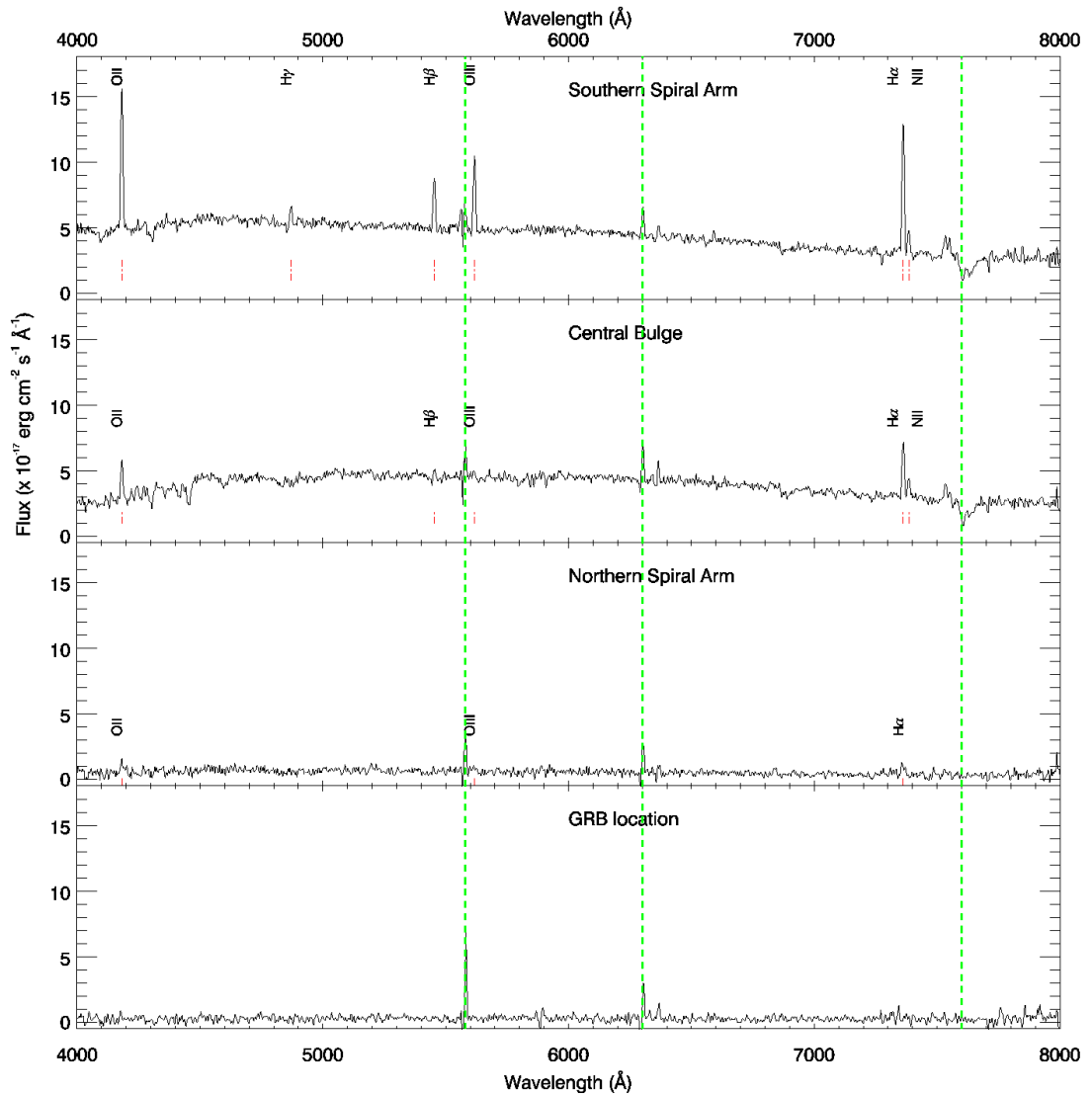


Figure 3.4: This shows the observed spectra in the northern spiral arm, the central bulge and the southern spiral arm. These correspond to subapertures 4, 6 and 8 from slit position 1. The lowest panel shows the observed spectrum at the GRB location. There are residual features from sky line subtraction at  $\sim 5600\text{\AA}$ ,  $\sim 6300\text{\AA}$  and  $\sim 7600\text{\AA}$  (shown by the dashed lines).

nebular emission lines and the strongest absorption bands.

Using the relative fluxes of  $H\alpha$  and  $H\beta$ , it is possible to determine the flux ratio at different points in the host galaxy, as shown in Figure 3.5. This gives an indication of the reddening in the host galaxy, which is important to consider as the metallicities and D4000 calculated may be affected by this value. Figure 3.5 shows that the southern spiral arm and central bulge are consistent with having little significant reddening. However, the northern spiral arm shows significant reddening, and this will affect the R23 calculations. In the following analysis, the values for N2 and R23 are not corrected for extinction. The extinction can be calculated using the  $H\alpha$  and  $H\beta$  ratio using equation 3.5 (Calzetti, Kinney, & Storchi-Bergmann, 1994). The extinction varies from  $-0.11_{-0.05}^{+0.04} \leq E(B - V) \leq 0.99_{-0.05}^{+0.04}$  mag.

$$E(B - V) = 0.935 \ln \left( \frac{\left( \frac{H\alpha}{H\beta} \right)}{2.88} \right) \quad (3.5)$$

The emission line fluxes in each subspectrum in slit position 1 are measured, and compute the metallicity profile along this slit position through the N2 indices, equation 3.6 (Pettini & Pagel, 2004). In addition to these indices, the R23 metallicities are computed where possible using equation 3.7 (Pettini & Pagel, 2004).

$$N2 \equiv \frac{[N_{II}]\lambda 6583}{H\alpha} \quad (3.6)$$

$$R23 \equiv \frac{([O_{II}] + [O_{III}])}{H\beta} \quad (3.7)$$

In the slit position 2 subspectra only emission line upper limits can be determined at the GRB location. The metallicity of the spiral arm that is covered by slit position 2 can be calculated through R23.

In Figure 3.5, The log(N2) index is shown (also converted into  $12 + \log(O/H)$ , calibrated using nearby extragalactic HII regions, as defined by Pettini & Pagel, 2004), the  $H\alpha$  flux and R23 metallicity as a function of distance in kpc from the centre of the galaxy (the centre is taken to be the centre of

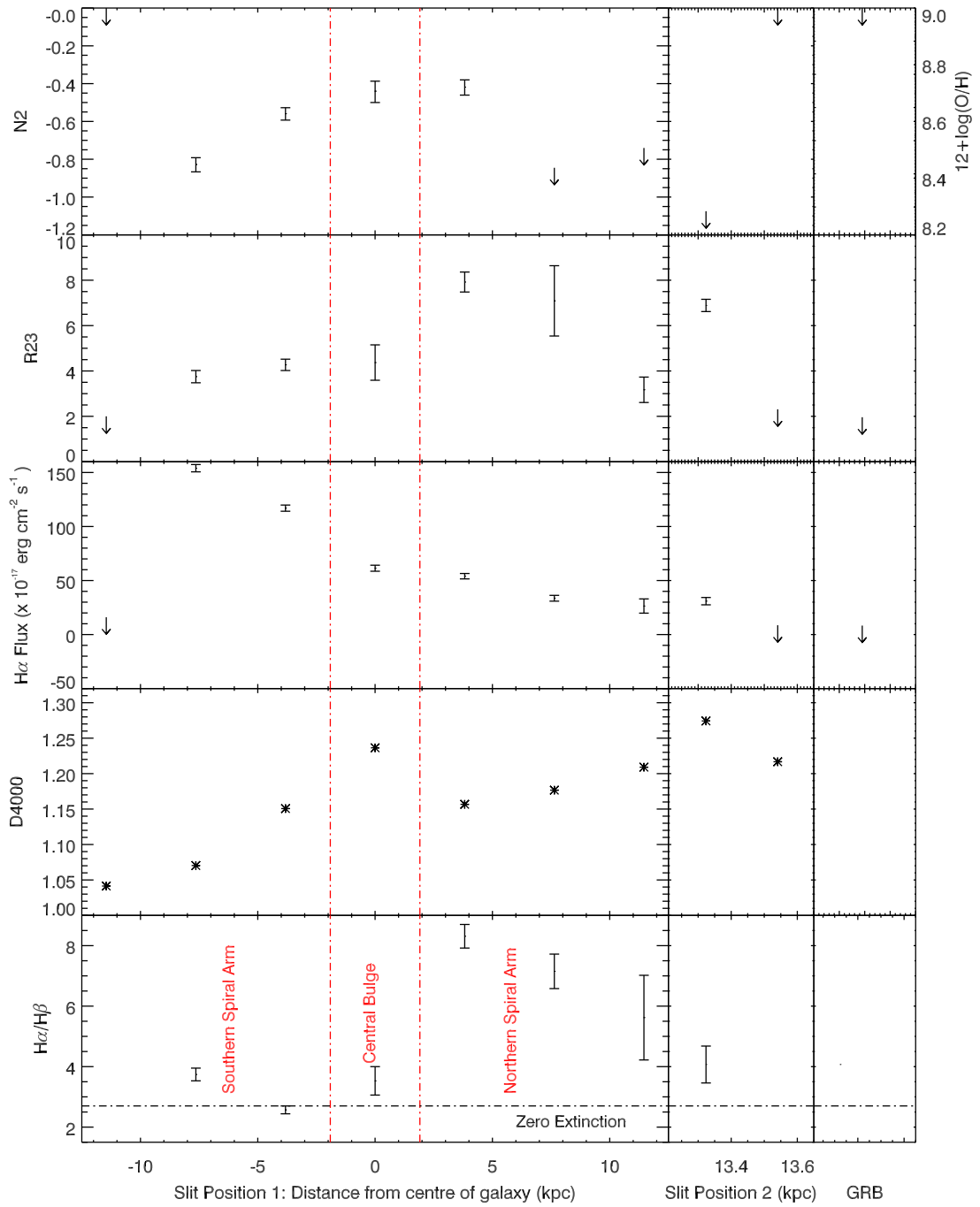


Figure 3.5: Panel 1 shows the  $\text{Log}(N_2)$ ,  $H\alpha$  Flux,  $R_{23}$ ,  $D_{4000}$  and the flux ratio of  $H\alpha$  to  $H\beta$  as a function of position from the centre of the host galaxy. Note that the  $H\alpha$  Flux can only be used as a relative value as it has not been absolutely calibrated. In the lowest panels, the  $H\alpha$  to  $H\beta$  ratio for zero extinction are shown. In the second panel is the data from slit position 2 along the spiral arm and the third shows the upper limits for the region in which the GRB occurred.

subaperture 6). In the three horizontal panels these values are provided for slit position 1, slit position 2 (for the spiral arm in subapertures 4 and 5, subaperture 6 is contaminated by a nearby star) and near the GRB location (subaperture 1). The  $\log(N2)$  index, where it was possible to measure, shows an increasing metallicity from the southern spiral arm, through the central bulge and into the northern spiral arm. The  $12+\log(O/H)$  value increases from 8.4 in the southern spiral arm to 8.7 in the northern spiral arm. This is reinforced by the findings for R23 metallicity, which also shows that the northern spiral arm has a higher metallicity than the central bulge and southern spiral arm. The R23 metallicity is converted into  $12+\log(O/H)$  using the KK04 method described in Kewley & Ellison (2008). The equations 3.8 – 3.12 are used to calculate the two values of  $12 + \log(O/H)$  by iterating equation 3.10 and equations 3.11 or 3.12. The degeneracy is broken between the two solutions using the result for  $\log(N2)$  given by equation 3.13. The errors on these values can be estimated from the errors on the R23 values shown in Figure 3.5, however there is an uncertainty associated with using the KK04 method in Kewley & Ellison (2008) which is difficult to quantify. The metallicity at 2 kpc from the centre of the host is found to be 8.9 or 8.1 in the southern spiral arm (it was not possible to break the degeneracy between the two solutions in this arm), 8.9 in the central bulge, 8.5 in the northern spiral arm and 8.5 in slit position 2 at 13.4 kpc from the centre of the galaxy. However, these values for metallicity calculated using R23 are likely to be affected by reddening in the host galaxy and the  $12+\log(O/H)$  metallicity is reliant on breaking the degeneracy of two solutions. Therefore, this analysis is based on the values obtained using  $\log(N2)$  where possible and use the R23 values to corroborate the general result. The values obtained for  $\log(N2)$  are less sensitive to reddening due to the close proximity of the two lines used to calculate this value. Taking the solar metallicity to be  $Z_{\odot}=8.69$  (Asplund et al., 2004), it is noted that the southern spiral arm has  $0.5 Z_{\odot}$  and the central bulge and northern spiral arms have a value of  $1 Z_{\odot}$ . In the southern spiral arm, a metallicity gradient can be inferred of  $-0.07 \text{ dex kpc}^{-1}$ , which is consistent with the Milky Way gradient of  $-0.09 \pm 0.01 \text{ dex kpc}^{-1}$  (Smartt & Rolleston, 1997; Rolleston et al., 2000). The  $H\alpha$  flux shows a decreasing trend from the southern spiral arm to the northern spiral arm. The results from the spiral arm in slit position 2 tend to be in agreement with the northern spiral arm in slit position 1. These results show that the southern spiral arm is an actively star forming region and this is in direct contrast to the northern spiral arm. The limits at the GRB location are provided for reference. The GRB is in the northern spiral arm, on the opposite side of the galaxy to the active star formation.

$$x = \log R_{23} \quad (3.8)$$

$$y = \log O_{32} \quad (3.9)$$

$$\log q = \frac{32.81 - 1.153y^2 + [12 + \log(\frac{O}{H})](-3.396 - 0.025y + 0.1444y^2)}{4.603 - 0.3119y - 0.163y^2 + [12 + \log(\frac{O}{H})](-0.48 + 0.0271y + 0.02037y^2)} \quad (3.10)$$

$$12 + \log(O/H)_{lower} = 9.40 + 4.65x - 3.17x^2 - \log q(0.272 + 0.547x - 0.513x^2) \quad (3.11)$$

$$12 + \log(O/H)_{lower} = 9.72 - 0.777x - 0.951x^2 - 0.072x^3 - 0.811x^4 - \log q(9.0737 - 0.0713x - 0.141x^2 + 0.0373x^3 - 0.058x^4) \quad (3.12)$$

$$12 + \log(O/H) = 9.37 + 2.03 \log(N2) + 1.26(\log(N2))^2 + 0.32(\log(N2))^3 \quad (3.13)$$

In addition to the emission line properties the 4000 Å break (D4000) is measured, which is a useful diagnostic for age and metallicity which can even be measured in relatively low signal to noise (sub)spectra. Shortward of 4000 Å is the start of stellar photospheric opacity, which takes into account the mean temperature of the stars. Hotter stars (with shorter lifetimes) have more ionised metals in their atmospheres, and hence a lower opacity, than cooler stars. This means that an older population of stars will have a higher opacity and, subsequently, a larger 4000 Å break (Bruzual, 1983; Poggianti & Barbaro, 1997; Gorgas et al., 1999; Kauffmann et al., 2003; Marcellac et al., 2006). Marcellac et al. (2006) have shown that D4000 is sensitive to metallicity once the age of the population exceeds a few billion years or when it is  $>1.6$ . D4000 is calculated using the ratio between two bands of the continuum, one redwards of the 4000 Å break and the other bluewards. The Balogh et al. (1999) definition of the D4000 continua is used, given in equation 3.14 with the wavelength ranges indicated in Å, which is less wide than the original definition by Bruzual (1983) and therefore less affected by dust reddening. The calculated values are plotted in Figure 3.5 and provide a qualitative estimate of the relative ages of the stars as a function of position in the galaxy. The estimated error for D4000 (calculated using the RMS of the spectrum and the size of the bands) for slit position 1 is  $\pm 0.12$  and for slit position 2 is  $\pm 0.65$ . As expected, it shows that the galactic centre hosts an older population of stars than the spiral arms. Interestingly, it also appears that the northern spiral arm hosts an older population of stars than the southern spiral arm. This reinforces the evidence of active star formation occurring within the southern spiral arm and not in the northern spiral arm. Due to large errors, it was not possible to calculate

D4000 at the GRB location.

$$D_{4000} = \frac{Red[4000 - 4100]}{Blue[3850 - 3950]} \quad (3.14)$$

Using the approximate metallicity of this galaxy,  $\log(O/H) + 12 \sim 8.6$  from  $\log(N2)$ , and the mass-metallicity relation as measured by Kewley & Ellison (2008) using galaxies in the Sloan Digital Sky Survey, the mass of the galaxy is estimated to be  $\sim 10^{10} M_{\odot}$ . This is consistent with the value calculated using the near-infrared mass-light ratio.

### 3.4 Discussion

In previous spatially resolved studies of low redshift GRB host galaxies, it has been determined that LGRBs are associated with regions of active star formation and hence provides support for the core collapse supernova progenitor theory, for example LGRB 980425 and LGRB 060218 (Fynbo et al., 2000; Wiersema et al., 2007; Christensen et al., 2008). Additionally, LGRBs at higher redshifts tend to occur in the brightest regions of the host galaxy (Fruchter et al., 2006; Svensson et al., 2010) and relatively small host galaxies (Wainwright et al., 2007). GRB 080905A is in direct contrast to these results, occurring on the opposite side of a relatively large spiral galaxy to the most active star formation region and significantly offset from the centre, so its progenitor is unlikely to be a massive star. The properties of this specific region of the host galaxy are in agreement with the findings of Prochaska et al. (2006) for typical SGRB environments. One of the theoretically predicted progenitors of SGRBs is the merger of a compact binary, for example two neutron stars or a neutron star and a black hole. Compact binaries are expected to be given a kick velocity during their formation which can allow them to travel large distances from their birthplace (Wang, Lai, & Han, 2006, and references therein). These events are expected to be associated with an older stellar population and offset from the host galaxy, as observed for GRB 080905A.

To summarize, GRB 080905A has short, hard prompt emission with properties expected for a compact binary merger progenitor. There was no associated supernova, it appears to be a low density environ-

ment and had a low luminosity. The host galaxy is a spiral galaxy with active star formation, but GRB 080905A occurred close to a spiral arm, dominated by a relatively old population, and on the opposite side of the galaxy from the spiral arm with most active star formation. Additionally, it was offset from the centre of the host galaxy by a projected radial distance of 18.5 kpc. Therefore, these observations have shown that GRB 080905A is unambiguously a short population GRB, whose properties suggest that the progenitor is likely to be a compact binary merger.

### 3.5 Conclusions

This Chapter has presented spatially resolved spectroscopy of the host galaxy of the short hard GRB 080905A, with a  $T_{90}$  of 1 s. The prompt emission had an isotropic total energy of  $\sim 5 \times 10^{49}$  erg in the energy band 15-150 keV. The X-ray and optical afterglows were observed, and the optical afterglow had a magnitude of  $R \sim 24$  mag at 8.5 hours after the burst fading to  $R > 25$  mag at 32 hours.

The host is an almost face on spiral galaxy (inclination  $\sim 23^\circ$ ) with a central bulge and at least 2 spiral arms, and is loosely classified as a Sb/c galaxy. The probability that GRB 080905A was chance aligned with this galaxy is  $< 1\%$ . The observed redshift of this galaxy is  $z = 0.1218 \pm 0.0003$ , the lowest definite redshift for a typical SGRB thought to originate from a compact binary merger. Using spatially resolved spectroscopy, a disparity between the two spiral arms is identified, with the southern arm showing a younger stellar population and more active star formation than the northern spiral arm. It is not possible to be more specific as a relative flux calibration is used, not absolute fluxes, due to the contamination from overlying stars and the entire host galaxy was not observed.

The optical afterglow is observed to be offset from the centre of the galaxy by a projected radial distance of 18.5 kpc and occurs in the northern region. This offset and the association with an older population in the northern spiral arm, in addition to the prompt emission properties, shows that GRB 080905A would fit in the Type I Gold sample GRB as defined by Zhang et al. (2009) with the progenitor being a compact binary merger.

GRB 080905A had a clearly identifiable host galaxy despite being significantly offset, however the

---

next Chapter studies GRB 090515 - a hostless SGRB which may share a common progenitor that is kicked further out of its host galaxy prior to merger.

# Chapter 4

## The unusual X-ray emission of the short *Swift* GRB 090515

### 4.1 Introduction

Here an analysis of GRB 090515 is presented, which is the best case for an early X-ray plateau in a SGRB, showing evidence of ongoing energy injection and giving clues about the central engine and progenitor.

GRB 090515 was one of the shortest GRBs observed by *Swift*, with among the lowest fluence, yet for  $\sim 200$  s it had the brightest SGRB X-ray afterglow and did not appear to be fading until a sudden steep decline at  $\sim 240$  s. After the first orbit, it was not detected again. Explaining this unusual X-ray behaviour is the subject of this Chapter and is published in Rowlinson et al. (2010b). The observations of GRB 090515 are described in Section 4.2, compared to other GRBs in Section 4.3 and the potential origin of the unusual X-ray emission is discussed in Section 4.4.

## 4.2 Observations

### 4.2.1 Swift Observations

All analysis has been performed by using standard routines in HEASOFT<sup>1</sup>, XSPEC (Dorman & Arnaud, 2001), QDP<sup>2</sup> and the automatic X-ray Telescope (XRT; Burrows et al., 2005a) data products produced by the UK Swift Science Data Centre (Evans et al., 2007, 2009).

*Swift* triggered on GRB 090515 at 04:45:09 UT on 15th May 2009 with BAT position RA = 10 56 41 and Dec = +14 27 22 (Beardmore et al., 2009). The Ultra-Violet and Optical Telescope (UVOT) enhanced refined XRT position was RA = 10 56 36.11 and Dec = +14 26 30.3 with an uncertainty of 2.7 arcsec (Osborne et al., 2009).

The  $T_{90}$  duration of GRB 090515 was  $0.036 \pm 0.016$  s (Barthelmy et al., 2009a). The spectrum of the prompt gamma-ray emission can be fit by a single power law, of photon index  $\Gamma_{\gamma} = 1.6 \pm 0.2$  (Barthelmy et al., 2009a). The fluence is  $2.0 \pm 0.8 \times 10^{-8}$  erg cm<sup>-2</sup> and the peak photon flux is  $5.7 \pm 0.9$  ph cm<sup>-2</sup> s<sup>-1</sup>. All values are in the 15 – 150 keV energy band. The BAT light curve is shown in Figure 4.1 as the grey data points and also shown in the inset with linear time. The BAT count rates were converted to flux in the energy band 0.3 – 10 keV using the average spectral index for the BAT and the XRT spectra. There is no evidence of extended emission detected in the BAT energy range (Norris, Gehrels, & Scargle, 2010).

A spectral lag analysis for GRB 090515 was completed using the cross correlation function method described in Ukwatta et al. (2010) and Section 3.2.1, the 8 ms time binned lightcurve and BAT channels 1, 2 and 3. Not enough emission was detected in channel 4 to make a lag measurement. The lag times are (with  $1\sigma$  errors): lag(Ch2-Ch1)=  $6 \pm 4$  ms, lag(Ch3-Ch2)=  $3 \pm 2$  ms and lag(Ch2-Ch1)=  $10 \pm 4$  ms. Typically SGRBs have negligible lag times (Norris & Bonnell, 2006; Yi et al., 2006) and LGRBs have typical lag times ranging from 20 ms to  $\sim 1000$  ms (Ukwatta et al., 2010), so it is interesting that GRB 090515 appears to have a small lag time.

<sup>1</sup><http://heasarc.gsfc.nasa.gov/lheasoft/>

<sup>2</sup><http://www.wastro.msfc.nasa.gov/qdp/>

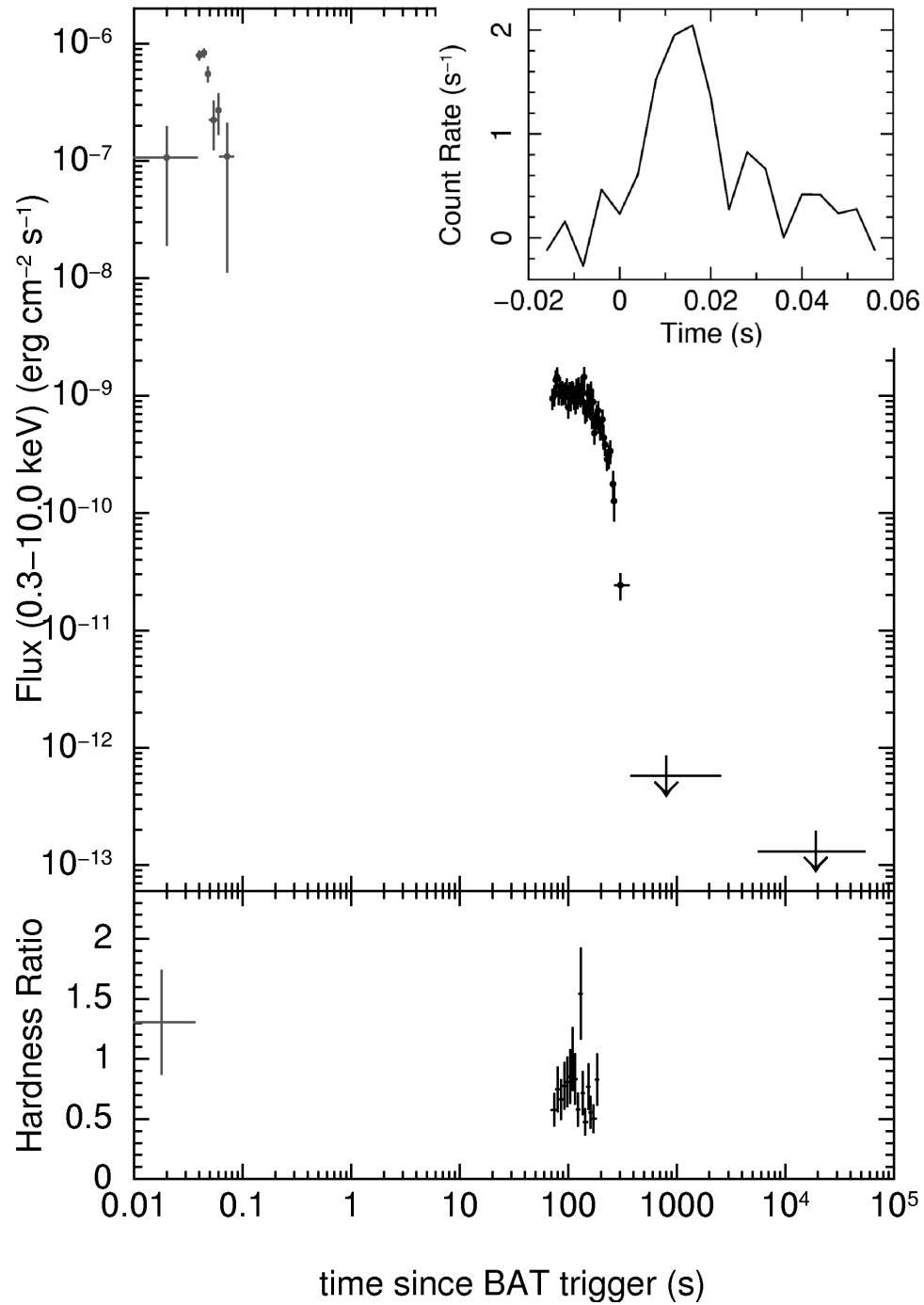


Figure 4.1: The combined light curve for GRB 090515, in grey are the BAT data and black are the XRT data. The BAT-XRT lightcurve was made using the method described in Section 3.2.2. In the lower box there is the hardness ratio for the BAT data ((50 – 100) keV/(25 – 50) keV) in grey and the hardness ratio for the XRT data ((1.5 – 10) keV/(0.3 – 1.5) keV) in black. Inset is the BAT count rate per detector light curve with linear time.

The X-ray spectrum in the 0.3 – 10 keV energy band is best fit by an absorbed power law with  $\Gamma_X = 1.88 \pm 0.14$  and  $N_H = 6.1_{-2.8}^{+3.0} \times 10^{20} \text{ cm}^{-2}$ , in excess of the Galactic  $N_H = 1.9 \times 10^{20} \text{ cm}^{-2}$  (Beardmore & Evans, 2009). The X-ray light curve is best fit by a broken power law with 2 breaks giving a reduced  $\chi^2_\nu$  of 0.86. The initial decay is relatively flat ( $\alpha_1 = 0.29_{-0.27}^{+0.08}$ ) with a break at  $T_1 = 156.2_{-26.2}^{+9.3} \text{ s}$  followed by a steeper decay of  $\alpha_2 = 2.51_{-0.70}^{+0.38}$ . At  $T_2 = 240.8_{-9.8}^{+7.4} \text{ s}$  it breaks to an extremely steep decay of  $\alpha_3 > 9$ . Although, the X-ray light curve can be fitted using a broken power law, it is noted that the decay appears to be a smooth curve. The X-ray light curve is shown in Figure 4.1 as the black data points and the lower panel shows the hardness ratio for the gamma-ray emission (in grey), i.e. the ratio of the 50 – 100 keV emission to the 25 – 50 keV emission, and the hardness ratio of the X-ray emission (in black, (1.5 – 10) keV/(0.3 – 1.5) keV). The hardness ratio is fairly constant during the plateau, with the exception of a point at  $\sim 120 \text{ s}$  that could be a flare and does correspond to a small peak in the X-ray light curve, but this may just be noise. There are insufficient counts to characterise the hardness ratio during the decay.

### 4.2.2 Early Optical Observations

The field of GRB 090515 was observed at early times by several optical telescopes but none detected an optical afterglow. The upper limits of the R band and white filter observations are given in Table 4.1. During the plateau phase, the optical flux density can be predicted, assuming that the X-ray and optical emission are from the same emitting region. If there is not a cooling break in the spectrum (i.e.  $\Gamma_X = \Gamma_{OX}$ ) then the optical flux is expected to be  $1.7 \times 10^{-26} \text{ erg cm}^{-2} \text{ s}^{-1} \text{ Hz}^{-1}$ , corresponding to an apparent magnitude of  $R = 15.6 \text{ mag}$ . This is brighter than all of the optical upper limits during the plateau, so the optical afterglow should have been observed. However, if there were a cooling break in the spectrum between optical and X-ray then  $\Gamma_{OX} = \Gamma_X - 0.5$  and, in this case, the optical flux density would be  $8.7 \times 10^{-29} \text{ erg cm}^{-2} \text{ s}^{-1} \text{ keV}^{-1} \text{ Hz}^{-1}$ , corresponding to an apparent magnitude of  $R = 21.3 \text{ mag}$ . This is slightly deeper than the optical upper limit provided by UVOT. Therefore, if the optical emission was from the same emitting region as the X-ray and there is a cooling break in the spectrum, there is a slim chance that the optical flux was below the observed limits so the non-detection is consistent with the X-ray data.

Table 4.1: The optical observations of the field of GRB 090515.

Telescope	Mid point time after trigger (s)	Exposure Time	Band	Upper Limit (magnitude)	Flux Upper Limit ( $\text{erg cm}^{-2} \text{s}^{-1} \text{Hz}^{-1}$ )
KAIT	20	540	R	19.1 <sup>(1)</sup>	$6.6 \times 10^{-28}$
Super LOTIS	43	10	R	17.7 <sup>(2)</sup>	$2.4 \times 10^{-27}$
ROTSE III	86	67	R	18.4 <sup>(3)</sup>	$1.3 \times 10^{-27}$
UVOT	142	146	White	20.35 <sup>(4)</sup>	$2.1 \times 10^{-28}$
UVOT	1228	488	White	21.24 <sup>(4)</sup>	$9.2 \times 10^{-29}$
KAIT	2078	540	R	20.5 <sup>(1)</sup>	$1.8 \times 10^{-28}$
Lick	2286	60	R	21.3 <sup>(5)</sup>	$8.7 \times 10^{-29}$
ROVOR	5496	4200	R	21.4 <sup>(6)</sup>	$7.9 \times 10^{-29}$

<sup>(1)</sup> Li et al. (2009), <sup>(2)</sup> Williams et al. (2009), <sup>(3)</sup> Rujopakarn et al. (2009), <sup>(4)</sup> Seigel & Beardmore (2009), <sup>(5)</sup> Perley, Kislak & Ganeshalingam (2009b), <sup>(6)</sup> Pace et al. (2009).

### 4.2.3 Gemini Observations

Optical observations of GRB 090515 were obtained using Gemini North and GMOS beginning at 06:26 UT, approximately 1.7 hours after the burst, with a second epoch observation being taken on the subsequent night, and a final comparison epoch on 28 November 2009. The images were obtained in the  $r$ -band, and were reduced via the standard IRAF Gemini tasks (Tody, 1993). The image conditions for the first epoch were excellent, with seeing of 0.5 arcsec, resulting in extremely deep imaging in the total exposure time of 1800 s. A full log of observations is shown in Table 4.2.

Within the refined XRT error circle, a single source is located at RA = 10 56 35.89 and Dec = +14 26 30.0, with a magnitude of  $r = 26.36 \pm 0.12$  mag, calibrated against existing SDSS observations of the field, shown in Figure 4.2. This source is still visible, but at lower significance in the shallower images obtained on 16 May ( $r = 26.54 \pm 0.33$  mag). In the final epoch there is no source visible at the afterglow location, to a limiting magnitude of  $r > 27.4$  mag confirming a fading counterpart. Therefore it is concluded that this is the optical afterglow of GRB 090515. At  $r = 26.36$  mag, this is the faintest GRB afterglow ever discovered at similar times after the burst, and confirms the necessity of rapid and deep observations with 8-metre class observatories. As the observed X-ray absorption is relatively low ( $N_{\text{H}} \sim 6 \times 10^{20} \text{ cm}^{-2}$ ), the faint optical afterglow is unlikely to be a consequence of extinction (unless it is at high redshift). The optical afterglow has a relatively flat lightcurve, with a decay slope of  $0.06^{+0.32}_{-0.19}$ .

Comparing this afterglow to the sample in Nysewander, Fruchter, & Pe'er (2009), it is noted that this is the first SGRB with a fluence below  $10^{-7} \text{ erg cm}^{-2}$  with a detected optical afterglow. Additionally, the afterglow at 1.7 hours is fainter than all the observed optical afterglows at 11 hours. GRB 080503 also had an initially very faint optical afterglow, but it then rebrightened to a peak of  $r \sim 25.5$  mag at 1 day and no host galaxy was identified (Perley et al., 2009a).

Assuming there is not a cooling break in the spectrum, i.e.  $\Gamma_X = \Gamma_{OX}$ , the X-ray flux, 0.3 - 10 keV, at the time of the optical observations can be predicted to be  $6.6 \times 10^{-15} \text{ erg cm}^{-2} \text{ s}^{-1}$ . This is consistent with the observed upper limit.

Table 4.2: Log of Gemini observations.

Epoch	Date start (UT)	Start time after trigger (s)	Exposure time (s)	Filter	Seeing (arcsec)	Airmass	Magnitude (mag)	Flux ( $\text{erg cm}^{-2} \text{s}^{-1} \text{Hz}^{-1}$ )
1	May 15 06:27 UT	$\sim 6100$	1800	r	0.5	1.021	$26.36 \pm 0.12$	$8.2 \times 10^{-31}$
2	May 16 05:44 UT	$\sim 9 \times 10^4$	1800	r	1	1.005	$26.54 \pm 0.33$	$6.95 \times 10^{-31}$
3	November 28 14:20 UT	$\sim 1.6 \times 10^7$	2800	r	0.8	1.226	$> 27.4$	$< 4.55 \times 10^{-31}$

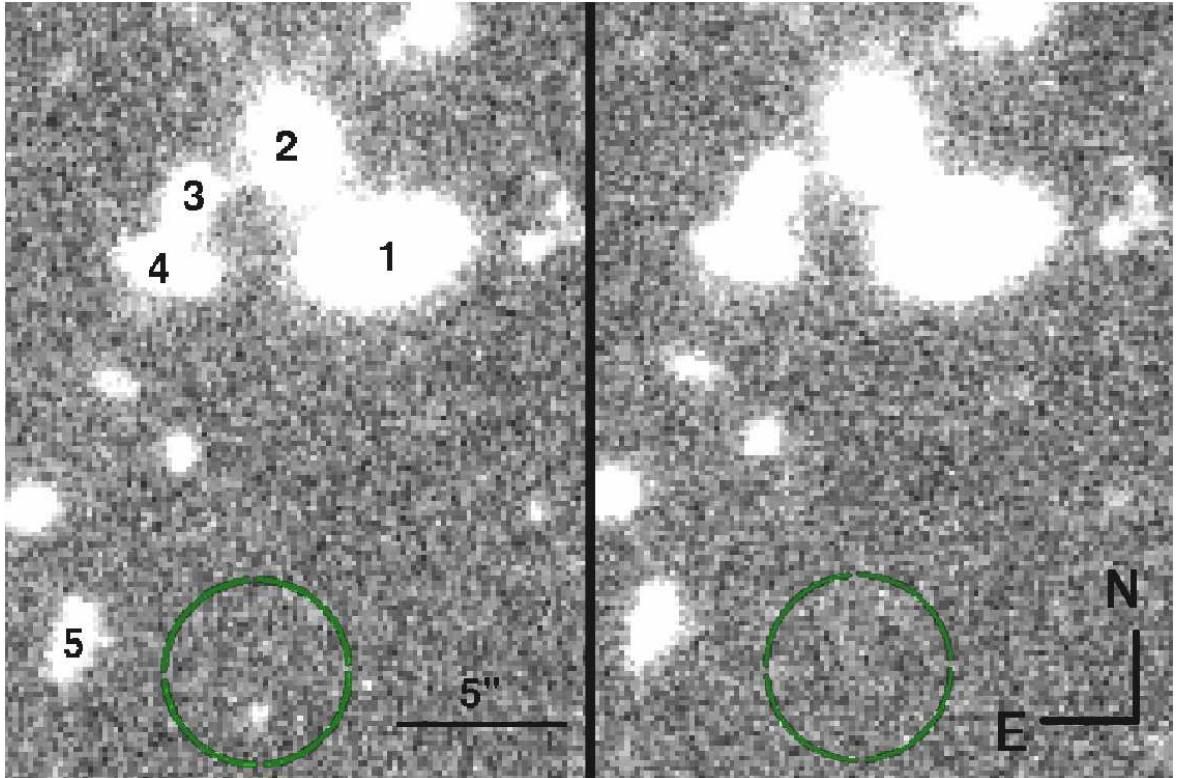


Figure 4.2: The circle marks the location of the XRT enhanced position of GRB 090515 on the Gemini r-band observations from epoch 1 (15<sup>th</sup> May 2009) on the left and epoch 3 (28<sup>th</sup> November 2009) on the right. An optical afterglow candidate is observed within the error circle. Labeled are the brightest nearby galaxies.

Labeled in Figure 4.2 are the five brightest nearby galaxies and Table 4.3 provides their magnitudes and offsets from the GRB location. These galaxies are candidates for the host galaxy of GRB 090515, with significant offsets, or the burst could be associated with a significantly fainter underlying host galaxy.

Berger (2010) studied the chance alignments of several galaxies in the field of GRB 090515 and concluded that galaxy 1, at  $z \sim 0.4$  has the lowest probability of chance alignment (0.1) and hence is most likely to be associated with GRB 090515. However, galaxy 5 also has a comparable probability of chance alignment (0.2). Tunnicliffe et al. (private communication) show for hostless GRBs, like GRB 090515, these galaxies are likely to be field galaxies and hence the galaxy with the lowest probability of chance alignment is not necessarily the host galaxy. Therefore, this Chapter assumes that the host galaxy and redshift of GRB 090515 is unknown.

Table 4.3: Photometry of the nearby galaxies, as labeled in Figure 4.2, calibrated using SDSS observations.

Galaxy	Magnitude	Offset (arcsec)
1	$20.2 \pm 0.1$	14
2	$21.3 \pm 0.1$	16
3	$22.5 \pm 0.1$	15
4	$22.6 \pm 0.1$	13
5	$23.4 \pm 0.1$	6

### 4.3 Comparison to other GRBs

The XRT light curve of the low fluence GRB 090515 is unusual as it goes from being the brightest SGRB in X-rays to one of the faintest within seconds. The fluence in X-rays during the plateau is significantly higher than the fluence in gamma-rays. Additionally, the final decay is the steepest decay observed to date (Evans et al., 2009). The X-ray spectral index of GRB 090515 is not unusual compared to other SGRBs. In Table 4.4, a summary is provided of the properties of the long and short GRBs to which GRB 090515 is compared in detail.

In Figure 4.3, the 15 – 150 keV fluence and 0.3 – 10 keV flux at  $t_0 + 100$  s is shown for all the SGRBs in the Swift sample with  $T_{90} \leq 2$  s and which were observed by XRT at this time. GRB 090515 is shown with a filled circle. As expected, the higher fluence GRBs tend to have higher flux X-ray afterglows. GRB 090515 is an exception to this alongside GRB 070724A; both of these bursts have an unusually high initial X-ray flux for their fluence. In Figure 4.4(a), the combined BAT-XRT light curves of GRB 090515 and GRB 070724A are compared. The initial XRT flux of 070724A appears to be consistent with flares (as there is a varying hardness ratio) and an underlying broken power law decay. There is no obvious plateau phase for GRB 070724A, but this may have occurred prior to the XRT observations. The steep decay phase of GRB 070724A, with  $\alpha = 3.44_{-0.35}^{+0.60}$  is much shallower than the steep decay of GRB 090515. Additionally, the optical afterglow of GRB 070724A had a magnitude of  $i = 23.79 \pm 0.07$  mag at 2.3 hours after the burst, corresponding to a flux of  $6.86 \times 10^{-30}$

Table 4.4: The GRBs considered in detail in this Chapter.

GRB	$T_{90}$ (s)	$\Gamma$ (15 – 150 keV)	Fluence (15 – 150 keV) ( $10^{-8}$ erg $\text{cm}^{-2}$ )
090515	$0.036 \pm 0.016$	$1.6 \pm 0.2$	$2.0 \pm 0.8$ <sup>(1),(2)</sup>
090607	$2.3 \pm 0.1$	$1.25 \pm 0.30$	$11 \pm 2$ <sup>(3)</sup>
080520A	$2.8 \pm 0.7$	$2.90 \pm 0.51$	$5.5 \pm 1.4$ <sup>(4)</sup>
080503	$170 \pm 20$	$2.00 \pm 0.13$	$200 \pm 10$ <sup>(5)</sup>
070724A	$0.4 \pm 0.04$	$1.81 \pm 0.33$	$3.0 \pm 0.7$ <sup>(6)</sup>
070616	$402 \pm 10$	$1.61 \pm 0.04$	$1920 \pm 30$ <sup>(7)</sup>
070209	$0.10 \pm 0.02$	$1.55 \pm 0.39$	$1.1 \pm 0.3$ <sup>(8)</sup>
060717	$3.0 \pm 1$	$1.72 \pm 0.38$	$6.5 \pm 1.6$ <sup>(9)</sup>
051221B	$61 \pm 1$	$1.48 \pm 0.18$	$113 \pm 13$ <sup>(10)</sup>
051105	$0.028 \pm 0.004$	$1.33 \pm 0.35$	$2.0 \pm 0.46$ <sup>(11)</sup>
050813	$0.6 \pm 0.1$	$1.19 \pm 0.33$	$4.4 \pm 1.1$ <sup>(12)</sup>
050509B	$0.048 \pm 0.022$	$1.5 \pm 0.4$	$0.78 \pm 0.22$ <sup>(13)</sup>
050421	$10.3 \pm 2$	$1.7 \pm 0.4$	$8.8 \pm 2.9$ <sup>(14)</sup>

- <sup>(1)</sup> Barthelmy et al. (2009a) <sup>(2)</sup> Sakamoto & Beardmore (2009) <sup>(3)</sup> Barthelmy et al. (2009b) <sup>(4)</sup> Sakamoto et al. (2008c) <sup>(5)</sup> Ukwatta et al. (2008) <sup>(6)</sup> Parsons et al. (2007) <sup>(7)</sup> Sato et al. (2007c) <sup>(8)</sup> Sakamoto et al. (2007) <sup>(9)</sup> Markwardt et al. (2006a) <sup>(10)</sup> Fenimore et al. (2005) <sup>(11)</sup> Barbier et al. (2005a) <sup>(12)</sup> Sato et al. (2005) <sup>(13)</sup> Barthelmy et al. (2005c) <sup>(14)</sup> Sakamoto et al. (2005)

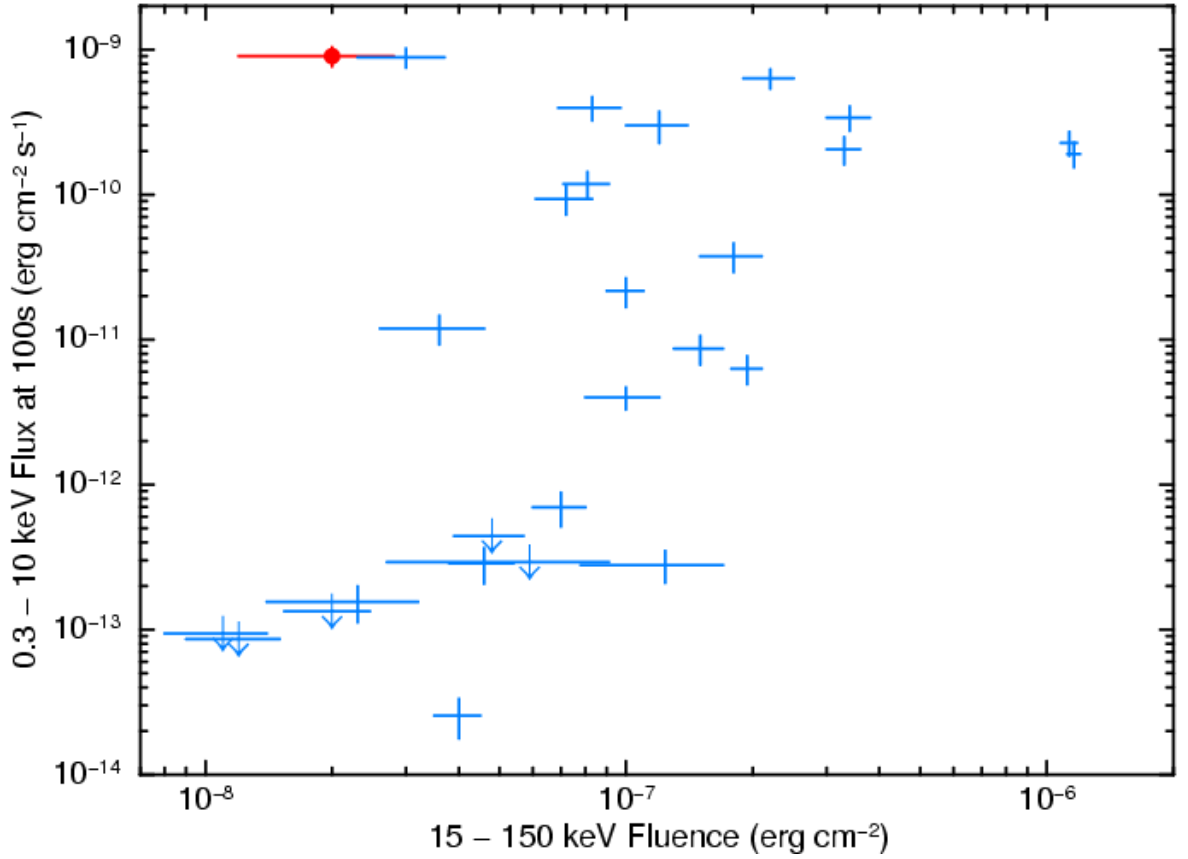


Figure 4.3: The fluence in the energy band 0.3 – 10 keV versus the 15 – 150 keV flux for all Swift SGRBs which were observed at 100s after the trigger time. The filled red circle marks the location of GRB 090515.

$\text{erg cm}^{-2} \text{ s}^{-1} \text{ Hz}^{-1}$ , with an associated host galaxy (Berger et al., 2009; Kocevski et al., 2010). This flux is almost an order of magnitude larger than the optical afterglow of GRB 090515 at 1.7 hours and GRB 090515 does not have an identified host galaxy. However, GRB 070724A does share many similarities with GRB 090515 so the possibility that they originate from a similar progenitor cannot be ruled out.

Figure 4.5(a) shows the lightcurves for the observed R band optical afterglows associated with SGRBs (published values converted from magnitudes into flux density in Jy, using the method described in Section 3.3.1), GRB 090515 is the faintest observed and one of the earliest detections after the trigger time. In Figure 4.5(b) the optical fluxes are divided by the XRT flux at 1000 s after the trigger time. When the XRT flux at 1000 s is considered, the optical afterglow of GRB 090515 is not unusually

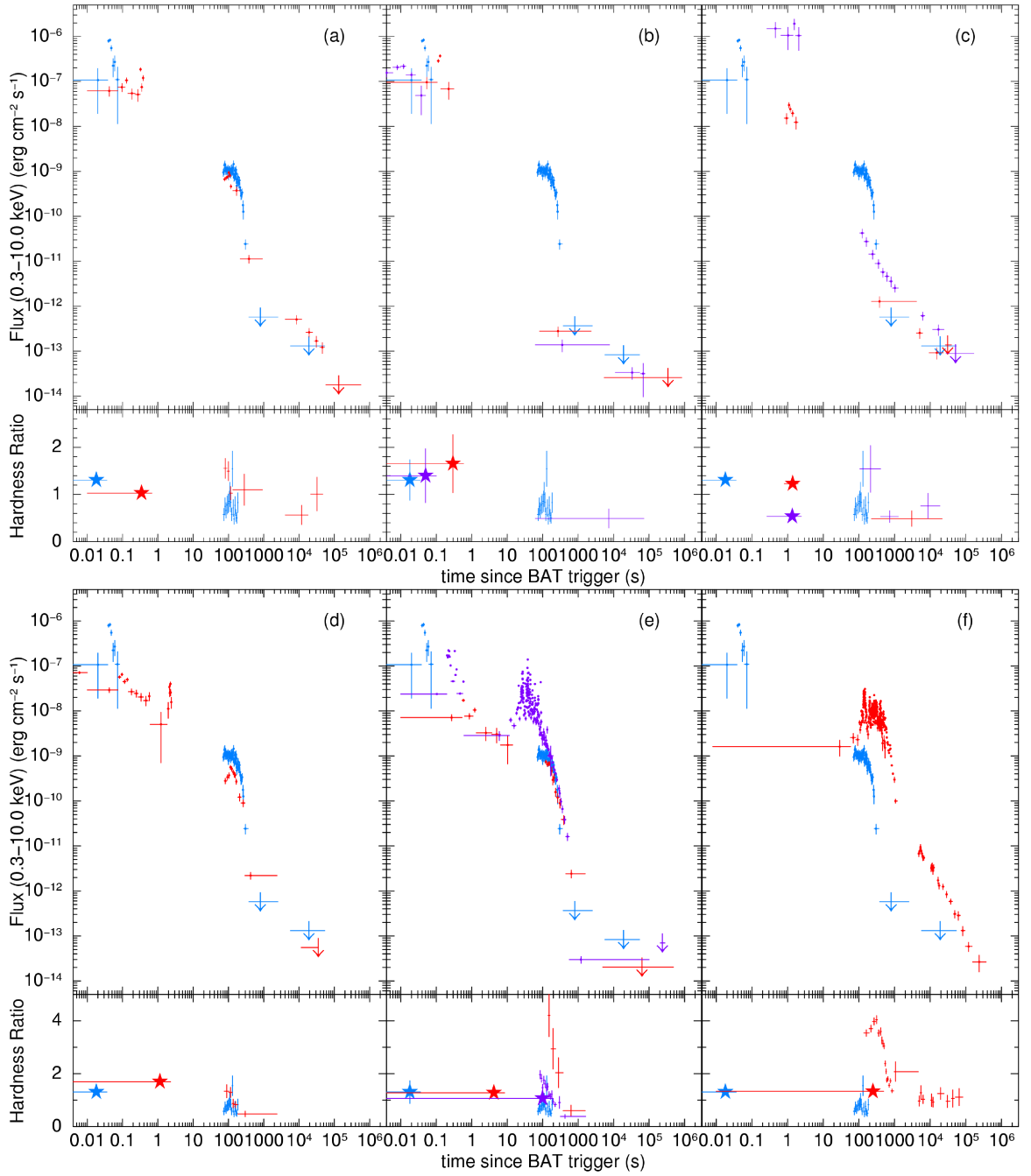


Figure 4.4: The BAT-XRT light curve and hardness ratios for GRB 090515 in blue in comparison to other GRBs. (a) GRB 070724A in red. (b) GRB 050813 in red and GRB 050509B in purple. (c) GRB 060717A in red and GRB 080520A in purple. (d) GRB 090607 in red. (e) GRB 050421 in red and GRB 080503 in purple. (f) GRB 070616 in red. In the lower boxes for each graph, there is the hardness ratio for the BAT data ((50 – 100) keV/(25 – 50) keV), with a star, and the hardness ratio for the XRT data ((1.5 – 10) keV/(0.3 – 1.5) keV).

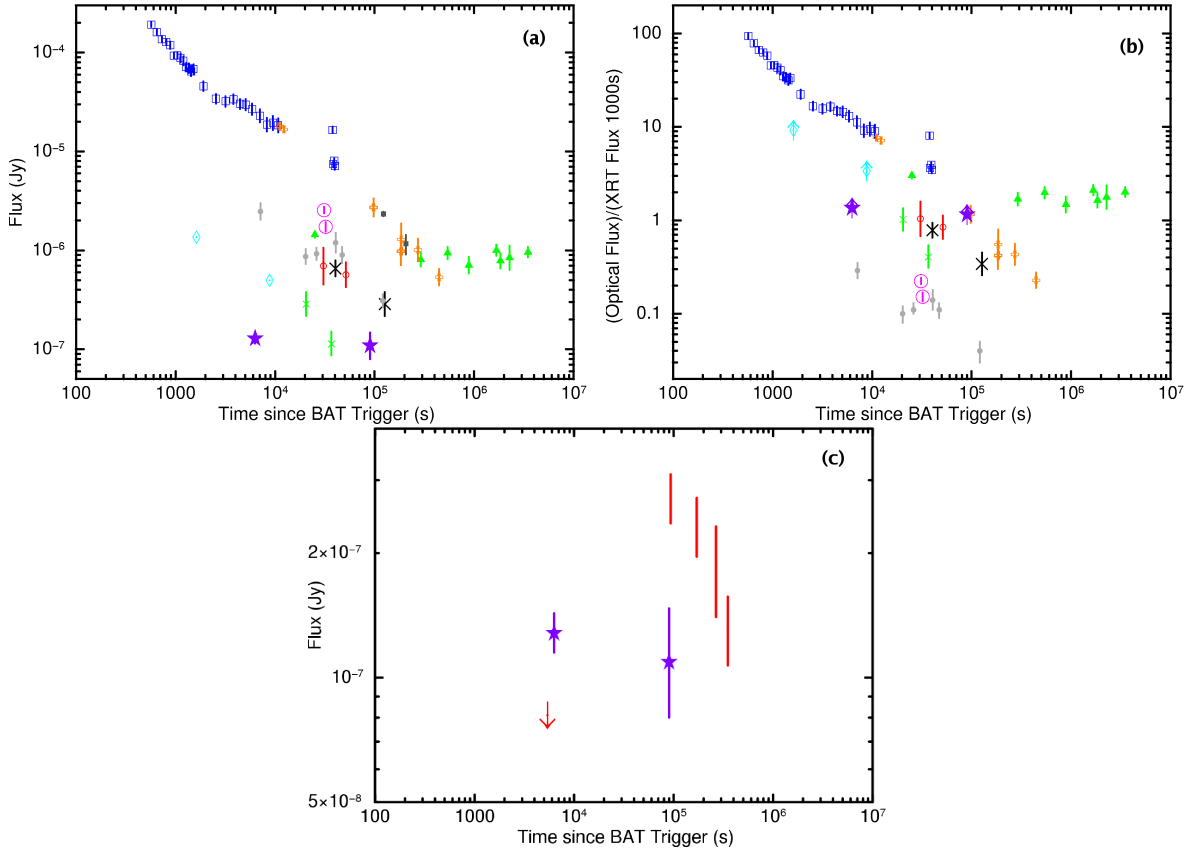


Figure 4.5: (a) The optical flux light curves for all observed SGRB afterglows in the R band. (b) Normalised using the XRT flux at 1000 s. Colour scheme: GRB 090515 - purple star, GRB 091109B - small green X (Levan et al., 2009; Malesani et al., 2009), GRB 090426 - dark blue open square (Antonelli et al., 2009; Xin et al., 2011), GRB 090305 - light blue open diamond (Cenko et al., 2009; Berger & Kelson, 2009), GRB 080905A - small red open circle (Rowlinson et al., 2010a), GRB 071227 - green filled triangle (Berger, Morrell, & Roth, 2007), GRB 070809 - large black X (Perley, Thoene, & Bloom, 2007; Perley et al., 2008), GRB 061201 - large pink open circle (Stratta et al., 2007), GRB 060121 - dark grey filled circle (Levan et al., 2006a), GRB 051221A - orange open cross (Soderberg et al., 2006), GRB 050709 - light grey filled square (Hjorth et al., 2005a). (c) The optical flux light curve for GRB 090515 (purple stars) with GRB 080503 (red).

faint compared to other SGRBs. The optical light curve for GRB 080503 (a short burst with extended emission Perley et al., 2009a) is shown in Figure 4.5(c) in comparison to GRB 090515.

### 4.3.1 GRBs with similar fluence to GRB 090515

As the fluence of GRB 090515 in the 15 – 150 keV energy band was one of the lowest observed for SGRBs, here it is compared to other low fluence GRBs.

GRB 050509B and GRB 050813 were short GRBs detected by the *Swift* satellite that were similar to GRB 090515 during the prompt emission phase. However, the combined BAT and XRT light curves for GRBs 050509B and 050813, shown in Figure 4.4(b), do not show the same X-ray plateau extending to  $\sim 200$  s after the burst. GRBs 050509B and 050813 have both been used to place constraints on the compact binary merger model of SGRBs (Gehrels et al., 2005; Hjorth et al., 2005b; Bloom et al., 2006; Ferrero et al., 2007). The observed upper limits for GRB 090515 at late times (after 400 s) are consistent with the later emission observed for GRBs 050509B and 050813. This suggests that the plateau and steep decay are an additional component in the light curve of GRB 090515.

GRB 051105 is a SGRB with an identical fluence to GRB 090515, but its afterglow was undetectable by XRT in observations starting 68 s after the burst (Mineo et al., 2005a). GRB 070209 had the lowest SGRB fluence and was also undetectable by XRT in observations starting 78 s after the burst (Sato et al., 2007b).

In Figure 4.4(c), the X-ray light curve of GRB 090515 is compared to the two lowest fluence LGRBs in the *Swift* sample which were detected by XRT. These are GRB 080520A and GRB 060717A, they both have significantly higher fluence in the 15 – 150 keV band than GRB 090515 (due to having longer durations), but are a lot fainter in X-rays, again suggesting additional X-ray emission in GRB 090515.

It is possible that these GRBs had plateau phases which end prior to the XRT observations. However, as *Swift* slewed promptly to these GRBs (observations typically starting within 100 s), a plateau phase would need to be significantly shorter than that observed for GRB 090515. The main exceptions to this are GRBs 060717A and 080520, which had XRT observations beginning when GRB 090515 was in the

steep decay phase.

### 4.3.2 GRBs with steep decays

The GRB with an X-ray light curve most similar to GRB 090515 is GRB 090607, which has a  $T_{90}$  just above the short-long boundary. They are compared in Figure 4.4(d). Both light curves show a distinctive steep decay at  $\sim 200$  s. However, the emission of GRB 090607 between 80 and 100 s is not a plateau as observed in GRB 090515 and, given the hard spectrum which softens as the emission decays (shown in the lower panel of Figure 4.4(d)), is more likely due to a flare at the start of the XRT observations.

## 4.4 Discussion

The steep decay in the unusual X-ray light curve of GRB 090515 cannot be explained using the external shock afterglow models. Instead, this Section considers if this GRB was a naked burst with faint, rapidly fading emission, or if the X-ray plateau is powered by an unstable millisecond pulsar.

### 4.4.1 An under-luminous naked LGRB

If a GRB occurs in a very low density ISM then the afterglow from external shocks between the jet and the ISM could be too faint for detection by *Swift*. Instead, there would just be the prompt emission followed by a rapid decline due to the ‘‘curvature effect’’ (Kumar & Panaitescu, 2000). This predicts a decay in flux described by:

$$f_{\nu} \propto \nu^{-\beta} t^{-2-\beta} \quad (4.1)$$

where  $\beta$  is the observed spectral energy index at frequency  $\nu$  ( $\beta = \Gamma - 1$ ), and  $t$  is the time since the trigger. A decay of  $\alpha = 2 + \beta = \Gamma + 1$  should be observed. GRB 090515 is compared here with a good candidate for a naked burst, GRB 050421 (Godet et al., 2006).

GRB 050421 was a weak long GRB detected by BAT following a steep decay, as shown in Figure 4.4(e), although the decay is not as steep as for GRB 090515. There is evidence of spectral evolution, as the emission is getting softer (the lower panel of Figure 4.4(e)); however, the spectral evolution is during the steep decay and not the plateau region. The initial hardness ratio for (1.5 – 10) keV/(0.3 – 1.5) keV is 6 times larger for GRB 050421 than GRB 090515. Godet et al. (2006) explained the steep decay ( $\alpha = 3.1 \pm 0.1$ ) of GRB 050421 by assuming it was a “naked burst”, i.e. there was no forward shock component of the afterglow as the interstellar medium (ISM) was not dense enough for the shock wave to produce a typical afterglow. The detected decaying emission is consistent with the “curvature effect”. GRB 080503, shown in Figure 4.4(e), has also been explained as a short “naked burst” with extended emission detected in the BAT (although not a plateau), the X-ray decay is consistent with the “curvature effect” ( $\alpha \sim 2-4$ ; Perley et al., 2009a). However, the steep decay for both of these are significantly shallower than the decay of GRB 090515, which was  $\alpha_3 > 9$  (with  $t_0$  at the start of the prompt emission).

GRB 090515 shares some similarities with GRB 050421 and GRB 080503 (Godet et al., 2006; Perley, Kislak & Ganeshalingam, 2009b). Zhang et al. (2009) suggested that the burst duration, observed by BAT, represents the duration that the jet is relativistic and, with a non-relativistic (or less relativistic) jet, the central engine can be active for longer than this time and may be observed by XRT. Therefore, the X-ray plateau observed for GRB 090515 could be a continuation of the prompt emission, which has fallen below the threshold of BAT. So with a more sensitive detector, GRB 090515 may have been identified as a LGRB. If true, the steep decay is expected to match the “curvature effect” like GRB 050421. During the plateau, the spectral index  $\Gamma_x$  is  $1.88 \pm 0.14$  predicting a steep decay slope of  $\alpha = 2.88 \pm 0.14$ . As the observed decay is significantly steeper than this, it does not fit the “curvature effect” theory. Using the method described by Liang et al. (2006), the  $t_0$  was shifted to the possible flare at the end of the plateau in GRB 090515. The steep decay becomes less extreme,  $\alpha = 3.7 \pm 0.6$ , but still marginally steeper than the predicted decay slope. This method relies on correctly identifying the time at which the central engine is last active and with a plateau in the light curve this point is difficult to identify. The steep decay of GRB 090515 following the plateau may be consistent with the “curvature effect” if a later location of  $t_0$  is identified. Alternatively, this could be associated with a narrow opening angle for the jet which creates the plateau, as in that case outside of  $1/\Gamma$  there would

be very little high latitude emission, giving a much steeper decay slope. It is also possible that the spectrum softens immediately prior to the steep decay, however there are not enough observed counts to produce a reliable X-ray spectrum at this time.

GRB 090515 can potentially be explained as an under-luminous naked long GRB, however this is reliant on the assumption that the plateau is powered by prolonged activity in the central engine.

#### 4.4.2 An unstable millisecond pulsar (magnetar) central engine

The bright X-ray plateau in the light curve of GRB 090515 could be associated with the formation, emission and collapse of a millisecond pulsar. There have been predictions that in some GRBs an unstable millisecond pulsar may be formed (Usov, 1992; Duncan & Thompson, 1992; Dai & Lu, 1998a,b; Zhang & Mészáros, 2001). At formation, there is enough rotational energy to prevent gravitational collapse. This energy can be released as electromagnetic radiation or gravitational waves, causing the pulsar to spin down until it reaches a critical point at which it is no longer able to support itself. At this point the pulsar collapses to a black hole and the emission stops. This would be evident in the X-ray light curve as a plateau caused by energy injection from the millisecond pulsar followed by an extremely steep decay when the pulsar collapses. Millisecond pulsars formed during the core collapse of a massive progenitor star might be expected to be associated with long GRBs and this has been suggested by Troja et al. (2007) and Lyons et al. (2010). GRB 090515 was an extremely short GRB, but a millisecond pulsar could be formed by two merging neutron stars (a potential progenitor of SGRBs), depending on various assumptions about the neutron stars' equations of state (Dai & Lu, 1998a; Dai et al., 2006; Yu & Huang, 2007).

Troja et al. (2007) and Lyons et al. (2010) studied LGRBs with a plateau and a steep decay and GRB 090515 shows similarities to them. In Figure 4.4(f), the light curve of GRB 090515 is compared to that of GRB 070616 (Starling et al., 2008), one of the sample chosen by Lyons et al. (2010) as potentially showing evidence of an unstable millisecond pulsar. When comparing the light curves, GRB 070616 appears to be a brighter and longer version of GRB 090515 but with a bright afterglow component at later times.

The following equations from Zhang & Mészáros (2001) (equations 4.2 and 4.3) were used to determine if GRB 090515 could be a millisecond pulsar, using  $T_{em,3}$ , the rest frame duration of the plateau in units of  $10^3$  s, and  $L_{em,49}$ , the luminosity of the plateau in units of  $10^{49}$  erg s<sup>-1</sup>, in the rest frame energy band 1 – 1000keV. The equations are rearranged to give equations 4.4 and 4.5, these are used to predict the magnetic field strength and the spin period of a pulsar formed by this method.

$$T_{em,3} = 2.05 (I_{45} B_{p,15}^{-2} P_{0,-3}^2 R_6^{-6}) \quad (4.2)$$

$$L_{em,49} \sim (B_{p,15}^2 P_{0,-3}^{-4} R_6^6) \quad (4.3)$$

$$B_{p,15}^2 = 4.2025 I_{45}^2 R_6^{-6} L_{em,49}^{-1} T_{em,3}^{-2} \quad (4.4)$$

$$P_{0,-3}^2 = 2.05 I_{45} L_{em,49}^{-1} T_{em,3}^{-1} \quad (4.5)$$

where  $I_{45}$  is the moment of inertia in units of  $10^{45}$  g cm<sup>2</sup>,  $B_{p,15}$  is the magnetic field strength at the poles in units of  $10^{15}$  G,  $R_6$  is the radius of the neutron star in  $10^6$  cm and  $P_{0,-3}$  is the initial period of the compact object in milliseconds. These equations apply to the electromagnetic dominated spin down regime, as the gravitational wave dominated regime would be extremely rapid and produce a negligible effect in this analysis. The standard values for a neutron star could be assumed, as in Lyons et al. (2010), so that  $I_{45} \sim 1$  and  $R_6 \sim 1$  which may be appropriate for a collapsar. However, as an unstable millisecond pulsar would be formed by merging two neutron stars the true values may be different, depending on the mass and equation of state. For a millisecond pulsar formed by a binary merger, the mass of the neutron star is taken to be  $M_{NS} = 2.1 M_{\odot}$  (Nice et al., 2005) and estimate  $I_{45} \sim 1.5$ . Although GRB 090515 has many properties similar to other SGRBs suggesting the progenitor is most likely a compact binary merger, there have been predictions that collapsars may also produce a SGRB (for example from an orphan precursor jet; Janiuk, Moderski, & Proga, 2008) and evidence that a significant fraction of SGRBs are related to collapsars rather than compact binary mergers (Virgili et al., 2011; Cui et al., 2010). So in the following analysis both progenitor models are compared by using different neutron star masses.

As a redshift was not obtained for this GRB, a range of redshifts were used from  $z = 0.2$  up to an upper limit of  $z = 5.0$  consistent with the detection of the optical afterglow. Emitters at high redshift have a characteristic break in their spectra caused by absorption from intergalactic neutral hydrogen between

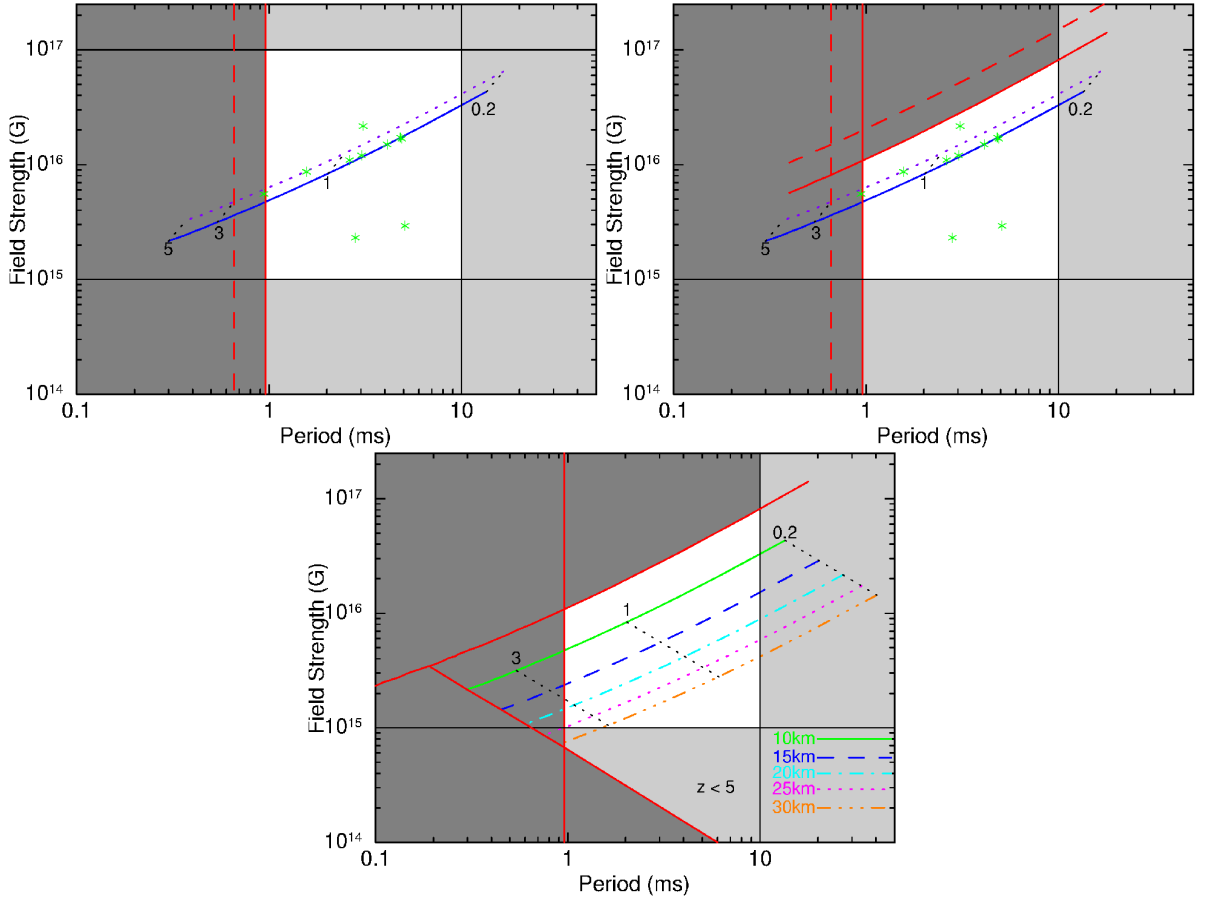


Figure 4.6: (a) The blue line shows the magnetic field and period for a millisecond pulsar formed during GRB 090515 as a function of redshift assuming a neutron star mass of  $1.4 M_{\odot}$  and the purple dotted line assumes a neutron star mass of  $2.1 M_{\odot}$ . The green stars are the 18 degree beamed LGRB sample from Lyons et al. (2010). The red line shows the limit at which the progenitor would violate the breakup spin period of a pulsar for a mass of  $1.4 M_{\odot}$  and the dashed red line is for a mass of  $2.1 M_{\odot}$ . The other regions are as defined in Lyons et al. (2010); dark grey shading corresponds to forbidden regions (assuming a mass of  $1.4 M_{\odot}$ ) and light grey are limits based on the previous studies (as discussed in the text). The dotted lines represent contours of equal redshift decreasing from left to right. (b) The upper magnetic field limit in (a) has been replaced by the red curved line giving the forbidden region assuming causality shaded in dark grey (assuming a mass of  $1.4 M_{\odot}$ ). This region will change depending on the mass of the neutron star, the rest frame duration and luminosity of the plateau. The red dashed curved line represents the forbidden region for a binary merger progenitor. (c) The different contours represent the effect of increasing the radius of the neutron star from 10 km to 30 km assuming a constant mass of  $1.4 M_{\odot}$ . Additionally, a limit is imposed on redshift due to detection of the afterglow in the R-band.

the observer and the source. This break is known as the Lyman break and can allow the determination of photometric redshifts, e.g. GRB 090423 at  $z = 8.2$  had a Lyman break between the Y and J band filters, resulting in a non-detection in the Y band observations (Tanvir et al., 2009). To have a detection in the R band, the Lyman break must be at a bluer wavelength than the R-band filter and an upper limit on the redshift can be obtained by assuming the Lyman break occurs immediately after the R-band, giving  $z \leq 5$ . The millisecond pulsar was assumed to be formed at  $t \sim 0$  and, hence, the observed frame duration of the plateau in the observer frame is 240 s (the restframe duration is then calculated for given redshifts). The luminosity of the plateau was calculated using the observed 0.3 – 10 keV flux of  $\sim 1 \times 10^{-9}$  erg cm $^{-2}$  s $^{-1}$ , the spectral index during the plateau (1.88) and a k-correction (Bloom, Frail, & Sari, 2001). These values were then substituted into the equations (4.4) and (4.5) to calculate  $B_{p,15}$  and  $P_{0,-3}$ . These are plotted as a blue contour in Figure 4.6(a) assuming it was formed from a collapsar and a purple contour if formed by a binary neutron star merger.

Also shown in Figure 4.6(a), are the regions in which a millisecond pulsar would be expected, as defined in Lyons et al. (2010): the red line represents the breakup spin-period for a neutron star of mass  $1.4 M_{\odot}$  ( $\geq 0.96$ ms, Lattimer & Prakash, 2004). Using equation 4.6 (Lattimer & Prakash, 2004), this limit is calculated for the binary merger scenario with a mass of  $2.1 M_{\odot}$  to be  $P \geq 0.66$  ms (where P is the minimum spin period of the neutron star in ms) and this is shown with a red dashed line.

$$P_{0,-3} \geq 0.81 M_{1.4}^{-1/2} R_6^{3/2} \text{ms} \quad (4.6)$$

The initial rotation period needs to be  $\leq 10$  ms (Usov, 1992), the upper limit for the magnetic field is  $\leq 10^{17}$  G (implied from observations of the giant flare from SGR 1806-20; Stella et al., 2005) and the lower limit for the magnetic field is  $\geq 10^{15}$  G (Thompson, 2007). This shows that GRB 090515 could have formed a millisecond pulsar if it had a redshift of  $0.3 < z < 1.8$  for a collapsar progenitor or a redshift of  $0.3 < z < 3.0$  for a binary merger progenitor. These are both very reasonable redshift ranges when compared to the sample of GRBs. The magnetic field for a given spin period is slightly lower for a binary merger progenitor than for a collapsar progenitor. Alongside the prediction by Troja et al. (2007) and Lyons et al. (2010) of a plateau followed by a steep decay for the lightcurve of a millisecond pulsar collapsing to a black hole, which matches the observed light curve for GRB 090515, this analysis provides a consistent case for GRB 090515 forming a millisecond pulsar irrespective of the two initial

progenitor models considered.

Using a causality argument, i.e. that the speed of sound on the neutron star cannot exceed the speed of light, a tighter constraint can be placed on the minimum possible radius,  $R_6$  and  $M_{1.4}$ , where  $M_{1.4}$  is the mass of the neutron star in  $1.4 M_\odot$ , using equation 4.7 (Lattimer et al., 1990). The moment of inertia, given in equation 4.8, is based on the assumption that the neutron star can be modelled as an uniform sphere.

$$R_6 > 0.6225M_{1.4} \quad (4.7)$$

$$I_{45} \sim M_{1.4}R_6^2 \quad (4.8)$$

This constraint on radius and moment of inertia for a given mass can be substituted into equations 4.4 and 4.5 to define a forbidden region for a given neutron star mass, plateau duration and luminosity. The forbidden region is described by equations 4.9 and 4.10 and is shown in Figure 4.6(b) for GRB 090515 assuming a mass of  $1.4 M_\odot$ , for a collapsar progenitor (red curved line), and  $2.1 M_\odot$ , for a binary merger progenitor (red curved dashed line).

$$B_{p,15}^2 > 10.8T_{em,3}^{-2}L_{em,49}^{-1} \quad (4.9)$$

$$P_{0,-3}^2 < 0.794M_{1.4}^3T_{em,3}^{-1}L_{em,49}^{-1} \quad (4.10)$$

It has been suggested that the radii of proto neutron stars may be as large as a few tens of kilometers (Ott et al., 2006), so in Figure 4.6(c) the effect of increasing the radius, from 10 km to 30 km, is shown for a mass of  $1.4 M_\odot$ , using the plateau luminosities and durations previously calculated for GRB 090515 assuming it is at a range of redshifts. For larger radii, the unstable millisecond pulsar has to be at higher redshifts, have a smaller magnetic field and larger period. As there is an R-band detection of the optical afterglow, the upper-limit  $z \leq 5$  is placed on the redshift .

In Figure 4.7, the effect of the different beaming angles considered by Lyons et al. (2010) assuming a mass of  $1.4 M_{\odot}$  is investigated. As the causality forbidden region shown in Figure 4.6(b and c) also depends on beaming angle the regions defined by Lyons et al. (2010) are used for clarity. Up to this point, only isotropic emission has been considered and this shows beaming the emission would greatly affect the results obtained. Simulations have shown that a relativistic jet can be produced by a magnetar (Bucciantini et al., 2009). If the emission was beamed by 4 degrees the observations would support the magnetar model if at  $z > 3$ . With a beaming angle of 18 degrees, GRB 090515 would need a redshift of  $1 < z < 5$  in order to satisfy the model and the constraints obtained by observing an optical afterglow. The more tightly the emission is beamed, the higher the redshift that the burst would need to be at in order to fit the magnetar model and this may explain why a host galaxy has not been identified.

## 4.5 Conclusions

GRB 090515 is a very unusual SGRB, it is the first SGRB with a fluence below  $10^{-7}$  erg cm $^{-2}$  with an observed optical afterglow at 1.75 hours ( $R=26.4\pm 0.1$  mag), and this is the faintest detected optical afterglow for a GRB at that time. Its low gamma-ray fluence would lead to the expectation of a significantly fainter X-ray light curve than observed at early times. Most importantly, the X-ray plateau followed by an extremely steep decay is very unusual, but may not be unique in the *Swift* sample. With a more sensitive detector, the plateau observed by XRT may have instead been identified as part of the prompt emission and GRB 090515 might instead have been classified as a LGRB. Therefore, it poses interesting questions about the progenitor model and for the classification of other GRBs. In this Chapter, two popular progenitor models for GRBs were considered, collapsars and compact binary mergers.

This Chapter suggests that the simplest explanation for the unusual light curve of GRB 090515 is that it shows prolonged emission from an unstable millisecond pulsar, followed by an extremely steep decay when the millisecond pulsar collapses. Given the short duration of the GRB and the other properties, the binary merger progenitor is favoured but cannot rule out a collapsar progenitor. For a collapsar progenitor, the proposed unstable millisecond pulsar with a spin period of 10 ms would have a magnetic

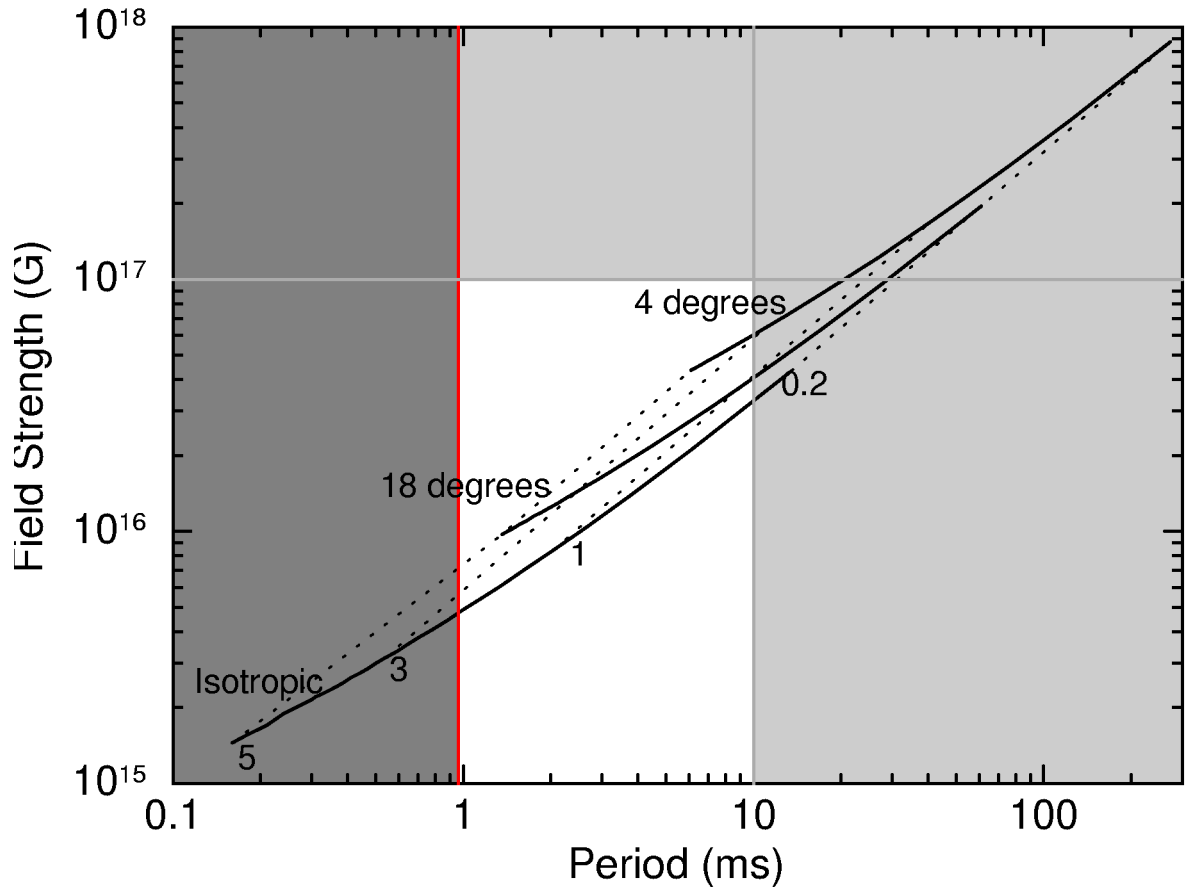


Figure 4.7: We show here the effect of beaming the emission of GRB 090515 assuming a mass of  $1.4 M_{\odot}$ . Solid lines show isotropic solution and the solutions for the two beaming angles considered in Lyons et al. (2010). The dotted lines represent contours of equal redshift decreasing from left to right. The forbidden regions are as defined for Figure 4.6(a).

field of  $\sim 3 \times 10^{16}$  G at  $z \sim 0.3$  and with a spin period of 1 ms the magnetic field would be  $\sim 5 \times 10^{15}$  G at  $z \sim 1.8$ . The binary merger progenitor model gives a spin period of 10 ms and a magnetic field of  $\sim 4 \times 10^{16}$  G at  $z \sim 0.3$  to a spin period of 0.66 ms and a magnetic field of  $\sim 5 \times 10^{15}$  G at  $z \sim 3.0$ . These values assume isotropic emission and a radius of 10 km.

In the next Chapter, the whole *Swift* sample of SGRBs are investigated for evidence of ongoing energy injection that may be similar to GRB 090515.

# Chapter 5

## Evidence of energy injection in SGRB lightcurves

### 5.1 Introduction

Observed features in X-ray lightcurves identify longevity of the central engine of GRBs, for example late time flares (e.g. Margutti et al., 2010) and plateaus (e.g. Nousek et al., 2006; Zhang et al., 2006). GRBs whose X-ray lightcurves have a steep decay and a plateau phase followed by a standard afterglow phase, have been identified as “canonical” lightcurves (Nousek et al., 2006; O’Brien et al., 2006; Zhang et al., 2006). The steep decay phase is associated with high latitude emission from the prompt emission followed by a late emission plateau giving the plateau phase. The fluence of this plateau can be comparable to the fluence of the prompt emission (O’Brien et al., 2006), and typically occur from  $10^2 - 10^3$  s till  $10^3 - 10^4$  s after the trigger time. The plateau is thought to provide evidence of ongoing central engine activity (Nousek et al., 2006; Zhang et al., 2006). Therefore, identifying GRBs with a “canonical” lightcurve can provide a sample with evidence of ongoing energy injection. Evans et al. (2009) studied 162 GRBs in the *Swift* sample identifying a “canonical” lightcurve in 42% of GRB X-ray lightcurves, including 2 SGRBs (051221A and 060313) out of 11 SGRBs analysed.

Although studies of flares and plateaus are typically conducted for LGRBs, fainter versions are evident in many SGRB X-ray lightcurves suggesting a long lived central engine. This is problematic for SGRB progenitor theories as accretion is expected to end within a few seconds and only a small fraction of the merger mass is available ( $0.01 - 0.1 M_{\odot}$  although this is dependant on the NS equation of state, Lee & Ramirez-Ruiz, 2007). Additionally, it is thought that the accretion disk gets destroyed after a few seconds (e.g. Metzger, Piro, & Quataert, 2008). There have been studies of fallback accretion, i.e. that the NS is shredded and parts ( $\leq 10\%$  of the original disk mass) are flung into highly eccentric orbits which accrete onto the central engine at late times giving flares in the X-ray lightcurve (Rosswog, 2007). Cannizzo, Troja, & Gehrels (2011) have attempted to explain plateaus by introducing a band of material at a large distance from the central engine.

An alternative theory is that during some GRBs a millisecond pulsar (magnetar) may be formed with enough rotational energy to prevent gravitational collapse (Usov, 1992; Duncan & Thompson, 1992; Dai & Lu, 1998a,b; Zhang & Mészáros, 2001). The progenitor of this system is typically thought to be a collapsar and LGRB candidates have been identified by Troja et al. (2007) and Lyons et al. (2010). However, it has also been proposed that such a magnetar could be formed by the merger of NSs (Dai & Lu, 1998a; Dai et al., 2006; Yu & Huang, 2007) or via the accretion induced collapse (AIC) of a white dwarf (WD) (Nomoto & Kondo, 1991; Usov, 1992; Metzger, Quataert, & Thompson, 2008). A candidate event for this is GRB 090515 with an unusual X-ray plateau followed by a steep decay (discussed in detail in Chapter 4 and Rowlinson et al., 2010b). The likelihood of producing this event is dependent on the equation of state of NSs. Morrison, Baumgarte, & Shapiro (2004) studied the effect that the equation of state of a NS and rotation would have on the remnant of a compact merger, i.e. whether a NS or a BH is formed (see also Shibata & Taniguchi, 2006). They showed that, even for the harder nuclear equations of state, the rotation of the NS could increase the maximum mass by  $\sim 50\%$  and hence mergers could often result in a NS. Using 6 known Galactic NS binaries and a range of equations of state, Morrison, Baumgarte, & Shapiro (2004) predict that the majority of mergers of the known binaries will form a NS.

The recent discovery of an  $1.97 M_{\odot}$  NS (Demorest et al., 2010) provides further supporting evidence of the possibility that high mass magnetars can be formed from NS mergers. Özel et al. (2010) show that, for a maximum non-rotating NS mass of  $M_{max} = 2.1 M_{\odot}$ , the merger of two NSs with a total

mass  $\leq 1.4M_{max}$  will have a delayed collapse to a BH (i.e. a magnetar phase). They also predict a regime in which the merged remnant does not collapse to form a BH, in this case the total mass is  $\leq 1.2M_{max}$ . If the maximum NS mass is  $2.1 M_{\odot}$ , then the merger of two NSs of masses up to  $1.3 M_{\odot}$  would result in a stable magnetar and the merger of two NSs with larger masses (up to  $1.5-1.7 M_{\odot}$ ) would form an unstable magnetar. As the majority of observed NSs have masses  $\sim 1.4 M_{\odot}$ , it seems reasonable to predict that many NS mergers could result in a magnetar. The stability of the final magnetar is dependent on the maximum possible mass of a NS. Its lifetime depends both on the rate that additional mass (if any) is accreted after formation, as well as the rate at which angular momentum is extracted by e.g. gravitational waves or magnetic torques (e.g. Shibata & Taniguchi, 2006; Oechslin, Janka, & Marek, 2007).

In this Chapter, the entire *Swift* sample of SGRBs ( $T_{90} \leq 2$  s) is used to identify those with a “canonical” like lightcurve suggesting ongoing central engine activity. These results are discussed in Section 5.2. A sub-sample with sufficient data are then studied for the signature of a magnetar (with or without collapse to a BH) which may signify the coalescence of two NSs. If found, this would provide additional support to this popular progenitor theory. The magnetar model is considered in section 5.3; with a description of the model and sample used, analysis of the available data and a discussion of the implications, e.g. for gravitational waves.

## 5.2 “Canonical” SGRB lightcurves

In this section, all *Swift* detected SGRBs,  $T_{90} \leq 2$  s, with an X-ray afterglow or which were promptly slewed to and observed by the X-ray Telescope (XRT) are considered. This allows the inclusion of SGRBs without an X-ray afterglow but do have a constraining upper limit. Out of this sample of 35 SGRBs, only 4 did not have a detected X-ray afterglow (GRBs 050906, 051105, 070209 and 070810B). Hence, 89% of *Swift* SGRBs have detectable X-ray afterglows. The X-ray lightcurves were obtained from the automated analysis on the UK *Swift* Science Data Centre website (Evans et al., 2007, 2009). The Burst Alert Telescope (BAT) lightcurves were created using standard pipelines in the HEASOFT package with  $3\sigma$  significance bins. The BAT observations were then shifted to  $0.3 - 10$  keV to make

Table 5.1: The broken powerlaw fits for the SGRB sample and the X-ray spectral indices for each regime ( $\Gamma_x$ ). These are subdivided into the “canonical” like GRBs with  $\alpha_2 \leq 0.5$  and  $0.5 \leq \alpha_2 \leq 1$ , those with all  $\alpha > 1$  and those with just a simple shallow decay ( $\alpha_1 \leq 1$ ). Where values are left blank there was insufficient data available to constrain them.

GRB	$\alpha_1$	$\Gamma_{x,1}$	$T_1$ (s)	$\alpha_2$	$\Gamma_{x,2}$	$T_2$ (s)	$\alpha_3$	$\Gamma_{x,3}$
“Canonical” like with $\alpha_2 \leq 0.5$								
051210	$1.55^{+0.11}_{-0.08}$	$1.21^{+0.25}_{-0.17}$	$2.7^{+0.9}_{-1.8}$	$0.36^{+0.31}_{-0.04}$	$2.03^{+0.01}_{-0.15}$	$137^{+8}_{-8}$	$3.56^{+0.24}_{-0.21}$	$2.49^{+1.70}_{-3.00}$
070724	$0.97^{+0.12}_{-0.05}$	$1.45^{+0.73}_{-0.64}$	$79^{+10}_{-35}$	$-1.13^{+0.69}_{-1.01}$	$1.66^{+0.24}_{-0.23}$	$110^{+2}_{-3}$	$1.15^{+0.07}_{-0.06}$	$1.45^{+0.48}_{-0.29}$
070809	$1.42^{+0.05}_{-0.04}$	$1.67^{+0.54}_{-0.30}$	$361^{+105}_{-128}$	$0.17^{+0.17}_{-0.41}$	$1.74^{+0.36}_{-0.37}$	$5485^{+7886}_{-2183}$	$1.00^{+0.22}_{-0.20}$	$1.20^{+0.25}_{-0.15}$
080426	$1.94^{+0.14}_{-0.14}$		$126^{+92}_{-25}$	$-0.36^{+0.48}_{-2.04}$	$1.63^{+0.48}_{-0.35}$	$422^{+255}_{-131}$	$1.25^{+0.07}_{-0.06}$	$2.30^{+0.10}_{-0.37}$
080702A	$1.11^{+0.26}_{-0.10}$	$1.10^{+1.50}_{-1.00}$	$174^{+205}_{-142}$	$0.25^{+0.39}_{-2.02}$	$1.18^{+0.85}_{-0.40}$	$420^{+189}_{-180}$	$1.59^{+0.52}_{-0.23}$	$3.30^{+0.83}_{-1.56}$
080905A				$0.44^{+0.51}_{-0.32}$		$124^{+39}_{-55}$	$2.48^{+0.30}_{-0.24}$	$1.63^{+0.36}_{-0.33}$
081024A	$0.70^{+0.13}_{-0.08}$		$0.7^{+3.6}_{-0.6}$	$0.40^{+0.11}_{-0.30}$	$5.50^{+2.50}_{-2.00}$	$81^{+4}_{-18}$	$4.79^{+0.37}_{-0.30}$	$2.19^{+0.85}_{-0.53}$
090426	$2.12^{+0.36}_{-0.45}$		$33^{+125}_{-3}$	$0.21^{+0.31}_{-0.34}$	$1.85^{+0.36}_{-0.24}$	$260^{+140}_{-127}$	$1.04^{+0.07}_{-0.06}$	$2.14^{+0.14}_{-0.14}$
090515	$2.76^{+0.55}_{-0.10}$		$0.30^{+0.00}_{-0.30}$	$0.28^{+0.07}_{-0.03}$	$1.85^{+0.17}_{-0.16}$	$156^{+9}_{-27}$	$2.51^{+0.59}_{-0.87}$	$2.12^{+0.39}_{-0.33}$
100625A	$3.63^{+0.01}_{-0.25}$		$1.90^{+2.40}_{-1.10}$	$0.36^{+0.36}_{-0.63}$	$2.09^{+0.30}_{-0.29}$	$222^{+52}_{-50}$	$3.15^{+0.94}_{-0.85}$	$2.66^{+0.53}_{-0.83}$
110112A	$1.65^{+0.08}_{-0.06}$	$1.45^{+1.08}_{-0.49}$	$144^{+90}_{-30}$	$-0.22^{+0.79}_{-0.65}$	$2.07^{+1.02}_{-0.57}$	$262^{+113}_{-80}$	$1.08^{+0.07}_{-0.07}$	$2.37^{+0.38}_{-0.44}$
“Canonical” like with $0.5 \leq \alpha_2 \leq 1$								
051221A	$1.50^{+0.09}_{-0.03}$	$2.07^{+0.22}_{-0.20}$	$681^{+320}_{-388}$	$0.59^{+0.07}_{-0.11}$	$2.03^{+0.09}_{-0.15}$	$46680^{+12810}_{-12920}$	$1.49^{+0.12}_{-0.11}$	$2.49^{+1.70}_{-3.00}$
060313	$2.84^{+2.13}_{-1.06}$	$1.55^{+0.29}_{-0.28}$	$324^{+107}_{-70}$	$0.74^{+0.08}_{-0.05}$	$1.82^{+0.16}_{-0.10}$	$7467^{+1511}_{-1491}$	$1.65^{+0.12}_{-0.11}$	$2.50^{+0.22}_{-0.28}$
060801				$0.53^{+0.05}_{-0.06}$	$1.59^{+0.23}_{-0.22}$	$315^{+21}_{-30}$	$5.83^{+0.86}_{-0.76}$	$2.18^{+0.63}_{-0.43}$

Table 5.1: Continued:

GRB	$\alpha_1$	$\Gamma_{x,1}$	$T_1$ (s)	$\alpha_2$	$\Gamma_{x,2}$	$T_2$ (s)	$\alpha_3$	$\Gamma_{x,3}$
“Canonical” like with $0.5 \leq \alpha_2 \leq 1$ (Continued)								
061201	$3.09^{+0.66}_{-0.46}$		$1.80^{+1.00}_{-0.50}$	$0.54^{+0.13}_{-0.14}$	$1.44^{+0.20}_{-0.19}$	$2209^{+802}_{-587}$	$1.84^{+0.17}_{-0.14}$	$2.26^{+0.38}_{-0.42}$
071227				$0.82^{+0.01}_{-0.01}$	$1.65^{+0.16}_{-0.15}$	$180^{+6}_{-8}$	$5.12^{+0.69}_{-0.46}$	$2.39^{+0.58}_{-0.49}$
080919				$0.86^{+0.04}_{-0.03}$	$2.31^{+1.01}_{-0.83}$	$351^{+195}_{-55}$	$4.83^{+0.77}_{-0.84}$	$2.35^{+1.01}_{-0.83}$
090510				$0.80^{+0.01}_{-0.01}$	$1.78^{+0.14}_{-0.14}$	$1412^{+136}_{-192}$	$2.18^{+0.17}_{-0.17}$	$2.22^{+0.20}_{-0.16}$
100117A				$0.85^{+0.01}_{-0.01}$	$1.59^{+0.12}_{-0.11}$	$238^{+17}_{-13}$	$3.76^{+0.58}_{-0.43}$	$2.30^{+0.35}_{-0.32}$
100702A	$1.67^{+0.15}_{-0.18}$		$0.1^{+0.4}_{-0.4}$	$0.74^{+0.18}_{-0.18}$	$2.05^{+0.13}_{-0.13}$	$194^{+14}_{-6}$	$4.86^{+0.52}_{-0.26}$	$2.41^{+0.28}_{-0.26}$
101219A				$0.80^{+0.04}_{-0.04}$	$1.33^{+0.72}_{-0.57}$	$195^{+7}_{-12}$	$1.88^{+0.23}_{-0.25}$	$1.63^{+0.37}_{-0.49}$
All $\alpha > 1$								
050813	$1.27^{+0.04}_{-0.03}$	$2.70^{+4.30}_{-1.20}$						
050906	$> 1.28$							
051105	$> 1.33$							
061217	$1.29^{+0.08}_{-0.05}$	$1.40^{+1.13}_{-0.86}$						
070209	$> 1.23$							
070429B	$1.54^{+0.05}_{-0.04}$	$3.10^{+1.00}_{-1.40}$						
070729	$1.29^{+0.05}_{-0.04}$	$1.62^{+0.86}_{-0.43}$						

Table 5.1: Continued:

GRB	$\alpha_1$	$\Gamma_{x,1}$	$T_1$ (s)	$\alpha_2$	$\Gamma_{x,2}$	$T_2$ (s)	$\alpha_3$	$\Gamma_{x,3}$
All $\alpha > 1$ (Continued)								
070810B	$>1.36$							
081101	$>1.21$							
081226	$1.45^{+0.05}_{-0.04}$	$3.84^{+0.96}_{-1.93}$						
090305A	$1.42^{+0.05}_{-0.04}$							
100206A	$1.80^{+0.05}_{-0.04}$	$3.30^{+3.30}_{-1.30}$						
Simple shallow decay $\alpha_1 \leq 1$								
050509B	$1.32^{+0.06}_{-0.04}$	$2.61^{+1.92}_{-0.94}$	$866^{+6652}_{-842}$	$0.08^{+0.34}_{-0.80}$	$2.08^{+1.26}_{-0.56}$			
060502B	$0.95^{+0.04}_{-0.03}$	$2.10^{+2.77}_{-0.81}$						
070714A	$2.23^{+0.18}_{-0.04}$		$123^{+4}_{-45}$	$0.62^{+0.06}_{-0.05}$	$2.24^{+0.33}_{-0.33}$			
090621B	$4.06^{+0.01}_{-0.49}$		$5^{+5}_{-1}$	$0.72^{+0.18}_{-0.16}$	$3.40^{+1.40}_{-1.00}$			
091109B	$4.02^{+0.01}_{-0.32}$		$4^{+1}_{-1}$	$0.64^{+0.08}_{-0.09}$				
100628A	$1.00^{+0.01}_{-0.01}$							

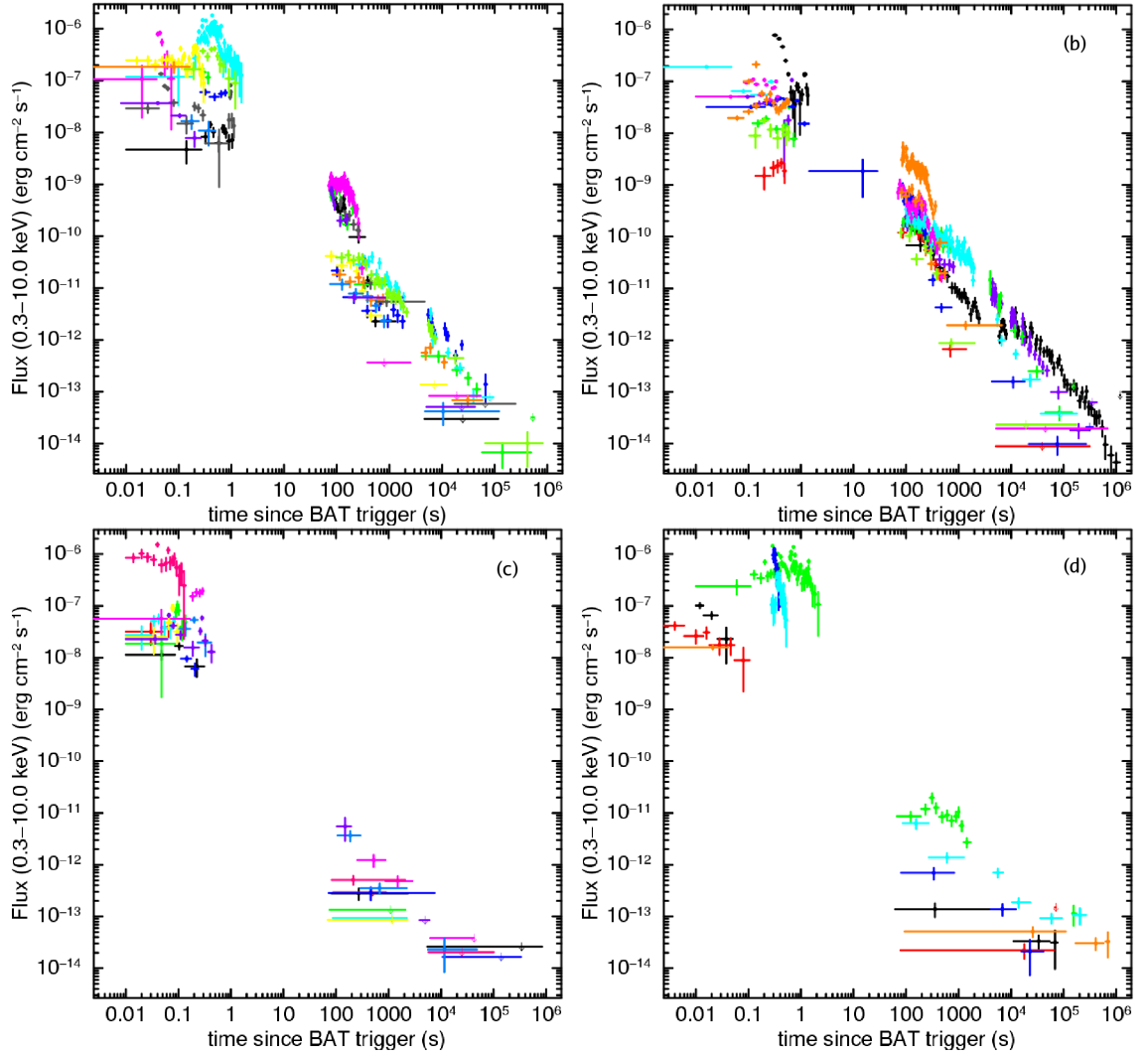


Figure 5.1: These are the BAT-XRT lightcurves (0.3 – 10 keV) sorted into 4 groups. a) These GRBs have a decay slope  $\alpha \leq 0.5$  in their “canonical” afterglows. Black - 051210, green - 070724, blue - 070809, light blue - 080426, cyan - 080702A, grey - 080905A, purple - 081024A, light green - 090426, magenta - 090515, yellow - 100625A, orange - 110112A. b) These have a decay slope of  $0.5 \leq \alpha \leq 1$  in their “canonical” afterglows. Black - 051221A, purple - 060313, red - 060801, green - 061201, blue - 071227, orange - 080919, light blue - 090510, magenta - 100117A, yellow - 101219A. c) These do not have a shallow decay phase,  $\alpha > 1$ . Black - 050813, red - 050906, green - 051105, blue - 061217, light blue - 070209, magenta - 070429B, yellow - 070810B, purple - 090305A, dark pink - 100206A. d) These have a single shallow power law decline where  $\alpha \leq 1$ . Black - 050509B, red - 060502B, green - 070714A, blue - 090621B, light blue - 091109B, orange - 100628A.

the BAT-XRT lightcurves used in this analysis (the full process is described in Section 3.2.2). All the SGRB BAT-XRT lightcurves were fitted with multiple power laws from the final decay phase in the BAT prompt emission throughout the total X-ray afterglow using QDP<sup>1</sup> and LCFIT (written by P. Evans). These fits were then used to identify these with a “canonical” like lightcurve. An XRT spectrum was created for each region of the lightcurve using the automatic data products on the UK *Swift* Science Data Centre website (Evans et al., 2007, 2009). The SGRB lightcurves are shown in Figure 5.1. It was assumed that  $F_\nu \propto \nu^{-\beta} t^{-\alpha}$  where  $\beta = \Gamma - 1$  is the spectral index,  $\Gamma$  is the photon index ( $\Gamma_\gamma$  is the photon index measured using BAT and  $\Gamma_x$  is the photon index measured using XRT) and  $\alpha$  is the temporal index. The steep decay phase following the prompt emission was defined to have a power law decay of  $\alpha_1$ , after which the decay can break to a decay of  $\alpha_2$  and a further break to  $\alpha_3$ . In a small number of cases there are more than two breaks in the lightcurve and  $\alpha_3$  was defined to be the final decay slope. The “canonical” like GRBs were classified as having  $\alpha_2 \leq 1$  and the break time  $T_2$  is defined to be the end of the plateau. For GRB 060313, the “canonical” like lightcurve occurs after the flaring at 100 s after the trigger. The lightcurve fits for all the SGRBs in the sample are provided in Table 5.1. However, there are several caveats which need to be considered with the results in this Section and for the magnetar fits in Section 5.3.2. As SGRB afterglows are often faint and fade rapidly, these lightcurves and spectra can be poorly sampled giving large errors on the values in Table 5.1. This could also cause breaks in the lightcurve to be missed due to large bin sizes (bins typically contain 20 photons in PC mode data so bins could have long durations; Evans et al., 2007). Additionally, the *Swift* satellite slews to observe GRBs after detection, leading to a characteristic gap between the BAT data and the XRT data, and XRT can only observe for short windows giving further gaps in the lightcurves which could also hide features in the lightcurves.

21 SGRBs (~60%) have lightcurves which seem to be fairly well fit with a “canonical” template, suggesting ongoing central engine activity. It is hard to rule out “canonical” lightcurves in other cases (since the plateau phase could be missed by the sampling or lost due to the faintness of the afterglow), but the available data do not seem to require it. The break times of the “canonical” like SGRBs are typically occurring orders of magnitude earlier than for the LGRBs (as shown in Figure 5.2). Histograms showing the various SGRB decay slopes are shown in Figure 5.3 with the values for LGRBs, deter-

<sup>1</sup><https://heasarc.gsfc.nasa.gov/docs/software/ftools/others/qdp/qdp.html>

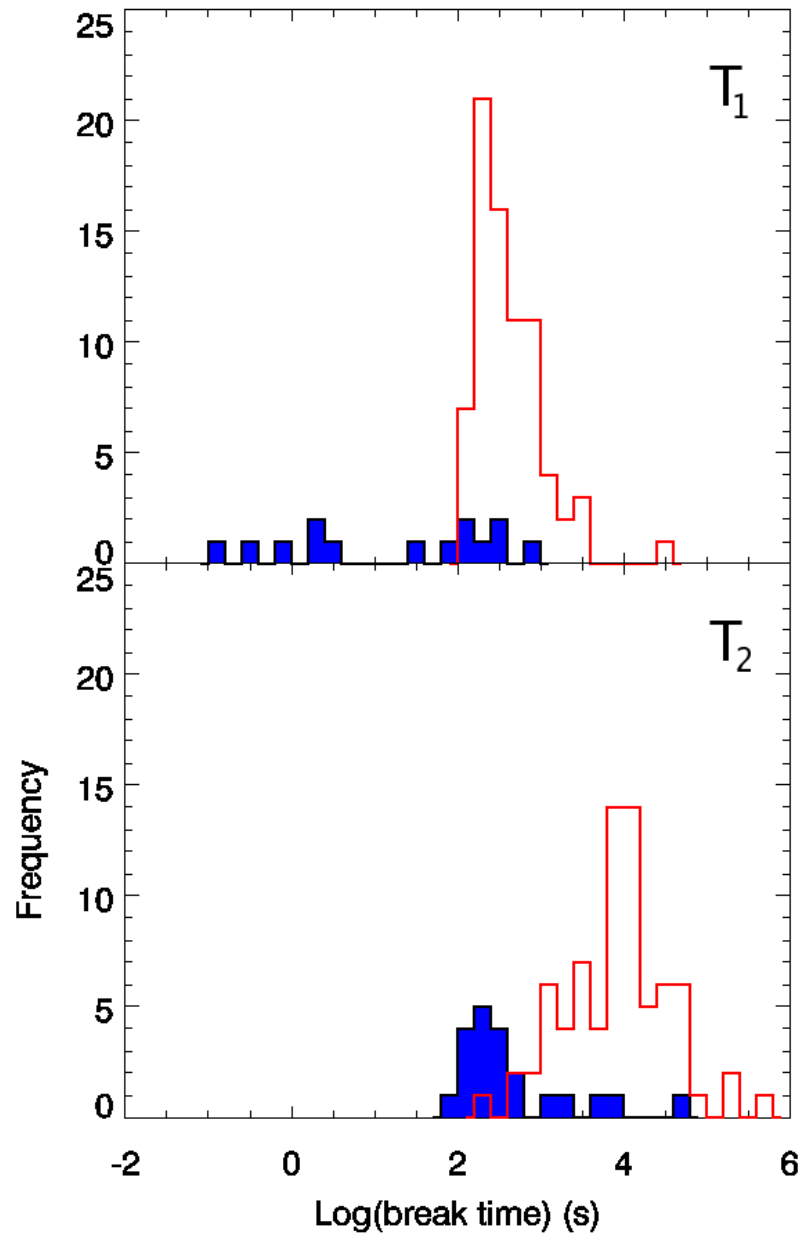


Figure 5.2: Histograms showing the break times for the “canonical” like lightcurves.  $T_1$  is the break from the steep decay phase to the plateau phase while  $T_2$  marks the end of the plateau. The blue filled histograms correspond to the SGRB sample used in this Chapter and overplotted in red are the LGRB values determined by Evans et al. (2009).

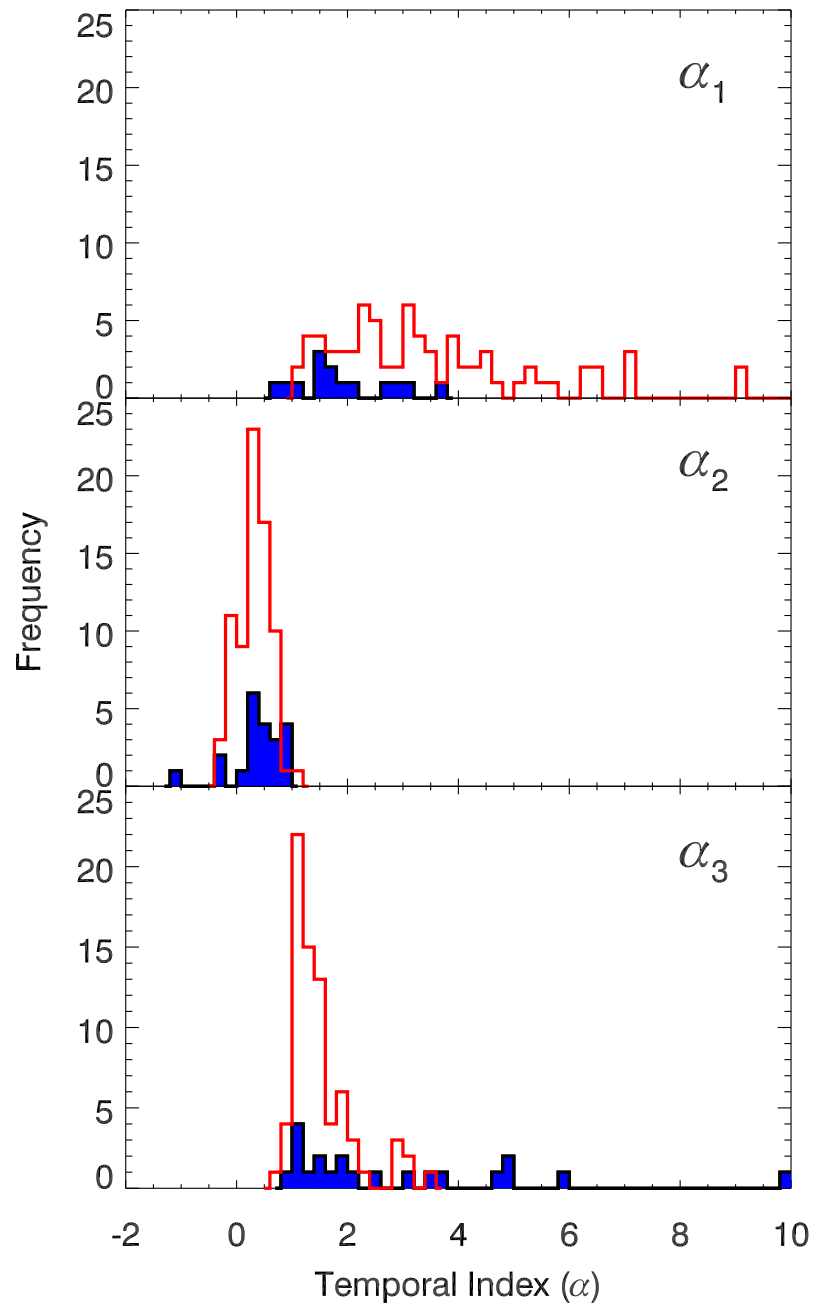


Figure 5.3: Histograms showing the temporal indices of the “canonical” like lightcurves.  $\alpha_1$  is the initial steep decay phase from the last decay in the prompt emission.  $\alpha_2$  are the plateau and shallow decay phase slopes.  $\alpha_3$  is the final afterglow decay slope. The blue filled histograms correspond to the SGRB sample used in this Chapter and overplotted in red are the LGRB values determined by Evans et al. (2009).

mined by Evans et al. (2009). The values for  $\alpha_1$  and  $\alpha_2$  are consistent with the LGRB sample, but the final decay phase ( $\alpha_3$ ) is typically steeper than for the LGRB counterparts. This category was further subdivided into those with plateaus where  $\alpha_2 \leq 0.5$  and  $0.5 \leq \alpha_2 \leq 1$ . This subdivision separates those with a clear plateau phase from those which may be a borderline case. 11 ( $\sim 30\%$ ) have  $\alpha_2 \leq 0.5$  and 10 ( $\sim 25\%$ ) with  $0.5 \leq \alpha_2 \leq 1$ . The remaining GRBs either do not have any shallow decay phase in their observed lightcurves ( $\sim 35\%$ ) or have a single, shallow power law decline with  $\alpha \leq 1$  ( $\sim 15\%$ ). In the following comparisons, the plateaus with  $\alpha_2 \leq 0.5$  (blue stars, the GRBs in Figure 5.1a) or  $0.5 \leq \alpha_2 \leq 1$  (green circles, the GRBs in Figure 5.1b) are considered in comparison to the final afterglow phase and compare these to GRBs which do not have a plateau phase (red triangles, the GRBs in Figure 5.1c) or an unbroken shallow decay (pink squares, the GRBs in Figure 5.1d).

The BAT fluence (15 – 150 keV) of these GRBs is plotted against their 0.3 – 10 keV flux at 100 s in Figure 5.4a. The GRBs which do not have a “canonical” lightcurve tend to have faint X-ray afterglows at 100 s ( $\leq 2 \times 10^{-11}$  erg cm $^{-2}$  s $^{-1}$ ) and relatively low fluences ( $\leq 2 \times 10^{-7}$  erg cm $^{-2}$ ). Those GRBs with a plateau tend to be clustered at somewhat higher fluences and their X-ray fluxes are significantly higher at 100 s ( $\sim 10^{-11}$  –  $10^{-9}$  erg cm $^{-2}$  s $^{-1}$ ). Figure 5.4b shows there is a wide variation in XRT flux at 100 s for SGRBs with similar prompt fluxes. The GRBs with a “canonical” like lightcurve have a systematically higher XRT flux at 100 s by several orders of magnitude. Although in many cases this could be a signal-to-noise issue, considering those with comparable fluences (e.g.  $10^{-7}$  erg cm $^{-2}$ ) suggests that the shallow decay phase is absent from these lightcurves rather than it simply being fainter than is detectable.

In Figure 5.5, the photon index is compared for the plateau and final decay phases. The GRBs get softer as they move into the afterglow decay phase as expected from typical spectral evolution. Additionally, the plateau phase tends to cluster around  $\Gamma \sim 2$ , similar to the plateau observed in LGRBs (O’Brien et al., 2006b; Dainotti et al., 2010) whereas there is more variation in  $\Gamma$  for the afterglow decay phase.

O’Brien et al. (2006) and Willingale et al. (2007) found that the prompt fluence is comparable to the plateau fluence for LGRBs. In order to compare this result to this SGRB sample, the average flux for the plateau phase was taken and multiplied by the time at which the decay broke to a more typical afterglow (assuming this component started at the initial trigger time) giving the 0.3 – 10 keV fluence.

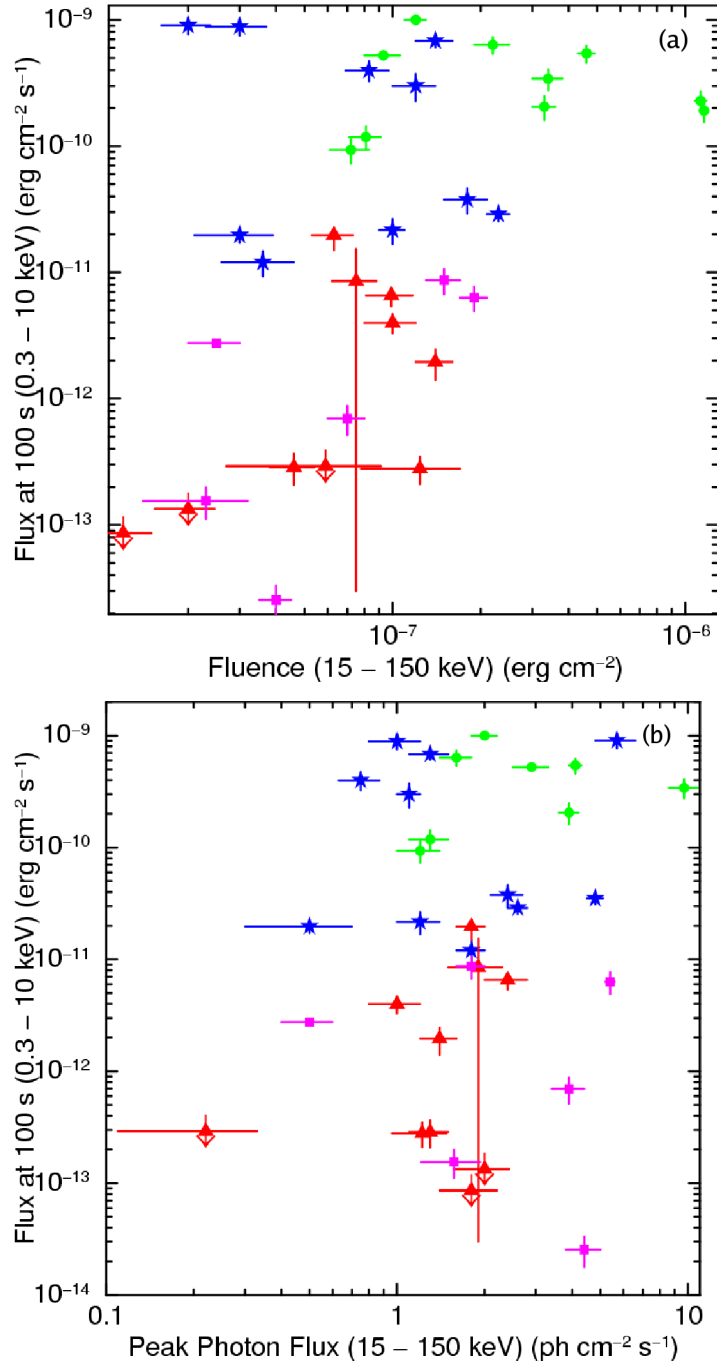


Figure 5.4: (a) The BAT fluence (15 – 150 keV) plotted against the XRT flux at 100 s (0.3 – 10 keV). Blue stars have  $\alpha_2 \leq 0.5$  and “canonical” lightcurve, green circles have  $0.5 \leq \alpha_2 \leq 1$  and “canonical” lightcurve, red triangles have  $\alpha_{1,2,3} > 1$  and pink squares have just a simple power law decline with  $\alpha_1 \leq 1$ . (b) The BAT peak photon flux (15-150 keV) against the XRT flux at 100 s (0.3 – 10 keV). Symbols are as in (a).

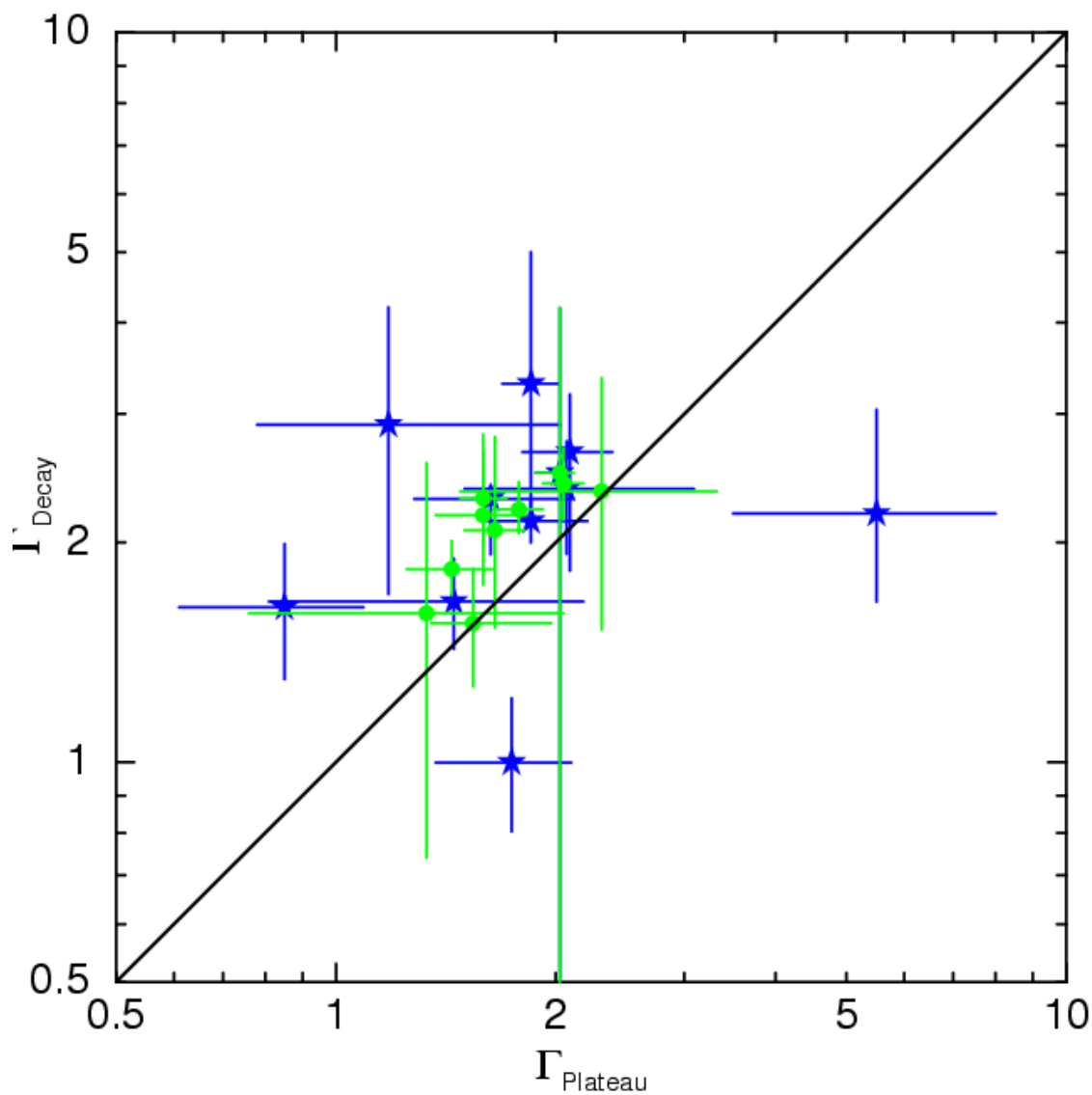


Figure 5.5: The photon index of the plateau or shallow decay phase in comparison to the final afterglow decay phase. Symbols are as Figure 5.4 and the black line shows where the photon indices would be equal.

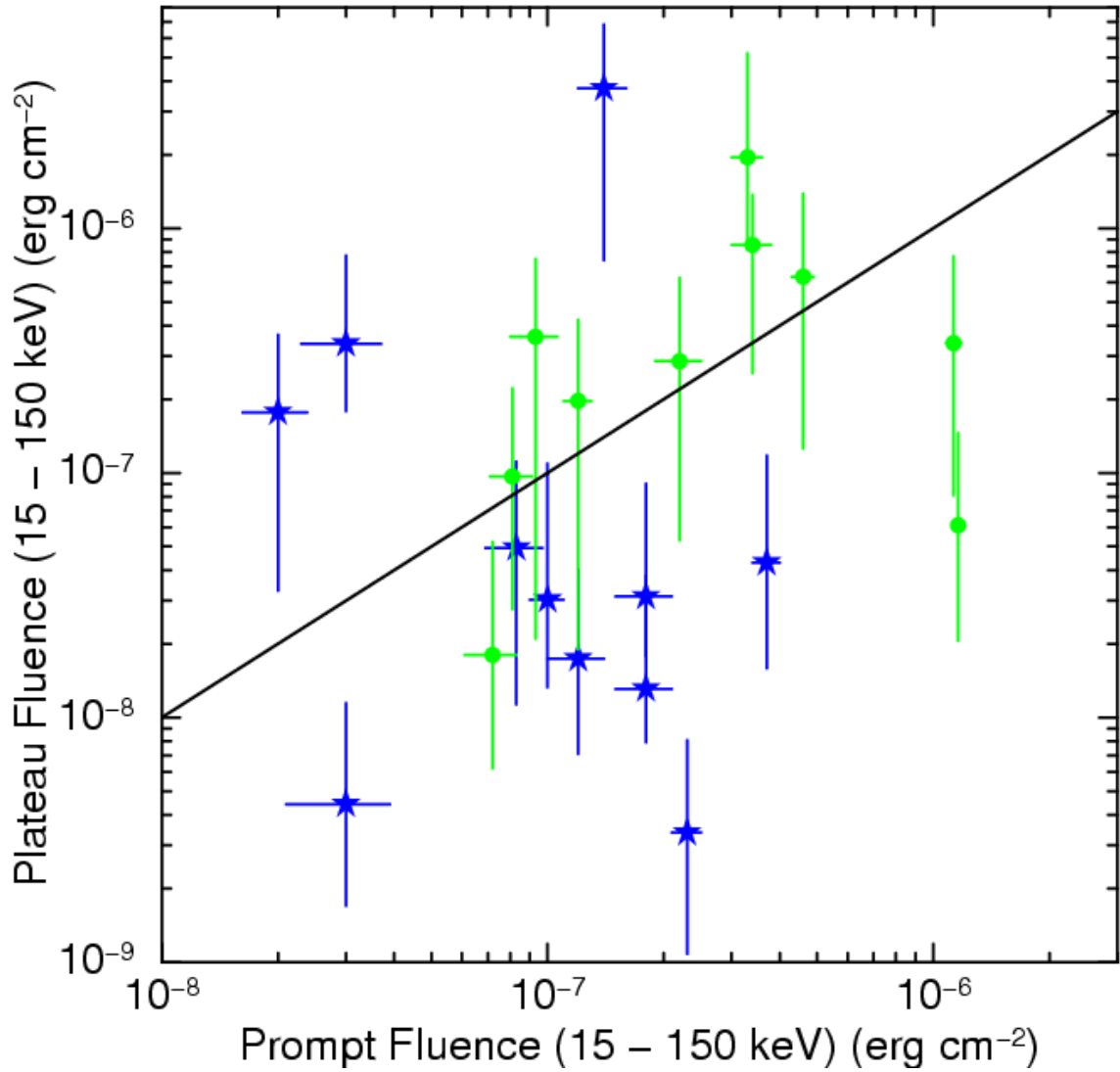


Figure 5.6: The prompt BAT 15 – 150 keV fluence in comparison to the shallow decay phase fluence shifted to the 15 – 150 keV energy band. Symbols are as defined in Figure 5.4 and the black line shows where the shallow decay phase fluence is equal to the prompt fluence.

This fluence was then converted to a 15 – 150 keV fluence using the spectral index. Figure 5.6 shows the prompt and plateau fluence are generally comparable, which is consistent with the result obtained for LGRBs. There are four significant outliers (GRBs 061201, 070724A, 080905A and 090515) whose plateaus are significantly more energetic than their prompt emission.

Figure 5.7 shows the spectral indices plotted against the temporal indices for the “canonical” like lightcurves. These show the same behaviour identified by Evans et al. (2009) for the “canonical” sample of GRBs. In particular Figure 5.7b shows evidence of energy injection during the plateau phase as described by Evans et al. (2009).

Dainotti et al. (2010) identified a correlation between the plateau phase luminosity and duration for LGRBs with a “canonical” lightcurve. Using redshifts where available or the average SGRB redshift ( $z \sim 0.72$ ) and a k-correction (Bloom, Frail, & Sari, 2001), the luminosity and restframe durations for the SGRB sample were calculated. These results are plotted in Figure 5.8 and the luminosity – duration correlation is identified. The SGRB sample gradient ( $-1.28 \pm 0.14$ ) is consistent with the LGRB sample ( $-1.06 \pm 0.28$ ; Dainotti et al., 2010). The SGRB plateau phases are typically more luminous and the plateau is shorter in duration than the LGRB counterparts. Cannizzo, Troja, & Gehrels (2011) argue that the relationship identified by Dainotti et al. (2010) is dominated by selection effects at  $z > 1.5$ . However, SGRBs are typically at lower redshift (the SGRBs with an observed redshift in this sample have an average redshift of  $z \sim 0.72$ ) so this sample lies well within the region which is not dominated by selection effects.

The plateau phases of GRB lightcurves are typically explained as ongoing central engine activity, for example on going accretion onto the central BH. However, ongoing accretion is problematic for NS-NS and NS-BH merger theories as there is insufficient surrounding material to maintain this accretion (Lee & Ramirez-Ruiz, 2007). Fallback accretion from material on highly eccentric orbits has been postulated to resolve this (Rosswog, 2007; Cannizzo, Troja, & Gehrels, 2011), however it is unclear how to produce the required reservoir of material at a fixed radius. In the remainder of this Chapter, it is suggested that the plateau phases could be powered by a magnetar formed via the merger of two NSs.

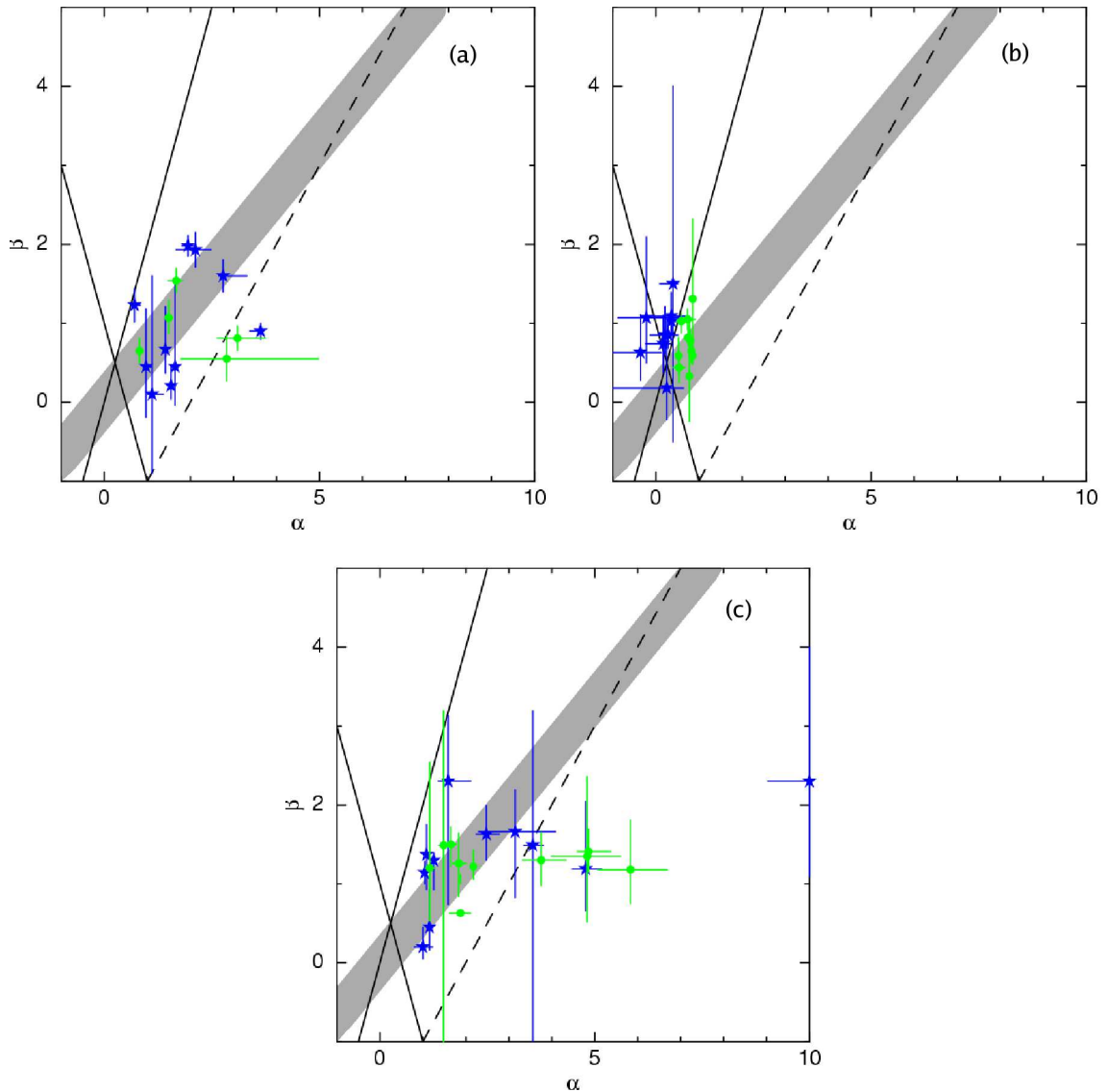


Figure 5.7: The spectral index  $\beta$  versus the temporal index  $\alpha$  for the three regimes of the “canonical” like lightcurves: (a) steep decay phase, (b) plateau phase and (c) standard afterglow phase. Where there is no XRT spectrum available for the steep decay phase, the BAT spectrum is used. All symbols are as defined in Figure 5.4 and the dashed black line shows where  $\alpha = \beta + 2$ . As in Evans et al. (2009), the afterglow closure relations predicted by Zhang & Mészáros (2004) are shown, the grey region is the slow cooling regime and the black lines are for the fast cooling regime.

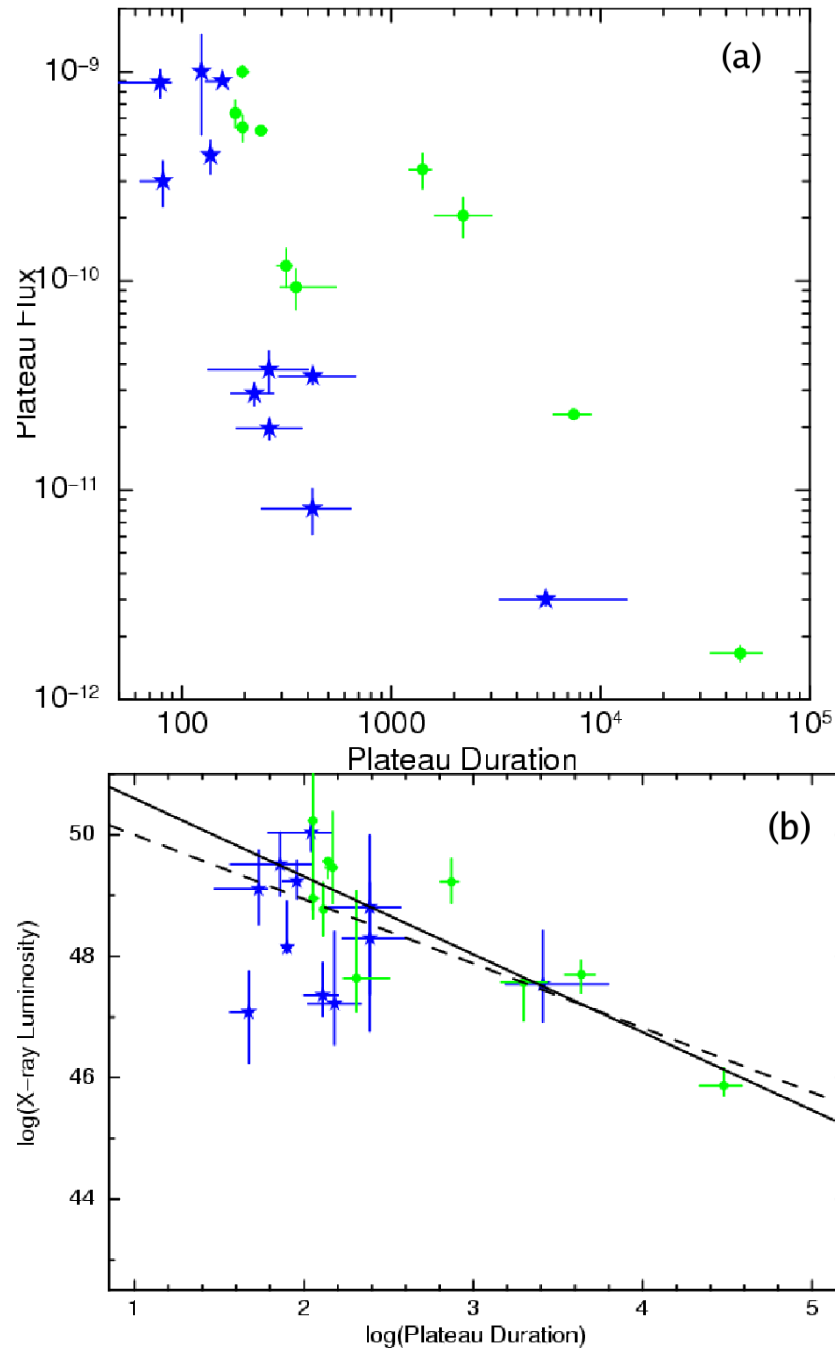


Figure 5.8: (a) The plateau phase flux versus the duration of this phase. Symbols are as defined in Figure 5.4. (b) The plateau phase luminosity, using published redshifts or the average redshift, versus the restframe duration of this phase. The black line shows the correlation between the luminosity and duration for the SGRB sample and the dashed line shows the relationship found by Dainotti et al. (2010).

## 5.3 Magnetar model

### 5.3.1 Theory

The model used here is as described in Zhang & Mészáros (2001) and was suggested to explain GRB 051221A with a long lived magnetar (Fan & Xu, 2006), for several LGRBs (Troja et al., 2007; Lyons et al., 2010; Yu, Cheng, & Cao, 2010) and for the short GRB 090515 (Rowlinson et al., 2010b). This model is consistent with the late time residual spin down phase driving a relativistic magnetar wind as described in Metzger et al. (2011). Equations 4.2, 4.3, 4.4 and 4.5 are used with an underlying powerlaw component. Previously, the plateau duration and luminosity were calculated and then input into the equations. In this Chapter, the equations are fit directly to the rest-frame light curves, taking into account the shape of the lightcurve (this is a comparable method to that used by Dall’Osso et al., 2011, who fitted a stable magnetar to the lightcurves of 4 LGRBs). The values of the magnetic field and spin period obtained were then used to derive the luminosity and plateau duration.

These equations apply to the electromagnetic dominated spin down regime, as the gravitational wave dominated regime would be extremely rapid and produce a negligible electromagnetic signal. The emission was assumed to be 100% efficient and isotropic as the beaming angle and emission mechanism remains very uncertain (see however section 3.4.4). The equations of vacuum dipole spin-down given above neglect the enhanced angular momentum losses due to neutrino-driven mass loss, which are important at early times after the magnetar forms (Metzger et al., 2011). Nevertheless, these expressions reasonably approximate the spin-down of very highly magnetized neutron stars of most relevance in this Chapter. Isotropic emission is also a reasonable assumption for relatively powerful magnetar winds, since (unlike following the collapse of a massive star) the magnetar outflow cannot be confined by the relatively small quantity of surrounding material expected following a NS merger or AIC (Bucciantini et al., 2011).

$$I_{45} \sim M_{1.4} R_6^2 \quad (5.1)$$

$$L_{em,49}(T) = L_{0,49} \left( 1 + \frac{T}{10^{-3} T_{em,3}} \right)^{-2} \quad (5.2)$$

Equation 5.1 was used to obtain the mass dependence of the model and equation 5.2 (from Zhang & Mészáros, 2001) to determine the time dependence of the magnetar emission.

The model also assumes there is a single power law decay,  $\alpha$ , underlying the magnetar component where  $F_\nu \propto \nu^{-\beta} t^{-\alpha}$ . This value has been set to  $\alpha = \Gamma_\gamma + 1$ , where  $\Gamma_\gamma$  is the photon index of the prompt emission, assuming that the decay slope is governed by the curvature effect (Kumar & Panaitescu, 2000), i.e. that the surrounding medium is very low density as might be expected for neutron star mergers. The normalisation of the power law decay fit is constrained using the last decay from the prompt emission. In a small number of cases, the decay slope is significantly different from prediction and  $\alpha$  was allowed to vary. If there is a steep decay phase after the plateau, it is assumed the magnetar has collapsed to a BH at the start of the steep decay (giving the Collapse Time parameter). The decay after collapse to a BH assumes the same powerlaw decay from the curvature effect, but starting at  $t_0 = t_{collapse}$ . It is important to note that the underlying lightcurve could be similar to other GRBs with a more complex afterglow light curve, but this work assumes that these are naked bursts (i.e. no surrounding ISM for neutron star mergers) and only the curvature effect is important.

This model was then written into a QDP COD file (COmponent Definition file, used to generate new models within QDP which can then be fitted to data sets) which, when fit to the restframe lightcurves, produces  $B_{p,15}$ ,  $P_{0,-3}$ ,  $R_6$ ,  $M_{1.4}$ ,  $\alpha$  and the collapse time where appropriate. In this analysis,  $M_{1.4}$  and  $R_6$  of the neutron star are constrained to be equal to 1 to reduce the number of free parameters in the model. This is consistent with the values determined by observations of three typical neutron stars:  $M \leq 2 M_\odot$  and  $7 \leq R \leq 11$  km (Özel, Baym, & Güver, 2010). As the model considers an extreme neutron star, it was noted that the mass and radius may differ from these results. However, this only has a relatively small affect on the magnetic fields and spin periods calculated (as shown in Chapter 4 and Rowlinson et al., 2010b) and so it is a reasonable approximation as this Chapter just demonstrates

the plausibility of the magnetar model fitting the SGRB lightcurves.

### 5.3.2 SGRBs fitted with the magnetar model

The selected GRBs are those SGRBs ( $T_{90} \leq 2$  s) with sufficient data to produce multiple data points in the X-ray lightcurve. This selection criteria excludes SGRBs with extended emission, which may share a common progenitor to SGRBs but this is still uncertain. 80% of SGRBs in the sample have been investigated for evidence of extended emission by Norris, Gehrels, & Scargle (2010) but only GRB 071227 has this component. The sample are listed in Table 5.2 and their magnetar fits are given in Table 5.3. The magnetar candidates fit the model well, the possible candidates are GRBs which may fit the magnetar model if assumptions are made and the other SGRBs are those which do not fit the model. The BAT-XRT lightcurves in the energy band 0.3 – 10 keV are created and then shifted into the restframe 1-10000 keV luminosity lightcurve using a k-correction (Bloom, Frail, & Sari, 2001) and the method described in Section 3.2.2. If no redshift is known the mean SGRB redshift is used,  $z = 0.72$ . These lightcurves were then fitted using the magnetar model, as shown in Figures 5.9. There are two potential outcomes: a stable long lived magnetar which does not collapse to form a BH and an unstable magnetar which collapses forming a BH after a few 100 s. The following Sections compare the properties of the stable magnetars (blue stars in the figures), the unstable magnetars which collapse to form a BH (green circles) and the SGRBs which do not fit the model (red triangles).

The lightcurves are fit over plateau region and the power law decay, including the last decay in the prompt emission and the X-ray observations. This removes the effect of the poorly understood flaring prompt emission not modeled by this method. The reduced  $\chi^2_{\nu}$  is determined for each fit and is determined to be a good fit to the model if  $\chi^2_{\nu} < 3$ . Some of the fits were poor, but with visual inspection this is sometimes associated with flares on the plateau or steep decay, for example GRB 100117A.

In Table 5.3 provides the derived plateau luminosity and plateau duration calculated using the magnetic field strengths, the spin periods and equations 4.2 and 4.3.

When fitting GRB 060313, which may show evidence of late time central engine activity (Roming et al., 2006), it was noted that the model fits part of the lightcurve extremely well. In this case, observe-

Table 5.2: Properties of the SGRB sample, the groups are identified using the fits provided in Table 5.3. The magnetar candidates fit the model well, the possible candidates are GRBs which may fit the magnetar model if certain assumptions are made about beaming or redshift and the other SGRBs are those which have a statistically poor fit to the magnetar model. These observed quantities, including host galaxy associations, offsets and optical afterglow detections, are from published papers and GCNs (references listed below), host offsets are quoted with errors if published. When the redshift is not known, the average redshift 0.72 was used and this is shown using brackets.

<sup>(1)</sup>Cummings et al. (2005); Soderberg et al. (2006) <sup>(2)</sup>Markwardt et al. (2006b); Roming et al. (2006) <sup>(3)</sup>Sato et al. (2006); Cucchiara et al. (2006) <sup>(4)</sup>Krimm et al. (2007); Perley et al. (2008) <sup>(5)</sup>Cummings et al. (2008b) <sup>(6)</sup>Barthelmy et al. (2008c) <sup>(7)</sup>Sato et al. (2009); Antonelli et al. (2009); Xin et al. (2011) <sup>(8)</sup>Ukwatta et al. (2009); de Pasquale et al. (2010); McBreen et al. (2010) <sup>(9)</sup>Barthelmy et al. (2009a); Rowlinson et al. (2010b)

GRB	z	T <sub>90</sub> (s)	Γ <sub>γ</sub>	Fluence (10 <sup>-7</sup> erg cm <sup>-2</sup> s <sup>-1</sup> )	Host	Host offset (arcsec)	Optical Afterglow
Magnetar candidates							
051221A <sup>(1)</sup>	0.55	1.4±0.2	1.39±0.06	11.6±0.4	y	0.12±0.04	Y
060313 <sup>(2)</sup>	(0.72)	0.7±0.1	0.71±0.07	11.3±0.5	?	0.4±0.6	Y
060801 <sup>(3)</sup>	1.13	0.5±0.1	0.47±0.24	0.81±0.10	?	2.4±2.4	N
070809 <sup>(4)</sup>	0.219	1.3±0.1	1.69±0.22	1.00±0.10	y	20	Y
080426 <sup>(5)</sup>	(0.72)	1.7±0.4	1.98±0.13	3.7±0.3	n	-	N
081024 <sup>(6)</sup>	(0.72)	1.8±0.6	1.23±0.21	1.2±0.2	n	-	N
090426 <sup>(7)</sup>	2.6	1.2±0.3	1.93±0.22	1.8±0.3	y	18	Y
090510 <sup>(8)</sup>	0.9	0.3±0.1	0.98±0.20	3.4±0.4	y	1	Y
090515 <sup>(9)</sup>	(0.72)	0.036±0.016	1.6±0.2	0.21±0.04	n	-	Y

Table 5.2: Continued:

<sup>(1)</sup>Baumgartner et al. (2010) <sup>(2)</sup>Krimm et al. (2010); Chornock & Berger (2011) <sup>(3)</sup>Sato et al. (2005b); La Parola et al. (2006) <sup>(4)</sup>Markwardt et al. (2006c); Stratta et al. (2007) <sup>(5)</sup>Barthelmy et al. (2007) <sup>(6)</sup>Krimm et al. (2008b) <sup>(7)</sup>Cummings et al. (2008a); Rowlinson et al. (2010a) <sup>(8)</sup>Krimm et al. (2009) <sup>(9)</sup>Barthelmy et al. (2010); Tanvir & Levan (2010b) <sup>(10)</sup>Barthelmy, Sakamoto & Stamatikos (2011); Levan, Tanvir & Baker (2011)

GRB	z	T <sub>90</sub> (s)	Γ <sub>γ</sub>	Fluence (10 <sup>-7</sup> erg cm <sup>-2</sup> s <sup>-1</sup> )	Host	Host offset (arcsec)	Optical Afterglow
Magnetar candidates							
100702A <sup>(1)</sup>	(0.72)	0.16±0.03	1.54±0.15	1.2±0.1	n	-	N
101219A <sup>(2)</sup>	0.718	0.6±0.2	0.63±0.09	4.6±0.3	y	-	N
Possible candidates							
051210 <sup>(3)</sup>	(0.72)	1.4±0.2	1.1±0.3	0.83±0.14	?	2.8±2.9	N
061201 <sup>(4)</sup>	0.111	0.8±0.1	0.81±0.15	3.3±0.3	?	17	Y
070714A <sup>(5)</sup>	(0.72)	2.0±0.3	2.6±0.2	1.5±0.2	n	-	N
080702A <sup>(6)</sup>	(0.72)	0.5±0.2	1.34±0.42	0.36±0.10	n	-	N
080905A <sup>(7)</sup>	0.122	1.0±0.1	0.85±0.24	1.4±0.2	y	9	Y
090621B <sup>(8)</sup>	(0.72)	0.14±0.04	0.82±0.23	0.7±0.1	n	-	N
100625A <sup>(9)</sup>	(0.72)	0.33±0.03	0.9±0.1	2.3±0.2	y	0±1.8	N
110112A <sup>(10)</sup>	(0.72)	0.5±0.1	2.14±0.46	0.3±0.1	y	-	Y

Table 5.2: Continued:

<sup>(1)</sup>Barthelmy et al. (2005c); Gehrels et al. (2005) <sup>(2)</sup>Parsons et al. (2007); Berger et al. (2009); Kocevski et al. (2010) <sup>(3)</sup>Sato et al. (2007b); Caito et al. (2010); D’Avanzo et al. (2009) <sup>(4)</sup>Baumgartner et al. (2008); Immler & Holland (2008); Covino et al. (2008) <sup>(5)</sup>Markwardt et al. (2009); Levan et al. (2009); Malesani et al. (2009) <sup>(6)</sup>Markwardt et al. (2010); Levan et al. (2010); Fong, Berger, & Fox (2010)

GRB	$z$	$T_{90}$ (s)	$\Gamma_{\gamma}$	Fluence ( $10^{-7}$ erg cm $^{-2}$ s $^{-1}$ )	Host	Host offset (arcsec)	Optical Afterglow
Other SGRBs							
050509B <sup>(1)</sup>	0.23	0.024±0.009	1.5±0.4	0.23±0.09	y	17.9±3.4	N
070724A <sup>(2)</sup>	0.46	0.40±0.04	1.81±0.33	0.30±0.07	y	0.7±2.1	N
071227 <sup>(3)</sup>	0.38	1.8±0.4	0.99±0.22	2.2±0.3	y	3.1	Y
080919 <sup>(4)</sup>	(0.72)	0.6±0.1	1.10±0.26	0.72±0.11	?	-	Y
091109B <sup>(5)</sup>	(0.72)	0.30±0.03	0.71±0.13	1.9±0.2	?	8	Y
100117A <sup>(6)</sup>	(0.72)	0.30±0.05	0.88±0.22	0.93±0.13	y	0.6	Y

Table 5.3: The sample of short GRBs used with their magnetar fits.  $E_{iso}$  is calculated using the fluences and redshifts in Table 5.2 and a k-correction (Bloom, Frail, & Sari, 2001). The values for  $\alpha$  are input into the model unless they are bracketed - in this case the values are fit within the model. If there is a steep decay phase, it is assumed that the magnetar collapses to form a BH and the model determines the collapse time. The values for  $P_{-3}$  and  $B_{15}$  are fitted from the model assuming isotropic emission. Also provided are  $\chi^2_\nu$  for each GRB fitted. Using the values of  $P_{-3}$  and  $B_{15}$  obtained from the model, the plateau luminosity and duration are derived using equations 4.2 and 4.3. The derived plateau duration describes the point at which the X-ray emission from the magnetar starts to turn over from the plateau phase to a powerlaw decay phase.

GRB	$E_{iso}$ (erg)	$P_{-3}$	$B_{15}$	$\alpha_1 = \Gamma_\gamma + 1$	Collapse time (s)	$\chi^2_\nu$	Plateau Luminosity (erg s $^{-1}$ )	Plateau Duration (s)
Magnetar candidates								
051221A	$1.83^{+0.45}_{-0.35} \times 10^{52}$	$8.97^{+0.34}_{-0.31}$	$2.10^{+0.16}_{-0.15}$	$(1.41^{+0.03}_{-0.04})$	-	1.5	$6.8^{+0.9}_{-0.8} \times 10^{45}$	$37300^{+6400}_{-5800}$
060313	$3.12^{+1.06}_{-0.79} \times 10^{53}$	$4.45^{+0.17}_{-0.16}$	$4.19^{+0.28}_{-0.28}$	1.71	-	0.7	$4.5^{+0.5}_{-0.5} \times 10^{47}$	$2310^{+350}_{-340}$
060801	$1.17^{+1.79}_{-0.71} \times 10^{53}$	$3.70^{+0.29}_{-0.22}$	$21.40^{+3.75}_{-3.27}$	1.47	326	2.1	$2.5^{+0.7}_{-0.6} \times 10^{49}$	$61^{+24}_{-20}$
070809	$8.87^{+9.06}_{-3.48} \times 10^{49}$	$5.71^{+1.33}_{-1.17}$	$15.34^{+1.32}_{-1.19}$	$(1.70^{+0.11}_{-0.08})$	-	1.2	$2.2^{+1.1}_{-0.9} \times 10^{48}$	$284^{+100}_{-88}$
080426	$3.48^{+0.67}_{-0.24} \times 10^{51}$	$9.25^{+0.42}_{-0.37}$	$13.37^{+2.32}_{-1.72}$	2.98	-	1.7	$2.4^{+0.6}_{-0.5} \times 10^{47}$	$980^{+350}_{-260}$
081024	$5.65^{+7.53}_{-3.16} \times 10^{51}$	$3.02^{+0.45}_{-0.32}$	$32.09^{+4.39}_{-5.82}$	2.33	125	2.9	$1.2^{+0.4}_{-0.4} \times 10^{50}$	$18^{+7}_{-8}$
090426	$3.98^{+1.30}_{-0.03} \times 10^{52}$	$2.38^{+0.10}_{-0.09}$	$5.78^{+1.10}_{-1.02}$	2.93	-	1.9	$1.0^{+0.3}_{-0.3} \times 10^{49}$	$350^{+140}_{-130}$
090510	$5.76^{+6.86}_{-3.10} \times 10^{52}$	$2.08^{+0.04}_{-0.04}$	$5.61^{+0.29}_{-0.26}$	1.98	-	2.0	$1.7^{+0.1}_{-0.1} \times 10^{49}$	$280^{+31}_{-28}$
090515	$3.44^{+3.55}_{-1.55} \times 10^{50}$	$2.30^{+0.06}_{-0.06}$	$13.75^{+1.28}_{-1.23}$	2.60	176	2.2	$6.7^{+1.0}_{-0.9} \times 10^{49}$	$58^{+11}_{-11}$
100702A	$2.28^{+1.46}_{-0.80} \times 10^{51}$	$3.02^{+0.15}_{-0.18}$	$22.94^{+1.59}_{-1.73}$	2.54	167	3.0	$6.4^{+0.9}_{-1.0} \times 10^{49}$	$35^{+6}_{-7}$
101219A	$1.69^{+0.79}_{-0.54} \times 10^{53}$	$2.09^{+0.12}_{-0.10}$	$6.24^{+1.06}_{-0.87}$	$(1.25^{+0.03}_{-0.03})$	138	2.5	$2.0^{+0.5}_{-0.4} \times 10^{49}$	$230^{+83}_{-68}$

Table 5.3: Continued:

GRB	$E_{iso}$ (erg)	$P_{-3}$	$B_{15}$	$\alpha_1 = \Gamma_\gamma + 1$	Collapse time (s)	$\chi_\nu^2$	Plateau Luminosity (erg s $^{-1}$ )	Plateau Duration (s)
Possible candidates								
051210	$5.98^{+13.5}_{-4.05} \times 10^{51}$	$0.67^{+0.06}_{-0.07}$	$5.01^{+0.95}_{-1.07}$	2.1	225	2.5	$1.2^{+0.3}_{-0.5} \times 10^{51}$	$37^{+15}_{-18}$
061201	$1.42^{+1.67}_{-0.69} \times 10^{51}$	$16.13^{+0.65}_{-0.59}$	$21.07^{+1.95}_{-1.59}$	1.57	-	0.9	$6.6^{+1.0}_{-0.8} \times 10^{46}$	$1200^{+240}_{-200}$
070714A	$3.28^{+3.08}_{-1.48} \times 10^{51}$	$12.99^{+1.29}_{-1.26}$	$19.48^{+5.29}_{-4.78}$	3.60	-	2.9	$1.3^{+0.6}_{-0.5} \times 10^{47}$	$910^{+530}_{-480}$
080702A	$1.20^{+4.90}_{-0.90} \times 10^{51}$	$21.80^{+2.24}_{-1.78}$	$58.23^{+19.68}_{-13.42}$	2.34	-	0.7	$1.5^{+0.8}_{-0.5} \times 10^{47}$	$290^{+200}_{-140}$
080905A	$6.16^{+12.3}_{-4.03} \times 10^{50}$	$14.12^{+1.84}_{-1.60}$	$74.85^{+14.69}_{-21.38}$	$(0.80^{+0.05}_{-0.09})$	274	1.4	$1.4^{+0.5}_{-0.7} \times 10^{48}$	$73^{+34}_{-45}$
090621B	$1.31^{+2.07}_{-0.80} \times 10^{52}$	$76.08^{+15.44}_{-9.84}$	$65.95^{+30.57}_{-19.04}$	$(4.73^{+1.34}_{-1.22})$	-	2.5	$1.3^{+1.0}_{-0.6} \times 10^{45}$	$2700^{+2800}_{-1700}$
100625A	$3.27^{+1.76}_{-1.15} \times 10^{52}$	$25.48^{+3.87}_{-4.04}$	$186.69^{+34.11}_{-27.49}$	$(2.83^{+0.63}_{-0.58})$	-	2.4	$8.3^{+3.3}_{-3.1} \times 10^{47}$	$38^{+18}_{-17}$
110112A	$2.91^{+5.85}_{-0.17} \times 10^{50}$	$19.55^{+1.35}_{-1.14}$	$28.09^{+5.09}_{-3.82}$	3.14	-	2.7	$5.4^{+1.6}_{-1.2} \times 10^{46}$	$990^{+390}_{-290}$
Other SGRBs								
050509B	$3.82^{+16.9}_{-2.87} \times 10^{49}$	$87.43^{+27.17}_{-19.63}$	$23.81^{+17.85}_{-13.08}$	2.5	-	4.6	$9.7^{+11.9}_{-8.7} \times 10^{43}$	$28000^{+45000}_{-33000}$
070724A	$1.13^{+1.87}_{-0.40} \times 10^{50}$	$1.39^{+0.24}_{-0.12}$	$27.61^{+1.28}_{-1.19}$	$(1.25^{+0.04}_{-0.04})$	90	5.7	$2.0^{+0.7}_{-0.3} \times 10^{51}$	$5^{+2}_{-1}$
071227	$6.07^{+9.45}_{-3.67} \times 10^{51}$	$3.40^{+0.19}_{-0.16}$	$31.61^{+1.47}_{-1.59}$	$(1.21^{+0.03}_{-0.02})$	170	4.1	$7.5^{+1.0}_{-0.8} \times 10^{49}$	$24^{+3}_{-3}$
080919	$5.18^{+9.34}_{-3.26} \times 10^{51}$	$18.15^{+1.63}_{-1.34}$	$79.91^{+35.79}_{-27.28}$	2.10	320	7.3	$5.9^{+3.9}_{-3.0} \times 10^{47}$	$110^{+97}_{-74}$
091109B	$5.25^{+3.95}_{-2.27} \times 10^{52}$	$21.67^{+2.43}_{-1.89}$	$14.59^{+4.14}_{-3.53}$	$(3.11^{+0.47}_{-0.46})$	-	4.0	$9.7^{+4.4}_{-3.7} \times 10^{45}$	$4500^{+2800}_{-2300}$
100117A	$1.42^{+2.08}_{-0.84} \times 10^{52}$	$1.29^{+0.12}_{-0.16}$	$13.48^{+0.92}_{-0.82}$	1.88	-	7.0	$6.6^{+1.4}_{-1.7} \times 10^{50}$	$19^{+4}_{-5}$

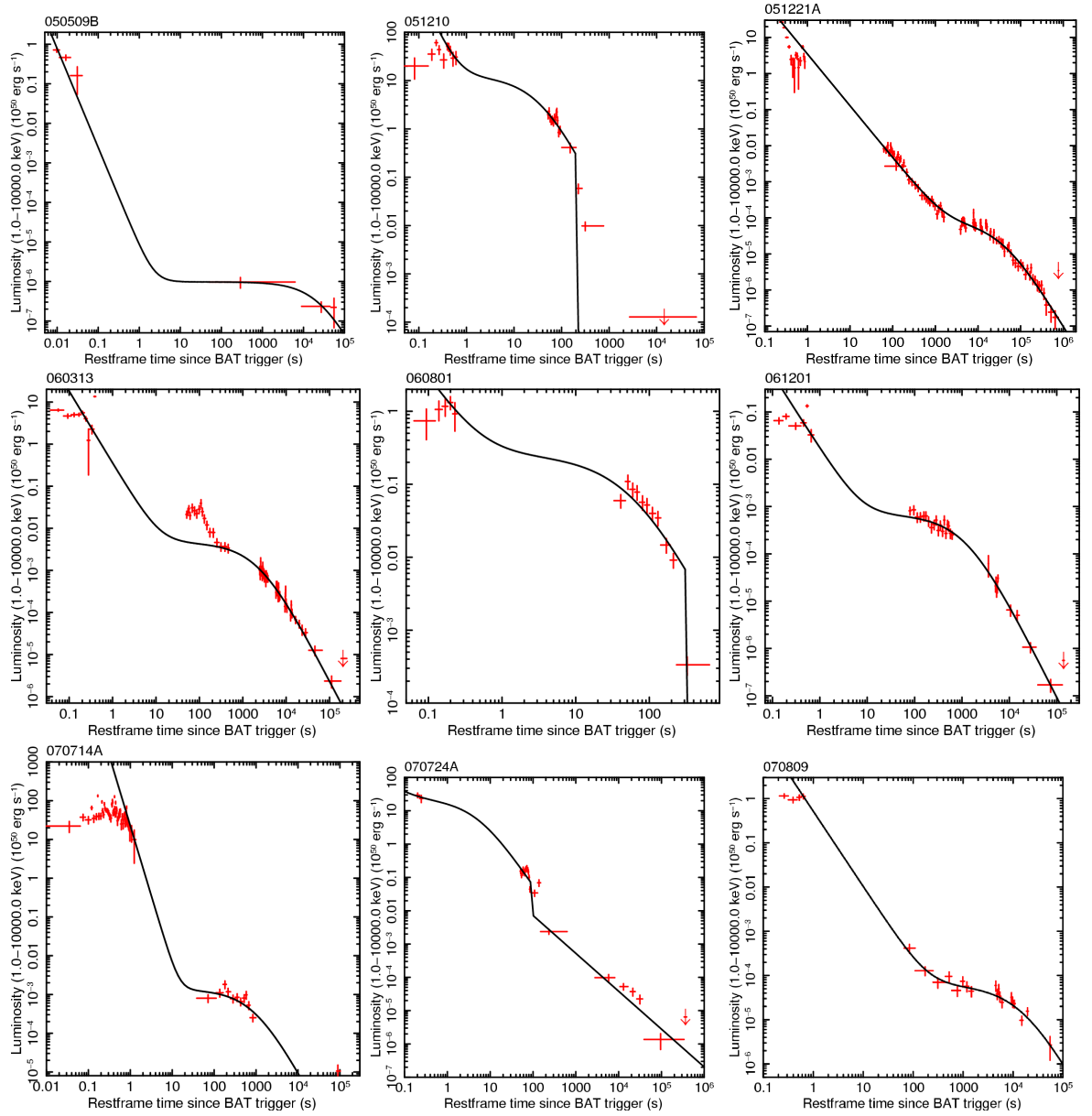


Figure 5.9: SGRB lightcurves fit with the magnetar model.

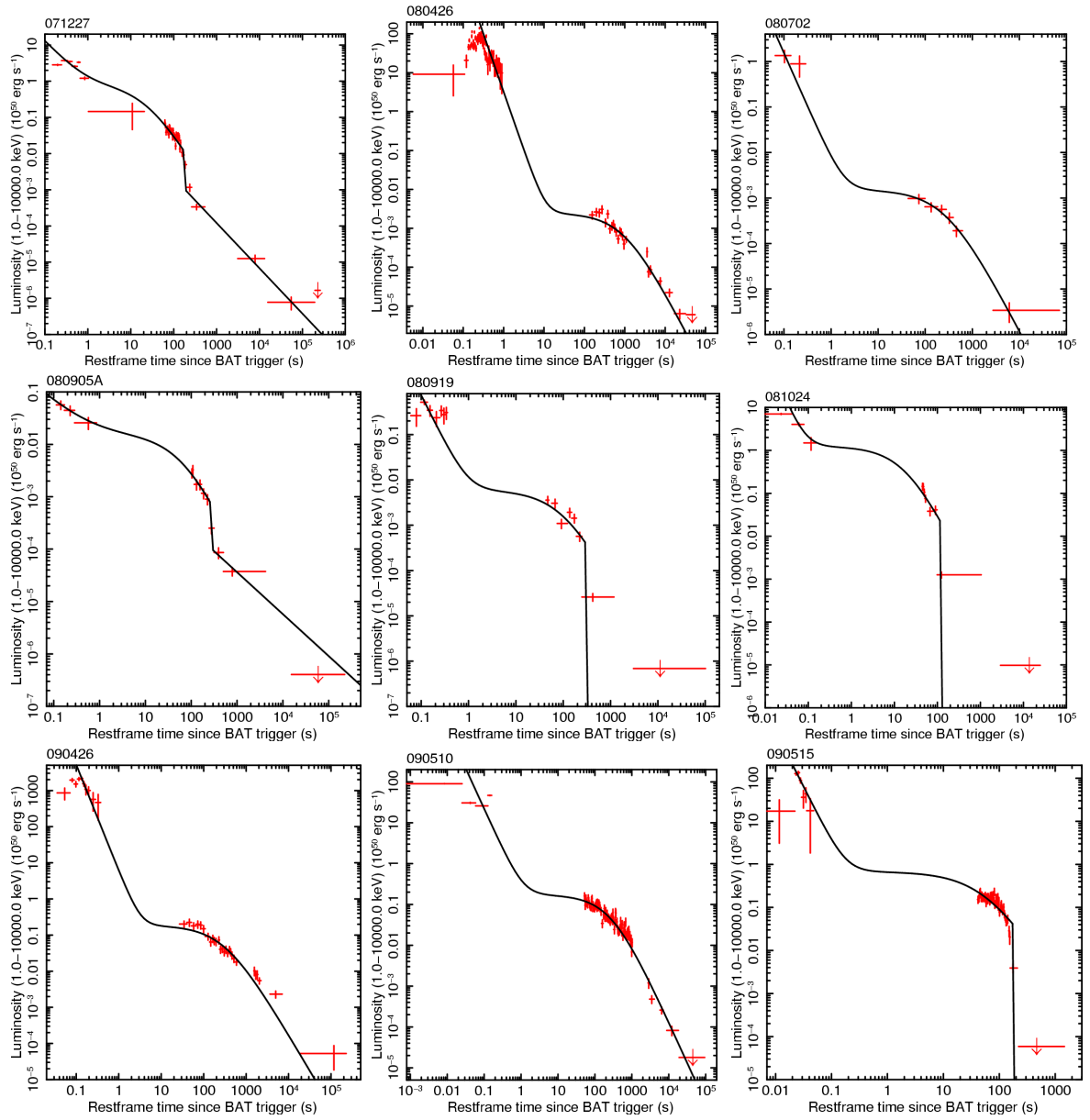


Figure 5.9: Continued:

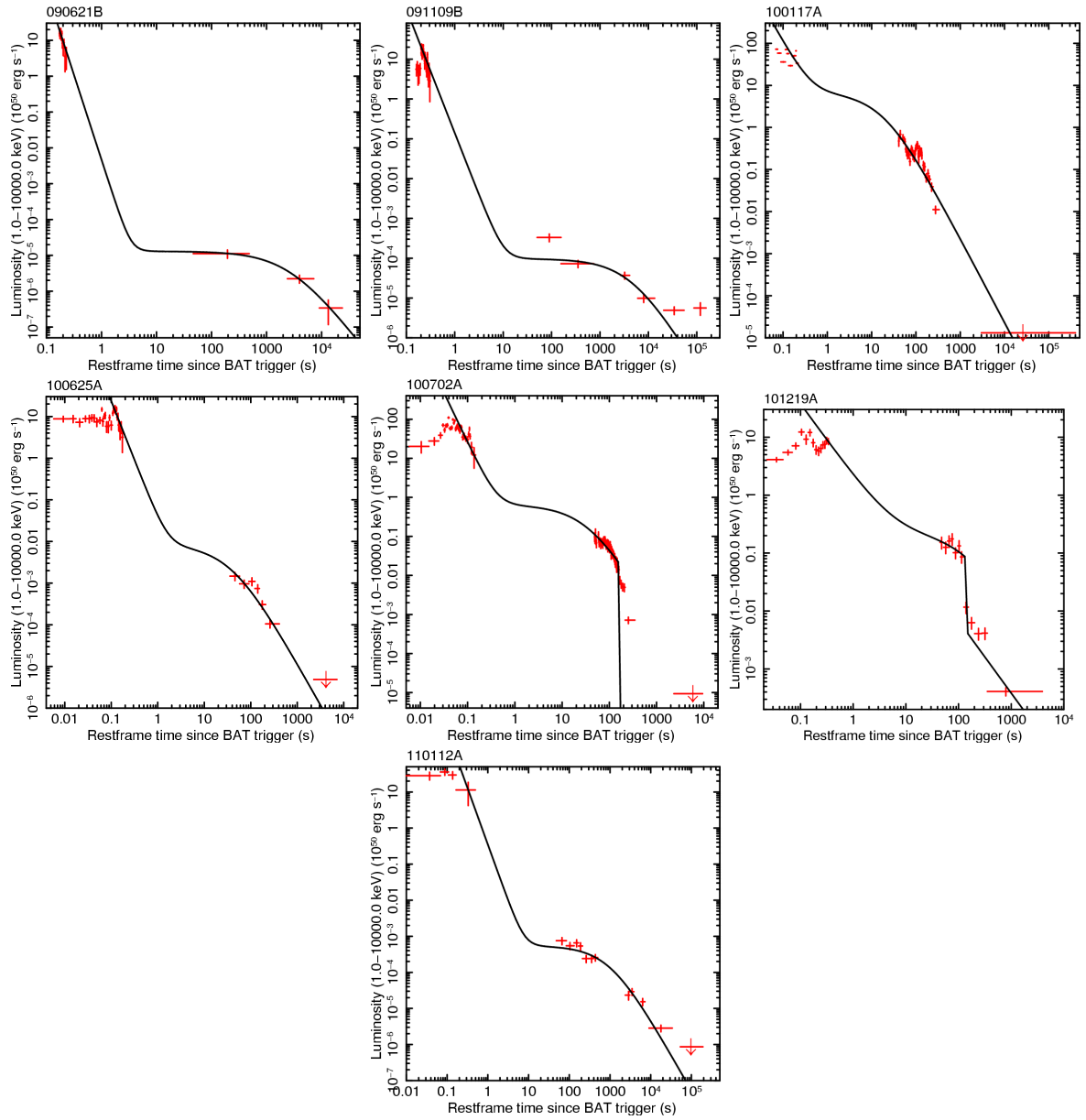


Figure 5.9: Continued:

tions between 50 – 200 s (the initial X-ray data) were ignored in the fit as this duration appears to be dominated by flares. If these data are included in the fit, then the magnetar model does not fit the data well. The model fits well to GRB 090515 predicting values similar to those given in Rowlinson et al. (2010b).

### 5.3.3 Analysis

Figure 5.10 shows the spin periods and magnetic fields determined for the sample of GRBs assuming isotropic emission. Eleven of the SGRBs had a good fit and lie within the correct region of the magnetic field strength and spin periods, these are the magnetar candidates listed in Table 5.2. Eight GRBs have good fits to the model but lie outside the allowed region (the possible candidates in Table 5.2). These GRBs may be in the allowed (unshaded) region if they were at a higher redshift as shown in Rowlinson et al. (2010b). Additionally, this region is defined using angular momentum conservation during the merger of two NSs (Usov, 1992) and is not a physically forbidden region. Therefore, the candidates with spin periods  $>10$  ms may remain good candidate magnetars. GRB 051210 is included in the possible candidates list as it is spinning faster than is allowed in the models, but it is worth noting that if the NS formed had a mass of  $2.1M_{\odot}$  then it would reside within the allowed region, as more massive NSs are able to spin at a faster rate. As GRB 051210 is a candidate which may collapse to form a BH, the higher mass solution is supported.

### Prompt and X-ray Properties

There are no obvious trends between the prompt properties and the derived values for the magnetic field and spin periods, so the magnetar model is unlikely to be strongly dependent on the prompt emission mechanism. In Figure 5.11, the prompt properties for the sample are shown and there are no obvious relationships.

Some of the model fits would predict a fairly shallow decay from the prompt emission, for example GRB 060801, which may lie above the BAT threshold. In these cases, it might be expected that extended emission is detectable in the prompt emission and this was not observed, so these fits may be

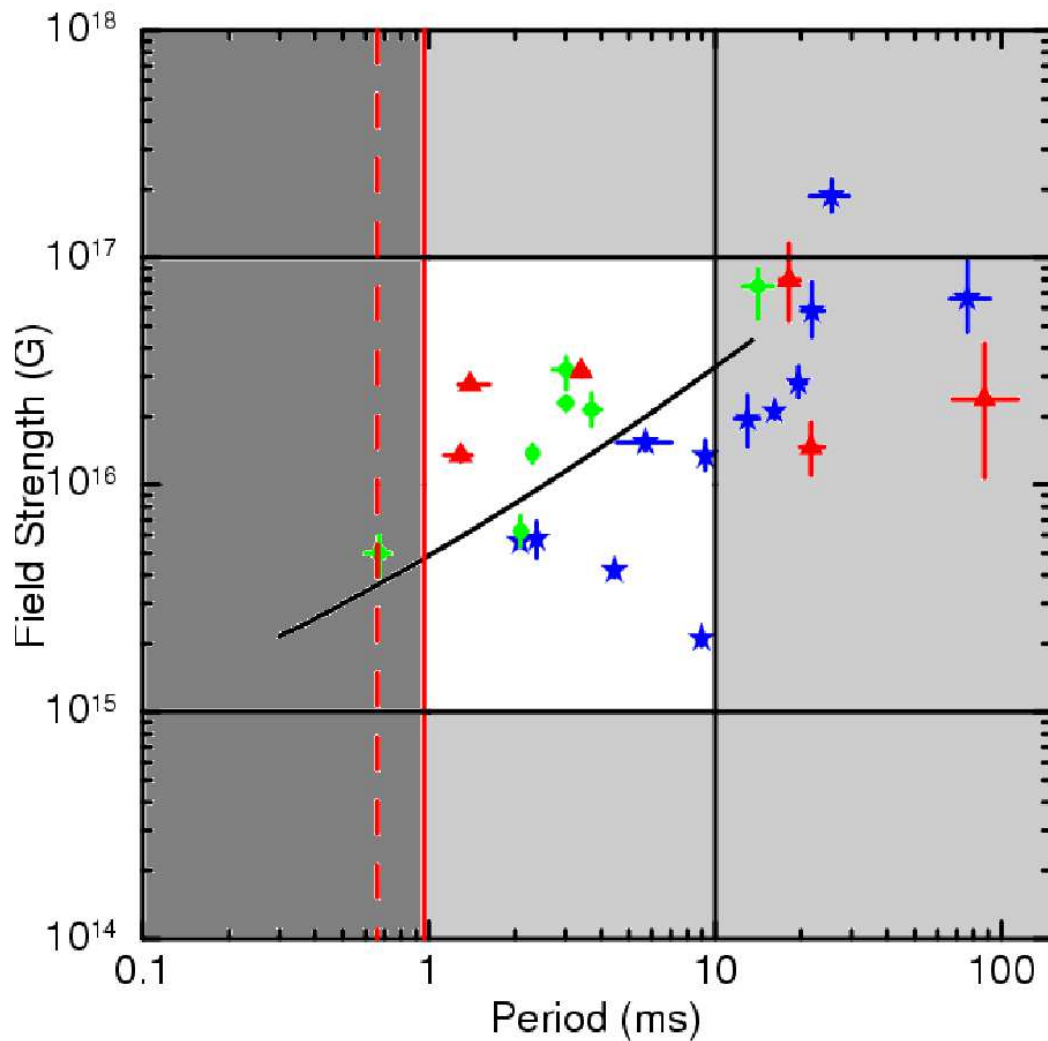


Figure 5.10: A graph showing the magnetic field and spin period of the magnetar fits produced. The solid (dashed) red line and dark shaded area represent the spin break up period for a collapsar (binary merger) progenitor (Lattimer & Prakash, 2004) and the unshaded region shows the allowed region for an unstable pulsar, as defined in (Lyons et al., 2010; Rowlinson et al., 2010b). The initial rotation period needs to be  $\leq 10$  ms (Usov, 1992) and the lower limit for the magnetic field is  $\geq 10^{15}$  G (Thompson, 2007). The black curve is the result predicted for GRB 090515 from Rowlinson et al. (2010b). Blue stars = good fit to the magnetar model with a stable magnetar, Green circles = good fit to the model with an unstable magnetar which collapses to form a BH, and Red triangles = poor fit to the model.

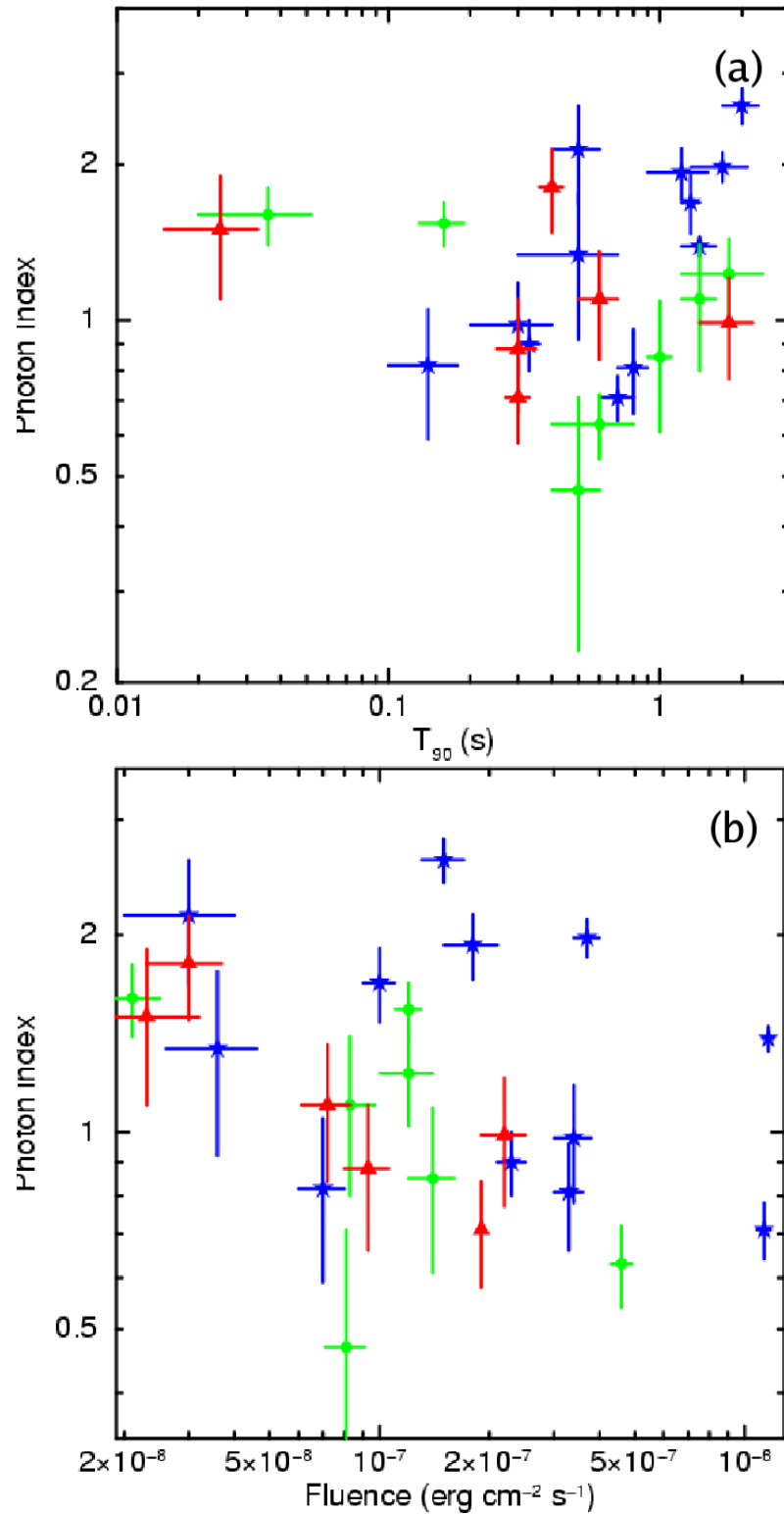


Figure 5.11: (a) The prompt photon index,  $\Gamma$  (15 – 150 keV) versus the  $T_{90}$  duration. (b) The prompt photon index,  $\Gamma$  (15 – 150 keV) versus the 15 – 150 keV fluence. Symbols are as in Figure 5.10.

incorrect. However, the majority of the candidate magnetars in the sample can be fitted with a steep decay from the prompt emission so no extended emission would be expected. The exceptions to this are GRBs 080905A and 060801 which do not appear to fit the model well. It is important to note that, although these fits are not as good, these GRBs cannot be discounted using this criterion. This is because the spectral properties of the magnetar component are not known or it is not known if spectral evolution is occurring, so this component may be spectrally soft and therefore undetectable by BAT.

In Figure 5.12(a), the 0.3 – 10 keV flux at 1000 s is compared to the flux at 100 s. The magnetar candidates tend to have a higher flux at 1000 s than the other SGRBs, with the exception of GRBs 051210, 060801, 080905A, 081024, 090515, 100702 and 101219A (i.e. the candidates which are modelled as collapsing to a BH). Two other GRBs show a similar trend to the magnetar candidates, these are 050509B, which visually fits the magnetar model well but does not have enough data to conclusively prove this, and GRB 091109B. This graph can be explained if all SGRBs are assumed to occur in a low density environment, resulting in little afterglow, and the only observed emission results from the curvature effect. The magnetar candidates which collapse to form a BH and the other SGRBs fade rapidly, whereas the stable magnetars are giving prolonged energy injection giving the higher late time X-ray fluxes. This analysis suggests that mergers collapsing straight to BHs have significantly fainter X-ray afterglows, which fade rapidly, and hence there may be a selection bias against these objects in this analysis (as sufficient data points were required to fit the model). When considering only the stable magnetar candidates, there is a large positive correlation (correlation coefficient = 0.84, whereas the whole sample had a poor correlation coefficient of 0.03) between the X-ray flux at 100 s and 1000 s. As this graph was produced independently from the magnetar model, this correlation suggests that there is a strong relationship between the early and late time X-ray flux for the stable magnetar sample. Figure 5.12(b) shows evidence of a similar correlation for the X-ray flux at 100 s in comparison to the flux at 10000 s, although with more scatter (correlation coefficient = 0.54). In Figures 5.12(c) and (d) the fluxes at 100 s and 1000 s are plotted versus the prompt 15 – 150 keV fluence observed. There is no evidence of a correlation between the flux at 100 s and the fluence for the whole sample but there is a possible correlation for the stable magnetar sample (correlation coefficient for all is 0.07 but 0.63 for the stable magnetar sample). In Figure 5.12(d) the possible correlation for the stable magnetar sample is very weak (0.22) but there is a weak correlation between the prompt fluence

and the 1000 s X-ray flux for the whole sample (correlation coefficient = 0.33).

For each GRB in the sample, a 0.3 – 10 keV XRT spectrum (using the automatic data products on the UK Swift Data Centre website Evans et al., 2007, 2009) for the model derived rest frame plateau duration (converted to observed frame durations) was extracted to compare the spectral properties in the magnetar emission phase. This was not possible for some of the sample as XRT observations started after the plateau phase had ended. Each spectrum was fitted in XSPEC using a power law,  $\Gamma_X$ , the Galactic  $N_H$  (neutral hydrogen column density, taken from Kalberla et al., 2005) and the intrinsic  $N_H$  at the redshift provided in Table 5.2. The spectral fits are provided in Table 5.4.

The photon index of the plateau phase,  $\Gamma_X$ , is compared to the photon index of the prompt emission,  $\Gamma_\gamma$ , in Figure 5.13(a). The plateau phase tends to be softer on average than the prompt emission. There is a slight correlation between these two values for the whole sample, with a correlation coefficient of 0.48. However, if the GRBs which do not fit the magnetar sample (i.e. the other SGRBS) are removed from the sample along with the outlier GRB 090621B (a possible candidate with extreme values for  $B_{15}$  and  $P_{-3}$  and a very soft plateau) this correlation becomes much more significant, with a correlation coefficient of 0.85, and this is shown in Figure 5.13(b). The relationship between these values is given by  $\Gamma_X = \Gamma_\gamma^a$ , where  $a = 0.26 \pm 0.15$ . This suggests that the spectrum of the plateau regime for the magnetar sample is dependent on the spectrum of the prompt emission and this is independent of the stability of the magnetar.

In Figure 5.14, the intrinsic and Galactic  $N_H$  values are compared. The majority of the SGRBs are consistent with having negligible intrinsic  $N_H$  observed in their spectra suggesting they are likely to have occurred in low density environments. The main exception is GRB 070714A which has a large and well constrained intrinsic  $N_H$  implying it may have occurred in a higher density environment. The  $N_H$  values can be used to estimate the  $A_V$  absorption using the Bohlin, Savage, & Drake (1978) conversion, given in Equation 5.3, and the E(B-V) conversions given in Pei (1992) for Galactic, Small Magellanic Cloud (SMC) and Large Magellanic Cloud (LMC) sightlines. For GRB 070714A the total  $N_H$  absorption corresponds to  $A_V \sim 11.9$  mag (Galactic),  $A_V \sim 11.3$  mag (SMC) and  $A_V \sim 12.2$  mag (LMC). Therefore, for GRB 070714A, it seems unlikely that the optical afterglow would be detectable. Other GRBs which may have significant intrinsic  $N_H$  include GRBs 051221A, 080426, 080919 and

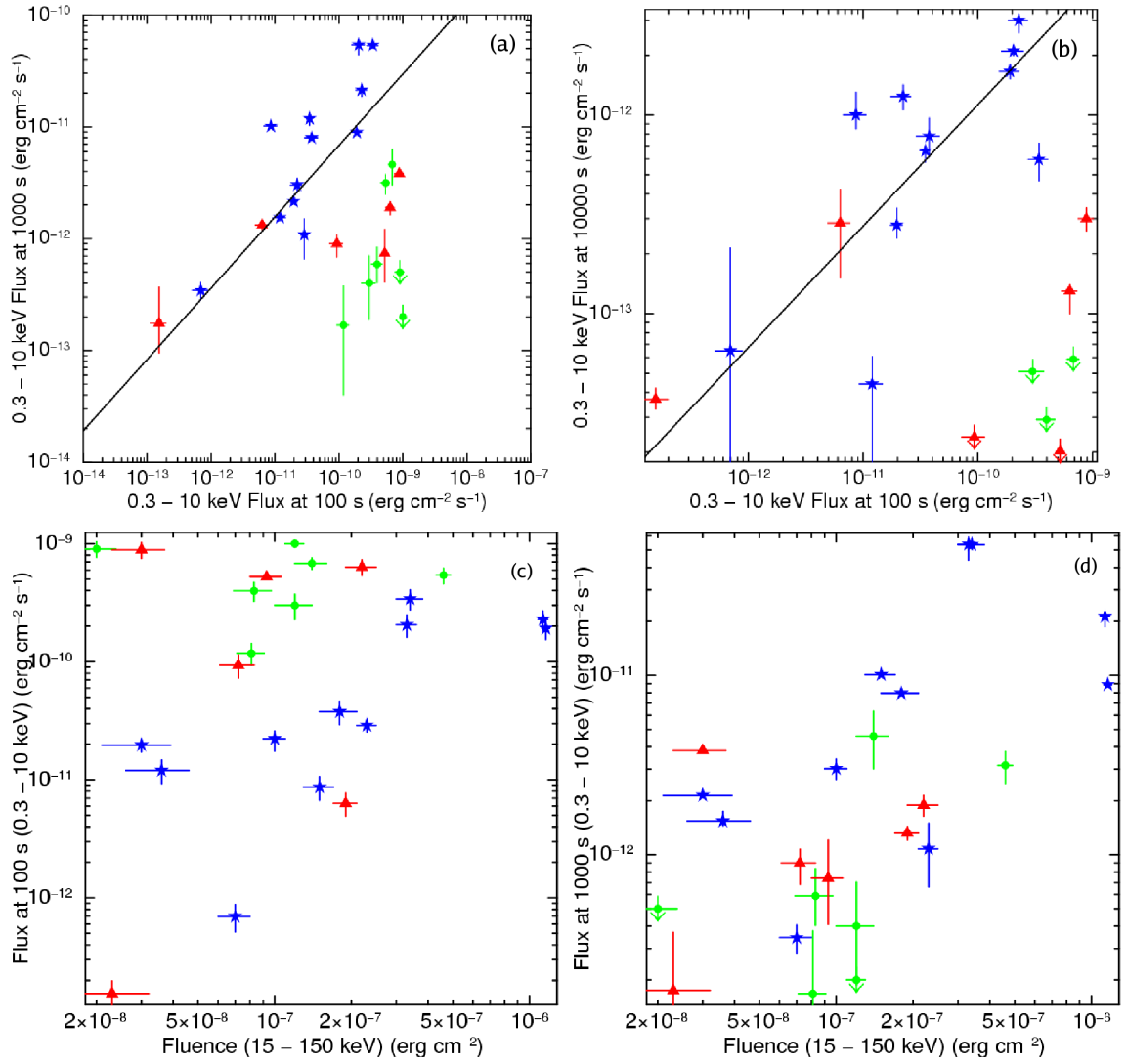


Figure 5.12: (a) The 0.3 – 10 keV flux at 100 s versus 1000 s. (b) The 0.3 – 10 keV flux at 100 s versus 10000 s. (c) The 15 – 150 keV fluence versus the 0.3 – 10 keV flux at 100 s. (d) The 15 – 150 keV fluence versus the 0.3 – 10 keV flux at 1000 s. Symbols are as in Figure 5.10.

GRB	$\Gamma_X$	Galactic $N_H$ ( $10^{20} \text{ cm}^{-2}$ )	Restframe Intrinsic $N_H$ ( $10^{20} \text{ cm}^{-2}$ )
<b>Magnetar candidates</b>			
051221A	$2.04^{+0.14}_{-0.13}$	$5.70 \pm 0.37$	$18.0^{+7.10}_{-6.60}$
060313	$1.61^{+0.16}_{-0.13}$	$5.00 \pm 1.17$	$0.00^{+5.84}_{-0.00}$
060801	$1.53^{+0.47}_{-0.43}$	$1.40 \pm 0.31$	$29.9^{+68.8}_{-29.9}$
070809	$1.73^{+0.83}_{-0.43}$	$6.40 \pm 0.17$	$2.95^{+14.9}_{-2.95}$
080426	$1.93^{+0.29}_{-0.27}$	$37.0 \pm 4.19$	$32.0^{+31.6}_{-25.5}$
090426	$2.03^{+0.19}_{-0.11}$	$1.50 \pm 0.11$	$0.00^{+36.0}_{-0.00}$
090510	$1.56^{+0.20}_{-0.19}$	$1.70 \pm 0.11$	$10.0^{+16.0}_{-10.0}$
090515	$1.89^{+0.25}_{-0.24}$	$1.90 \pm 0.25$	$13.1^{+11.6}_{-10.5}$
101219A	$1.65^{+0.32}_{-0.31}$	$4.90 \pm 0.87$	$56.8^{+26.7}_{-20.4}$
<b>Possible candidates</b>			
061201	$1.44^{+0.20}_{-0.19}$	$5.20 \pm 1.58$	$6.77^{+4.25}_{-3.88}$
070714A	$2.12^{+0.37}_{-0.35}$	$9.20 \pm 1.25$	$214^{+51.8}_{-45.7}$
080702A	$1.57^{+0.85}_{-0.76}$	$15.0 \pm 1.50$	$125^{+251}_{-121}$
090621B	$2.50^{+1.60}_{-1.00}$	$19.0 \pm 1.96$	$42.8^{+108}_{-42.8}$
110112A	$2.07^{+0.46}_{-0.24}$	$5.50 \pm 0.40$	$7.86^{+12.7}_{-7.86}$
<b>Other SGRBs</b>			
050509B	$1.92^{+1.09}_{-0.60}$	$1.60 \pm 0.04$	$8.00^{+8.10}_{-8.00}$
080919	$2.23^{+1.02}_{-0.84}$	$26.0 \pm 3.78$	$105^{+126}_{-75.8}$
091109B	$1.96^{+0.64}_{-0.43}$	$9.20 \pm 0.96$	$14.5^{+27.9}_{-14.5}$

Table 5.4: The 0.3 – 10 keV spectral fits for the derived plateau durations given in Table 5.3. Provided are the photon index,  $\Gamma_{X,plateau}$ , the Galactic  $N_H$  and the restframe intrinsic  $N_H$  using the redshifts provided in Table 5.2.

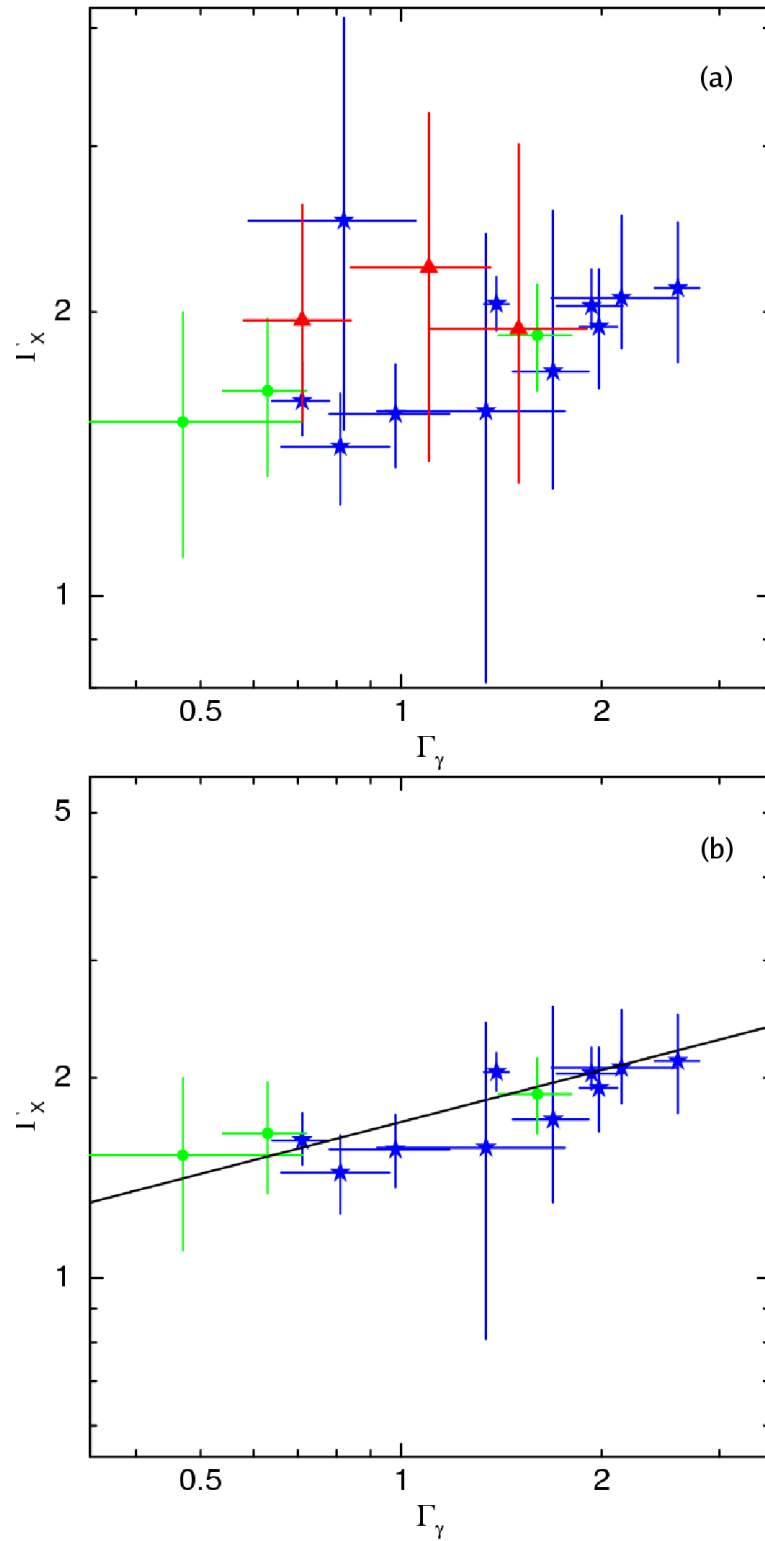


Figure 5.13: A comparison between the prompt emission photon index (15 – 150 keV) and the plateau photon index (0.3 – 10 keV). (a) shows the whole sample considered and (b) focuses on the candidates which show evidence of a correlation between the prompt and plateau emission. Symbols are as in Figure 5.10.

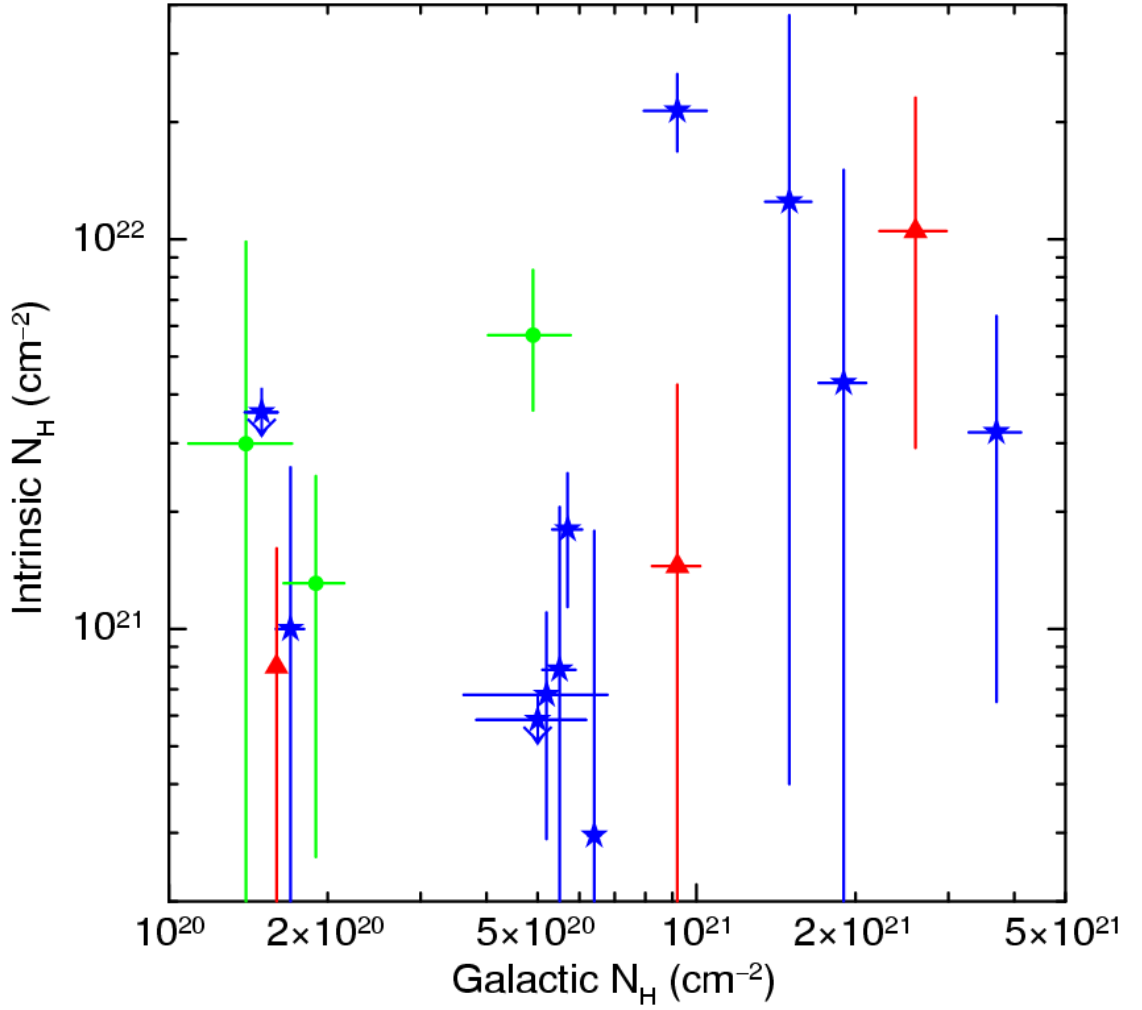


Figure 5.14: The intrinsic rest frame  $N_H$  in comparison to the Galactic  $N_H$ . The arrows represent two GRBs which had zero intrinsic  $N_H$  fitted in their spectra, the maximum error has been plotted as an upper limit for their intrinsic  $N_H$ . Symbols are as in Figure 5.10.

101219A. In contrast, GRB 090426 has an extremely low total  $N_H$  corresponding to  $A_V \sim 0.080$  mag (Galactic),  $A_V \sim 0.076$  mag (SMC) and  $A_V \sim 0.082$  mag (LMC).

$$\frac{N_H}{E(B - V)} = 5.8 \times 10^{21} \text{ atoms cm}^{-2} \text{ mag}^{-1} \quad (5.3)$$

### Optical Afterglows

A 1 keV flux lightcurve showing the prompt, X-ray and the most constraining optical observation during the plateau phase was created for each burst in the sample. These were produced using the simple relation given in equation 5.4 (assuming a simple power law spectrum and a spectral index  $\beta_x = \Gamma_x - 1$ ) to shift the observed fluxes at a measured energy to 1 keV.

$$F_{\nu(1keV)} = F_{\nu(measured)} \left( \frac{E(measured)}{1keV} \right)^{\beta_{x,o}} \quad (5.4)$$

$\Gamma_x$  was obtained from the time averaged PC mode spectra produced by the automated analysis on the UK *Swift* Data Centre website (Evans et al., 2007, 2009). The 0.3 – 10 keV BAT XRT lightcurves were shifted to flux at 1 keV using equation 5.4. The optical magnitudes were converted into flux for the wavelength of the optical filter used and then shifted to 1 keV using equation 5.4. As there may be a cooling break inbetween the optical and X-ray observations (Sari, Piran, & Narayan, 1998), the two extreme cases are taken i.e.  $\beta_o = \beta_x$  and  $\beta_o = \beta_x - 0.5$ . The errors on the observed optical magnitudes and the errors on  $\Gamma_x$  are used to define the region on the lightcurve that the optical data could reside in (dark grey - no cooling break, light grey - cooling break, note there is overlap between these two regimes). If the optical and X-ray data are consistent, then the X-ray data points should lie within the shaded regions for the optical data.

The 1 keV flux lightcurves for GRBs which fit the magnetar model are shown in Figure 5.15. GRBs 051221A and 090426 have optical afterglows which are consistent with their X-ray afterglows. GRB 061201 may also be consistent but would require the most extreme errors and cooling break. 53% have optical afterglows that are inconsistent with their X-ray afterglows, signifying either significant optical absorption or an extra component in the X-ray afterglow. However, as shown in Section 5.3.3 and Figure 5.14 using absorption in the X-ray spectra, the majority of the candidates are consistent with occurring in a low density environment. Only GRBs 080426 and 101219A have inconsistent afterglows and evidence of significant absorption in their X-ray spectra. In the remaining 26% the optical upper

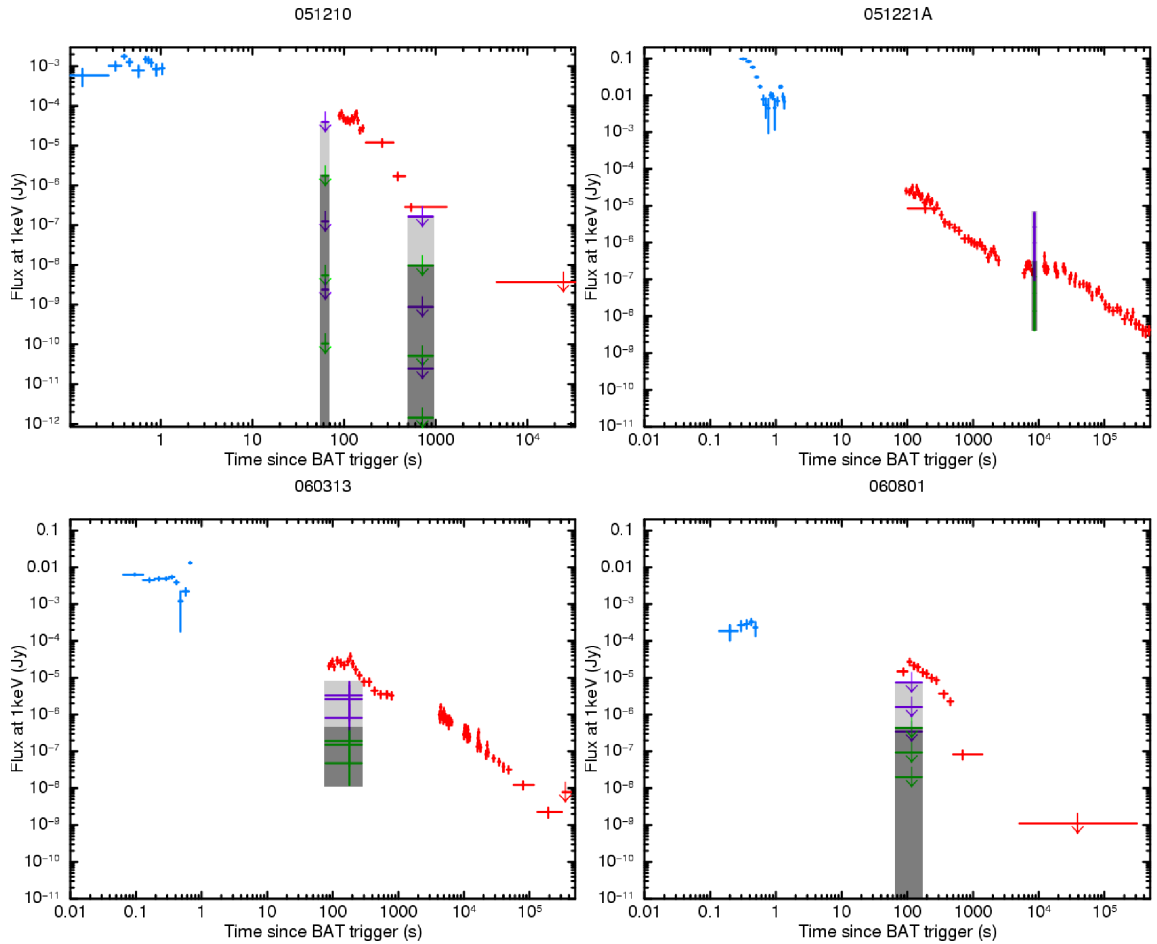


Figure 5.15: 1 keV flux lightcurves with 1 optical observation, light shaded region = optical observation assuming a cooling break and dark shaded region = optical observation assuming no cooling break. The references are for the optical observation used. If the X-ray and optical observations are consistent with originating from the same source, the X-ray data points should pass through the shaded regions. These are the magnetar candidate SGRB sample. GRB 051210 - Jelinek et al. (2005) - inconsistent, GRB 051221A - Soderberg et al. (2006) - optical observations are consistent with X-ray observations, GRB 060313 - Roming et al. (2006) - inconsistent and GRB 060801 - Brown & Racusin (2006) - inconsistent.

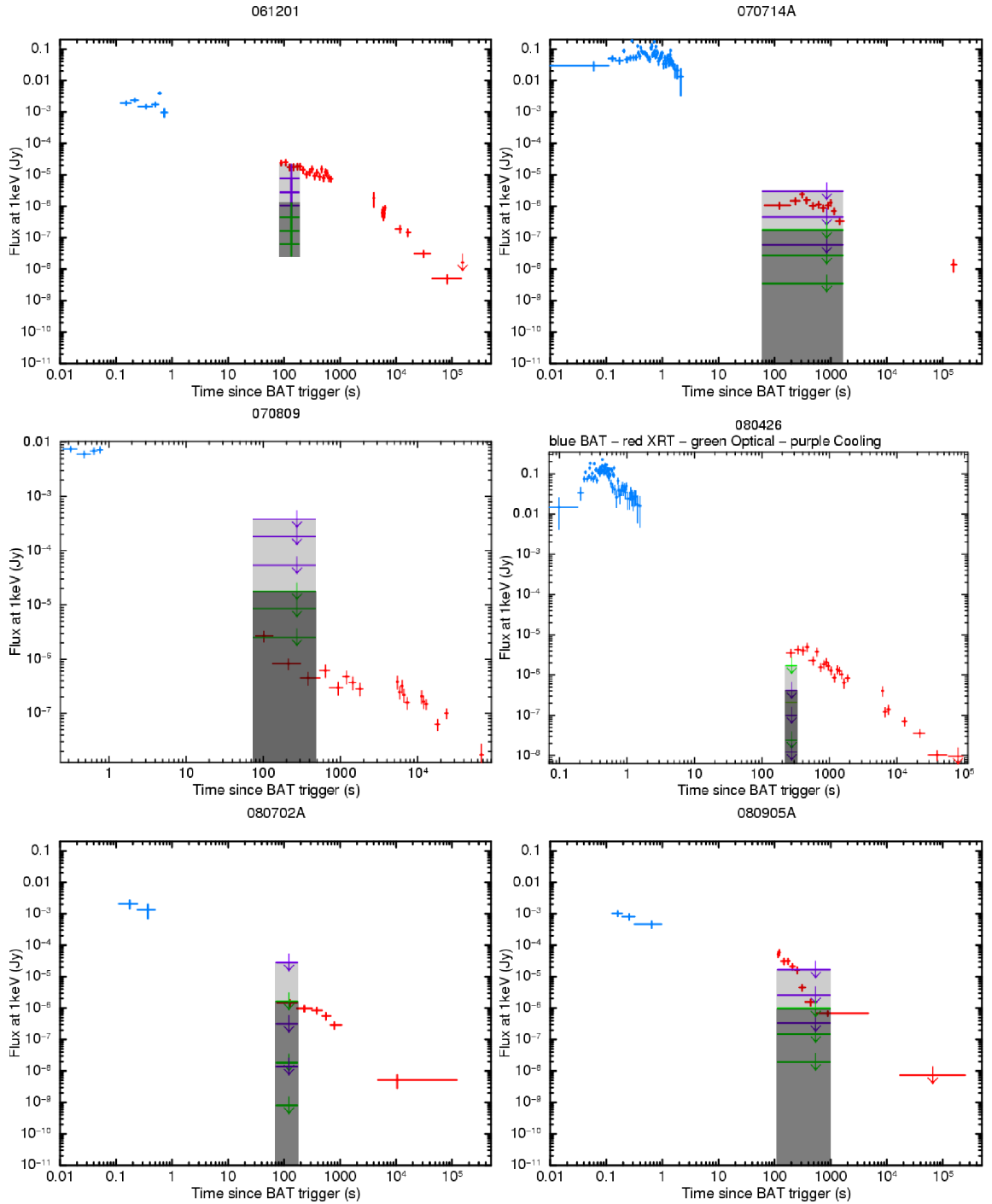


Figure 5.15: Continued: GRB 061201 - Stratta et al. (2007) - only consistent for with most extreme cooling break and errors, GRB 070714A - Chester & Grupe (2007) - upper limits inconclusive if there is an extreme cooling break. GRB 070809 - Chester & Marshall (2007) - upper limits inconclusive, GRB 080426 - Oates & Ziaepour (2008) - inconsistent and GRB 080702A - de Pasquale (2008) - upper limits inconclusive, GRB 080905A - Brown & Pagani (2008) - upper limits inconclusive.

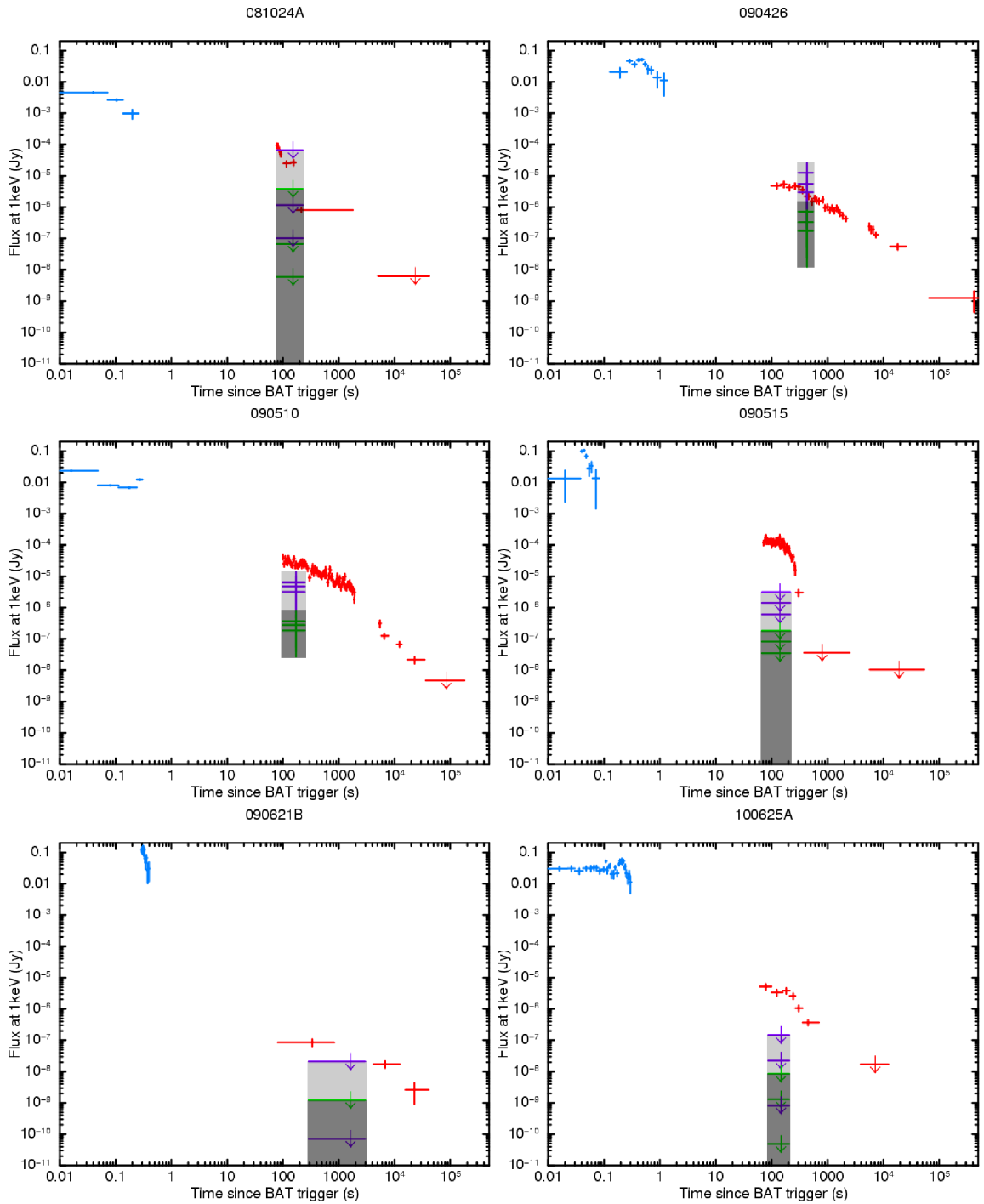


Figure 5.15: Continued: GRB 081024A - de Pasquale & Stratta (2008) - upper limits inconclusive, GRB 090426 - Oates & Cummings (2009) - optical observations are consistent with X-ray observations, GRB 090510 - Kuin & Hoversten (2009) - inconsistent. GRB 090515 - Seigel & Beardmore (2009) - inconsistent, GRB 090621B - Curran (2009) - inconsistent and GRB 100625A - Landsman & Holland (2010) - inconsistent.

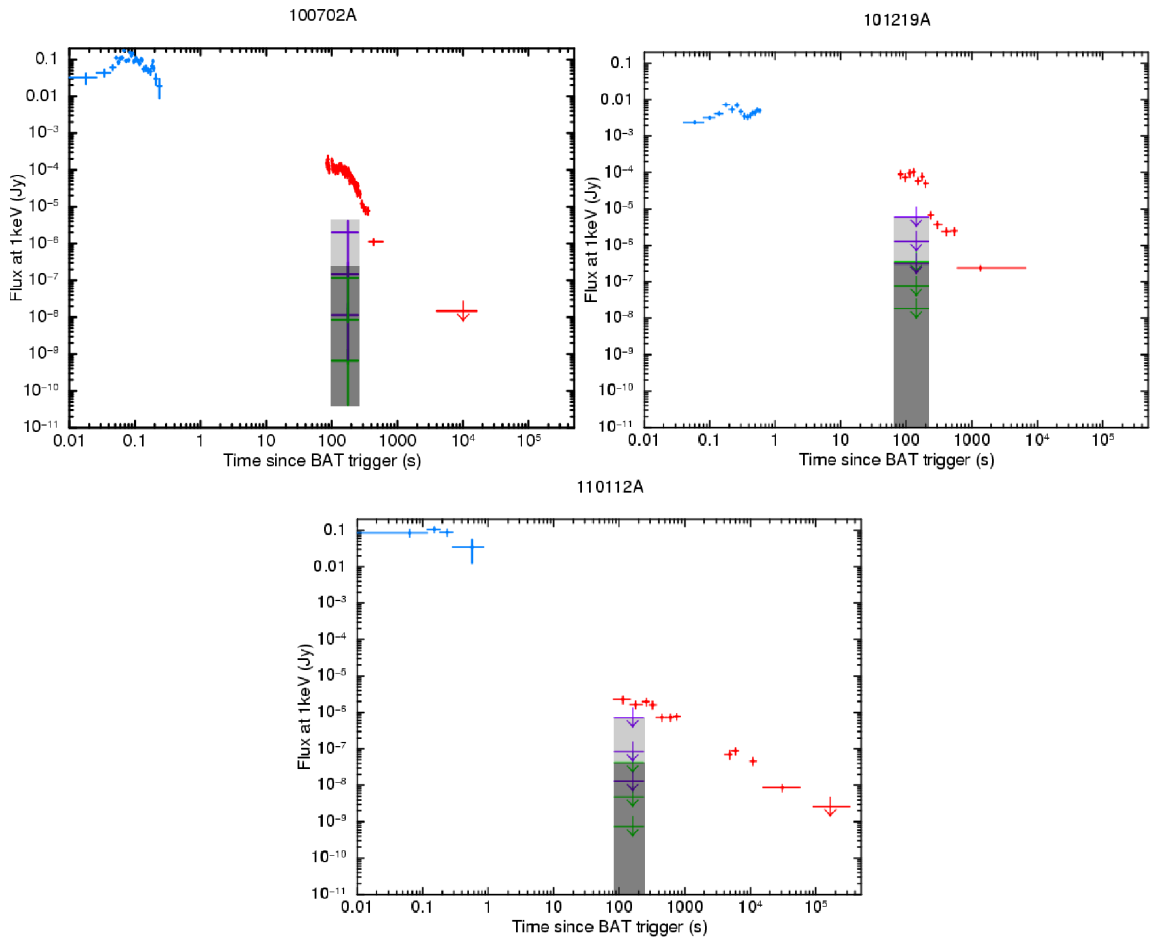


Figure 5.15: Continued: GRB 100702A - de Pasquale & Siegel (2010) - inconsistent, GRB 101219A - Kuin & Gelbord (2010) - inconsistent and GRB 110112A - Breeveld & Stamatikos (2011) - inconsistent.

limits are not constraining enough. Of the GRBs which do not fit the magnetar model, only GRB 100117A has an optical afterglow which is definitely inconsistent with the X-ray afterglow (as shown in Figure 5.16).

Figure 5.17 compares the average X-ray fluxes at 1 keV to the optical fluxes at 1 keV with (b) and without (a) a cooling break. The average X-ray flux was calculated using the flux at the start of the optical observation and the flux at the end of the observation. If there is an extra component in the X-ray emission, the data points will lie below the black line in both Figures. This supports the previous analysis, i.e. there are several magnetar candidates with inconsistent optical emission, some which would rely on the most extreme uncertainties and cooling breaks. However the sample of SGRBs

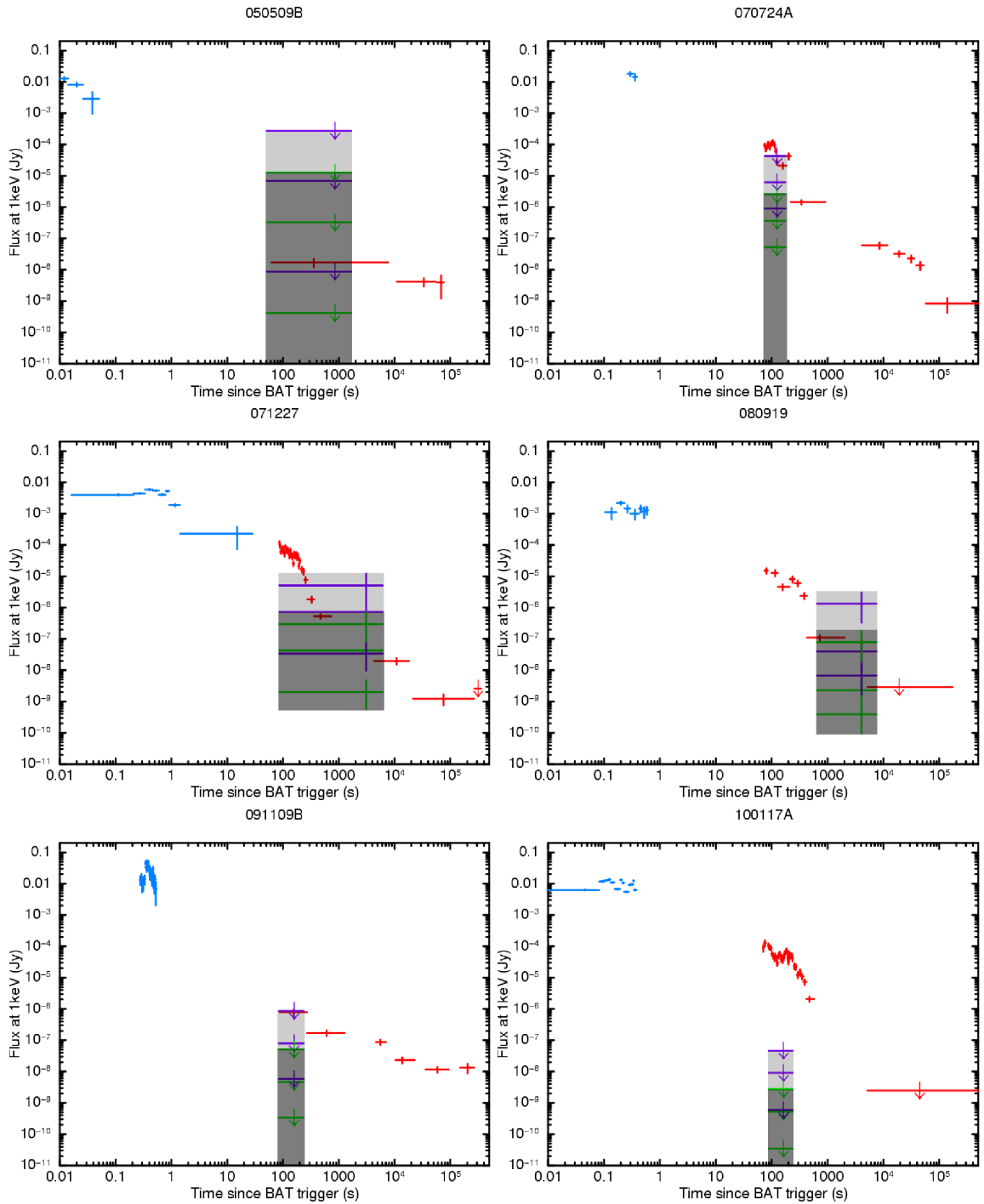


Figure 5.16: As Figure 5.15, the GRBs shown here are from the other SGRB sample GRB 050509B - Breeveld et al. (2005) - consistent, GRB 070724A - de Pasquale & Ziaepour (2007) - upper limits inconclusive if there is an extreme cooling break, GRB 071227 - Cucchiara & Sakamoto (2007) - likely consistent, GRB 080919 - Immler & Holland (2008) - likely consistent, GRB 091109B - Oates (2009) - upper limits inconclusive if there is an extreme cooling break, and GRB 100117A - de Pasquale, Holland, & Oates (2010) - extremely inconsistent.

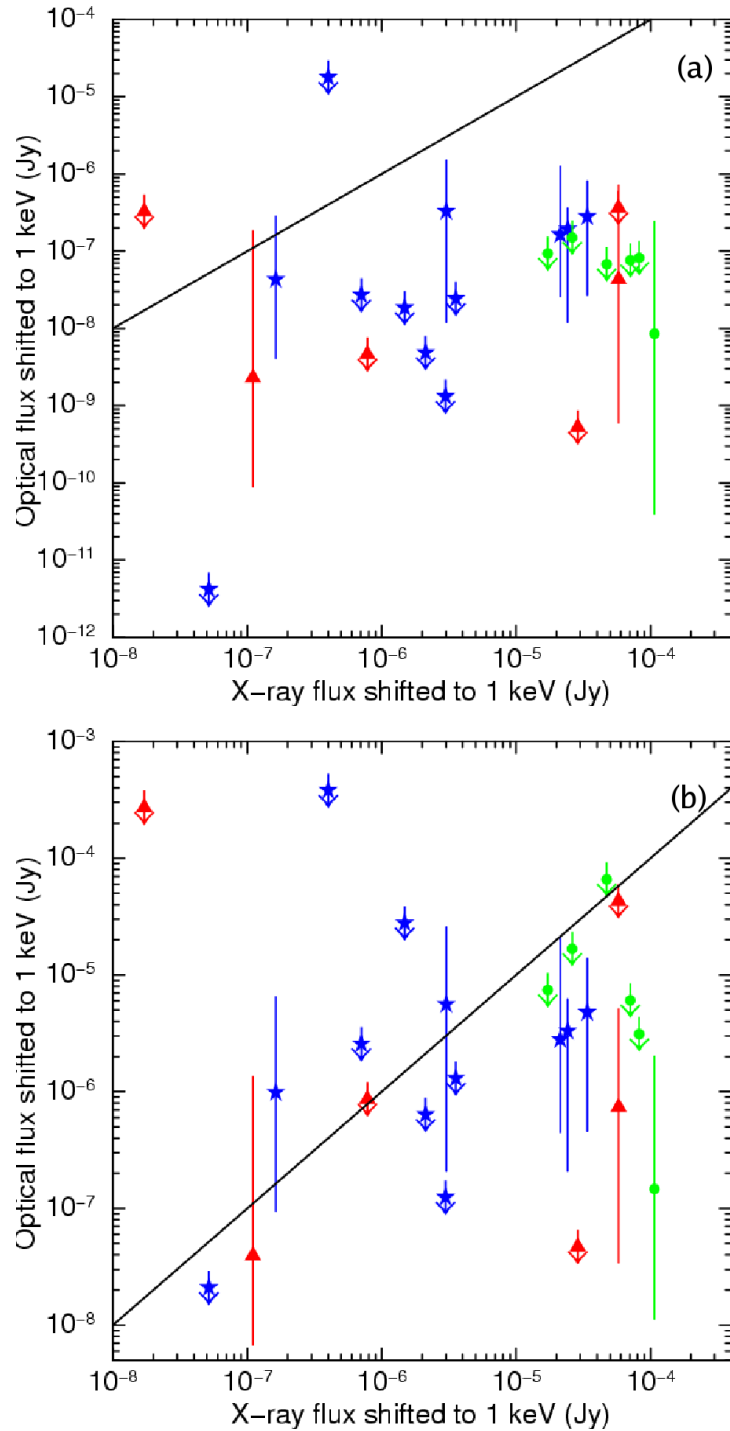


Figure 5.17: The optical flux shifted to 1 keV is plotted against the average X-ray flux during the optical observation also shifted to 1 keV. The solid black line represents where these are equal, as expected if they are consistent with each other. In (a) it is assumed there is no cooling break between the optical and X-ray observations and in (b) it is assumed there is the most extreme cooling break. Symbols are as in Figure 5.10.

which do not fit the magnetar model are more likely to have consistent X-ray and optical observations, and when they are not consistent it is likely due to flaring activity in their X-ray lightcurves.

Although there is some evidence that the magnetar candidates have additional X-ray emission, it is not known what spectrum is expected from a newly formed magnetar and hence those whose optical emission is consistent with their X-ray emission cannot be completely discounted.

### 5.3.4 Discussion

#### Specific cases

GRB 070809 is one of the best fitting stable magnetar candidates and lies within the allowed regions. This GRB had a faint optical afterglow and is offset by 20 kpc from a galaxy at  $z = 0.219$  (Perley et al., 2008), making it an ideal candidate for a magnetar formed via the merger of two NSs. However it is important to be cautious about this candidate host galaxy association as the likelihood this is an unrelated field galaxy is 5 – 10% (Tunnicliffe et al. private communication).

GRB 061201, with a spin period of  $\sim 16$  ms, fits the magnetar model well but is spinning slower than expected. This relies on the correct host galaxy identification and hence redshift, as it would fit the model if at a higher redshift. Additionally, the approximate 10 ms limit imposed by Usov (1992) is dependent on the initial radius of the collapsing object and the radius of the final NS. This limit is also derived for the model involving AIC of a WD. Therefore there is some level of flexibility in this imposed limit. This, and other GRBs close to this boundary, are still considered to be potential candidate magnetars.

GRB 051221A is consistent with having energy injection in its lightcurve out to  $\sim 2 \times 10^4$  s (Burrows et al., 2006; Soderberg et al., 2006). Fan & Xu (2006) explained this as energy injection from a magnetar. The model used in this Chapter fits this GRB very well. Jin et al. (2007) proposed an alternative two jet model to explain the lightcurves without requiring additional energy injection.

GRB 060313 has been included in the magnetar sample by ignoring the first 50 – 200 s of the lightcurve

due to the flaring activity, this gives a good fit to the later data but this result should be treated with caution. Flares could be associated with on-going accretion onto the newly formed magnetar. Alternatively, Dai et al. (2006) and Gao & Fan (2006) suggest that the X-ray flares originate from reconnection of twisted magnetic fields within the NS. Margutti et al. (2011) have conducted a systematic study into SGRB flares, including the flares observed in GRB 060313, and concluded that the flares are consistent with a central engine origin.

Included in this sample are SGRBs whose progenitors are subject to significant debate, particularly GRB 090426 at  $z \sim 2.6$  which could have originated from a collapsar instead of a binary merger although that has not been ruled out (Antonelli et al., 2009; Levesque et al., 2010; Thöne et al., 2011; Xin et al., 2011). GRB 090426 fits the model well, irrespective of the progenitor, but the progenitor debate is important to note as this Chapter is specifically studying possible NS binary merger progenitors.

### **The Wider Sample**

Interestingly, seven of the magnetar candidates require collapse to a BH (051210, 060801, 080905A, 081024, 090515, 100702A and 101219A) although, when considering their wider properties, it is noted that GRBs 060801, 080905A and 081024 do not appear to fit the model well. This implies that, if these SGRBs are making magnetars, they only collapse to a BH in a small number of cases. Comparing the derived plateau durations and the collapse times provided in Table 5.3, the magnetar typically (but not always) collapses to a BH after the plateau phase, i.e. when the magnetar has spun down significantly. The collapse time is related to the mass of the magnetar and the spin period at which the differential rotation can no longer support gravitational collapse. The discrepancy between collapse time and plateau duration are hence likely to be reliant upon the mass of the magnetar. Additionally, there may be ongoing accretion on to the magnetar (remnants of the merger) which may raise the mass of the magnetar above the critical point prior to significant spin down. Interestingly, those candidates which collapse to form a BH and are within the allowed (unshaded) region of Figure 5.10 have a higher magnetic field for a given spin period than the candidates which do not collapse to a BH.

Many of the magnetar candidates lie within, or near to, the predicted plateau luminosity and duration

relation in Metzger et al. (2011) when considering uncertainties due to redshift, efficiency and beaming. However, there are candidates whose plateaus are significantly shorter than predicted or at a lower luminosity. It is important to note that this analysis and that of Metzger et al. (2011) assumes a NS mass of  $1.4M_{\odot}$  and this is likely to be significantly higher for a NS merger progenitor (e.g.  $2.1M_{\odot}$ ). This has a small affect on the values of the magnetic field strength and the spin period calculated in this model (as shown in Rowlinson et al., 2010b) but does not significantly affect the predicted regions of Metzger et al. (2011).

### Accretion Effects

This model does not account for ongoing accretion onto the magnetar, from the surrounding torus of material formed during the merger. This would effect the results obtained, especially if accretion increases the NS mass to more than can be supported as this results in collapse to a BH. Additionally, accretion could explain flares observed overlaying the plateau model. Flares may also be associated with ongoing magnetar activity as described in Dai et al. (2006).

Piro & Ott (2011) studied the affect of accretion onto magnetars formed during SNe, however their results are also applicable to these magnetars. The main difference for SGRBs is the significantly reduced reservoir of material available for accretion and have a different accretion rate. This section assumes the simplest accretion rate published by Metzger et al. (2010b) assuming that accretion starts at 0.16s after the trigger time, this gives a total accretion disk mass of  $\sim 0.3 M_{\odot}$ . Accretion onto the magnetar occurs when the propeller regime ends, given by equation 5.5 from Piro & Ott (2011) where  $\mu_{33} = B_{15}R_6^3$ .

$$\dot{M} < 6.0 \times 10^{-3} \mu_{33}^2 M_{1.4}^{-5/3} P_{0,-3}^{-7/3} M_{\odot} \text{ s}^{-1} \quad (5.5)$$

As before, an initial NS mass of  $1.4 M_{\odot}$  and radius of  $10^6$  cm is assumed. Figure 5.18a shows the accretion rate as a function of time after formation. Figure 5.18b shows the evolution of the spin

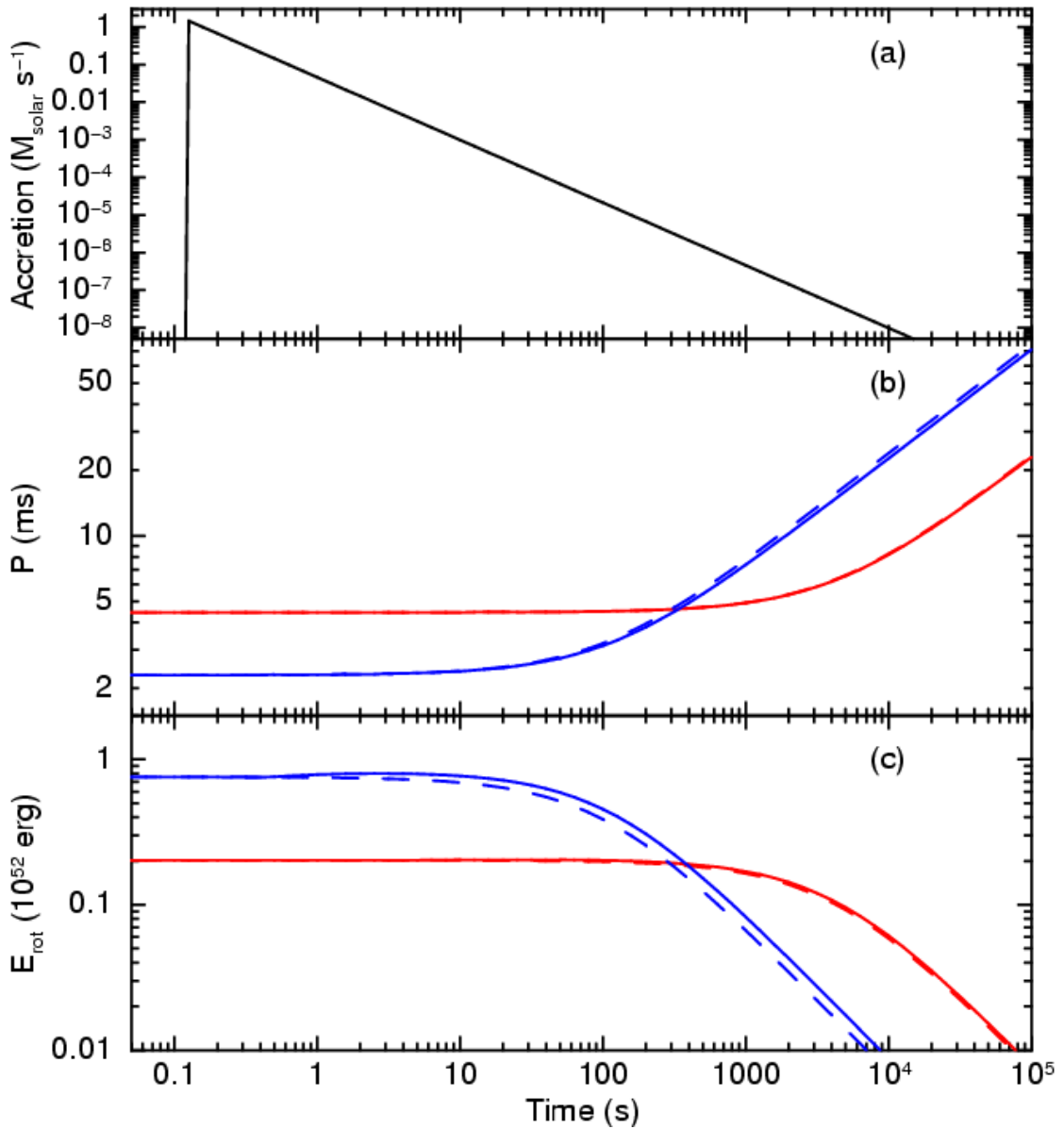


Figure 5.18: (a) The accretion rate as a function of time assuming the accretion rate for a compact binary merger Metzger et al. (2010b) starting at 0.16 s after the trigger time giving a total accretion disk mass of  $\sim 0.3 M_{\odot}$ . (b) The evolution of the spin period of the magnetar for the two accretion rates, red - the magnetar predicted for GRB 060313 and blue - GRB 090515. Solid lines include accretion and dashed lines have no accretion. In these plots, accretion has a very small or negligible effect. (c) The amount of rotational energy available in the magnetar for each case.

period of two different magnetars (using the parameters for GRBs 060313 and 090515 as these have contrasting magnetar properties) assuming there is accretion onto the magnetar or no accretion. When there is significant accretion (e.g. GRB 090515) it can marginally prevent spin down and affect the rotational energy (Figure 5.18c) available, although these are negligible effects for the low accretion rates considered.

It is worth noting that accretion would potentially have a very large effect on the results obtained for LGRB magnetar candidates (e.g. the sample in Lyons et al., 2010) as these are thought to have a significantly higher mass accretion disk and an accretion rate similar to that proposed by Piro & Ott (2011). In that case, the energy reservoir could reach values in excess of  $10^{53}$  ergs for particular combinations of the initial conditions. This additional energy source could be a potential explanation for large flares observed in some of the LGRB candidate lightcurves.

Figure 5.19 shows the total mass accreted after the propeller regime has ended. The linear correlation between the duration of the propeller regime and the mass accreted is caused by the relationship:  $\dot{M} \propto t^{-5/3}$  (i.e. the sooner the propeller regime ends, the greater the mass that can be accreted). The candidates which accrete the most mass are those which also collapse to form a BH within a few hundred seconds, leading to the suggestion that accretion may indeed be driving this collapse. The stable magnetar outlier is GRB 100625A which was also well fit by the unstable magnetar model but the stable model was chosen to reduce the number of free parameters in the model.

### Energy Constraints

Considering all these potential candidates, up to 76% of the SGRBs in this sample could be fit with the magnetar model when using their X-ray lightcurves. Table 5.3 gives the isotropic energy released during the prompt emission phase of the GRB. These values tend to be consistent with the maximum expected energy output from the magnetar central engine model,  $E_{iso} < 3 \times 10^{52}$  erg (Metzger et al., 2011). However, this value is exceeded for some good candidates, GRBs 060313 and 101219A which may be due to using the average redshift and the actual events are at significantly lower redshift. Additionally, GRBs 060801, 090426, 090510 and 100625A also exceed this value but it is important to

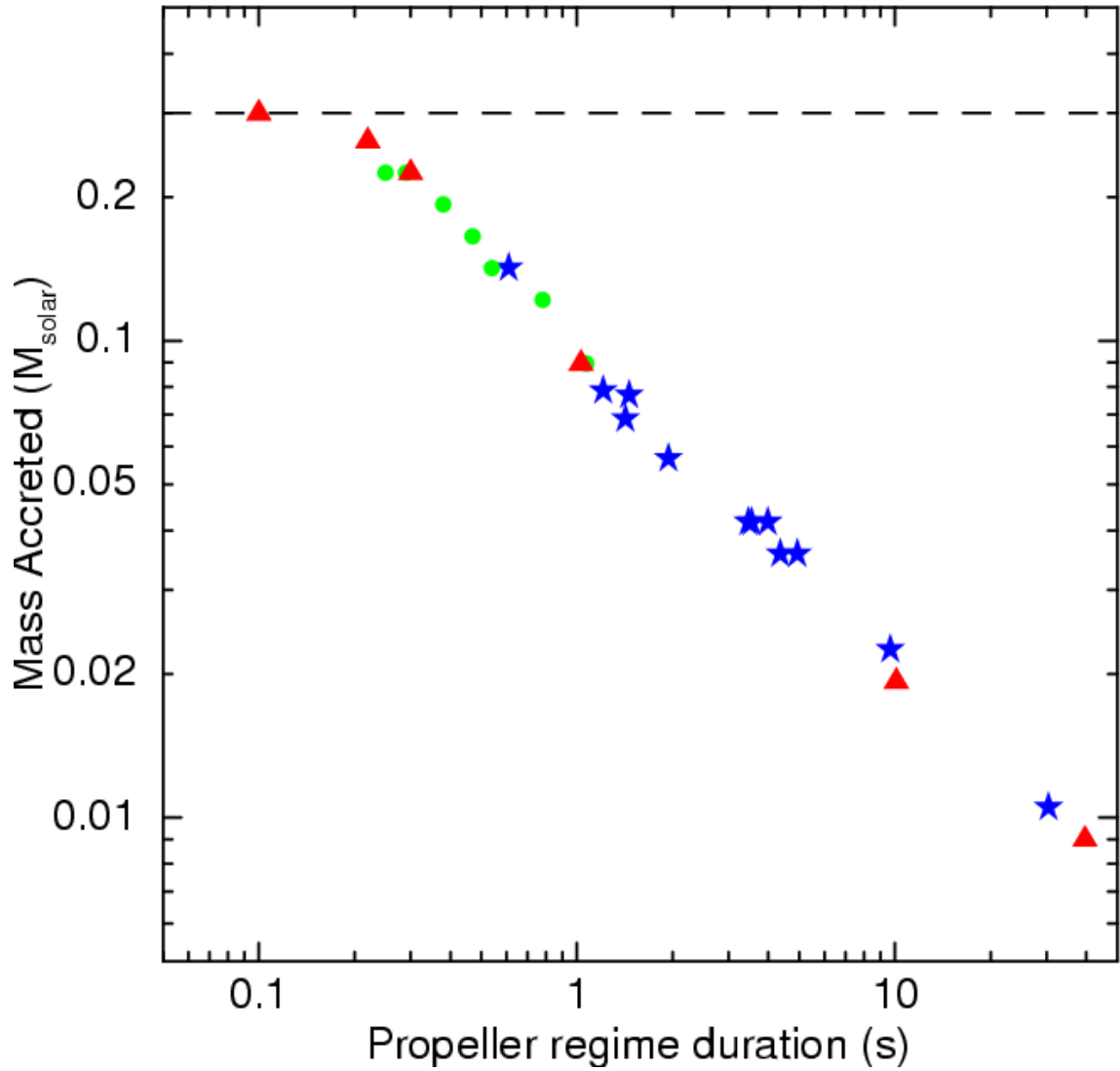


Figure 5.19: The amount of mass accreted by the magnetar against the duration of the propeller regime. The dashed line represents the maximum mass available in the accretion disk and is  $0.3 M_{\odot}$  an upper limit for the amount of mass which can be accreted. Symbols are as in Figure 5.10.

note that 090426 and 100625A may be consistent within errors and beaming has not been corrected for. With a reasonable beaming correction, all of these GRBs would lie well below the maximum expected energy output. Another consideration is  $E_{iso} \propto M_{1.4} P_{0,-3}^{-2}$ , so if magnetars can have masses up to  $2.1M_{\odot}$  then the maximum energy output could be as high as  $E_{iso} \sim 1 \times 10^{53}$  erg. In this case, the  $E_{iso}$  for GRBs 060801, 090426 and 100625A would be consistent. Additionally, if the newly formed magnetar is accreting, it is possible to spin up the magnetar creating a larger store of rotational energy. It is concluded that the energy output of all the magnetar candidate GRBs are likely to be consistent with magnetar central engines prior to any beaming corrections. Figure 5.20 shows the energy emitted during the plateau phase (plateau luminosity multiplied by the duration) against the isotropic energy emitted during the prompt emission. Only two GRBs which fit the magnetar model emit more energy during the plateau phase, GRBs 051210 and 090515.

Beaming has not been corrected for in this Chapter, which will undoubtedly affect these results by increasing the spin period and the magnetic field strengths as shown in Rowlinson et al. (2010b). Beaming, with a half-opening angle of  $30^{\circ}$ , has been shown to form via the formation of an ordered magnetic field during the merger of two  $1.5 M_{\odot}$  NSs which collapse to form a BH (Rezzolla et al., 2011). However, the beaming angles of SGRBs and associated magnetars remain unconstrained. 100% efficiency has also been assumed in the conversion of rotational energy into EM radiation. This will not be the case and acts counter to the beaming argument as this reduces the spin period and the magnetic field strengths. For example GRB 090515 has  $B \sim 1.4 \times 10^{16}$  G and  $P \sim 2.3$  ms assuming 100% efficiency, at 10% efficiency these drop drastically to  $B \sim 4.4 \times 10^{15}$  G and  $P \sim 0.73$  ms. Given the uncertainties in both beaming and efficiency, it is noted that the real values of the magnetic field strength and the spin period may vary by a factor of 3. When taking into account that many of this sample do not have redshifts and that most of those with redshifts rely on chance alignments with host galaxies, there are further uncertainties in the real values. It is important to note however, that these GRBs do show evidence of ongoing energy injection and they qualitatively fit the model well, despite the wide range of values caused by these uncertainties.

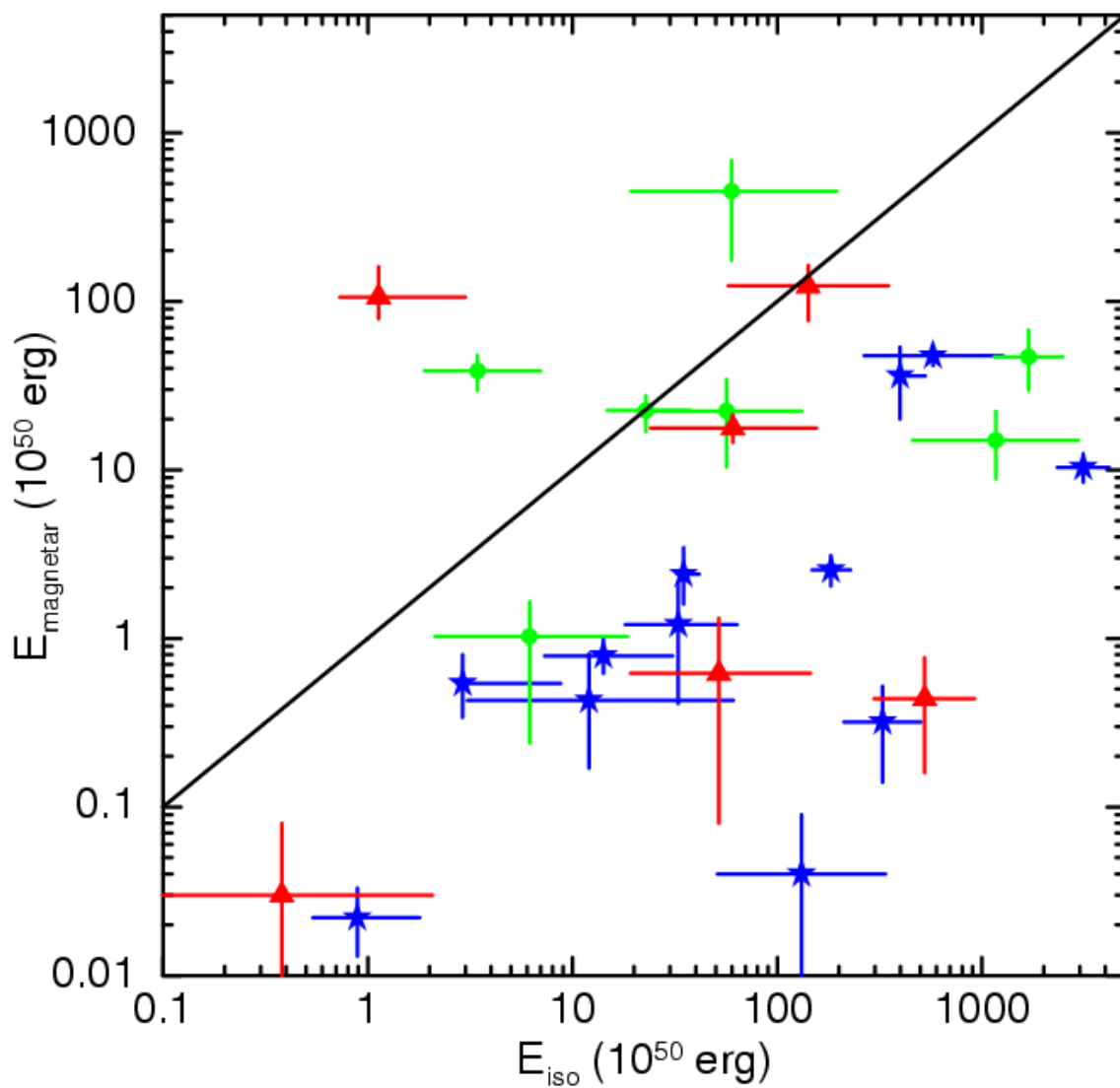


Figure 5.20: The energy emitted during the plateau phase compared to the isotropic energy emitted during the prompt phase. Symbols are as in Figure 5.10.

### Merger rates of NS-NS binaries

The merger rates of compact binary mergers have been studied but remain highly uncertain. Some studies predict more NS-NS mergers than NS-BH mergers (Belczynski et al., 2006). Alternatively, Lee & Ramirez-Ruiz (2007) show that the rates of NS-NS mergers and NS-BH mergers are consistent. In any case, the NS-BH mergers are thought to be more luminous so observable out to higher redshifts. No predictions of the relative rates have been made for EM detections but they have been made for gravitational wave observatories. Bethe & Brown (1998) predict that LIGO would detect roughly equal numbers of these events or more NS-BH mergers while Abadie et al. (2010b) predict that Advanced-LIGO will detect more NS-NS mergers. O’Shaughnessy et al. (2008) calculate the expected NS-NS merger and NS-BH merger rates in the local Universe and they are roughly consistent. If it is assumed that this is comparable to the relative rates for electromagnetic observatories, then the finding that 44 – 76% of the SGRBs in this sample could be modelled with a magnetar would be consistent with all the NS-NS mergers forming a magnetar (although these values are not well constrained by the rate calculations or this model).

If this model is correct then it may contribute to the number of known magnetars in our Galaxy. O’Shaughnessy et al. (2008) predict the merger rate of NS-NS systems per Milky-Way like galaxy to be  $\sim 10^{-5} - 10^{-4}$  mergers per year. Assuming that magnetars are active for  $\sim 10^4$  years (Duncan & Thompson, 1992), this implies that 0.1–1 known Galactic magnetars could be formed by this method. There are many uncertainties within this calculation, but it shows that NS-NS mergers may be the progenitor for a small percentage of known magnetar population and could explain magnetars without associated SNRs.

#### 5.3.5 Gravitational Wave Signals

These objects pose an interesting source of gravitational waves as there are predicted signals for all of the stages this system would go through: inspiral, magnetar and final collapse to BH. Here is a simplified calculation, assuming the amplitude,  $h$ , of the gravitational waves are proportional to the inverse of the distance, using some of the published predictions. The maximum distance out to which

Advanced LIGO (with a sensitivity of  $h \sim 4 \times 10^{-24}$ ) and the Einstein Telescope (ET,  $h \sim 3 \times 10^{-25}$  Hild et al., 2011) could observe this phase is calculated and given in Table 5.5. The gravitational wave amplitude is quoted for a distance of  $z \sim 0.1$  or 390 Mpc. The magnetar phase prediction is an upper limit assuming a spin period of 1 ms,  $I_{45} = 1.5$  for a binary merger progenitor, and an ellipticity  $\epsilon = 1$ . Advanced LIGO predictions by Abadie et al. (2010b) are for NS-NS mergers. Although an ET limit of 5900 Mpc ( $z \sim 0.9$ ) is quoted this may be an underestimate as there are predictions that ET can observe NS-NS mergers out to  $z \sim 2$  (Sathyaprakash, Schutz, & Van Den Broeck, 2010).

Piro & Ott (2011) investigate the potential of accreting magnetars to emit gravitational waves using the spin parameter  $\beta$ . If  $\beta \geq 0.14$  then secular instabilities are excited within the NS and if  $\beta \geq 0.26$  then bar-mode instabilities occur. Figure 5.21 shows the evolution of the spin parameter for two of the candidate magnetars used previously, GRBs 060313 and 090515. At no point do these magnetars exceed  $\beta = 0.14$ , however it is important to note that this model assumes the magnetar was formed from a collapsing star. If the magnetar is formed by merging two NSs, a bar mode instability could potentially occur during formation. Baiotti, Giacomazzo, & Rezzolla (2008) completed simulations comparing high mass NS-NS binary mergers and low mass mergers. They found that low mass mergers form a hyper massive NS which exhibits extreme oscillations due to having a large bar mode instability. While the NS settles into a more stable configuration it emits strong gravitational waves.

Shibata & Taniguchi (2006) also study different masses relative to the maximum mass of a NS. They determined that if  $M < M_{max}$  then the NS will emit gravitational waves until it is a stable sphere and collapse to a black hole is dependant on the gravitational wave emission (possibly collapsing within 50 ms) or on forces such as magnetic breaking. In this case, they predict that advanced gravitational wave detectors will be able to observe these events out to 50 Mpc. Alternatively if  $M \sim M_{max}$ , then it collapses rapidly to spherical shape and hence is more likely to create a stable NS which may collapse at late times due to magnetic breaking. The gravitational waves from the more massive NS would be detectable to 10 Mpc. These predictions are consistent with those from Corsi & Mészáros (2009).

In both Baiotti, Giacomazzo, & Rezzolla (2008) and Shibata & Taniguchi (2006), instabilities in the NS formed by a compact merger produce detectable gravitational waves in contrast to the spherical collapse model of Piro & Ott (2011). However Piro & Ott (2011) showed that accretion may have an

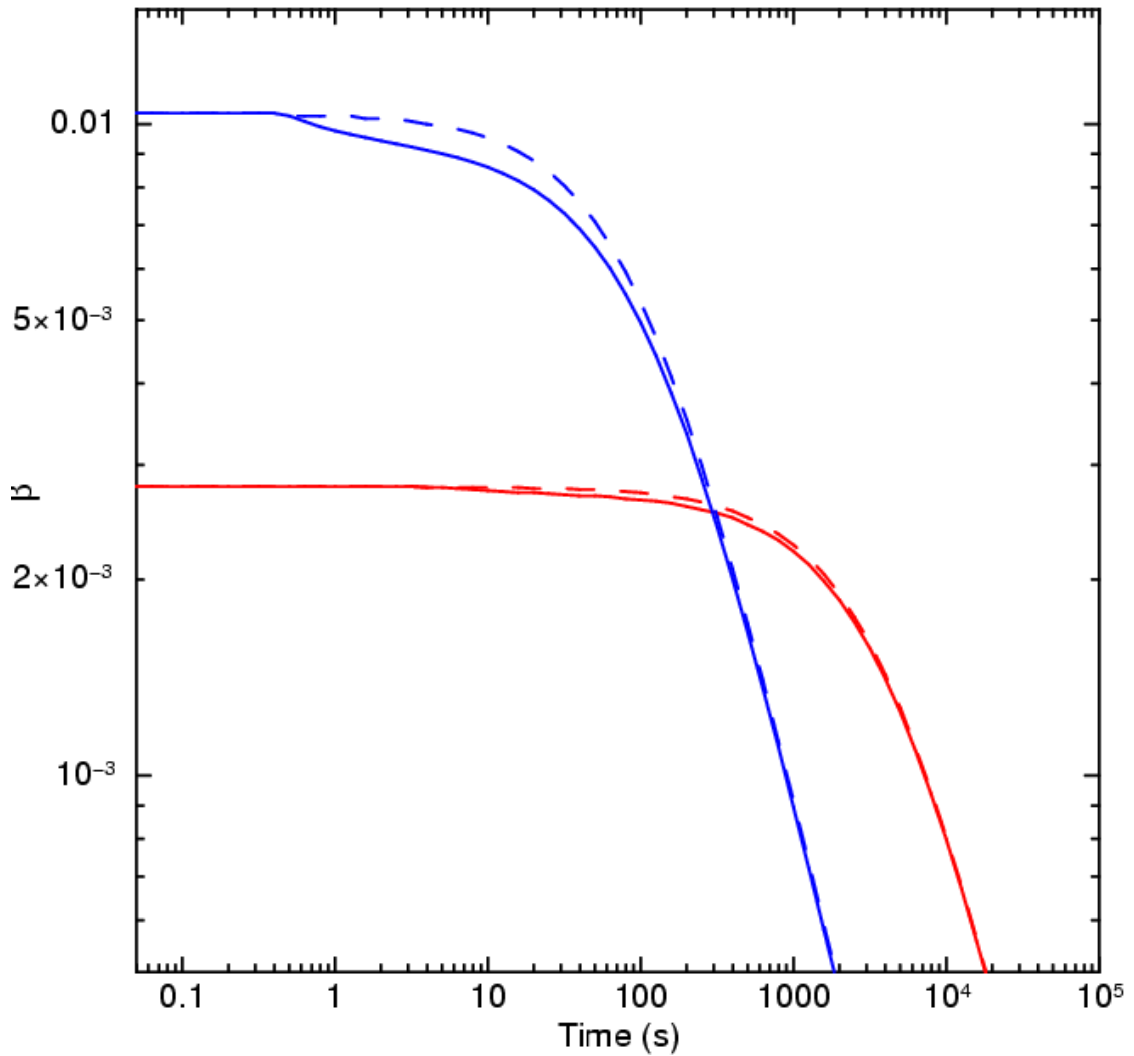


Figure 5.21: The spin parameter  $\beta$  for the magnetar candidates in Figure 5.18, red - GRB 060313 and blue - GRB 090515, assuming they collapse to immediately form a spherical NS. The solid lines assume accretion and dashed lines have no accretion. When accretion occurs it can slightly reduce the GW emission. A GW emission is only expected in this model when  $\beta \geq 0.14$ .

Table 5.5: Gravitational wave predictions for the three different regimes in this magnetar model and applied to future observatories. The distances quoted are luminosity distances.

Phase	Citation	Predicted Amplitude (h)	Distance used (Mpc)	A-LIGO limit (Mpc)	ET Limit (Mpc)	Amplitude at $z \sim 0.1$ (h)
Inspiral	Abadie et al. (2010b)	$4 \times 10^{-24}$	445	445	5900	$4.6 \times 10^{-24}$
Magnetar	Corsi & Mészáros (2009)	$< 1.7 \times 10^{-23}$	10	$< 43$	$< 570$	$< 4 \times 10^{-25}$
Collapse to BH	Novak (1998)	$4 \times 10^{-23}$	10	100	1300	$1 \times 10^{-24}$

important affect on the gravitational wave signal. Therefore, these objects are potentially important sources of gravitational waves and further analysis combining all these factors and the new limits on maximum NS masses is required.

The predictions by Metzger et al. (2011) do not take into account the loss of energy via gravitational waves and this may play a significant role for the formation of a magnetar via the merger of two NSs. If the energy losses via gravitational waves are significant, then the magnetar will spin down more rapidly leading to shorter plateau durations than predicted which is consistent with some of these candidates.

## 5.4 Conclusions

This chapter first considered the BAT-XRT lightcurves of all *Swift* detected SGRBs ( $T_{90} \leq 2$  s) and identified “canonical” like lightcurves. The following conclusions were drawn:

- $\sim 60\%$  of SGRBs have a “canonical” like lightcurve with evidence of ongoing energy injection from the central engine during the plateau phase.
- Although the “canonical” lightcurve phases show many similarities with LGRBs, they are typically orders of magnitude earlier and there is much more variation in the temporal indices.
- The plateau fluence is generally comparable to the prompt fluence, consistent with the results for LGRBs, although there are 3 cases where the plateau fluence is significantly higher.
- The luminosity and duration of the plateau phase is found to be consistent with the identified correlation for “canonical” LGRB lightcurves identified by Dainotti et al. (2010).

Following on from the study of GRB 090515, this work has shown that the X-ray lightcurves of some SGRBs considered could be explained with energy injection from a magnetar which can collapse to form a BH. This is not unexpected as, if one magnetar can be made through this route (GRB 090515), the equation of state of NSs allows this outcome for other NS-NS mergers. This has been shown to be possible for Galactic binaries and reasonable equations of state by Morrison, Baumgarte, &

Table 5.6: A summary showing the main features studied. This gives best magnetar candidates found, possible candidates and SGRBs which do not fit the model. “Fits Model” : has a reduced  $\chi^2 < 3$  (GRB 050509B visually fits well but not enough data points to confirm) “Allowed region” : fits within the required parameter space in Figure 5.10 (? = could fit with various assumptions), “Prompt properties” : the model does not predict unobserved extended emission (if predicted this is a ? as it may be spectrally soft), “Extra component” : there is evidence of an extra component in the X-ray afterglow which is not observed in the optical note this could also be due to absorption (? = borderline case or optical upper limit not constraining), “Predicted region” : do the values for the plateau luminosity and the plateau duration, calculated using equations 4.2 and 4.3, lie within the predicted region in Metzger et al. (2011)? (? = outside region but would fit with reasonable assumptions) and “Magnetar candidate” : yes if fits model and lies in allowed region, ? for a possible candidate, no if definitely not a candidate.

GRB	Fits model	Allowed region	Prompt properties	Extra component	Predicted region	Magnetar candidate
050509B	No	No	Yes	?	No	No
051210	Yes	?	?	Yes	?	?
051221A	Yes	Yes	Yes	No	No	Yes
060313	Yes	Yes	Yes	Yes	Yes	Yes
060801	Yes	Yes	?	Yes	Yes	Yes
061201	Yes	?	Yes	?	?	?
070714A	Yes	?	Yes	?	?	?
070724A	No	Yes	?	?	No	No
070809	Yes	Yes	Yes	?	Yes	Yes
071227	No	Yes	?	No	Yes	No
080426	Yes	Yes	Yes	Yes	?	Yes
080702A	Yes	?	Yes	?	Yes	?

Table 5.6: Continued:

GRB	Fits model	Allowed region	Prompt properties	Extra component	Predicted region	Magnetar candidate
080905A	Yes	?	?	?	No	?
080919	No	?	Yes	No	No	No
081024	Yes	Yes	?	?	Yes	Yes
090426	Yes	Yes	Yes	No	Yes	Yes
090510	Yes	Yes	Yes	Yes	Yes	Yes
090515	Yes	Yes	Yes	Yes	Yes	Yes
090621B	Yes	?	Yes	Yes	?	?
091109B	No	No	Yes	?	No	No
100117A	No	Yes	?	Yes	No	No
100625A	Yes	?	Yes	Yes	?	?
100702A	Yes	Yes	Yes	Yes	Yes	Yes
101219A	Yes	Yes	Yes	Yes	Yes	Yes
110112A	Yes	?	Yes	Yes	?	?

Shapiro (2004). The recent discovery of a  $1.97 M_{\odot}$  NS (Demorest et al., 2010) also has the important consequence of NS mergers being more likely to make a magnetar (Özel et al., 2010). Table 5.6 summarises the findings of Section 5.3, if the candidate fits the model and lies in the allowed region it is considered to be a firm candidate and if they fit the model and could lie in the allowed region with given assumptions then they are possible candidates. The main conclusions are:

- 11 firm candidates (44%) and 8 possible candidates (32%) were found, suggesting that 44 – 76% of SGRBs form a magnetar. Of the 11 firm candidates, 5 are thought to collapse to form a BH and when including possible candidates, 7 out of 19 may collapse to form a BH. This implies that 37–45% of events forming magnetars would collapse to a BH within the first few hundred seconds.
- This Chapter focuses on NS-NS merger progenitors, however the AIC of a WD could also produce a SGRB and leave behind a rapidly rotating magnetar with similar X-ray emission properties. Among other observational signatures, the very different gravitational wave signals between these events may someday allow these progenitors to be distinguished.
- All SGRBs with a plateau in the X-ray lightcurve could potentially be explained by this model.
- There is a clear correlation between the X-ray flux at 100 s with that at 1000 s and 10000 s for the candidates which form a stable magnetar. The late time fluxes are significantly lower for the unstable magnetar cases and the sample which do not fit the model.
- There is a possible correlation between the photon index for the prompt emission and the photon index in the plateau phase for the magnetar candidates.
- There is excess emission in the X-ray afterglows not observed in the optical afterglows for 53% of the magnetar sample. Only 2 magnetar candidates clearly do not have this excess emission and 1 borderline case. However, it is unclear if this is related to the magnetar model.
- Many of the magnetar candidates lie within or close to the predictions of Metzger et al. (2011). Some have significantly shorter plateaus than predicted but this may be associated with gravitational wave emission.

- Accretion onto the newly formed magnetar formed by a NS-NS binary merger has a negligible affect on the spin periods and hence the rotational energy budget of the magnetar. However, it can be shown that accretion can have a significant affect for collapsar progenitors. This may explain late time flares for collapsar progenitors and these calculations suggest the rotational energy budget could exceed  $10^{53}$  erg for some combinations of initial spin periods and magnetic fields.
- The unstable magnetar candidates, those which collapse to form a BH, are potentially accreting more material than the stable candidates. This is suggested as a potential solution for why they collapse at late times.
- The rate of magnetar formation found in this model are consistent with upper limits set by the Galactic magnetar birth rate and the predicted NS merger rate, although the latter are still highly uncertain.
- These objects are highly interesting targets for future gravitational wave observatories as they are predicted to emit gravitational waves during merger, the magnetar phase (likely to be increased via accretion and bar mode instabilities) and, in some cases, the final collapse to form a BH. ET would be particularly useful for this as it could be used to probe these events out to  $z > 0.9$ , which covers the majority of the expected redshift distribution of SGRBs.
- For the candidates which form a stable magnetar: Duncan & Thompson (1992) showed that the amount of energy available for an SGR giant flare is  $E \propto 3 \times 10^{47} B_{15}^2$  erg. Hence a young magnetar, with magnetic fields of  $B_{15} \sim 10$ , could produce a giant flare with an energy of  $3 \times 10^{49}$  erg. This value is comparable to the isotropic energy of some SGRBs (e.g. GRB 080905A at  $z \sim 0.12$ , Rowlinson et al., 2010a) so would be observable in the local Universe. Both of the merger and giant flare events are very rare, however considering these models it is possible (although very unlikely) that in the future there may be two spatially co-incident SGRBs. This has also been proposed for LGRBs by Giannios (2010) and they suggest that these magnetar candidates could be identified by discovering an old spatially coincident radio GRB afterglow in nearby galaxies.

This work does not show conclusive proof that SGRBs are forming magnetars, however it does show that these models could fit a large proportion of the observed SGRBs, could explain much of the evidence for late time central engine activity in SGRBs, and this may have important observational consequences.

# Chapter 6

## Conclusions

Since the discovery of GRBs in 1967, it has become increasingly evident that there are at least two different types of GRB. LGRBs have been associated with core collapse SN, whereas the progenitors of SGRBs are still debated. The observations of the *Swift* satellite have enabled the localisation and multiwavelength followup of SGRBs, with almost 7 years worth of observations available (including the detection of >30 SGRB X-ray afterglows) it is now possible to start studying the properties of SGRBs in depth. This Thesis has focused on SGRBs detected by the IPN and the *Swift* Satellite and has used these observations to place constraints on the current progenitor theories.

### **6.1 Progress towards the progenitors and central engines of SGRBs**

#### **6.1.1 Extragalactic SGR giant flares**

Following the detection of a giant flare from SGR 1806-20, it has been hypothesised that SGR giant flares are detectable in the nearby Universe and would have similar prompt emission properties to a SGRB. Therefore this is a progenitor candidate for a small percentage of SGRBs which may be associated with nearby galaxies. Included in Chapter 2 are new results for three SGRBs and their suggested host galaxy associations, all detected by the IPN, whose progenitors may be extragalactic SGRs: GRB

051103 with M81, GRB 070201 with M31 and GRB 110406A with NGC404. Unfortunately, due to the nature of the IPN, the position errors obtained for these GRBs are very large and cannot conclusively associate the GRBs with their candidate host galaxies.

- GRB 051103 remains inconclusive, the prompt properties and undetected optical afterglow are consistent with both an extremely energetic extragalactic SGR giant flare and a typical SGRB with little optical afterglow. However, if it were an SGR it would be likely to require an alternative formation route to that normally suggested for SGRs as there is no evidence of a SNR within the error ellipse and the error ellipse only crosses the outer boundary of M81. There is a candidate Galactic magnetar lying outside the plane of the Galaxy which may be consistent with a different formation route (Callingham et al., 2011), if confirmed this would be consistent with the findings for GRB 051103.
- GRB 070201 also remains inconclusive, but is a more convincing candidate than GRB 051103. It was noted prior to this Thesis that the error trapezium crosses a region of active star formation within M31. Chapter 2 has associated a likely SNR with a faint X-ray source within the error trapezium with a  $<0.1\%$  probability of chance alignment. The separation of these sources and their other properties are consistent with known SGRs, making it a candidate quiescent counterpart to this GRB. This, in addition to the prompt emission which is consistent with the giant flare from SGR 1806-20, provides strong support for the SGR giant flare progenitor theory for GRB 070201.
- GRB 110406A was recently detected by the IPN, however it was Sun constrained for many weeks preventing any multiwavelength follow up. In Chapter 2, it is noted that the prompt emission and putative host galaxy properties make it an ideal extragalactic SGR giant flare candidate.

It has been shown, using a probability argument based on 3 Galactic giant flares observed, that it is very unlikely that GRB 051103 and GRB 070201 are both extragalactic SGR giant flares. Based on the literature and the results obtained in Chapter 2, GRB 070201 appears to be the strongest candidate. The presence of active star formation in M31 and NGC404 provide further supporting evidence as massive stars are the theorised progenitor of SGRs. However, as this Thesis has discussed, there are alternative

formation routes for SGRs which would explain the location of GRB 051103, for example WD-WD mergers and the AIC of a WD.

No extragalactic SGR giant flare has been confirmed to date as this requires a firm host galaxy association and ideally an association with a quiescent X-ray source and SNR. This will require rapid and deep follow up observations to identify the multiwavelength afterglow giving more accurate positions. Satellites such as *Swift* and *SVOM* (see Section 6.2.1), with rapid follow-up capabilities, are ideal for this study. These are relatively rare events within the field of view of instruments such as *Swift* so the likelihood of detection is low. Despite this, it is surprising that a definite candidate has not been well localised yet and it is anticipated that the chance of detection is good in the future.

### 6.1.2 Compact Binary Mergers

The merger of two NSs or a NS and a BH is the most popular progenitor theory for SGRBs, however no conclusive observational evidence has been obtained to date. This Thesis has compared the observed properties of several SGRBs to those expected from a compact binary merger. The main findings are:

- GRB 080905A was detected offset from a spiral galaxy, with a chance alignment of  $<1\%$ , and is at the lowest confirmed redshift for a SGRB. The X-ray and optical afterglows were faint and the isotropic energy was  $\sim 5 \times 10^{49}$  erg. These properties are consistent with a binary merger occurring in a low density environment. Spatially resolved spectroscopy was obtained for the host galaxy, the first time this has been completed for a SGRB, showing that GRB 080905A occurred offset from the spiral arm with least active star formation and a relatively old population. This is consistent with the merger of a compact binary system which has been kicked out of its the host galaxy.
- GRB 090515 was a hostless SGRB with the faintest detected optical afterglow to date and an undetectable X-ray afterglow at late times. The prompt and late time properties are consistent with a compact binary merger.
- The *Swift* SGRB sample used in Chapter 5, along with GRB 090515, have shown that  $\sim 60\%$  of

SGRBs show evidence of late time energy injection within their X-ray afterglows. This energy injection results in similar behaviour to that observed in the LGRBs with “canonical” lightcurves, but the stages all occur much earlier in the lightcurves for the SGRB sample. This energy injection is problematic for the typical compact binary merger progenitor theory.

The *Swift* satellite revolutionised the study of SGRBs, however it remains difficult to detect the faint and rapidly fading optical afterglows as this requires rapid follow up on an 8 m class telescope. This means that host galaxy associations and redshifts, such as that obtained for GRB 080905A, are also very difficult to obtain. Particularly difficult to obtain are absorption redshifts from SGRB afterglows, which are vital for unambiguously identifying host galaxies and redshifts, however this requires faster responses with large optical facilities.

Although not considered in this Thesis, there are suggestions that the SGRB population should be further subdivided. For example SGRBs at  $z > 1$  (e.g. GRB 090426 at  $z = 2.609$ ; Levesque et al., 2009) and those appearing to be associated with young stellar populations (e.g. GRB 050709; Covino et al., 2006). These may just be the tail of LGRBs in the overlapping distribution of  $T_{90}$  durations (Figure 1.1) or may have a different progenitor (e.g. Virgili et al., 2011).

More data are required to further the understanding of the progenitors and central engines of SGRBs. This would also aid in determining the overlap between SGRB and LGRB populations and clarifying the nature of the EE SGRBs. The European Extremely Large Telescope (EELT, construction will begin in 2012 to be completed in the 2020s; Gilmozzi & Spyromilio, 2008) will be very useful in the detection of even fainter afterglows and study the local environments within the host galaxies of SGRBs in detail using spatially resolved spectroscopy.

### 6.1.3 Magnetars as the central engine of some SGRBs

Chapters 4 and 5 of this Thesis have shown that there is evidence of ongoing central engine activity within some SGRB observations that is inconsistent with the typical compact binary merger progenitor models. There is now increasing observational evidence which suggests that the equation of state of

NSs is relatively hard, allowing more massive NSs than previously thought. It has been proposed that two merging NSs could form a magnetar, whose late time stability depends upon the masses of the two NSs, and can emit a vast amount of rotational energy as observable electromagnetic radiation. The possibility that such a magnetar could produce the energy injection observed in SGRB afterglows has been investigated.

- GRB 090515 has the most unusual X-ray afterglow observed to date for a SGRB. Chapter 4 showed that the X-ray afterglow of GRB 090515 can be naturally explained using an unstable magnetar which powers an X-ray plateau for  $\sim 240$  s and then collapses to form a BH. The other properties of GRB 090515 point to a compact binary merger so this is the first NS-NS merger candidate which is thought to form an unstable magnetar.
- A sample of *Swift* detected SGRBs are fitted with the magnetar model in Chapter 5, allowing for both stable and unstable magnetars, and the model was able to explain much of the observed energy injection within SGRB lightcurves. This, alongside recent advances in understanding of NSs, leads to the suggestion that many NS-NS mergers form a magnetar which inject energy into the afterglows at late time. Thus solving the problems of energy injection with the typical merger theory.
- As stable magnetars may be formed via the merger of two NSs, this provides an additional mechanism for the production of SGRs which may go on to produce observable giant flares.

The magnetar model could explain energy injection within SGRBs and is consistent with recent results. However, the theoretical model requires further work to determine the emission mechanism, efficiency and beaming angles. The NS equation of state is also very important for this model and observations are starting to place interesting constraints on this.

Magnetars are also proposed to be the central engine of LGRBs and several candidates have been proposed (including those in Lyons et al., 2010). It would be very interesting to fit the QDP magnetar model, used in Chapter 5, to LGRB X-ray lightcurves to determine if magnetars could also realistically explain the majority of the plateaus observed in LGRB lightcurves. The LGRB candidates can then be compared to the SGRB candidates.

The extended emission observed in EE SGRBs has also been proposed to originate from a magnetar central engine (e.g. Bucciantini et al., 2011). However, the emission mechanism is thought to be different to that seen in the plateau phase. The model currently has too many free parameters for fitting to lightcurves. The EE SGRBs also have evidence for energy injection at later times in their lightcurves. Future work could combine the two different parts of the magnetar model to determine if they can consistently explain the observed X-ray lightcurves of the EE SGRBs.

## 6.2 The future

There are many missions which will prove highly useful to the study of SGRBs in the future. Some of these have already been mentioned in the text, e.g. the EELT in Sections 2.5 and 6.1.2, and this section focuses on the future contributors which are expected to have the most impact on the study of SGRBs.

### 6.2.1 Detection of SGRBs

*Swift* is now nearly 7 years old and still discovering new, unusual GRBs. It will continue to add to the SGRB sample and hopefully will detect an extragalactic SGR giant flare. However, *Swift* will not be operational indefinitely. The *Space-based multi-band astronomical Variable Object Monitor* (SVOM; Götz et al., 2009b) is expected to launch in 2016/17 and will operate in a similar manner to *Swift* by detecting the GRB and then slewing to point an X-ray telescope and Optical telescope at the location to obtain accurate positions. However, as the gamma-ray detector, ECLAIRS (4 –250 keV), operates in a softer energy band than BAT (15 – 350 keV) it is unclear how many typical short hard GRBs it will detect. BAT operates at a softer energy band than BATSE and has found a smaller percentage of SGRBs (~10% compared to ~25%), so ECLAIRS may also detect far fewer.

Further in the future, the *Joint Astrophysics Nascent Universe Satellite* (JANUS; Burrows et al., 2010) has been proposed. However, *JANUS* aims to detect high redshift GRBs and will use an X-ray telescope to detect them. As this is an even softer detector, it is unclear what the chances are that *JANUS* will detect SGRBs. Another proposal was the *Energetic X-ray Imaging Survey Telescope* (EXIST; Grindlay

et al., 2003), also using softer detectors to find high redshift GRBs, but *EXIST* was unranked in the Astro2010 Decadal Survey and is now going to be redesigned<sup>1</sup>.

Therefore, after *Swift* and *SVOM* the future looks very bleak for the detection of typical SGRBs and obtaining rapid positions as missions are targeting the softer high redshift GRBs. This is unfortunate as upcoming instruments such as Advanced-LIGO make it an exciting time for the study of SGRBs.

### 6.2.2 LOFAR

In 2010 the LOw Frequency ARray (LOFAR, 10 – 250 MHz) became operational and aims to detect a wide range of transient objects. Stappers et al. (2011) describes the methods which LOFAR will use to detect a wide range of transient objects and this will likely include GRBs. The work of LOFAR on transient objects will then be applied to the study of transients with the upcoming Square Kilometer Array (SKA)<sup>2</sup>.

van Eerten & MacFadyen (2011) have modelled the multi wavelength afterglow lightcurves of SGRBs and predicted the detectability for instruments such as LOFAR. Additionally, it has been shown that LOFAR may detect orphan SGRB afterglows even years afterwards assuming that they formed via a compact binary merger (Nakar & Piran, 2011).

As shown in Chapters 4 and 5, the merger of two NSs may also form a magnetar. The magnetar is predicted to produce a radio flare which is detectable by LOFAR (Pshirkov & Postnov, 2010). The duration and magnitude of this flare is dependent on the lifetime of the magnetar. In Pshirkov & Postnov (2010) the radio flare only lasts for a few ms as they assume the magnetar is short lived. The radio signal becomes a precursor to the SGRB with a flux,  $F$ , given by equation 6.1 where  $L_{50}$  is the luminosity of the flare in units of  $10^{50}$  erg  $s^{-1}$ ,  $\gamma$  is the Lorentz factor and  $D$  is the distance to the merger in Gpc. They predict an observable signal for nearby SGRBs. They do not consider the possibility that the magnetar could last for significantly longer durations (as seen in Chapters 4 and 5) so it will be very interesting to see if LOFAR indeed detects these flares and their durations as this would provide

---

<sup>1</sup><http://exist.gsfc.nasa.gov/>

<sup>2</sup><http://www.skatelescope.org/>

supporting evidence for the magnetar model.

$$F(120 \text{ MHz}) \sim 6 \times 10^{2+15\gamma} L_{50}^{1+\gamma} \left( \frac{1 \text{ Gpc}}{D} \right)^4 \text{ Jy} \quad (6.1)$$

### 6.2.3 ALMA

The Atacama Large Millimeter/submillimeter Array (ALMA, operational at a limited level from the end of 2011; Brown, Wild, & Cunningham, 2004) will be ideal for studying the afterglows of GRBs as it operates at the peak wavelengths for the afterglow synchrotron emission (de Ugarte Postigo et al., 2011). Additionally, ALMA observations are not affected by interstellar dust allowing the study of dark and high redshift (up to  $z \sim 10$ ) GRB afterglows. de Ugarte Postigo et al. (2011) also show that ALMA will be able to conduct spatially resolved spectroscopy of host galaxies in a similar manner to that conducted in Chapter 3 for GRB 080905A but at wavelengths ideal for studying the molecular emission lines.

### 6.2.4 Neutrino Detectors

GRBs are predicted to emit copious amounts of neutrinos (e.g. Waxman, 1997; Razzaque, Mészáros, & Waxman, 2003) and several neutrino experiments have attempted to detect these sources. Indeed the detection of neutrinos could aid in confirming the central engine and emission mechanisms of GRBs (e.g. identify a magnetar central engine formed during a compact binary merger and when collapse to a BH occurs; Sekiguchi et al., 2011).

IceCube (Achterberg et al., 2006) has already been used in its partially completed state to search for neutrinos from individual GRBs giving 90% upper limits (Abbasi et al., 2010). The full configuration is now complete and this will be able to either detect these neutrinos from GRBs or place constraining upper limits on them.

The ANTARES (Astronomy with a Neutrino Telescope and Abuss environmental RESearch) neutrino detector, online from 2008, aims to detect neutrinos from GRBs (ANTARES Collaboration, 2011a). To date, no cosmic sources have been detected (ANTARES Collaboration et al., 2011b).

### 6.2.5 Advanced LIGO and ET

As described in Section 1.5.2, one of the best methods to confirm the progenitor of SGRBs would be the detection of a SGRB with a spatially and temporally coincident gravitational wave detection. Not only would this identify the progenitor, the gravitational wave signal is predicted to be able to place tight constraints on the equation of state of NSs, measure the masses of the merging objects and provide the actual distance to the merger (e.g. Read et al., 2009; Hotokezaka et al., 2011). This “smoking gun” observation has not been achieved with LIGO as it does not probe far enough into the Universe. When Advanced-LIGO comes online in 2014, the prospects of detection significantly improve as the detection limit of 445 Mpc (Abadie et al., 2010b) is much closer to the nearest confirmed SGRB ( $\sim 560$  Mpc, GRB 080905A). If Advanced-LIGO fails to detect a signal coincident with a SGRB, this will start placing very interesting constraints on the progenitors of SGRBs. To follow on from Advanced-LIGO, the ET has been proposed and many co-incident detections would be expected. Typically the predicted signal focuses on the compact binary inspiral immediately prior to the actual merger. In Chapter 5 of this Thesis, it is shown that other signals may be expected from the same source and predicted limits are provided for Advanced-LIGO and ET.

However, the coincident detection relies upon a satellite which is able to detect SGRBs being operational when these instruments come on line and, as discussed in Section 6.2.1, this may not be the case depending upon the lifetime of *Swift* and the SGRB detection capabilities of *SVOM*.

## 6.3 Final concluding remarks

The work presented in this Thesis has extended the previous knowledge of SGRBs by presenting and interpreting new observational data. In many ways the data support the favoured compact binary merger

progenitor but there are still many significant discrepancies and open questions. With the in depth follow up of more SGRBs and the use of multimessenger observations, it will be possible to start constraining the theoretical models and possibly solve the ongoing mystery of SGRBs.

# BIBLIOGRAPHY

- Abadie J., et al., 2010a, *PhRvD*, 82, 102001
- Abadie J., et al., 2010b, *CQGra*, 27, 173001
- Abbasi R., et al., 2010, *ApJ*, 710, 346
- Abbott B., et al., 2008, *ApJ*, 681, 1419
- Ackermann M., et al., 2010, *ApJ*, 716, 1178
- Achterberg A., et al., 2006, *APh*, 26, 155
- Adelman-McCarthy J. K., et al., 2008, *ApJS*, 175, 297
- Akerlof C., et al., 1999, *Nature*, 398, 400
- Akerlof C., et al., 2000, *ApJ*, 542, 251
- Akerlof C. W., Zheng W., Pandey S. B., McKay T. A., 2011, *ApJ*, 726, 22
- Alard C., 2000, *A&AS*, 144, 363
- Alard C., Lupton R. H., 1998, *ApJ*, 503, 325
- Amati L., et al., 2002, *A&A*, 390, 81
- Amati L., 2006, *MNRAS*, 372, 233
- Amati L., 2010, *arXiv*, arXiv:1002.2232

ANTARES Collaboration, 2011a, arXiv, arXiv:1104.1607

ANTARES Collaboration, et al., 2011b, arXiv, arXiv:1108.0292

Antonelli L. A., et al., 2009, A&A, 507, L45

Appenzeller I., Rupprecht G., 1992, Msngr, 67, 18

Aptekar, R. et al., 1995, Space Sci. Rev. 71, 265

Asplund, M., Grevesse, N., Sauval, A. J., Allende Prieto, C., Kiselman, D., 2004, A&A, 417, 751

Atteia, J.-L. et al., 2003, AIP Conf. Proc. 662, Eds. G. Ricker and R. Vanderspek, (AIP: New York), 17

Atwood W. B., et al., 2009, ApJ, 697, 1071

Baade W., Arp H., 1964, ApJ, 139, 1027

Baiotti L., Giacomazzo B., Rezzolla L., 2008, PhRvD, 78, 084033

Balogh, M. L., Morris, S. L., Yee, H. K. C., Carlberg, R. G., Ellington, E., 1999, ApJ, 527, 54

Band, D. et al., 1993, Ap. J. 413, 281

Barbier L., et al., 2005a, GCN Circ., 4194, 1

Barbier L., et al., 2007, GCN Circ., 6623, 1

Barkov M. V., Pozanenko A. S., 2011, arXiv, arXiv:1103.4246

Baron E., Cooperstein J., Kahana S., Nomoto K., 1987, ApJ, 320, 304

Barthelmy S. D., et al., 2005a, SSRv, 120, 143

Barthelmy, S. D., et al., 2005b, Nature, 438, 994

Barthelmy S., et al., 2005c, GCN Circ., 3385, 1

Barthelmy S., et al., 2006, GCN Circ., 5256, 1

Barthelmy S. D., et al., 2007, GCN Circ., 6622, 1

Barthelmy S. D., et al., 2008a, GCN Circ., 8113, 1

Barthelmy S. D., et al., 2008b, GCN Circ., 8458, 1

Barthelmy S. D., et al., 2008c, GCN Circ., 8404, 1

Barthelmy S., et al., 2009a, GCN Circ., 9364, 1

Barthelmy S., et al., 2009b, GCN Circ., 9494, 1

Barthelmy S. D., et al., 2010, GCN Circ., 10891, 1

Barthelmy S. D., Sakamoto T., Stamatikos M., 2011, GCN Circ., 11557, 1

Barkov M. V., Komissarov S. S., 2008, MNRAS, 385, L28

Baumgartner W. H., et al., 2008, GCN Circ., 8275, 1

Baumgartner W. H., et al., 2010, GCN Circ., 10926, 1

Beardmore A.P., et al., 2009, GCN Circ., 9356, 1

Beardmore A.P., Evans, P.A., 2009, GCN Circ., 9368, 1

Belczynski K., Perna R., Bulik T., Kalogera V., Ivanova N., Lamb D. Q., 2006, ApJ, 648, 1110

Bethe H. A., Brown G. E., 1998, ApJ, 506, 780

Berger E., 2005, GCN Circ., 3801, 1

Berger, E., et al., 2005, Nature, 438, 988

Berger E., 2007, ApJ, 670, 1254

Berger E., Morrell N., Roth M., 2007, GCN Circ., 7151, 1

Berger E., 2009, ApJ, 690, 231

Berger E., Cenko S. B., Fox D. B., Cucchiara A., 2009, ApJ, 704, 877

Berger E., Kelson D., 2009, GCN Circ., 8934, 1

Berger E., 2010, ApJ, 722, 1946

Bertin E., Arnouts S., 1996, A&AS, 117, 393

Bibby J. L., Crowther P. A., Furness J. P., Clark J. S., 2008, MNRAS, 386, L23

Bissaldi, E., McBreen, S., Connaughton, V., von Kienlin, A., 2008, GCN Circ., 8204, 1

Blandford R. D., Znajek R. L., 1977, MNRAS, 179, 433

Bloom J. S., Djorgovski S. G., Kulkarni S. R., Frail D. A., 1998, ApJ, 507, L25

Bloom J. S., et al., 1999, Nature, 401, 453

Bloom, J. S., Frail, D. A., Sari, R., 2001, AJ, 121, 2879

Bloom, J. S., Kulkarni, S. R., Djorgovski, S. G., 2002, AJ, 123, 1111

Bloom, J. S., et al., 2006, ApJ, 638, 354

Bloom J. S., Butler N. R., Perley D. A., 2008, AIPC, 1000, 11

Boella G., Butler R. C., Perola G. C., Piro L., Scarsi L., Bleeker J. A. M., 1997, A&AS, 122, 299

Boggs, S. et al., 2007, ApJ. 661, 458

Bohlin R. C., Savage B. D., Drake J. F., 1978, ApJ, 224, 132

Bonnarel F., et al., 2000, A&AS, 143, 33

Bothwell M. S., et al., 2011, MNRAS, 415, 1815

Breeveld A., et al., 2005, GCN Circ., 3397, 1

Breeveld A., Stamatikos M., 2011, GCN Circ., 11560, 1

Brown R. L., Wild W., Cunningham C., 2004, AdSpR, 34, 555

Brown P. J., Racusin J. L., 2006, GCN Circ., 5385, 1

Brown, P. J. & Pagani, C. 2008, GCN 8208

Bruzual, A. G., 1983, ApJ, 273, 105

Bucciantini N., Quataert E., Metzger B. D., Thompson T. A., Arons J., Del Zanna L., 2009, MNRAS, 396, 2038

Bucciantini N., Metzger B. D., Thompson T. A., Quataert E., 2011, arXiv, arXiv:1106.4668

Burrows D. N., et al., 2005a, SSRv, 120, 165

Burrows D. N., et al., 2005b, Sci, 309, 1833

Burrows D. N., et al., 2006, ApJ, 653, 468

Burrows D. N., et al., 2007, RSPTA, 365, 1213

Burrows D. N., Roming P. W. A., Fox D. B., Herter T. L., Falcone A., Bilén S., Nousek J. A., Kennea J. A., 2010, SPIE, 7732,

Butler N. R., et al., 2005, ApJ, 621, 884

Butler N. R., Kocevski D., Bloom J. S., Curtis J. L., 2007, ApJ, 671, 656

Caito L., Amati L., Bernardini M. G., Bianco C. L., de Barros G., Izzo L., Patricelli B., Ruffini R., 2010, A&A, 521, A80

Callingham J. R., Farrell S. A., Gaensler B. M., Lewis G. F., Middleton M. J., 2011, arXiv, arXiv:1108.0697

Calzetti D., Kinney A. L., Storchi-Bergmann T., 1994, ApJ, 429, 582

Campana S., et al., 2006, Nature, 442, 1008

Cannizzo J. K., Troja E., Gehrels N., 2011, ApJ, 734, 35

Cano Z., et al., 2011, MNRAS, 174

Cardelli, J. A., Clayton, G. C. & Mathis, J. S. 1989, ApJ, 345, 245

Castro-Tirado A. J., Gorosabel J., 1999, A&AS, 138, 449

Cenko S., Cobb B.E., Perley D.A., Bloom J.S., 2009, GCN Circ., 8933, 1

Cenko S. B., et al., 2010, ApJ, 711, 641

Chapman R., Priddey R. S., Tanvir N. R., 2009, MNRAS, 395, 1515

Chester M. M., Grupe D., 2007, GCN Circ., 6633, 1

Chester M. M., Marshall F. E., 2007, GCN Circ., 6751, 1

Chiappetti L., et al., 2005, A&A, 439, 413

Chincarini G., et al., 2010, MNRAS, 406, 2113

Chornock R., Berger E., 2011, GCN Circ., 11483, 1

Christensen, L., Hjorth, J., & Gorosabel, J., 2004, A&A, 425, 913

Christensen, L., Vreeswijk, P. M., Sollerman, J., Thöne, C. C., Le Floch, E. & Wiersema, K. 2008, A&A, 490, 45

Chuang K. W., White R. S., Klebesadel R. W., Laros J. G., 1992, ApJ, 391, 242

Church R. P., Levan A. J., Davies M. B., Tanvir N., 2011, MNRAS, 355

Cline T. L., et al., 1980, ApJ, 237, L1

Coburn W., Boggs S. E., 2003, Nature, 423, 415

Colgate S. A., 1968, CaJPS, 46, 476

Corbel S., Wallyn P., Dame T. M., Durouchoux P., Mahoney W. A., Vilhu O., Grindlay J. E., 1997, ApJ, 478, 624

Corsi A., Mészáros P., 2009, ApJ, 702, 1171

Corsi A., Guetta D., Piro L., 2010, ApJ, 720, 1008

Costa, E., et al., 1997, Nature, 387, 783

Covino S., et al., 2006, A&A, 447, L5

Covino S., et al., 2008, GCN Circ., 8271, 1

Crowther P. A., Bibby J. L., Furness J. P., Simon Clark J., 2011, AdSpR, 47, 1341

Cucchiara A., Fox D. B., Berger E., Price P. A., 2006, GCN Circ., 5470, 1

Cucchiara A., Sakamoto T., 2007, GCN Circ., 7150, 1

Cucchiara A., et al., 2011, ApJ, 736, 7

Cui X.-H., Aoi J., Nagataki S., Xu R.-X., 2010, AIPC, 1279, 136

Cummings J., et al., 2005, GCN Circ., 4365, 1

Cummings, J., et al., 2008a, GCN Circ., 8187, 1

Cummings J., et al., 2008b, GCN Circ., 7640, 1

Cummings J. R., Page K. L., Beardmore A. P., Gehrels N., 2009, ATel, 2127, 1

Curran P. A., Starling R. L. C., O'Brien P. T., Godet O., van der Horst A. J., Wijers R. A. M. J., 2008, A&A, 487, 533

Curran P. A., 2009, GCN Circ., 9552, 1

D'Avanzo P., et al., 2009, A&A, 498, 711

Dai Z. G., Lu T., 1998a, A&A, 333, L87

Dai Z. G., Lu T., 1998b, PhRvL, 81, 4301

Dai Z. G., Wang X. Y., Wu X. F., Zhang B., 2006, Sci, 311, 1127

Daigne F., Mochkovitch R., 1998, MNRAS, 296, 275

Daigne F., Mochkovitch R., 2000, A&A, 358, 1157

Daigne, F., Rossi, E. M., & Mochkovitch, R., 2006, MNRAS, 372, 1034

Dainotti M. G., Willingale R., Capozziello S., Fabrizio Cardone V., Ostrowski M., 2010, ApJ, 722, L215

Dall'Osso S., Stratta G., Guetta D., Covino S., de Cesare G., Stella L., 2011, A&A, 526, A121

de Grijs R., O'Connell R. W., Becker G. D., Chevalier R. A., Gallagher J. S., III, 2000, AJ, 119, 681

Demorest P. B., Pennucci T., Ransom S. M., Roberts M. S. E., Hessels J. W. T., 2010, Nature, 467, 1081

de Pasquale M., et al., 2003, ApJ, 592, 1018

de Pasquale M., Ziaepour H., 2007, GCN Circ., 6660, 1

de Pasquale M., 2008, GCN Circ., 7932, 1

de Pasquale M., Stratta G., 2008, GCN Circ., 8406, 1

de Pasquale M., et al., 2010, ApJ, 709, L146

de Pasquale M., Siegel M. H., 2010, GCN Circ., 922, 1

de Pasquale M., Holland S. T., Oates S., 2010, GCN Circ., 344, 1

de Ugarte Postigo A., et al., 2006, ApJ, 648, L83

de Ugarte Postigo, A., Malesani, D., Levan, A. J., Hjorth, J., Tanvir, N. R., 2008, GCN Circ., 8195, 1

de Ugarte Postigo A., et al., 2011, arXiv, arXiv:1108.1797

Dermer C. D., Atoyan A., 2006, ApJ, 643, L13

Della Valle M., et al., 2006, Nature, 444, 1050

Devereux N. A., Price R., Wells L. A., & Duric N., 1994, AJ, 108, 1667

Djorgovski S. G., Kulkarni S. R., Bloom J. S., Goodrich R., Frail D. A., Piro L., Palazzi E., 1998, ApJ, 508, L17

Donaghy T. Q., et al., 2006, astro, arXiv:astro-ph/0605570

Dorman B., Arnaud K. A., 2001, ASPC, 238, 415

Duncan R. C., Thompson C., 1992, ApJ, 392, L9

Eichler, D., Livio, M., Piran, T., Schramm, D. N., 1989, Nature, 340, 126

Eichler D., 2002, MNRAS, 335, 883

Eldridge J. J., Langer N., Tout C. A., 2011, MNRAS, 692

Evans P. A., et al., 2007, A&A, 469, 379

Evans, P. A., Osborne, J. P., Goad, M. R., 2008, GCN Circ., 8203, 1

Evans P. A., et al., 2009, MNRAS, 397, 1177

Fahlman G. G., Gregory P. C., 1981, Nature, 293, 202

Falcone A. D., et al., 2006, ApJ, 641, 1010

Fan Y. Z., Zhang B., Proga D., 2005, ApJ, 635, L129

Fan Y.-Z., Xu D., 2006, MNRAS, 372, L19

Fenech D. M., Muxlow T. W. B., Beswick R. J., Pedlar A., Argo M. K., 2008, MNRAS, 391, 1384

Fenimore, E., Evans, W., Klebesadel, R., Laros, J., and Terrell, J., 1981, Nature, 289, 42

Fenimore E. E., Klebesadel R. W., Laros J. G., 1996, ApJ, 460, 964

Fenimore E., et al., 2005, GCN Circ., 4382, 1

Feroci M., Hurley K., Duncan R. C., Thompson C., 2001, ApJ, 549, 1021

Ferrero P., et al., 2007, AJ, 134, 2118

Figer D. F., Najarro F., Geballe T. R., Blum R. D., Kudritzki R. P., 2005, ApJ, 622, L49

Fishman G. J., Meegan C. A., Parnell T. A., Wilson R. B., Paciasas W., Mateson J. L., Cline T. L.,  
Teegarden B. J., 1985, ICRC, 3, 343

Foley S., McGlynn S., Hanlon L., McBreen S., Martin-Carrillo A., McBreen B., Topinka M., Meehan  
S., 2009, BaltA, 18, 279

Fong, W.-f., Berger, E., Fox, D. B., 2010, ApJ, 708, 9

Fox, D. B., et al., 2005, Nature, 437, 845

Frail D. A., Kulkarni S. R., Nicastro L., Feroci M., Taylor G. B., 1997, Nature, 389, 261

Frail, D. A., et al., 1999, ApJL, 525, L81

Frail D. A., et al., 2001, ApJ, 562, L55

Frederiks D. D., Palshin V. D., Aptekar R. L., Golenetskii S. V., Cline T. L., Mazets E. P., 2007a, *AstL*, 33, 19

Frederiks D. D., Golenetskii S. V., Palshin V. D., Aptekar R. L., Ilyinskii V. N., Oleinik F. P., Mazets E. P., Cline T. L., 2007b, *AstL*, 33, 1

Freedman W. L., et al., 1994, *ApJ*, 427, 628

Fruchter A. S., et al., 1999, *ApJ*, 519, L13

Fruchter, A. S., et al., 2006, *Nature*, 441, 463

Fryer C. L., 2004, *ApJ*, 601, L175

Fynbo, J. P. U. et al. 2000, *ApJ*, 542, L89

Fynbo J. U., et al., 2001, *A&A*, 369, 373

Fynbo J. P. U., et al., 2004, *ApJ*, 609, 962

Fynbo, J. P. U. et al. 2006, *Nature* 444, 1047

Gaensler B. M., Slane P. O., Gotthelf E. V., Vasisht G., 2001, *ApJ*, 559, 963

Gaensler B. M., McClure-Griffiths N. M., Oey M. S., Haverkorn M., Dickey J. M., Green A. J., 2005, *ApJ*, 620, L95

Galama T. J., et al., 1998, *Nature*, 395, 670

Gal-Yam A., et al., 2006, *Nature*, 444, 1053

Gal-Yam A., et al., 2008, *ApJ*, 686, 408

Gao W.-H., Fan Y.-Z., 2006, *ChJAA*, 6, 513

Gehrels N., et al., 2004, *ApJ*, 611, 1005

Gehrels N., et al., 2005, *Nature*, 437, 851

Gehrels N., et al., 2006, *Nature*, 444, 1044

Gehrels N., et al., 2008, ApJ, 689, 1161

Ghirlanda G., Ghisellini G., Celotti A., 2004, A&A, 422, L55

Ghirlanda G., Ghisellini G., Firmani C., 2005, MNRAS, 361, L10

Ghirlanda G., Nava L., Ghisellini G., Firmani C., Cabrera J. I., 2008, MNRAS, 387, 319

Ghirlanda G., Nava L., Ghisellini G., Celotti A., Firmani C., 2009, A&A, 496, 585

Ghirlanda G., Ghisellini G., Nava L., 2010, A&A, 510, L7

Ghisellini G., Celotti A., 1999, ApJ, 511, L93

Ghisellini G., Ghirlanda G., Nava L., Celotti A., 2010, MNRAS, 403, 926

Giannios D., 2010, MNRAS, 403, L51

Gilmozzi R., Spyromilio J., 2008, SPIE, 7012

Giuliani A., et al., 2010, ApJ, 708, L84

Goad M. R., et al., 2007, A&A, 476, 1401

Godet O., et al., 2006, A&A, 452, 819

Gogus E., et al., 2011, arXiv, arXiv:1107.4050

Golenetskii S., et al., 2005, GCN Circ., 4197, 1

Golenetskii S., Aptekar R., Mazets E., Pal'Shin V., Frederiks D., Cline T., 2006, GCN Circ., 4564, 1

Golenetskii S., Aptekar R., Mazets E., Pal'Shin V., Frederiks D., Cline T., 2007, GCN Circ., 6615, 1

Golenetskii S., et al., 2011, GCN Circ., 11893, 1

Goodman J., 1986, ApJ, 308, L47

Gorgas, J., Cardiel, N., Pedraz, S., González, J. J., 1999, A&AS, 139, 29

Gorosabel J., et al., 2005, A&A, 437, 411

Götz D., Laurent P., Lebrun F., Daigne F., Bošnjak Ž., 2009, ApJ, 695, L208

Götz D., et al., 2009b, AIPC, 1133, 25

Grindlay J. E., Craig W. W., Gehrels N. A., Harrison F. A., Hong J., 2003, SPIE, 4851, 331

Grupe D., Burrows D. N., Patel S. K., Kouveliotou C., Zhang B., Mészáros P., Wijers R. A. M., Gehrels N., 2006, ApJ, 653, 462

Guiriec, S., et al., 2011, ApJL, 727, L33

Halpern J. P., et al., 2000, ApJ, 543, 697

Hamuy M., Suntzeff N. B., Heathcote S. R., Walker A. R., Gigoux P., Phillips M. M., 1994, PASP, 106, 566

Harrison F. A., et al., 1999, ApJ, 523, L121

Heise J., in't Zand J. J. M., Kulkarni S. R., Costa E., 2001, GCN Circ., 1138, 1

Hild S., et al., 2011, CQGra, 28, 094013

Hirschi R., Meynet G., Maeder A., 2005, A&A, 443, 581

Hjorth J., et al., 2003, Nature, 423, 847

Hjorth J., et al., 2005a, Nature, 437, 859

Hjorth J., et al., 2005b, ApJ, 630, L117

Hogg, D. W., Pahre, M. A., McCarthy, J. K., Cohen, J. G., Blandford, R., Smail, I., & Soifer, B. T., 1997, MNRAS, 288, 404

Horváth I., 1998, ApJ, 508, 757

Hotokezaka K., Kyutoku K., Okawa H., Shibata M., Kiuchi K., 2011, PhRvD, 83, 124008

Hullinger D., et al., 2005, GCN Circ., 4400, 1

Hulse R. A., Taylor H. J., 1974, BAAS, 6, 453

Hurley K., et al., 1996, ApJ, 463, L13

Hurley, K. et al., 1999, *Nature* 397, 41

Hurley K., et al., 2000b, *ApJ*, 528, L21

Hurley K., et al., 2000a, *ApJ*, 534, L23

Hurley K., et al., 2005, *Nature*, 434, 1098

Hurley, K., et al., 2006, *Ap. J. Supp. Ser.* 164, 124

Hurley K., et al., 2010a, *AIPC*, 1279, 330

Hurley K., et al., 2010b, *MNRAS*, 403, 342

Hurley K., et al., 2011, *GCN Circ.*, 1900, 1

Ilbert O., et al., 2006, *A&A*, 457, 841

Immler S., Kuntz K. D., 2005, *ApJ*, 632, L99

Immler S., Holland S. T., 2008, *GCN Circ.*, 8277, 1

Inan U. S., Lehtinen N. G., Moore R. C., Hurley K., Boggs S., Smith D. M., Fishman G. J., 2007, *GeoRL*, 34, 8103

Inoue S., 2004, *MNRAS*, 348, 999

Israel G. L., et al., 2010, *MNRAS*, 408, 1387

Jakobsson, P., Hjorth, J., Fynbo, J. P. U., Watson, D., Pedersen, K., Björnsson, G., & Gorosabel, J., 2004, *ApJL*, 617, L21

Jakobsson, P., et al., 2006, *A&A*, 447, 897

Jakobsson P., Fynbo J. P. U., 2007, *arXiv*, arXiv:0704.1421

Janiuk A., Moderski R., Proga D., 2008, *ApJ*, 687, 433

Janka H.-T., Aloy M.-A., Mazzali P. A., Pian E., 2006, *ApJ*, 645, 1305

Jelinek M., Kubanek P., Prouza M., Nekola M. F., Hudec R., 2005, *GCN Circ.*, 4319, 1

Jin Z. P., Yan T., Fan Y. Z., Wei D. M., 2007, ApJ, 656, L57

Kalberla P. M. W., Burton, W. B., Hartmann, D., Arnal, E. M., Bajaja, E., Morras, R., Pöppel W. G. L.,  
2005, A&A, 440, 775

Kaneko Y., Preece R. D., Briggs M. S., Paciesas W. S., Meegan C. A., Band D. L., 2006, ApJS, 166,  
298

Kann D. A., et al., 2010, ApJ, 720, 1513

Kauffmann, G., et al., 2003, MNRAS, 341, 33

Kennicutt R. C., Jr., 1998, ARA&A, 36, 189

Kewley, L. J., Ellison, S. L., 2008, ApJ, 681, 1183

King A. R., Pringle J. E., Wickramasinghe D. T., 2001, MNRAS, 320, L45

King A., O'Brien P. T., Goad M. R., Osborne J., Olsson E., Page K., 2005, ApJ, 630, L113

King A., Olsson E., Davies M. B., 2007, MNRAS, 374, L34

Klebesadel R. W., Strong I.B., & Olson R.A., 1973, ApJ, 182, L85

Klebesadel R. W., Evans W. D., Glore J. P., Spalding R. E., Wymer F. J., 1980, ITGRS, 18, 76

Kobayashi S., Piran T., Sari R., 1997, ApJ, 490, 92

Kocevski D., et al., 2010, MNRAS, 404, 963

Kouveliotou C., Meegan C. A., Fishman G. J., Bhat N. P., Briggs M. S., Koshut T. M., Paciesas W. S.,  
Pendleton G. N., 1993, ApJ, 413, L101

Krimm H., et al., 2006, GCN Circ., 5704, 1

Krimm H., et al., 2007, GCN Circ., 6732, 1

Krimm H. A., Beardmore A. P., Gehrels N., Page K. L., Palmer D. M., Starling R. L. C., Ukwatta T. N.,  
2008, GCN Circ., 8312, 1

Krimm H., et al., 2008b, GCN Circ., 7926, 1

Krimm H. A., et al., 2009, GCN Circ., 9551, 1

Krimm H. A., et al., 2010, GCN Circ., 11467, 1

Kuin N. P. M., Hoversten E. A., 2009, GCN Circ., 9342, 1

Kuin N. P. M., Gelbord J. M., 2010, GCN Circ., 11472, 1

Kulkarni S. R., Frail D. A., 1993, Nature, 365, 33

Kulkarni S. R., et al., 1998, Nature, 395, 663

Kulkarni S. R., et al., 1999, ApJ, 522, L97

Kulkarni S. R., Kaplan D. L., Marshall H. L., Frail D. A., Murakami T., Yonetoku D., 2003, ApJ, 585, 948

Kulkarni, S. R., 2005, astro, arXiv:astro-ph/0510256

Kumar P., Panaitescu A., 2000, ApJ, 541, L51

Kumar P., Panaitescu A., 2008, MNRAS, 391, L19

Kumar H. S., Safi-Harb S., 2010, ApJ, 725, L191

La Parola V., et al., 2006, A&A, 454, 753

Landsman W., Holland S., 2010, GCN Circ., 892, 1

Langer N., Norman C. A., 2006, ApJ, 638, L63

Lattimer, J. M., Schramm, D. N., 1976, ApJ, 210, 549

Lattimer J. M., Prakash M., Masak D., Yahil A., 1990, ApJ, 355, 241

Lattimer J. M., Prakash M., 2004, Sci, 304, 536

Lattimer J. M., Prakash M., 2010, arXiv, arXiv:1012.3208

Lazzati D., Rossi E., Ghisellini G., Rees M. J., 2004, MNRAS, 347, L1

Lazzati D., Ghirlanda G., Ghisellini G., 2005, MNRAS, 362, L8

Lee W. H., Ramirez-Ruiz E., 2007, NJPh, 9, 17

Lee J. C., et al., 2011, ApJS, 192, 6

Leibler C. N., Berger E., 2010, ApJ, 725, 1202

Lenters G. T., et al., 2003, ApJ, 587, 761

Levan A., et al., 2005, ApJ, 622, 977

Levan A. J., et al., 2006a, ApJ, 648, L9

Levan A. J., Wynn G. A., Chapman R., Davies M. B., King A. R., Priddey R. S., Tanvir N. R., 2006b,  
MNRAS, 368, L1

Levan, A. J. et al. 2007 MNRAS, 378, L1439

Levan A. J., et al., 2008, MNRAS, 384, 541

Levan A. J., Tanvir N. R., Hjorth J., Malesani D., de Ugarte Postigo A., D'Avanzo P., 2009, GCN Circ.,  
10154, 1

Levan A. J., Graham J., Fruchter A., Tanvir N., Cucchiara A., Fox D., Berger E., Chornock R., 2010,  
GCN Circ., 10349, 1

Levan A. J., Tanvir N., Baker D., 2011, GCN Circ., 11559, 1

Levesque E. M., et al., 2009, MNRAS, 1657

Levesque E. M., et al., 2010, MNRAS, 401, 963

Levesque E. M., Kewley L. J., Graham J. F., Fruchter A. S., 2010b, ApJ, 712, L26

Levesque E. M., Soderberg A. M., Kewley L. J., Berger E., 2010c, ApJ, 725, 1337

Li, L.-X., Paczyński, B., 1998, ApJ, 507, L59

Li W., Chornock R., & Filippenko A.V., 2009, GCN Circ., 9358, 1

Liang E. W., et al., 2006, ApJ, 646, 351

Lipunov, V. et al. 2005, GCN Circ. 4206

Lorimer D. R., 2005, LRR, 8, 7

Lupton, R. 2005, <http://www.sdss.org/dr4/algorithms/sdssUBVRITransform.html#Lupton2005>

Lyons N., O'Brien P. T., Zhang B., Willingale R., Troja E., Starling R. L. C., 2010, MNRAS, 402, 705

MacFadyen A. I., Woosley S. E., 1999, ApJ, 524, 262

Magnier E. A., Prins S., van Paradijs J., Lewin W. H. G., Supper R., Hasinger G., Pietsch W., Truemper J., 1995, A&AS, 114, 215

Magrini L., Perinotto M., Corradi R. L. M., Mampaso A., 2001, A&A, 379, 90

Malesani D., et al., 2004, ApJ, 609, L5

Malesani, D., et al., 2008, GCN Circ., 8190, 1

Malesani D., de Ugarte Postigo A., Levan A. J., Tanvir N. R., Hjorth J., D'Avanzo P., 2009, GCN Circ., 10156, 1

Mallozzi R. S., Paciesas W. S., Pendleton G. N., Briggs M. S., Preece R. D., Meegan C. A., Fishman G. J., 1995, ApJ, 454, 597

Mangano V., et al., 2007, A&A, 470, 105

Marcillac, D., Elbaz, D., Charlot, S., Liang, Y. C., Hammer, F., Flores, H., Cesarsky, C., Pasquali, A., 2006, A&A, 458, 369

Margutti, R., Guidorzi, C., Chincarini, G., Bernardini, M. G., Genet, F., Mao, J., & Pasotti, F., 2010, MNRAS, 406, 2149

Margutti R., et al., 2011, arXiv, arXiv:1107.1740

Markwardt C., et al., 2006a, GCN Circ., 5330, 1

Markwardt C., et al., 2006b, GCN Circ., 4873, 1

Markwardt C., et al., 2006c, GCN Circ., 5882, 1

Markwardt C. B., et al., 2009, GCN Circ., 10152, 1

Markwardt C. B., et al., 2010, GCN Circ., 10338, 1

Martin D. C., et al., 2005, ApJ, 619, L1

Matonick D. M., Fesen R. A., 1997, ApJS, 112, 49

Matsuoka M., et al., 2009, PASJ, 61, 999

Mazzali P. A., et al., 2007, ApJ, 661, 892

Mazzali P. A., et al., 2008, Science, 321, 1185

Mazets E. P., et al., 1979, Nature, 282, 587

Mazets E. P., Golenetskii S. V., 1981, Ap&SS, 75, 47

Mazets E. P., Golenetskii S. V., Gurian I. A., Ilinskii V. N., 1982, Ap&SS, 84, 173

Mazets E. P., et al., 1999, Astron. Lett., 25, 635

Mazets, E. et al., 2004, in Proc. of the Third Rome Workshop on Gamma-Ray Bursts in the Afterglow Era, Eds. M. Feroci, F. Frontera, N. Masetti, and L. Piro, ASP Conf. Ser. 312, 102

Mazets E. P., et al., 2008, ApJ, 680, 545

McBreen, S., et al., 2008, ApJ, 677, L85

McBreen S., et al., 2010, A&A, 516, A71

McMahon R. G., Walton N. A., Irwin M. J., Lewis J. R., Bunclark P. S., Jones D. H., 2001, NewAR, 45, 97

McMahon E., Kumar P., Piran T., 2006, MNRAS, 366, 575

Meegan C. A., Fishman G. J., Wilson R. B., Horack J. M., Brock M. N., Paciesas W. S., Pendleton G. N., Kouveliotou C., 1992, Nature, 355, 143

Meegan C., et al., 2009, ApJ, 702, 791

Melandri A., et al., 2008, *ApJ*, 686, 1209

Mereghetti S., Cremonesi D., Feroci M., Tavani M., 2000, *A&A*, 361, 240

Mereghetti S., Götz D., Borkowski J., 2004, *AdSpR*, 34, 2729

Mereghetti, S., et al., 2005, *Ap. J.* 624, L105

Mereghetti S., 2008, *A&ARv*, 15, 225

Meszáros P., Rees M. J., 1992, *ApJ*, 397, 570

Mészáros P., Rees M. J., 1993, *ApJ*, 418, L59

Mészáros P., Rees M. J., 1997, *ApJ*, 482, L29

Mészáros P., 2001, *Sci*, 291, 79

Mészáros P., 2006, *RPPh*, 69, 2259

Metzger M. R., Djorgovski S. G., Kulkarni S. R., Steidel C. C., Adelberger K. L., Frail D. A., Costa E., Frontera F., 1997, *Nature*, 387, 878

Metzger, B. D., Piro, A. L., Quataert, E., 2008, *MNRAS*, 390, 781

Metzger B. D., Quataert E., Thompson T. A., 2008, *MNRAS*, 385, 1455

Metzger B. D., et al., 2010, *MNRAS*, 406, 2650

Metzger B. D., Arcones A., Quataert E., Martínez-Pinedo G., 2010b, *MNRAS*, 402, 2771

Metzger B. D., Giannios D., Thompson T. A., Bucciantini N., Quataert E., 2011, *MNRAS*, 413, 2031

Mineo T., et al., 2005a, *GCN Circ.*, 4188, 1

Mirabel F. I., Fuchs Y., 1999, *astro*, arXiv:astro-ph/9912446

Molkov S., Hurley K., Sunyaev R., Shtykovsky P., Revnivtsev M., Kouveliotou C., 2005, *A&A*, 433, L13

Moorwood A. F., 1997, *SPIE*, 2871, 1146

Morrison I. A., Baumgarte T. W., Shapiro S. L., 2004, ApJ, 610, 941

Mukherjee S., Feigelson E. D., Jogesh Babu G., Murtagh F., Fraley C., Raftery A., 1998, ApJ, 508, 314

Mundell C. G., et al., 2007, Sci, 315, 1822

Nakagawa Y. E., Sakamoto T., Sato G., Gehrels N., Hurley K., Palmer D. M., 2008, ApJ, 681, L89

Nakajima, H., Shimokawabe, T., Mori, Y. A., Kudou, Y., Kawai, N., 2008, GCN Circ., 8202, 1

Nakar E., Gal-Yam A., Piran T., Fox D. B., 2006, ApJ, 640, 849

Nakar E., 2007, AdSpR, 40, 1224

Nakar E., Piran T., 2011, arXiv, arXiv:1102.1020

Narayan, R., Paczynski, B., Piran, T., 1992, ApJ, 395, L83

Nardini M., Ghisellini G., Ghirlanda G., Celotti A., 2011, AdSpR, 47, 1407

Nice D. J., Splaver E. M., Stairs I. H., Löhmer O., Jessner A., Kramer M., Cordes J. M., 2005, ApJ, 634, 1242

Nicuesa Guelbenzu A., et al., 2011, A&A, 531, L6

Nomoto K., Kondo Y., 1991, ApJ, 367, L19

Norris J. P., Share G. H., Messina D. C., Dennis B. R., Desai U. D., Cline T. L., Matz S. M., Chupp E. L., 1986, ApJ, 301, 213

Norris J. P., Nemiroff R. J., Bonnell J. T., Scargle J. D., Kouveliotou C., Paciesas W. S., Meegan C. A., Fishman G. J., 1996, ApJ, 459, 393

Norris J. P., Marani G. F., Bonnell J. T., 2000, ApJ, 534, 248

Norris, J. P., & Bonnell, J. T. 2006, ApJ, 643, 266

Norris J. P., Gehrels N., Scargle J. D., 2010, ApJ, 717, 411

Norris J. P., Gehrels N., Scargle J. D., 2011, ApJ, 735, 23

Nousek J. A., et al., 2006, ApJ, 642, 389

Novak J., 1998, PhRvD, 57, 4789

Nysewander, M., Fruchter, A. S., Pe'er, A., 2009, ApJ, 701, 824

Oates S. R., Ziaeeepour H., 2008, GCN Circ., 7642, 1

Oates S. R., 2009, GCN Circ., 10157, 1

Oates S. R., Cummings J. R., 2009, GCN Circ., 9265, 1

O'Brien P. T., Willingale R., Osborne J. P., Goad M. R., 2006, NJPh, 8, 121

O'Brien, P. T., et al., 2006b, ApJ, 647, 1213

Oechslin R., Janka H.-T., Marek A., 2007, A&A, 467, 395

Ofek, E. et al., 2005, GCN Circ. 4208

Ofek E. O., et al., 2006, ApJ, 652, 507

Ofek E. O., 2007, ApJ, 659, 339

Ofek, E. O., et al., 2007, ApJ, 662, 1129

Ofek E. O., et al., 2008, ApJ, 681, 1464

Oppenheimer B. R., Bloom J. S., Eikenberry S. S., Matthews K., 1998, ATel, 26, 1

Osborne J.P., Beardmore A.P., Evans P.A., Goad M.R., 2009, GCN Circ., 9367, 1

O'Shaughnessy R., Kim C., Kalogera V., Belczynski K., 2008, ApJ, 672, 479

Ott C. D., Burrows A., Thompson T. A., Livne E., Walder R., 2006, ApJS, 164, 130

Özel F., Baym G., Güver T., 2010, PhRvD, 82, 101301

Özel F., Psaltis D., Ransom S., Demorest P., Alford M., 2010, ApJ, 724, L199

Pace C.J., Pearson R.L., Ward Moody J., 2009, GCN Circ., 9371, 1

Paciesas W. S., et al., 1999, ApJS, 122, 465

Paczynski B., 1986, ApJ, 308, L43

Paczynski B., Xu G., 1994, ApJ, 427, 708

Paczynski B., 1998, ApJ, 494, L45

Pagani, C., Racusin, J., 2008, GCN Circ., 8185, 1

Palmer D. M., et al., 2005, Nature, 434, 1107

Panaitescu A., Kumar P., 2001, ApJ, 554, 667

Panaitescu A., 2006, MNRAS, 367, L42

Panaitescu A., 2011, MNRAS, 400

van Paradijs, J., et al., 1997, Nature, 386, 686

Parsons A., et al., 2007, GCN Circ., 6656, 1

Paturel G., Petit C., Prugniel P., Theureau G., Rousseau J., Brouty M., Dubois P., Cambrésy L., 2003, A&A, 412, 45

Pei Y. C., 1992, ApJ, 395, 130

Peng, C. Y., Ho, L. C., Impey, C. D. & Rix, H.-W. 2002, AJ, 124, 266

Perley D. A., Thoene C. C., Bloom J. S., 2007, GCN Circ., 6774, 1

Perley D. A., Bloom J. S., Modjaz M., Miller A. A., Shiode J., Brewer J., Starr D., Kennedy R., 2008, GCN Circ., 7889, 1

Perley, D. A., et al., 2009a, ApJ, 696, 1871

Perley D.A., Kislak M., Ganeshalingam M., 2009b, GCN Circ., 9372, 1

Pettini, M. & Pagel, B. E. J. 2004, MNRAS, 348, L59

Pian E., et al., 2006, Nature, 442, 1011

Pineau F. X., Motch C., Carrera F., Della Ceca R., Derrière S., Michel L., Schwobe A., & Watson M., G., 2011, A&A, 527, A126

Piran T., 1999, NuPhS, 70, 431

Piran T., 2004, RvMP, 76, 1143

Piranomonte S., et al., 2008, A&A, 491, 183

Piro L., 2001, AIPC, 599, 295

Piro A. L., Ott C. D., 2011, arXiv, arXiv:1104.0252

Poggianti, B. M., Barbaro, G., 1997, A&A, 325, 1025

Popham R., Woosley S. E., Fryer C., 1999, ApJ, 518, 356

Prochaska, J. X., et al. 2006, ApJ, 642, 989

Pshirkov M. S., Postnov K. A., 2010, Ap&SS, 330, 13

Quilligan F., McBreen B., Hanlon L., McBreen S., Hurley K. J., Watson D., 2002, A&A, 385, 377

Racusin J. L., et al., 2008, Nature, 455, 183

Racusin J. L., et al., 2009, ApJ, 698, 43

Ramirez-Ruiz E., Fenimore E. E., 2000, ApJ, 539, 712

Ramirez-Ruiz E., Merloni A., 2001, MNRAS, 320, L25

Razzaque S., Mészáros P., Waxman E., 2003, PhRvL, 90, 241103

Read J. S., Markakis C., Shibata M., Uryū K., Creighton J. D. E., Friedman J. L., 2009, PhRvD, 79, 124033

Rees M. J., Meszaros P., 1992, MNRAS, 258, 41P

Rees M. J., Meszaros P., 1994, ApJ, 430, L93

Rezzolla L., Giacomazzo B., Baiotti L., Granot J., Kouveliotou C., Aloy M. A., 2011, ApJ, 732, L6

Rhoads J. E., 1997, ApJ, 487, L1

Rhoads J. E., 1999, ApJ, 525, 737

Rieke, G. H., Lebofsky, M. J. 1985, ApJ, 288, 618

Rizzuto D., et al., 2007, MNRAS, 379, 619

Robitaille T. P., Whitney B. A., 2010, ApJ, 710, L11

Rolleston, W. R. J., Smartt, S. J., Dufton, P. L., Ryans, R. S. I., 2000, A&A, 363, 537

Roming P. W. A., et al., 2005, SSRv, 120, 95

Roming P. W. A., et al., 2006, ApJ, 651, 985

Rosswog S., Liebendörfer M., Thielemann F.-K., Davies M. B., Benz W., Piran T., 1999, A&A, 341, 499

Rosswog S., Ramirez-Ruiz E., 2003, MNRAS, 343, L36

Rosswog S., 2005, ApJ, 634, 1202

Rosswog S., 2007, MNRAS, 376, L48

Rosswog S., 2010, arXiv, arXiv:1012.0912

Rowlinson A., et al., 2010a, MNRAS, 408, 383

Rowlinson, A., et al. 2010b, MNRAS, 409, 513

Rowlinson A., O'Brien P. T., Tanvir N. R., Levan A. J., 2011, GCN.1, 1909, 1

Ruderman M., 1975, NYASA, 262, 164

Rujopakarn W., Schaefer B.E., Rykoff E.S., 2009, GCN Circ., 9357, 1

Rutledge R. E., Fox D. B., 2004, MNRAS, 350, 1288

Sakamoto T., et al., 2005, GCN Circ., 3305, 1

Sakamoto T., et al., 2007, GCN Circ., 6087, 1

Sakamoto T., et al., 2008a, ApJ, 679, 570

Sakamoto T., et al., 2008b, ApJS, 175, 179

Sakamoto T., et al., 2008c, GCN Circ., 7761, 1

Sakamoto T., Beardmore A.P., 2009, GCN Circ., 9365, 1

Sakamoto T., et al., 2011, ApJS, 195, 2

Salvaterra R., et al., 2009, Nature, 461, 1258

Sandage A., Tammann G. A., 2006, ARA&A, 44, 93

Sari R., Piran T., Narayan R., 1998, ApJ, 497, L17

Sari R., Piran T., Halpern J. P., 1999, ApJ, 519, L17

Sari R., Piran T., 1999a, A&AS, 138, 537

Sari R., Piran T., 1999b, ApJ, 517, L109

Sathyaprakash B. S., Schutz B. F., Van Den Broeck C., 2010, CQGra, 27, 215006

Sato G., et al., 2005, GCN Circ., 3793, 1

Sato G., et al., 2005b, GCN Circ., 4318, 1

Sato G., et al., 2006, GCN Circ., 5381, 1

Sato G., et al., 2007a, ApJ, 657, 359

Sato G., et al., 2007b, GCN Circ., 7148, 1

Sato G., et al., 2007c, GCN Circ., 6086, 1

Sato G., et al., 2009, GCN Circ., 9263, 1

Savchenko V., et al., 2011, GCN Circ., 11890, 1

Schlegel, D. J., Finkbeiner, D. P. & Davis, M. 1998, ApJ, 500, 525

Schmidt W. K. H., 1978, Nature, 271, 525

Schneid E. J., et al., 1992, A&A, 255, L13

Seigel M.H., Beardmore A.P., 2005, GCN Circ., 9369, 1

Sekiguchi Y., Kiuchi K., Kyutoku K., Shibata M., 2011, PhRvL, 107, 051102

Shaviv N. J., Dar A., 1995, ApJ, 447, 863

Shen R.-F., Zhang B., 2009, MNRAS, 398, 1936

Shibata M., Taniguchi K., 2006, PhRvD, 73, 064027

Skrutskie M. F., et al., 2006, AJ, 131, 1163

Smartt, S. J., Rolleston, W. R. J., 1997, ApJ, 481, L47

Smith, D. M. et al., 2002, Solar Physics, 210, 33

Soderberg A. M., et al., 2005, ApJ, 627, 877

Soderberg A. M., et al., 2006, ApJ, 650, 261

Soria R., Perna R., 2008, ApJ, 683, 767

Stanek K. Z., et al., 2003, ApJ, 591, L17

Stappers B. W., et al., 2011, A&A, 530, A80

Starling R. L. C., et al., 2008, MNRAS, 384, 504

Starling R. L. C., et al., 2009, MNRAS, 400, 90

Starling R. L. C., et al., 2011, MNRAS, 411, 2792

Steele I. A., Mundell C. G., Smith R. J., Kobayashi S., Guidorzi C., 2009, Nature, 462, 767

Stella L., Dall’Osso S., Israel G. L., Vecchio A., 2005, ApJ, 634, L165

Stratta G., et al., 2007, A&A, 474, 827

Svensson K. M., Levan A. J., Tanvir N. R., Fruchter A. S., Strolger L.-G., 2010, MNRAS, 405, 57

Swartz D. A., Ghosh K. K., McCollough M. L., Pannuti T. G., Tennant A. F., Wu K., 2003, ApJS, 144, 213

Tanvir, N. R., et al., 2004, MNRAS, 352, 1073

Tanvir, N. R., Chapman, R., Levan, A. J., & Priddey, R. S. 2005, *Nature*, 438, 991

Tanvir N. R., et al., 2009, *Nature*, 461, 1254

Tanvir N. R., et al., 2010a, *ApJ*, 725, 625

Tanvir N. R., Levan A. J., 2010b, *GCN Circ.*, 10905, 1

Tauris T. M., van den Heuvel E. P. J., 2006, *csxs.book*, 623

Tauris T. M., Langer N., Kramer M., 2011, *MNRAS*, 1138

Taylor J. H., Wolszczan A., Damour T., Weisberg J. M., 1992, *Nature*, 355, 132

Tedds J. A., 2009, *arXiv*, arXiv:0906.1535

Thilker D. A., et al., 2010, *ApJ*, 714, L171

Thompson C., 1994, *MNRAS*, 270, 480

Thompson C., Duncan R. C., 1995, *MNRAS*, 275, 255

Thompson C., Lyutikov M., Kulkarni S. R., 2002, *ApJ*, 574, 332

Thompson T. A., Chang P., Quataert E., 2004, *ApJ*, 611, 380

Thompson T. A., 2007, *RMxAC*, 27, 80

Thomsen B., et al., 2004, *A&A*, 419, L21

Thöne, C. C., et al. 2008, *ApJ*, 676, 1151

Thöne C. C., et al., 2011a, *MNRAS*, 414, 479

Thöne C. C., et al., 2011, *MNRAS*, 414, 479

Thronson, H. A., Jr., & Greenhouse, M. A. 1988, *ApJ*, 327, 671

Tiengo A., et al., 2007, *Ap&SS*, 308, 33

Tody D., 1993, *ASPC*, 52, 173

Tominaga N., Deng J., Mazzali P. A., Maeda K., Nomoto K., Pian E., Hjorth J., Fynbo J. P. U., 2004, ApJ, 612, L105

Tristram P., Castro-Tirado A. J., Yock P., Gorosabel, J., de Ugarte Postigo, A., 2008, GCN Circ., 8181, 1

Troja E., et al., 2007, ApJ, 665, 599

Troja, E., King, A. R., O'Brien, P. T., Lyons, N., & Cusumano, G. 2008, MNRAS, 385, L10

Ubertini P., Corsi A., Foley S., McGlynn S., de Cesare G., Bazzano A., 2011, AdSpR, 47, 1374

Ukwatta T., et al., 2008, GCN Circ., 7673, 1

Ukwatta T. N., et al., 2009, GCN Circ., 9337, 1

Ukwatta, T. N., et al. 2010, ApJ, 711, 1073

Usov V. V., 1992, Nature, 357, 472

Valentim R., Rangel E., Horvath J. E., 2011, MNRAS, 409

van den Heuvel E. P. J., 2010, NewAR, 54, 140

van Eerten H. J., MacFadyen A. I., 2011, arXiv, arXiv:1105.2485

van Kerkwijk M. H., Breton R. P., Kulkarni S. R., 2011, ApJ, 728, 95

Vasisht G., Kulkarni S. R., Frail D. A., Greiner J., 1994, ApJ, 431, L35

Vianello G., Götz D., Mereghetti S., 2009, A&A, 495, 1005

Villasenor J. S., et al., 2005, Nature, 437, 855

Virgili F. J., Zhang B., O'Brien P., Troja E., 2011, ApJ, 727, 109

Vlahakis, N., Königl, A., 2003, ApJ, 596, 1104

Vrba F. J., Henden A. A., Luginbuhl C. B., Guetter H. H., Hartmann D. H., Klose S., 2000, ApJ, 533, L17

Wainwright, C., Berger, E., Penprase, B. E. 2007, ApJ, 657, 367

Walter F., Brinks E., de Blok W. J. G., Bigiel F., Kennicutt R. C., Thornley M. D., Leroy A., 2008, AJ, 136, 2563

Walton N. A., Richards A. M. S., Padovani P., Allen M. G., 2006, IAUS, 232, 398

Wang X. Y., Wu X. F., Fan Y. Z., Dai Z. G., Zhang B., 2005, ApJ, 623, L29

Wang C., Lai D., Han J. L., 2006, ApJ, 639, 1007

Watson, M. G., et al., 2009, A&A, 493, 339

Waxman E., 1997, ApJ, 485, L5

Waxman E., Kulkarni S. R., Frail D. A., 1998, ApJ, 497, 288

Weisberg J. M., Taylor J. H., 2005, ASPC, 328, 25

Wenzel K. P., Marsden R. G., Page D. E., Smith E. J., 1992, A&AS, 92, 207

Wheeler J. C., Yi I., Höflich P., Wang L., 2000, ApJ, 537, 810

Wiersema, K., et al. 2007, A&A, 464, 529

Wigger C., Hajdas W., Arzner K., Güdel M., Zehnder A., 2004, ApJ, 613, 1088

Williams G.G., Updike A., & Milne P.A., 2009, GCN Circ., 9360, 1

Willingale R., et al., 2007, ApJ, 662, 1093

Winkler C., Pace O., Volonté S., 1993, ESAJ, 17, 207

Woosley S. E., 1993, ApJ, 405, 273

Woosley S. E., Bloom J. S., 2006, ARA&A, 44, 507

Xin L.-P., et al., 2011, MNRAS, 410, 27

Xu D., et al., 2009, ApJ, 696, 971

Yamaoka, K., et al., 2009, PASJ 61, S35

- Yi, T., Liang, E., Qin, Y., & Lu, R. 2006, MNRAS, 367, 1751
- Yoon S.-C., Langer N., Norman C., 2006, A&A, 460, 199
- Yoshida A., Namiki M., Otani C., Kawai N., Murakami T., Ueda Y., Shibata R., Uno S., 2000, AdSpR, 25, 761
- Yu Y., Huang Y.-F., 2007, ChJAA, 7, 669
- Yu Y.-W., Cheng K. S., Cao X.-F., 2010, ApJ, 715, 477
- Zhang B., Mészáros P., 2001, ApJ, 552, L35
- Zhang B., Mészáros P., 2004, IJMPA, 19, 2385
- Zhang B., Fan Y. Z., Dyks J., Kobayashi S., Mészáros P., Burrows D. N., Nousek J. A., Gehrels N., 2006, ApJ, 642, 354
- Zhang, B., Zhang, B.-B., Liang, E.-W., Gehrels, N., Burrows, D. N., Mészáros, P., 2007, ApJ, 655, L25
- Zhang, B., et al., 2009, ApJ, 703, 1696
- Zhang B., Pe'er A., 2009b, ApJ, 700, L65
- Zhang B.-B., et al., 2011, ApJ, 730, 141
- Zou Y.-C., Fan Y.-Z., Piran T., 2009, MNRAS, 396, 1163